Going the distance: Metropolitan scale entanglement of NV-centers over deployed telecom fiber

Stolk, A.J.

DOI
10.4233/uuid:7bb93266-4657-4622-ab62-7ed4de9f6278

Publication date
2024

Document Version
Final published version

Citation (APA)
Stolk, A. J. (2024). *Going the distance: Metropolitan scale entanglement of NV-centers over deployed telecom fiber.* [Dissertation (TU Delft), Delft University of Technology].
https://doi.org/10.4233/uuid:7bb93266-4657-4622-ab62-7ed4de9f6278

Important note
To cite this publication, please use the final published version (if applicable).
Please check the document version above.

GOING THE DISTANCE: METROPOLITAN SCALE ENTANGLEMENT OF NV-CENTERS OVER DEPLOYED TELECOM FIBER

Dissertation

for the purpose of obtaining the degree of doctor
at Delft University of Technology,
by the authority of the Rector Magnificus, Prof. dr. ir. T.H.J.J. van der Hagen,
Chair of the Board for Doctorates,
to be defended publicly on
Monday, 11th November 2024 at 15:00 o'clock

by

Adriaan Johannes STOLK

Master of Science in Applied Physics,
Delft University of Technology, The Netherlands,
born in De Ronde Venen, The Netherlands.

This dissertation has been approved by the promotor:
Prof. dr. ir. R. Hanson

Composition of the doctoral committee:

Rector Magnificus	Chairperson
Prof. dr. ir. R. Hanson	Delft University of Technology, Promotor
Dr. ir. T. H. Taminiau	Delft University of Technology, Copromotor
Independent members:	
Prof. dr. C. Becher	Universität des Saarlandes
Prof. dr. H. de Riedmatten	ICFO
Prof. dr. L. DiCarlo	Delft University of Technology
Dr. M. Blaauboer	Delft University of Technology
Dr. B. J. Hensen	Leiden University
Reserve members:	
Prof. dr. ir. L. M. K. Vandersypen	Delft University of Technology

Cover art: Entangled by Bjørn Staal - @_nonfigurativ_
Printed by: Gildeprint - The Netherlands

ISBN: 978-94-6384-662-2

An electronic version of this dissertation is available at
http://repository.tudelft.nl/.

Contents

SUMMARY

The efforts to bring quantum states, fundamental building blocks of nature, from research labs into the outside world are intensifying. The generation and processing of remote quantum states between nodes in a network would allow for new applications such as distributed quantum computing, quantum enhanced sensing and quantum communication. Various demonstrations of such a quantum network have been shown in a lab setting, such as the generation of a three node GHZ-state, device-independent quantum key distribution and memory enhanced quantum communication. Color centers in diamond have been at the forefront of these developments due to their optically active spin interface, long coherence times and nuclear spin registers. The Nitrogen Vacancy (NV-) center is the color center of choice in this thesis, which we describe in Chapter 2. We explain what an NV-center is, how to control it and how we can use them to generate remote entanglement.

Going beyond the previous maximum distance between the nodes (up to 1.3 km) is mainly limited by the photon loss over optical fiber. Furthermore, difference in the wavelength of the photons used for entanglement swapping can prohibit faithful entanglement generation. To overcome both these challenges we show the interference of photons emitted by remote, spectrally detuned NV center-based network nodes. We realize this by using quantum frequency conversion (QFC) to the telecom L-band (Chapter 3). We find a high indistinguishability over the full range of the emission duration, confirming the removal of the spectral information initially present. More importantly, the approach implements fully separated and independent control over the nodes, time-multiplexing of control and quantum signals, and active feedback to stabilize the output frequency.

We show the versatility of the QFC process by using it to link a diamond NV center quantum network node with 795 nm photonic time-bin qubits compatible with Thulium and Rubidium quantum memories (Chapter 4). Using a two-photon quantum interference measurement we find a high indistinguishability of (89±2)% between converted 795 nm photons and the native NV center photons. Additionally, we show that our interface can be used to teleport an unknown quantum state of a 795 nm photonic qubit to the NV center spin qubit, achieving a teleportation fidelity of (76±1)%, above the classical bound.

Next, we turn take on the challenge of generating entanglement between distant nodes in the high photon-loss regime. In this regime, the entanglement generation rate can be significantly increased by using a phase-stable protocol previously used a three node quantum network inside the lab. In Chapter 5 we present a phase synchronization scheme for a metropolitan quantum network, operating in the low-loss telecom L-band. It is specifically designed to solve the challenges introduced by remote operation such as using independent excitation lasers, long communication delays between nodes and optical power limitations. We investigate the resulting optical phase stability of the fully

deployed system over a continuous period of 10 hours, reporting a short-term stability standard deviation of $\sigma \approx 30$ deg and a long-term stability of the average optical phase to within a few degrees.

Finally, we leverage the findings of Chapters 3 and 5 into the first realization of a quantum link between remote quantum processors deployed in the field. We show this by generating heralded entanglement between two NV centers, one in Delft and one in The Hague, connected with 25 km of deployed telecom fiber (Chapter 6). We minimize the effects of fiber photon loss by quantum frequency conversion of the qubit-native photons to the telecom L-band (Chapter 3) and by embedding the link in an extensible phase-stabilized architecture (Chapter 5) enabling the use of the loss-resilient single-photon entangling protocol. The long coherence times and quantum control of the NV-center electron spin allow us to wait for the signal of successful heralding of entanglement in the midpoint in Rijswijk to arrive back on the nodes. This enables us to deliver a single, live entangled state on the nodes irrespective of the heralding detection pattern. This shows the feasibility of building large quantum networks at metropolitan distances, and has all the required capabilities for the realization of future quantum protocols at large distances.

SAMENVATTING

De inspanningen om kwantumtoestanden, de fundamentele bouwstenen van de natuur, van het lab naar de buitenwereld te brengen worden steeds intensiever. Het genereren en verwerken van kwantum toestanden tussen afgezonderde knooppunten in een netwerk kunnen leiden tot nieuwe applicaties zoals gedistribueerde kwantum berekeningen, kwantum-verbeterde sensoren en kwantum communicatie. Verschillende demonstraties van zo'n kwantumnetwerk hebben plaatsgevonden in een lab setting, zoals het genereren van een drie-knooppunt GHZ-toestant, apparaat-onafhankelijke kwantum sleutel distributie en geheugen-verbeterd kwantum communicatie. Kleurcentra in diamaant staan voorop in deze ontwikkelingen door hun optisch actieve interface met een elektronspin, lange coherentie tijden en toegant tot een nucleair spin register. Het Stikstof-Gat centrum is het centrum van onze interesse in deze thesis, die we in Hoofdstuk 2 beschrijven. We bespreken hier wat een Stikstof-Gat centrum is, hoe je deze kunt besturen, en hoe we ze kunnen gebruiken om verstrengelde toestanden te maken over lange afstanden.

Het verbreken van de maximale behaalde afstand tussen twee knooppunten (van 1.3 kilometer) is hoofdzakelijk gelimiteerd door de verliezen van fotonen over optische fiber. Bovendien kunnen verschillen in de golflengte van de photonen die gebruikt worden voor het maken van de verstrengeling er voor zorgen dat er fouten optreden tijdens het proces. Om te laten zien dat we beide uitdagingen kunnen overkomen laten we de interferentie zien van fotonen die zijn uitgestuurd door afzonderlijke, spectraal verstemde Stikstof-Gat centra. Dit doen wij door gebruik te maken van Kwantum Frequentie Conversie (KFC) naar de telecom L band (Hoofdstuk 3). We vinden een hoge graad van ononderscheidbaarheid van de fotonen over de volledige duratie van de uitzendtijd, dat bevestigd de succesvolle verwijdering van de spectrale informatie die er eerst was. Nog belangrijker, de aanpak gebruikt volledige gescheiden en onafhankelijke aansturing van de knooppunten, tijd-multiplexing van aansturing en kwantum signalen en actieve feedback voor de stabilizatie van de uitgangsfrequentie.

In Hoofdstuk 4 laten we de veelzijdigheid zien van het KFC process door het te gebruiken om een op een Stikstof Gat centrum gebaseerde kwantum netwerk knooppunt te koppelen aan 795 nm fotonische time-bin qubits die compatibel zijn met op Thulium en Rubidium gebaseerde kwantumgeheugens. Door gebruik te maken van een tweephoton interferentiemeting vinden we een hoge graad van ononderscheidbaarheid van (89±2)% tussen geconverteerde 795nm fotonen en de oorspronkelijke Stikstof-Gat centrum fotonen. Bovendien laten we zien dat ons interface gebruikt kan worden om een onbekende kwantumstoestand te teleporteren van een 795nm fotonische qubit naar een SG centrum spin qubit, waar we een teleportatiegetrouwheid behaald wordt van (76±1)%, boven de klassieke grens.

Vervolgens pakken we de uitdaging aan voor het genereren van verstrengeling tussen knooppunten op lange afstand in het regime van hoge verliezen van fotonen. In dit

regime kan het de snelheid van het genereren van verstrengeling aanzienlijk verhoofd worden door gebruik te maken van een fase-stabiel protocol, eerder gebruikt voor een 3-knooppunt kwantum netwerk binnen een lab. In Hoofdstuk 5 presenteren we een fase-synchronizatie schema kwantumnetwerken op grootstedelijke schaal, dat werkt in de telecom L-band met lage transmissieverliezen. Het is specifiek ontwikkeld om de uitdagingen op te lossen die worden geintroduceerd door de aansturing op lange afstand, zoals het gebruik van individuele excitatie lasers, lange communicatievertragingen en limitaties op het optische vermogen dat beschikbaar is. We onderzoeken de resulterende stabilizatie van het volledig uitgerolde systeem over een aaneengesloten tijdsperiode van 10 uur, en rapporteren een korte-termijn stabiliteit met een standaardafwijking van $\sigma \approx 30$deg en ene lange-termijn stabiliteit van de gemiddelde optsiche fase van een aantal graden.

Tot slot maken we in Hoofdstuk 6 gebruik van de ontwikkelingen in Hoofdstukken 3 en 5 voor de realizatie van een kwantumverbinding tussen kwantum processoren die in het veld zijn ingezet op lange afstand. We laten dit zien doormiddels het genereren van aangekondigde verstrengeling tussen twee Stikstof Gat centra, één in Delft en één in Den Haag, verbonden door 25km optische fiber in de grond. We minimalizeren de effecten van transmissieverliezen van de fotonen door middel van kwantum frequentie conversie naar de telecom L-band (Hoofdstuk 3) en door de verbinding te combineren met de uitbreidbare fase-stabilizatie architectuur (Hoofdstuk 5). De lange coherentietijd en kwantum aansturing van de Stikstof Gat elektron spin stellen ons in staat om te wachten op het signaal van een succesvolle aankondiging van verstrengeling vanuit het tussenstation in Rijswijk. Hierdoor kunnen we altijd dezelfde en een “levende” verstrengelde toestand afleveren op de knooppunten, onafhankelijke van het klikpatroon van de detectoren in het tussenstation. Dit werk tootn de haalbaarheid van het bouwen van grote kwantumnetwerken op de grootstedelijke schaal, en heeft alle benodigde capabiliteiten voor het realizeren van toekomstige kwantumprotocollen over lange afstanden.

1

INTRODUCTION

Not only is the universe stranger than we think, it is stranger than we can think.

Werner Heisenberg

1.1. COMMUNICATION ACROSS THE GLOBE

Global communication has revolutionized how people interact across the world. Different forms of communication have been realized through history, with people spreading messages by employing runners that relay written messages, electrical signals over copper wire conducting telephone calls and optical fibers travelling the ocean floor as the backbone of the global Internet. It has enabled all kinds of applications: providing a search engine to quickly browse the Internet, conducting financial transactions or performing computations on a remote server. In the age that we live in now, classical communication has made it possible to connect people at any two locations in the world. This has been made possible by transmitting information while following the laws of classical physics.

Different from classical mechanics, Quantum Mechanics (QM) has its roots in the early 20^{th} century. It was used to further understanding of natures' smallest particles such as atoms and sub-atomic particles, as well as describe fundamental properties of energy and radiation. Central to the quantum mechanical description is a concept called quantization, where properties of a particle, such as electronic charge or velocity, are now constrained to have discrete values instead of forming a continuum. The evolution of those properties within those values can be described by the Schrödinger equation[1], which has solutions resembling waves called the wavefunction, and includes wave-like effects such as interference. This wavefunction squared is a probability distribution, and dictates that a property of the particle can take on more than one values at once, so-called superposition. But when measuring this property, the outcome is discrete and reveals only one of the values. Given many identical copies of such a particle in a superposition, the occurrence of the different measurement outcomes reveal the probability distribution that underlies the wavefunction. This fundamentally new way of describing

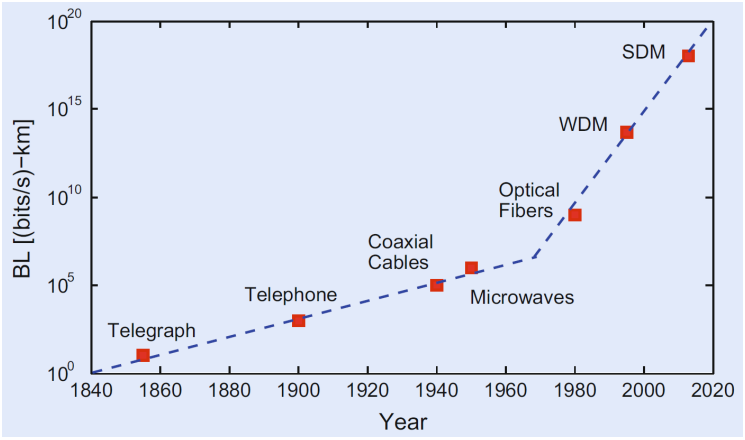

Figure 1.1: Dramatic increase of almost 20 orders of magnitude in the bits-kilometer product during the period 1840–2015. It shows both the combination of rapid increase in transmission bandwidth and distance allowed per repeater. The emergence of new technologies is marked by red squares. Dashed line shows the trend as an aid for the eye. Notice the change in slope around 1977 is when optical fibers were first used for optical communications. Figure taken from *Optical communication: Its history and recent progress, in Optics in Our Time* [8] under the Creative Commons Attribution 4.0 International License.

nature has led to new insights in how the world works, and is currently the best theory for describing the world around us on the small scale.

Later on, these new insights led to a period of various scientific breakthroughs such as the LASER[2] (Light Amplification by Stimulated Emission of Radiation) and Nuclear Magnetic Resonance[3] that found their way into all kinds of modern technology, the so called the first quantum revolution. Some of this technological development, mainly in the field of the generation[4, 5], amplification[6] of light in turn has allowed for an expansion of a global internet to a scale that only few have been able to predict at the time of its inception. These inventions have enabled the impact of classical communication to grow to incredible size, with almost 5 *billion* people connected globally[7] and a over an estimated 4000 petabytes (that is 400.000 gigabytes) of information transmitted per day. This has all been enabled by the incredible rise of new technologies fueling the exponential growth that started in the year 1875, and has even accelerated more than a 100 years later into the 21st century due to the first quantum revolution, as shown in Fig. 1.1. But what QM is probably most well-known for is its counter-intuitive predictions about reality, challenging the way we think about everything around us.

Namely, QM predicts observations of the world around us that have no counterpart in the classical description of nature. One of these predictions is the existence of *entanglement,* where the properties of two objects, no matter how far apart, can not be described individually, but can only by a shared quantum state. For certain quantum states, this leads to correlations in the outcomes if one measures these properties and compares the results, even when the outcomes of a single object are completely random. This effect, when first predicted, has intrigued many scientists[9] and it has taken almost a century to conclusively show[10–13] that it is indeed the better description of nature,

compared to the earlier classical (local-realist) theories scientists had about reality. Furthermore, this property of entanglement is leading us on a new path of technological innovations, the second Quantum Revolution.

1.2. THE SECOND QUANTUM REVOLUTION

The way that the second quantum revolution is changing the world can be summarized as the application of QM on information theory. Information theory describes information and its various operations (e.g. encoding, storage, processing and communication) with a classical smallest unit called bits, which can take the value 0 or 1. Quantum Information (QI) uses a quantum mechanical smallest unit called qubits [14] (with discrete levels 0 and 1) to describe information. However the laws of QM allow for a re-imagining of computing [15, 16]. Concepts such as to superposition and entanglement have turned out to be very powerful concepts for information processing.

This new description of information processing is called quantum computing, and opens a whole new paradigm of information processing, where information can be encoded in superposition of the 0 and 1 state. Additionally information in an entangled states shows correlations correlations between qubits not present in classical bits. It has been shown theoretically that these unique effects can actually be exploited have a computational advantage over the best known classical algorithms[17, 18] for certain tasks. There have been many theoretical proposal for dramatically speeding up classical computations, and current quantum devices are being used to perform computations which are intractable on even the world's largest supercomputers[19–22]. Realizing a speed-up of useful algorithms that help solve humanities problems is one of the great promises of quantum computing, and a big part of this is building the hardware to run the proposed quantum algorithms and designing encodings that can deal with errors that corrupt the computation.

Another area where the application of QM on information theory is expected to lead to new applications is in the field of Quantum Communication (QC). It describes the use of superposition and entanglement between distant parties that want to share information with each, and the extended capabilities beyond what you can do with just sharing bits[23, 24]. A key element to these networks is the sharing of quantum states between many distant parties connected via quantum channels, a so called quantum network. These states can be for instance be measured, where the correlations between generation and the measurement outcomes generate a classical bit string called a secret key[25], so called Quantum Key Distribution (QKD). Laws from QM such as the no-cloning theorem, that states that an arbitrary quantum state can not be perfectly copied[26, 27], prevent an eavesdropper to listen in on the key exchange without being detected. These secret keys are a valuable resource to realize secure communications, and many classical algorithms need a secret key to perform this task. Currently methods for secret key sharing is based on the computational hardness of certain computations[28–30], and are under threat by quantum computation to be rendered no longer secure in the not so distant future. However, when the quantum states that are shared over the network are entangled, one can prove that it is possible to exchange a key without making any assumptions on the powers of the eavesdropper. This Device

Independent QKD provides an alternative to existing technology that is not based on hard computations for its security, but derives its security from the fundamental laws of QM[31, 32].

Entangled states between distant parties can be used for more than DI-QKD. One can for instance scale up the capabilities of a smaller quantum computing system by making multiple copies of that system and linking them together to make a distributed quantum computer[33–35]. This modular approach reduces the complexity of the individual quantum computing system and provides a way to scale up to computing power. Another application is the ability of a user to perform blind quantum computation in the cloud[36], where a client can request a server to perform quantum computations that reports the outcome, without the server knowing which computation has been done with which outcome. Another potential use-case is the use of entanglement to improve time sharing over a network of clocks [37]. By adding the resource of entanglement one could achieve synchronization not possible by performing measurements and classical communication. As is the case with quantum computing, quantum communication is at an early stage, and finding novel applications is an active research field with many exciting developments.

What is already clear at this stage is that the sharing of entangled states between many and distant parties will be a crucial aspect of any application for quantum networks. Generating these entangled states in a controlled lab environment and over short distances is already no small feat. However, in order to reach the true capabilities of a Quantum Internet[38, 39], we will have to be able to realize entangled states over large distances, and allow for many parties all over the world to connect.

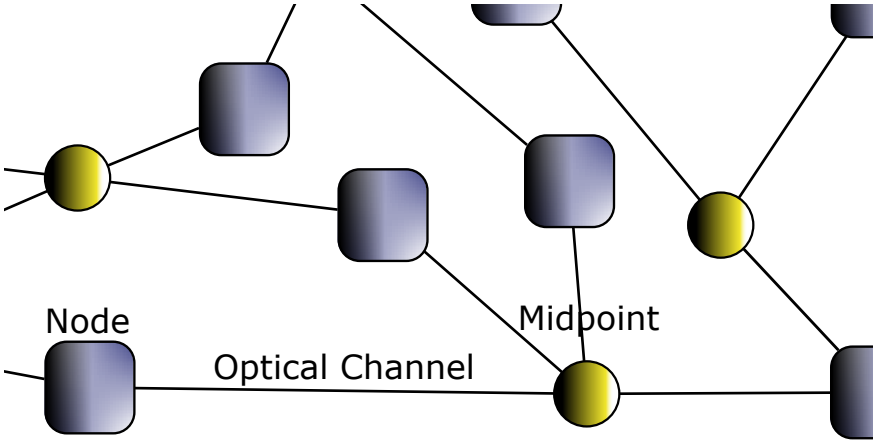

Figure 1.2: **Schematic of a Quantum Network** Quantum nodes are connected via photonic channels, where measurements on photons in a midpoint heralds the entanglement between the nodes

1.3. QUANTUM NETWORKS: STATE OF THE ART

Of the various ways of sharing entanglement between distant locations, using a combination of solid-state qubits at the nodes and photonic flying qubits has the largest capabilities to perform quantum protocols[39], schematically shown in Fig. 1.2. The main advantage of these platforms is that they combine the ability to generate entangled states over large distances, with the processing power of a solid-state qubit system. In general, they achieve this by entangling the photonic qubit with a stationary qubit, and then sending the photonic qubit from two nodes to a central location, where the which-path information is removed via interference on a beamsplitter. Subsequent measurement of the photonic qubits projects the stationary qubits in an entangled state. Various protocols exist for entanglement generation, of which we will discuss two in more details later on in this work.

Platforms pioneering this way of entanglement generation have shown many developments in the past decades towards generating entanglement between distant parties. Various hardware platforms are being investigated, such as trapped ions, neutral atoms, defects in diamond and quantum dots[40–47]. These platforms have shown the ability to generate entangled states in various physical realizations, highlighting the breadth of possible ways to make progress towards the Quantum Internet. One example, and of interest for this thesis, of such physical realizations is the Nitrogen-Vacancy (NV) centre in diamond. It has been extensively studied in the context of quantum networks as a capable end node, as well as a platform for novel sensing techniques.

The NV centre is an optically active defect, where two carbon atoms are replaced a substitutional Nitrogen (N) atom, adjacent to a Vacancy (V). The effective electron spin that is 'captured' by this centre can be optically addressed, where the resonant emission lies in the visible band of the spectrum (637 nm). The spin state of this electron can be used as a qubit, and further developments have culminated into high-fidelity optical initialization (>99.8%) and readout (>97%) of the qubit, fast control using microwave pulses and coherence times of exceeding a second[48] have all been shown. The usage of nuclear spins in the form of ^{13}C atoms in the vicinity of the NV center as memory qubits, has given an additional way for storage and computation. Recent results showed a seven qubit entangled state in a ten qubit register[49], with new sensing techniques showing 50 individual spins[50].

Entanglement generation between remote NV centres has also been shown, via the interference of photons at the natural emission wavelength for distances up to 1.3 km[11] and with rates up to 40 Hz[47]. Leveraging the available memory qubits, entanglement distillation on a two-node link[51], the generation of genuine three-party entangled states and entanglement swapping[52], and teleportation of a quantum state between non-neighbouring nodes[53] on a multi-node network have been pioneering experiments of algorithms on for quantum information processing over a network. These lab demonstrations show the strength of the diamond platform for quantum networks, and provide a valuable platform for the integration of a software control stack[54, 55]

1

1.4. QUANTUM NETWORKS: GOING THE DISTANCE

In order for quantum networks to be useful in the real world, they face additional challenges compared to the previously mentioned lab setting. We can put the challenges in three categories

1. First communication times between the nodes becomes non-negligible (100us+) compared to important timescales of the quantum systems. The large distance also demands that the network nodes operate independently, because it prohibits the sharing of lasers or microwave sources often shared between nodes that are located in the same lab.

2. Second, propagation losses of optical signals whether in free-space or in fiber, increase rapidly with distance. To leverage the already available fiber infrastructure, using a low-loss wavelength[56, 57] can significantly reduce the losses. The fibers connecting nodes will extend for tens of kilometers and photon loss becomes a critical parameter that must be mitigated.

3. Third, the qubit systems must be able to store quantum information for extended times and the network system must be capable of applying real-time feedback to the qubits upon successful entanglement generation. This capability will enable more advanced network applications taht require the heralded delivery of shared entangled states ready for further use.

Solutions to these require a careful examination and understanding of all the different requirements the full system needs to fulfill to generate entanglement. In general, it is necessary to have some frame of reference, either in time (synchronization) or frequency (phase/frequency-locking), to perform experiments with qubits or entanglement. If the distribution of these systems involve the sharing and duplication of the signals of a single source, the losses over a long distance might prevent this from being done directly. Furthermore, the bandwidth with which active feedback can be performed, will be limited by the communication time between those location. While commercial solutions for these challenges are starting to become available[58, 59], it is currently nontrivial to operate these systems, as well as to integrate them into the quantum experiments. Therefore careful examination of all the solutions previously found for these requirements needs to be done, and solutions for all of them need to be compatible with the long distance.

Solution to the second challenge have been explored in various ways. If the natural emission wavelength of the quantum system used is not in a the low loss band, one can perform the conversion of single photons to the telecom band using Quantum Frequency Conversion (QFC)[60]. This has been achieved for various systems, such as quantum dots[61, 62], trapped atoms[63, 64] and ions[65, 66], and colour centres in diamond[67–69]. This conversion can theoretically achieve unit efficiency, but practical losses of optical components used results in $\approx 50\%$ total conversion efficiency. More impactful is that the process adds background photons to the (weak) quantum signal, which posed a challenge for their implementation for entanglement generation. Recently these conversion techniques have allowed for the first demonstrations of entangled nodes over 10s of kilometres of fiber, with the nodes in nearby labs[70, 71]. In other

work, entanglement was generated over a metropolitan scale[72, 73], but without satisfying the third requirement of allowing for further processing on the entangled state.

To overcome this third challenge, it is needed to combine long-lived qubits with fast processing of live measurement outcomes during the process of entanglement generation. It crucial that the qubit states are addressable after the successful heralding of entanglement, and not destroyed by either a measurement or the environment. In systems where the end nodes use solid-state qubits to store the entanglement, this requires the decoupling of the stationary qubits from the environment, until the signal that the heralded has successfully reached the end nodes. There is currently no system that solves these challenges while having large separation between the nodes and in a way compatible with our current fibre infrastructure.

1.5. THESIS OVERVIEW

This thesis is motivated by making it possible to generate solid-state entanglement generation over existing fibre infrastructure on a metropolitan scale. It combines the excellent spin properties of the NV-centre in diamond and state-of-the-art QFC techniques with novel stabilization schemes compatible with telecom fibre and large separation. We expect that many techniques described in this work will also be relevant for other quantum networks based on other physical systems such other colour centers in solid-state devices. The results as shown in the subsequent chapters are briefly outlined below.

In **Chapter 2** we introduce the methods used to operate an NV-centre as a quantum network node, highlighting the properties that make it a successful candidate for quantum networks. We discuss the level-structure and spin-states, as well as the control techniques used to manipulate them. Further we describe the entanglement generation protocols and present their (dis-)advantages. Additionally, we describe the two different techniques used for Quantum Frequency Conversion. Lastly, we describe the concept of the phase synchronization of optical fields using active optical feedback.

In **Chapter 3** we show the interference of the emission of two remote and spectrally detuned NV-centres in the telecom L-band. We realize this result by converting the single-photon emission of both nodes to the same frequency via QFC and guide via optical fibres to a central beam splitter. The resulting interference is well explained by our model using independently measured parameters, and is mainly limited by background counts introduced by the QFC process.

In **Chapter 4** we describe the interference of emission from an NV-centre with a photon state compatible with a quantum memory. We then show that we can use this interference to teleport a quantum state onto the NV centre using a Bell-state measurement of the two-photon state.

In **Chapter 5** we describe the synchronization of the optical phase that is central to the entanglement generation. We discuss the relevant sources of drift, and describe our full approach in synchronizing this phase. We present measurement characterizing the performance at various timescales.

In **Chapter 6** we demonstrate heralded solid-state entanglement generation between two nodes located in Delft and Den Haag, showing for the first time this the realization of a quantum link between processors at the metropolitan scale. We use commercially

available fibre to connect to locations, and perform all our stabilization and synchronization schemes over the same fibre bundle.

In **Chapter 7** we summarize the results and provide a conclusion based on the main results. We discuss future improvements both in near term improvements of quantum networks, but also for future directions towards a global Quantum Internet.

REFERENCES

[1] E. Schrödinger, *Quantisierung als eigenwertproblem,* Annalen der Physik **384**, 361–376 (1926).

[2] T. H. MAIMAN, *Stimulated optical radiation in ruby,* Nature **187**, 493–494 (1960).

[3] I. I. Rabi, J. R. Zacharias, S. Millman and P. Kusch, *A new method of measuring nuclear magnetic moment,* Phys. Rev. **53**, 318 (1938).

[4] Z. Alferov, V. Andreev, V. Korolkov, E. Portnoi and D. TRETIAKOV, *Coherent radiation of epitaxial heterojunction structures in the alas-gaas system(coherent emission in epitaxial structures with heterojunctions in alas-gaas system),* Soviet Physics-Semiconductors **2**, 1289 (1969).

[5] I. Hayashi, M. B. Panish, P. W. Foy and S. Sumski, *Junction lasers which operate continuously at room temperature,* Applied Physics Letters **17**, 109–111 (1970).

[6] R. Mears, L. Reekie, I. Jauncey and D. Payne, *Low-noise erbium-doped fibre amplifier operating at 1.54μm,* Electronics Letters **23**, 1026 (1987).

[7] H. Ritchie, E. Mathieu and E. Ortiz-Ospina, *Adoption of communication technologies,* (2023).

[8] G. P. Agrawal, *Optical communication: Its history and recent progress,* in *Optics in Our Time* (Springer International Publishing, 2016) p. 177–199.

[9] A. Einstein, B. Podolsky and N. Rosen, *Can quantum-mechanical description of physical reality be considered complete?* Physical Review **47**, 777–780 (1935).

[10] J. S. Bell, *On the einstein podolsky rosen paradox,* Physics Physique Fizika **1**, 195–200 (1964).

[11] B. Hensen *et al.*, *Loophole-free bell inequality violation using electron spins separated by 1.3 kilometres,* Nature **526**, 682 (2015).

[12] L. K. Shalm *et al.*, *Strong loophole-free test of local realism,* Phys. Rev. Lett. **115**, 250402 (2015).

[13] M. Giustina *et al.*, *Significant-loophole-free test of bell's theorem with entangled photons,* Physical Review Letters **115** (2015), 10.1103/physrevlett.115.250401.

[14] B. Schumacher, *Quantum coding,* Phys. Rev. A **51**, 2738 (1995).

[15] R. P. Feynman, *Simulating physics with computers,* International Journal of Theoretical Physics **21**, 467–488 (1982).

[16] J. Preskill, *Quantum computing 40 years later,* (2021).

[17] P. Shor, *Algorithms for quantum computation: discrete logarithms and factoring,* in *Proceedings 35th Annual Symposium on Foundations of Computer Science*, SFCS-94 (IEEE Comput. Soc. Press, 1994).

[18] L. K. Grover, *A fast quantum mechanical algorithm for database search,* in *Proceedings of the twenty-eighth annual ACM symposium on Theory of computing - STOC '96*, STOC '96 (ACM Press, 1996).

[19] F. Arute *et al.*, *Quantum supremacy using a programmable superconducting processor,* Nature **574**, 505–510 (2019).

[20] H.-S. Zhong *et al.*, *Quantum computational advantage using photons,* Science **370**, 1460–1463 (2020).

[21] Y. Wu *et al.*, *Strong quantum computational advantage using a superconducting quantum processor,* Phys. Rev. Lett. **127**, 180501 (2021).

[22] A. D. King *et al.*, *Computational supremacy in quantum simulation,* (2024).

[23] C. H. Bennett and G. Brassard, *Experimental quantum cryptography: the dawn of a new era for quantum cryptography: the experimental prototype is working],* ACM SIGACT News **20**, 78–80 (1989).

[24] H. J. Kimble, *The quantum internet,* Nature **453**, 1023 (2008), number: 7198 Publisher: Nature Publishing Group.

[25] C. H. Bennett and G. Brassard, *Quantum cryptography: Public key distribution and coin tossing,* Theoretical Computer Science **560**, 7–11 (2014).

[26] J. L. Park, *The concept of transition in quantum mechanics,* Foundations of Physics **1**, 23–33 (1970).

[27] W. K. Wootters and W. H. Zurek, *A single quantum cannot be cloned,* Nature **299**, 802–803 (1982).

[28] R. L. Rivest, A. Shamir and L. Adleman, *A method for obtaining digital signatures and public-key cryptosystems,* Communications of the ACM **21**, 120–126 (1978).

[29] V. S. Miller, *Use of elliptic curves in cryptography,* in *Advances in Cryptology — CRYPTO '85 Proceedings* (Springer Berlin Heidelberg, 1985) p. 417–426.

[30] N. Koblitz, *Elliptic curve cryptosystems,* Mathematics of computation **48**, 203 (1987).

[31] A. K. Ekert, *Quantum cryptography and bell's theorem,* in *NATO ASI Series* (Springer US, 1992) p. 413–418.

[32] A. Ekert and R. Renner, *The ultimate physical limits of privacy,* Nature **507**, 443 (2014), number: 7493 Publisher: Nature Publishing Group.

[33] L. Jiang, J. M. Taylor, A. S. Sørensen and M. D. Lukin, *Distributed quantum computation based on small quantum registers,* Phys. Rev. A **76**, 062323 (2007).

[34] D. Cuomo, M. Caleffi and A. S. Cacciapuoti, *Towards a distributed quantum computing ecosystem,* IET Quantum Communication **1**, 3–8 (2020).

[35] M. Caleffi *et al.*, *Distributed quantum computing: a survey,* (2022).

[36] A. Broadbent, J. Fitzsimons and E. Kashefi, *Universal blind quantum computation,* in *2009 50th Annual IEEE Symposium on Foundations of Computer Science* (IEEE, 2009).

[37] P. Kómár *et al.*, *A quantum network of clocks,* Nature Physics **10**, 582–587 (2014).

[38] H. J. Kimble, *The quantum internet,* Nature **453**, 1023 (2008).

[39] S. Wehner, D. Elkouss and R. Hanson, *Quantum internet: A vision for the road ahead,* Science **362**, eaam9288 (2018).

[40] D. L. Moehring *et al.*, *Entanglement of single-atom quantum bits at a distance,* Nature **449**, 68–71 (2007).

[41] I. Usmani *et al.*, *Heralded quantum entanglement between two crystals,* Nature Photonics **6**, 234 (2012).

[42] J. Hofmann *et al.*, *Heralded Entanglement Between Widely Separated Atoms,* Science **337**, 72 (2012).

[43] S. Ritter *et al.*, *An elementary quantum network of single atoms in optical cavities,* Nature **484**, 195 (2012), number: 7393 Publisher: Nature Publishing Group.

[44] H. Bernien *et al.*, *Heralded entanglement between solid-state qubits separated by three metres,* Nature **497**, 86–90 (2013).

[45] A. Delteil *et al.*, *Generation of heralded entanglement between distant hole spins,* Nature Physics **12**, 218 (2016), number: 3 Publisher: Nature Publishing Group.

[46] R. Stockill *et al.*, *Phase-Tuned Entangled State Generation between Distant Spin Qubits,* Physical Review Letters **119**, 010503 (2017), publisher: American Physical Society.

[47] P. C. Humphreys *et al.*, *Deterministic delivery of remote entanglement on a quantum network,* Nature **558**, 268 (2018), number: 7709 Publisher: Nature Publishing Group.

[48] M. H. Abobeih *et al.*, *One-second coherence for a single electron spin coupled to a multi-qubit nuclear-spin environment,* Nature Communications **9**, 2552 (2018).

[49] C. Bradley *et al.*, *A Ten-Qubit Solid-State Spin Register with Quantum Memory up to One Minute,* Physical Review X **9**, 031045 (2019).

[50] G. L. van de Stolpe *et al.*, *Mapping a 50-spin-qubit network through correlated sensing,* Nature Communications **15** (2024), 10.1038/s41467-024-46075-4.

[51] N. Kalb *et al.*, *Entanglement distillation between solid-state quantum network nodes,* Science **356**, 928–932 (2017).

[52] M. Pompili *et al.*, *Realization of a multinode quantum network of remote solid-state qubits,* Science **372**, 259–264 (2021).

[53] S. L. N. Hermans *et al.*, *Qubit teleportation between non-neighbouring nodes in a quantum network,* Nature **605**, 663–668 (2022).

[54] A. Dahlberg *et al.*, *A link layer protocol for quantum networks,* in *Proceedings of the ACM Special Interest Group on Data Communication*, SIGCOMM '19 (ACM, 2019).

[55] M. Pompili *et al.*, *Experimental demonstration of entanglement delivery using a quantum network stack,* npj Quantum Information **8**, 1 (2022).

[56] K. Kao and G. Hockham, *Dielectric-fibre surface waveguides for optical frequencies,* Proceedings of the Institution of Electrical Engineers **113**, 1151–1158 (1966).

[57] T. Miya, Y. Terunuma, T. Hosaka and T. Miyashita, *Ultimate low-loss single-mode fibre at 1.55 μm,* Electronics Letters **15**, 106 (1979).

[58] W. Hänsel *et al.*, *Ultra-low phase noise all-pm er:fiber optical frequency comb,* in *Advanced Solid State Lasers*, ASSL (OSA, 2015).

[59] E. F. Dierikx *et al.*, *White rabbit precision time protocol on long-distance fiber links,* IEEE Transactions on Ultrasonics, Ferroelectrics, and Frequency Control **63**, 945 (2016).

[60] H. Takesue, *Single-photon frequency down-conversion experiment,* Phys. Rev. A **82**, 013833 (2010).

[61] K. De Greve *et al.*, *Quantum-dot spin–photon entanglement via frequency downconversion to telecom wavelength,* Nature **491**, 421–425 (2012).

[62] L. Yu *et al.*, *Two-photon interference at telecom wavelengths for time-bin-encoded single photons from quantum-dot spin qubits,* Nature Communications **6** (2015), 10.1038/ncomms9955.

[63] M. Bock *et al.*, *High-fidelity entanglement between a trapped ion and a telecom photon via quantum frequency conversion,* Nature Communications **9**, 1998 (2018).

[64] T. van Leent *et al.*, *Long-distance distribution of atom-photon entanglement at telecom wavelength,* Phys. Rev. Lett. **124**, 010510 (2020).

[65] T. Walker *et al.*, *Long-distance single photon transmission from a trapped ion via quantum frequency conversion,* Phys. Rev. Lett. **120**, 203601 (2018).

[66] V. Krutyanskiy *et al.*, *Light-matter entanglement over 50 km of optical fibre,* npj Quantum Information **5**, 72 (2019).

[67] A. Dréau, A. Tchebotareva, A. E. Mahdaoui, C. Bonato and R. Hanson, *Quantum frequency conversion of single photons from a nitrogen-vacancy center in diamond to telecommunication wavelengths,* Phys. Rev. Appl. **9**, 064031 (2018).

[68] A. Tchebotareva *et al.*, *Entanglement between a diamond spin qubit and a photonic time-bin qubit at telecom wavelength,* Phys. Rev. Lett. **123**, 063601 (2019).

[69] E. Bersin *et al., Telecom networking with a diamond quantum memory,* PRX Quantum **5** (2024), 10.1103/prxquantum.5.010303.

[70] T. van Leent *et al., Entangling single atoms over 33 km telecom fibre,* Nature **607**, 69 (2022).

[71] C. M. Knaut *et al., Entanglement of nanophotonic quantum memory nodes in a telecom network,* Nature **629**, 573–578 (2024).

[72] X.-Y. Luo *et al., Postselected entanglement between two atomic ensembles separated by 12.5 km,* Phys. Rev. Lett. **129**, 050503 (2022).

[73] J.-L. Liu *et al., Creation of memory–memory entanglement in a metropolitan quantum network,* Nature **629**, 579–585 (2024).

2

METHODS FOR A METROPOLITAN QUANTUM LINK USING NV-CENTERS

Many of today's problems are a result of yesterdays solutions.

Thomas Sowell

In this Chapter we describe the theoretical background and experimental techniques that are used throughout this thesis. We first introduce basic knowledge of the Nitrogen Vacancy center as a quantum network node and discuss methods to generate entanglement between distant nodes. We provide the background for the two Quantum Frequency conversion methods used in this work, and discuss their differences. Finally we mention theory behind measuring, changing and stabilizing the phase of optical fields.

Parts of this Chapter are published in Optica Quantum 2, 189-195 (2024)[1]. These sections are denoted with an asterix* in the caption.

2.1. THE NV CENTRE AS A QUANTUM NETWORK NODE

In this section we introduce the system of choice for implementing our quantum network node. This system is the Nitrogen Vacancy (NV-)center in diamond, an atomic defect in the diamond carbon lattice. It is sometimes also called a color center or optically active defect, because of its interaction with light. We will describe the NV composition and consequential electronic structure, its nuclear spin environment and finally methods or initialization, readout and control of both the NV center and nuclear spins.

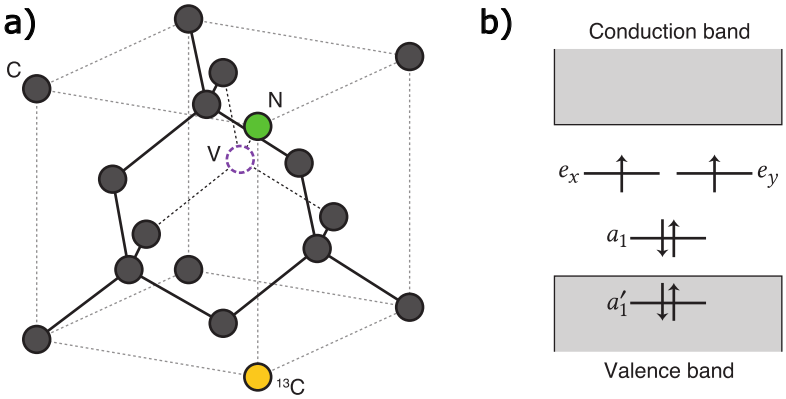

Figure 2.1: **The Nitrogen-Vacany center in Diamond.** a) Schematic of the Carbon (black) atoms in a diamond lattice, where a substitutional Nitrogen (green) and a neighboring vacancy (purple outline) form the Nitrogen-Vacancy (NV) center. A nearby ^{13}C nuclear spin is shown (yellow). b) Molecular orbits are filled with electrons from the surrounding atoms, plus an electron from nearby charge traps form the negatively charged NV^- configuration. Optically addressable are between levels that lie within the bandgap of diamond, resulting in trapped ion-like transitions. Image adapted from Pfaff [2] and Bernien [3]

2.1.1. NV ELECTRONIC STRUCTURE

The NV center consists of a Nitrogen atom replacing a Carbon atom, next to a vacant lattice site (Fig. 2.1a)). Three electrons from the dangling bonds from three Carbon atoms surrounding the vacancy, as well as two electrons from the Nitrogen give the NV-center five electrons in its neutral charge state, NV^0, with effective electron spin $S = \frac{1}{2}$. If an electron from the environment is captured by this system, it is in the NV^- state, with effective electron spin $S = 1$, which is an interesting system to use for quantum information purposes [4], and used throughout this thesis.

The atomic orbitals together form a set of 4 molecular orbitals, of which the three at highest energy lie completely in the bandgap of the diamond (5.5 eV, Fig. 2.1b). The 6 electrons occupy the two lowest orbitals with 2 electrons each, and the two degenerate orbitals e_x and e_y with a single electron each in the triplet configuration. The electronic ground state and first excited state have their energies within the bandgap, which makes transitions between them possible without losing an electron, and makes this system behave like a trapped ion in a solid state device.

The optically addressable transitions are shown in Fig. 2.2a, where the spin triplet

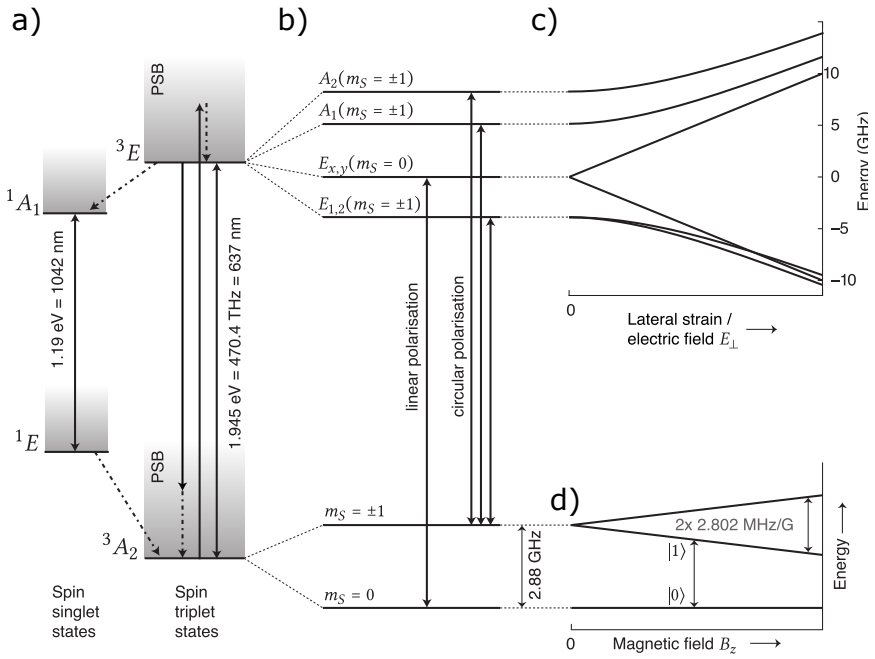

Figure 2.2: **Electronic levelstructure of** NV^-. a) The spin triplet states can be excited via a transition in the optical domain (470.4 THz = 637 nm). Excitation and emission can be either resonant, or off-resonantly via phonon states (grey shading). Decay via the spin singlet can happen via an inter-system crossing in the excited state, which leads to the flipping of the spin state. b) At cryogenic temperatures multiple transitions can be spectrally resolved, which are a result of the ground state and excited state splittings due to spin-orbit and spin-spin interactions. These transitions can be individualy adressed and used for initialization and readout of the spin, and spin-photon entangled state generation. c) Strain and electric fields can affect the energy levels and transitions, resulting in variations of energy splittings of different NVs and allowing for tuning of the emission spectrum. d) Using the Zeeman effect, the $m_S = \pm 1$ states can be split with a magnetic field along the z-direction, and a qubit subspace can be defined. Adapted from [2, 3, 5]

states can be addressed resonantly with a photon at a wavelength of ~637 nm, or off-resonantly with a lower wavelength (typ. 515 nm). Subsequent decay back to the ground state can happen direct, or via the spin singlet states. The direct decay ($^3E \rightarrow {}^3A_2$) tends to preserve the spin state, and is usually accompanied by a phonon, called the Phonon sideband (PSB), which makes the emitted photon at a lower energy (therefore higher wavelength). Photons not accompanied by a phonon are emitted at exactly the transition energy, which happens ~2.5 % of the time[6], set by the Debye-Walle factor, are called the Zero-phonon Line (ZPL). The ZPL emission can be used to generate entanglement between separate NV centers, see sec. 2.2. State dependent decay via the singlet ($^3E \rightarrow {}^1A_1 \rightarrow {}^1E \rightarrow {}^3A_2$) introduces a spin-flipping channel, which can be used for spin initialisation via optical pumping[7, 8].

The NV-center ground state can be manipulated even at room temperature, where off-resonant excitation both provides means to initialize and readout the $m_S = 0$ and $m_S = \pm 1$ states[9]. These methods are used to characterize new samples in order to find

NV centers that are promising for low-temperature experiments. For instance, NV centers with the correct orientation in the crystal lattice (along the < 111 > crystal axis) can be indentified via the sensitivity of the fluorescence to the polarization of the excitation. Additionally, electron-spin resonance (ESR) measurements can be done to identify NV-centers without any strongly coupled nuclear spins (^{13}C) nearby. After the identification of these NV centers, Solid Immersion Lenses (SILs) are fabricated on top of the NV centers and an anti-reflective coating is deposited on the surface to reduce total internal reflection. Gold structures deposited on the diamond serve as electrodes for DC electric fields and a microwave stripline for AC field delivery. This diamond sample is then placed on a printed circuit board (PCB), with the contacts bonded to the PCB, that allow for contact with the outside world when placed in a cryostat.

At low (<10 K) temperatures we can resolve the optical transitions from the different spin states $m_S = 0$ or ± 1 in the electronic ground state, that are split due to spin-orbit coupling, see Fig. 2.2b. In general, transitions from $m_S = 0$ to the levels E_x / E_y have the lowest probability to decay via the singlet, and are spin-preserving. The transitions from $m_S = \pm 1$ are more likely to decay via the singlet. The combination of these two effects allow for both high spin initialization [8] via optical pumping (P_{init} =1 µW, t_{init} ~1.5 µs) and optical readout of the spin state via spin-dependent fluorescence [10] by exciting resonantly and measuring PSB photons (P_{RO} =1 nW, t ~5 µs). The energy spacing of these transitions depends on the local strain of the diamond (Fig. 2.2c), and can also be tuned via an external electric fields[11, 12].

By applying an external DC magnetic field, we can split the $m_S = \pm 1$ manifold, see fig 2.2. The ground state Hamiltonian of the electronic spin is given by

$$\frac{H_{GS}}{\hbar} = DS_z^2 + \gamma_e \left(S_x B_x + S_y B_y + S_z B_z \right), \tag{2.1}$$

where $\hbar$ is the reduced Planck constant, $D = 2\pi \times 2.88$GHz the zero-field splitting and $\gamma_e = 2\pi \times 2.802\,\text{MHzG}^{-1}$ the electron gyromagnetic ratio. S_i are the spin-1 Pauli matrices and B_i the magnetic field along direction $\hat{i}$. We have ignored the hyperfine splitting due to the nearby ^{14}N nuclear spin ($I_N = 1$), as well as any super-hyperfine splitting due to nearby ^{13}C spins ($I_C = \frac{1}{2}$), for the treatment of which we refer to [13] and [14]. Only a small (30G) field in the $\hat{z}$ direction is needed to split the $m_S = \pm 1$ states. This is done with a small permanent magnet inside the cryostat, and makes the individually transitions addressable with a microwave field around 3 GHz. This allows us to define a qubit within this manifold, where the electron spin state with $m_S = 0 \equiv |0\rangle$ and $m_S = +1 \equiv |1\rangle$. Short pulses ($t_{pulse}$ ~200 ns) are used to perform universal rotations $R_{\hat{\phi}}(\theta)$ within this qubit subspace with high fidelity (99 %), where $\hat{\phi}$ the rotation axis in the equator plane set by the phase of the pulse, and θ the rotation angle set by the pulse energy. For more information on the microwave pulses and their implementation we refer to [15, 16]. Because this qubit is also used to communicate with other nodes via the optical interface, we also sometimes refer to it as the communication qubit, a process we will explain in Section 2.2.

2.1.2. QUBIT COHERENCE

The electron spin has shown to be an excellent qubit[17]. Both the longitudinal relaxation (characterized by the timescale T_1), the free induction decay time (T_2^*) and the coherence time under decoupling (T_{DD}) are relevant timescale .

The T_1 is the timescale on which the computational basis states ($|0\rangle, |1\rangle$) decay in to a mixed state. In theory, this process is due to two-phonon processes in the diamond lattice, which is dominating at room temperature[18]. At low temperatures, these processes are frozen out, and in practice the T_1 is limited by the non-ideal extinction of outside control fields. For example, residual microwave and laser fields that are incident on the electron spin provide an unwanted driving in the qubit subspace, or via the optically exited state. Experimental design providing high suppression (>100 dB) of the optical fields and active microwave switching has shown to allow for T_1 times exceeding 1 hour[17]. For the experiments in this work, the relevant timescales are <1 ms and can neglect the effects due to the T_1 by using appropriate optical suppression.

The free induction decay T_2^* describes the timescale on which a qubit in a superposition state $|\psi\rangle = \frac{|0\rangle+|1\rangle}{\sqrt{2}}$ decoheres to the mixed state by picking up random and unknown phases. These are mainly due to the non-zero nuclear spin ^{13}C isotope ($I = \frac{1}{2}$), which naturally occurs with 1.1 % in the carbon lattice of diamond. These spins have a different configuration over time, and therefore apply a different effective magnetic field in the $\hat{z}$ direction. The NV-centers used in this work are in diamonds with naturally abundant 1.1 % ^{13}C concentration, and the T_2^* is typically 5 µs, and would significantly impact the experiments in this work if not mitigated. Fortunately many techniques have been developed to counter the noise generated by the nuclear spin environment, which is on a slow timescale. Therefore it can be mitigated by applying echo or re-focusisng pulses to protect the qubit[19]. In principle, this technique can be used to extend the coherence time T_2 up to a second[17], with some knowledge of the nuclear spin environment. For the experiments shown in this work, a single echo $\pi-$pulse is sufficient to limit the impact of dephasing on our experiments in Chapter 6.

2.1.3. ADDITIONAL QUBITS

Another exciting development is instead of only being a source of noise, some of the nuclear spins can be individually controlled via their interactions with NV center electron spin. This can be done both for spins with a strong coupling strength $\boldsymbol{A}$ to the NV electron spin $\left(|\boldsymbol{A}| > \frac{1}{T_2^*}\right)$ by using separate microwave pulses [20, 21], but also on nuclear spins that are weakly coupled with $\left(|\boldsymbol{A}| \ll \frac{1}{T_2^*}\right)$ [22, 23]. They can serve as an excellent memory for qubit states[24], with memory lifetimes up to a minute.

2.2. PHOTON- AND REMOTE ENTANGLEMENT GENERATION

So far we have discussed the properties of the NV electron spin and nuclear spin environment, its excellent spin properties and its use it quantum experiments. However, one of the most exciting capabilities of the NV center is the ability to generate entanglement between remote locations. Entanglement between two NV centers has been demonstrated

in numerous experiments over the last ten year [25–29], as well as a multi-node network of three NV center based nodes [16, 30], making it one of the most studied solid-state systems for entanglement generation. In this section we will describe the theory and methods used in this thesis to generate entanglement between remote NV centers using the ZPL emission as flying qubits. Only the ZPL fraction of the emission can be used, because any simultaneous phonon emission will reveal information of the current spin-state to the environment.

The ZPL photons can used to generate an entangled state with the spin of the NV electron by preparing the communication qubit in superposition, using a short (~1 ns) spin-selective excitation, and subsequent spontaneous emission:

$$|\psi\rangle = \alpha|0\rangle|vac\rangle+\beta|1\rangle|vac\rangle \underbrace{\longrightarrow}_{\text{Opt. Exc.}} \alpha|exc\rangle|vac\rangle+\beta|1\rangle|vac\rangle \underbrace{\longrightarrow}_{\text{Spont.Em.}} \alpha|0\rangle|a\rangle+\beta|1\rangle|vac\rangle, \tag{2.2}$$

where $\alpha^2+\beta^2=1$ and $|a\rangle(|vac\rangle)$ a photon in mode a (vacuum).

In general, we locally generate a state of the form in Eq. 2.2, and send the photonic qubits to the same location. At that location, we would like to perform a Bell-state measurement on the photonic qubits, which projects the communication qubits in an entangled state and heralds a succesful entanglement generation. In the ideal case, this photonic Bell-state measurement projects the joint photonic qubit state on one of the for Bell-states

$$|\Psi^+\rangle = \frac{|01\rangle+|10\rangle}{\sqrt{2}} \tag{2.3}$$

$$|\Psi^-\rangle = \frac{|01\rangle-|10\rangle}{\sqrt{2}} \tag{2.4}$$

$$|\Phi^+\rangle = \frac{|00\rangle+|11\rangle}{\sqrt{2}} \tag{2.5}$$

$$|\Phi^-\rangle = \frac{|00\rangle-|11\rangle}{\sqrt{2}}, \tag{2.6}$$

where the state $|mn\rangle$ describes the photon from the first (second) node in qubit state $m(n)$. It is non-trivial to perform this measurement on two (photonic) qubits, and in reality we perform measurement that can not distinguish all four Bell-states. The usual method to perform this Bell-state measurement on two photonic modes is to use linear optics: a 50 : 50 beamsplitter takes the two photonic qubits as input (a,b), and the outputs (c,d) are directed to two (non photon number resolving) single-photon detectors. This method can only resolve two (Ψ^+,Ψ^-) of the four Bell-states, which we will discuss later.

There are different ways we can encode quantum information photons, where two ways used in this thesis are the time-bin and photon-number encoding. We will describe these two encodings and their subsequent protocols to generate NV electron spin-spin entanglement and discuss their (dis-)advantages. A crucial component for both of the protocols is however the ability to generate photons which are indistinguishable from each other. We therefore first discuss what makes photons indistinguishable, and describe the method how to quantify this property.

2.2.1. PHOTON INDISTINGUISHABILITY

For both entanglement generation protocols used in this thesis a crucial aspect is the indistinguishability of the photons involved in the entanglement generation. We can call two photons indistinguishable if there is no measurement possible to tell the two apart. There are many Degrees Of Freedom (DOF) in which photons can differ from each other: polarization, frequency and arrival time are the most common, and using polarizers, spectral filters and time-resolved detection respectively can be used to discern photons in these degrees of freedom. In order for entanglement swapping to succeed with high-fidelity, a high degree of indistinguishability is required. A canonical way to measure the 'amount' of indistinguishability is with a two-photon quantum interference experiment, also called Hong-Ou Mandel[31] inteference. It describe the vanishing of the coincidence rate, or bunching, of two photons incidient on a beamsplitter. The beampsplitter plays a central role, which will describe first.

We can write the relation of the output modes of the beamsplitter to the input modes as:

$$|a\rangle = \frac{1}{\sqrt{2}}(|c\rangle + |d\rangle) \tag{2.7}$$

$$|b\rangle = \frac{1}{\sqrt{2}}(|c\rangle - |d\rangle) \tag{2.8}$$

with $|x\rangle$ a photon in the mode x and. We can define a coincidence measurement operator $M_{coinc} = |c\rangle\langle c| \otimes |d\rangle\langle d|$, as having a photon in each of the output arms. In the ideal case of having an identical copy of the same photon in each of the input arms we can show that the two-photon state on the output is given by

$$|a\rangle|b\rangle \underbrace{\rightarrow}_{Eq.2.7} \frac{1}{2}(|c\rangle + |d\rangle)(|c\rangle - |d\rangle) = \frac{1}{2}(|c\rangle|c\rangle + |c\rangle|d\rangle - |c\rangle|d\rangle - |d\rangle|d\rangle) = \left|\psi^{out}\right\rangle, \tag{2.9}$$

where there are no photons in separate output modes due to the equivalence and therefor destructive interference of the $|c\rangle|d\rangle$ and $|d\rangle|c\rangle$ terms. Therefore, the probability of measuring a coincidence $Tr\left(\left|\psi^{out}\right\rangle\left\langle\psi^{out}\right| M_{coinc}\right) = 0$. However, next to the spatial mode x, the photon can have any of the previously described DOFs. We combine them into the state $|D_x\rangle$, leading to the full quantum state to be

$$\left|\phi\right\rangle_x = |x\rangle|D_x\rangle = |x, D_x\rangle\,. \tag{2.10}$$

This extra state $|D_x\rangle$ is unknown to us, as if it was drawn from a random distribution when the photon was generated. Suppose we have two of these photons as input on the beamsplitter, one on each arm. Applying the beamsplitter operation to get the output modes we get

$$|a, D_a\rangle|b, D_b\rangle \underbrace{\longrightarrow}_{Eq.2.7} \frac{1}{2}(|c, D_a\rangle + |d, D_a\rangle)(|c, D_b\rangle - |d, D_b\rangle) \tag{2.11}$$

When we now evaluate the probability of measuring a coincidence finding that, by using Eq. 2.10 and $\langle x|y\rangle = 0$ and $\langle x|x\rangle = 1$

$$p_{coinc} = Tr\left(\left|\psi^{out}\right\rangle\left\langle\psi^{out}\right| M_{coinc}\right) = \left\langle\psi^{out}\right| M_{coinc} \left|\psi^{out}\right\rangle = \frac{1}{2}\left(1 - |\langle D_a|D_b\rangle|^2\right). \quad (2.12)$$

This result shows us that the probability of measuring a *coincidence* after the beamsplitter, depends on the *overlap* between the DOFs of the two input states! If we have perfect overlap ($\langle D_a|D_b\rangle = 1$), e.g. the DOFs do not contain any information that gives away input photon (a or b) is in the output mode, we recover the result in Eq. 2.9 of the indistinguishable case. However, if the DOF are orthogonal ($\langle D_a|D_b\rangle = 0$), e.g. for two orthogonal polarization, no interference takes place, and coincidences are measured just as frequently as no coincidence ($p = 0.5$). Fortunately for us, it is possible to generate highly indistinguishable photons from remote NV centers, by taking special care in overlapping all degrees of freedom of the photons. In Chapter 3 we use this interference experiment to measure the overlap between the emission of two spectrally detuned NV-centers, where the frequency difference is erased by using Quantum Frequency Conversion (see sec. 2.3) to the telecom L band. Furthermore, the visibility can also be measured between photonic modes coming from different systems, which is done in Chapter 4 to asses the indistinguishability with a weak-coherent state and NV center photons.

2.2.2. DOUBLE-CLICK PROTOCOL

One of the protocols used to generate remote entanglement between two NV centers was proposed by Barrett and Kok[32]. In short, it uses the time-bin encoding ($|early\rangle$ or $|late\rangle$) for the photonic qubit, and heralds the entanglement of the communication qubits after detection of a photon from **both** nodes, hence the alternative name the double-click protocol. It starts off by preparing the communication qubit of each node in an equal superposition of $|0\rangle$ and$|1\rangle$. Then, two rounds of optical excitation with a $\pi-$pulse on the communication qubit in between, generate the entangled state:

$$\left|\psi\right\rangle^{BK} = \frac{1}{\sqrt{2}}\left(|1\rangle|1\rangle_e|0\rangle_l + e^{i\Delta\phi_{opt}}|0\rangle|0\rangle_e|1\rangle_l\right) \equiv \frac{1}{\sqrt{2}}\left(|1\rangle|e\rangle + e^{i\Delta\phi_{opt}}|0\rangle|l\rangle\right) \quad (2.13)$$

where the subscript e,l denotes the early and late time-bin, A,B the communication qubit on node A or B respectively, $\Delta\phi_{opt} = \phi_{late} - \phi_{early}$ the optical phase difference between the two excitation rounds. Because the excitation rounds happen quickly after each-other (~200 ns), this phase difference tends to be small. Also, when sending the time-bin qubit through an optical channel, any effects such as dispersion on the early part of the state also happen to the late qubit very shortly after, making this qubit robust against propagation over long distances. We can therefore assume $e^{i\Delta\phi} = 1$ for the further derivation, but in reality this term can lead to errors.

The time-bin qubits of each of the nodes are overlapped on a beamsplitter, where the mode coming from node $A(B)$ is input to mode $a(b)$. By using the beamsplitter operation from Eq. 2.7, assuming perfectly indistinguishable photons and only considering terms where there are two detection events, we get the un-normalized state:

$$\left|\psi\right\rangle_A^{BK}\left|\psi\right\rangle_B^{BK} = (|10\rangle_{A/B} + |01\rangle_{A/B})(|e,c\rangle|l,c\rangle - |e,d\rangle|l,d\rangle) \quad (2.14)$$

$$(|10\rangle_{A/B} - |01\rangle_{A/B})(|e,d\rangle|l,c\rangle - |e,c\rangle|l,d\rangle) \quad (2.15)$$

where the state $|x,y\rangle$ represents a photon in time-bin $x \in [e,l]$ in beamsplitter mode $y \in [c,d]$. We can now use the detection pattern in the modes c,d to project the communication qubits in an entangled state. We notice that, if both photons are measured in the same detector (c,c or d,d), we find a + sign in the spin state, and when we measure the photons in different detectors (c,d or d,c), we find a minus sign in the phase of the spin state. This allows us to write down the density matrix condition on which pattern occurred, giving

$$|\psi\rangle\langle\psi|_{A/B}^{BK} = |\Psi^{\pm}\rangle\langle\Psi^{\pm}| \tag{2.16}$$

which is a pure state given the detection outcome.

This protocol can theoretically generate a maximally entangled state between the remote communication qubits, but in the presence of experimental errors such as double excitation, gate errors and detector darkcounts, fidelities of ≈90 % have been achieved[27]. The effect of photon loss on the time-bin encoding makes that we leave the qubit subspace, and consequentially the Bell-state measurement heralds no entanglement. One of the downsides of this protocol is that the probability to generate entanglement scales as

$$p_{BK} = \frac{1}{2}\eta_A\eta_B \tag{2.17}$$

where η_N is the probability to measure a photon emitted from the communication qubit at node N. When η_A is small, the rate at which the entanglement generation succeeds slows down significantly. A large improvement in successrate can be achieved by using the single-click protocol, which we explain in the next subsection.

The Bell-state measurement done here with linear optics is not fully as defined in Eq. 2.3, but with only the ability to distinguish the Bell-states Ψ^+ and Ψ^-. The described Bell-state measurement between two time-bin encoded photonic qubits can also be used to teleport a photon state onto the state of the communication qubit. For an experimental demonstration of teleportation of a telecom memory compatible qubit state onto the NV center electron spin and a detailed description of the teleportation protocol we refer to Chapter 4.

2.2.3. SINGLE-CLICK PROTOCOL

The single-click protocol, as the name suggests, can herald entanglement by measuring a single photon [33, 34]. It uses the photon-number state encoding ($|vac\rangle, |photon\rangle$) for the photonic qubit, prepares the communication qubit in an unequal superposition, and, after overlapping of the photon state on a beamsplitter, heralds an entangled state upon the measurement of a *single* photon. Both nodes start by preparing their unequal superposition of the communication qubit, and perform a single round of excitation to generate the state

$$|\psi\rangle^{SC} = e^{i\phi_{opt}}\alpha|0\rangle|1\rangle + \sqrt{1-\alpha}|0\rangle|vac\rangle, \tag{2.18}$$

where $\alpha \in (0, 0.5)$ the so-called bright-state population and ϕ_{opt} the optical phase of the emitted photon. This optical phase is no longer a global phase term, as only one of the communication qubit states picks it up. We now assume that the α parameter is chosen equally on each node, and we can ignore non-idealities such as detector background counts.

Again, the photonic qubits are sent to the same location where they interfere on the beamsplitter. The (unnormalized) state, assuming indistinguishable photons and neglecting terms without any photons detected, then becomes

$$\left|\psi\right\rangle_A^{SC}\left|\psi\right\rangle_B^{SC} = \alpha^2\left(\left|c\right\rangle\left|c\right\rangle - \left|d\right\rangle\left|d\right\rangle\right)\left|00\right\rangle\left(e^{i(\phi_B)}\left|00\right\rangle\right) + \tag{2.19}$$

$$\alpha\sqrt{1-\alpha}\left|c\right\rangle\left(\left|01\right\rangle + e^{i\Delta\phi}\left|10\right\rangle\right) + \tag{2.20}$$

$$\alpha\sqrt{1-\alpha}\left|d\right\rangle\left(\left|01\right\rangle - e^{i\Delta\phi}\left|10\right\rangle\right). \tag{2.21}$$

up to a global phase where again $|c\rangle, |d\rangle$ is a photon present in mode c or d respectively, and $\Delta\phi$ the phase difference between the photonic modes at the position of the beamsplitter. Our photon detectors can not distinguish the photon number in the output, so $|c\rangle|c\rangle \equiv |c\rangle$. Even with photon-number resolving detectors, if the photon-losses are significant $(\eta_N)^2 \ll \eta_N$, the chance of measuring two photons is small, which makes this term not distinguishable from when a single photon was emitted. Writing the state in the density matrix form, and normalizing accordingly we arrive at

$$\left|\psi\right\rangle\left\langle\psi\right|_{A/B}^{SC} = (1-\alpha)\left|\Psi^{\pm}(\Delta\phi)\right\rangle\left\langle\Psi^{\pm}(\Delta\phi)\right| + \alpha\left|00\right\rangle\left\langle 00\right| \tag{2.22}$$

where $\Psi^{\pm}(\Delta\phi) = \frac{|01\rangle \pm e^{i\Delta\phi}|10\rangle}{2}$. This shows that which shows that conditioned on a single click in the detectors, the communication qubits are projected in a maximally entangled state with phase $\Delta\phi$ with probability $1-\alpha$, and in a separable state $|00\rangle$ with probability α. This makes the fidelity scale as

$$F = 1 - \alpha \tag{2.23}$$

which approaches for vanishingly small α. However, at this limit, the probability to generate entanglement, which scales at

$$p_{SC} = \alpha * \left(\eta_1 + \eta_2\right) \propto \sqrt{p_{BK}} \tag{2.24}$$

which scales much favourable in the transmission efficiencies for $\alpha \gg \eta_{1,2}$. This is the main benefit of the single-click protocol, and allows for order of magnitude higher rates of entanglement generation, given the current performance of optical interfaces and transmission efficiency.

What we can observe is that even in the ideal case, the single-click protocol can not generate a perfect Bell-state, in contrast with the Barrett-Kok protocol 2.16. Furthermore, the entangled state phase is dependent on the phase difference between the optical modes at the beamsplitter. This means that for a faithful generation of the same entangled state each time, this phase must be either known, or it has to be stable over the full duration over which many copies of the states are generated. This includes all relevant phases such as: optical phase of the excitation and phase errors due to optical path differences from the NV center to the beamsplitter. This makes the protocol technically demanding, but has shown possible to realize in the lab. In experiments with other infidelities such as detector darkcounts, photon indistinguishability and residual phase noise, fidelities exceeding 80 % have been achieved [16] at a rate of $\sim 10\,\mathrm{s}^{-1}$.

Chapter 5 shows how to implement a phase-stable architecture over a metropolitan fiber link. Using this architecture, Chapter 6 then shows that the single-click protocol can be used on a metropolitan scale to generate entanglement between two NV centers.

2.2.4. MEASURING QUANTUM STATES

Given an unknown quantum state ρ, there are various ways to show that it is an entangled state. One of the ways to quantify this entanglement is to perform state tomography. This is done by performing measurements on many copies of the state ρ in different bases and to estimate the full density matrix ρ, This then allow for the calculation of the 'degree of entanglement' via metrics such as concurrence or logarithmic negativity. The reconstruction of the two-qubit density matrix ρ_M can be done by decomposing it in the 2-qubit Pauli basis spanned by $[\mathbf{P} = \sigma_i \otimes \sigma_j]$ for $i, j \in 0,1,2,3$ with

$$\sigma_0 = \begin{pmatrix} 1 & 0 \\ 0 & 1 \end{pmatrix}, \sigma_1 = \begin{pmatrix} 0 & 1 \\ 1 & 0 \end{pmatrix}, \sigma_2 = \begin{pmatrix} 0 & -i \\ i & 0 \end{pmatrix}, \sigma_3 = \begin{pmatrix} 1 & 0 \\ 0 & -1 \end{pmatrix} \tag{2.25}$$

by writing

$$\rho_M = \sum_{P_i \in \mathbf{P}} p_i P_i, \text{ with } p_i = Tr\left(P_i \rho_M\right) \tag{2.26}$$

This requires measuring all 16 operators, which can be reduced to the 9 two-qubit operators by re-using the measurement outcomes from the measured correlator e.g. $\langle ZZ \rangle$ to calculate $\langle IZ \rangle$ and $\langle ZI \rangle$. Depending on the rate of entanglement generation, full state tomography can be time consuming, especially for states with higher dimensions. Additionally measurement uncertainties and systematic errors can make this reconstruction procedure predict non-physical density matrices. A way to prevent non-physical density matrices is to use Bayesian estimation for density matrix estimation, which takes into account the properties of the density matrix, and uses the tomography outcomes as an input [35, 36]. We therefore only applied this technique for when the measurement rate was sufficiently high, see Chapter 6 supplement.

A more data efficient way to investigate if two-qubit state ρ_M is entangled is by calculating the fidelity with one of the (ideal) Bell-states 2.3. If we know that the state ρ_M should be close to one of the ideal Bell states ρ_I, we can calculate the fidelity via

$$\mathbf{F}(\rho_M, \rho_I) = Tr\left(\sqrt{\sqrt{\rho_M}\rho_I\sqrt{\rho_M}}\right)^2. \tag{2.27}$$

When $\mathbf{F}(\rho_M, \rho_I) > 0.5$ the state is entangled. Because of the only 4 non-zero elements of the $\Psi^{\pm}$ Bell-states, this value can be experimentally estimated with only 3 two-qubit measurements, given by

$$\mathbf{F} = \frac{1}{4}\left(1 - \langle ZZ \rangle \pm \langle XX \rangle \pm \langle YY \rangle\right) \tag{2.28}$$

where the $\pm$ corresponds to the fidelity with the $\Psi^{\pm}$ Bell-state and $\langle ZZ \rangle$ the correlation between the Z measurement outcomes on each node (equivalent for X and Y). This reduces the amount of correlators to be measure significantly, and allows for a smaller uncertainty on the measured values within the same amount of time. This method is used in Chapter 6 for characterization of the entangled state over the metropolitan link.

2.3. QUANTUM FREQUENCY CONVERSION: THEORY

In this section we discuss the methods for the conversion of the frequency (and therefore wavelength) of light, including for weak fields of single photons. We restrict ourselves to the field of three-wave-mixing (TWM) in non-linear materials (NLM). We will work towards a description of Difference Frequency Generation (DFG), which is the generation of a lightfield at frequency ω_s, by means of the interaction of two input fields at frequency ω_p, ω_i. This process plays a central role in Chapters 3 and 4, and employing a new type of converter with better performance played a major role in the work described in Chapter 6.

First we give a short description of the theory behind non-linear optics, and show the phase-matching and energy conservation conditions. For a more detailed description on this topic we refer to [37–39], from which much inspiration was taken when writing this section. We then describe the two different ways to satisfy these equations in our frequency converters as used in this work, called critical- and quasi-phasematching. We describe the performance of each of the approaches, and mention their use in the later Chapters.

2.3.1. THEORY OF NON-LINEAR OPTICS

In a dielectric medium, the electric field $\boldsymbol{E}$ induces a polarization $\boldsymbol{P}$. In the most general case, the relation between electric field and polarization is given by the power series

$$P_i = \epsilon_0 \sum_{j\in\hat{\boldsymbol{r}}} \chi^{(1)}_{ij} E_j + \epsilon_0 \sum_{j\in\hat{\boldsymbol{r}}} \sum_{k\in\hat{\boldsymbol{r}}} \chi^{(2)}_{ijk} E_j E_k + \ldots, \tag{2.29}$$

with $\hat{\boldsymbol{r}}$ the Cartesian coordinates $[\hat{x}, \hat{y}, \hat{z}]$, ϵ_0 the permittivity of free-space, and $\chi^{(n)}_{\ldots}$ tensors of rank $n+1$ which are called the nth-order susceptibilities that describe the dielectric. In words, an electric field in direction j, can induce a polarization in direction i, with a strength $\epsilon_0\chi^{(1)}_{ij}$, and two electric fields in direction j,k induce a polarization in direction i with strength $\epsilon_0\chi^{(2)}_{ijk}$. We call the first contribution $P^{(1)}_i$ the linear term, and the second term $P^{(2)}_i$ the non-linear, and we neglect the higher order terms. We can write the *combined* electric field with components $n \in N = [1, 2, \ldots]$ with frequency ω_n as

$$\boldsymbol{E} = \sum_{n=-N}^{N} E(\omega_n) e^{-i\omega_n t}, \tag{2.30}$$

with $E(\omega_n) \equiv \boldsymbol{A}_n e^{i\boldsymbol{k}_n\cdot\vec{r}}$ the spatial amplitude and phase, described by the amplitude vector $\boldsymbol{A}_n$ and wavevector $\boldsymbol{k}_n$ related to the frequency ω_n. By defining $\omega_{-n} = -\omega_n$, the negative summation range handles the complex conjugation for us.

Suppose we have two of these fields at frequencies ω_1 and ω_2 (so $N = 2$) incident on a medium, using Eq. 2.30 and Eq. 2.29 we can find the expression of the polarization as:

$$P^{(1)}_i = \epsilon_0 \sum_{j\in\hat{\boldsymbol{r}}} \sum_{n=N}^{-N} \chi^{(1)}_{ij}(\omega_n) E_j(\omega_n) e^{-i\omega_n t} \tag{2.31}$$

$$P^{(2)}_i = \epsilon_0 \sum_{j,k\in\hat{\boldsymbol{r}}} \sum_{n,m=N}^{-N} \chi^{(2)}_{ijk}(\omega_n+\omega_m, \omega_n, \omega_m) E_j(\omega_n) E_k(\omega_m) e^{-i(\omega_n+\omega_m)t}. \tag{2.32}$$

The first, linear term $P_i^{(1)}$ only contains the ω_1 and ω_2 that are in the original input field. For small field amplitudes E_n, this term dominates and linear optics effects such as diffraction and dispersion can be described. It also is used to describe effects such as acousto-optic effect, mentioned in the later section 2.5.4, where $P_i^{(1)}$ is modulated with pressure waves.

When the electric field intensities E_n are large (and corresponding higher-order susceptibilities large enough), the higher order term $P_i^{(2)}$ become non-negligible and its effects can be observed. One example is the electro-optic effect, where an externally applied electric field $\boldsymbol{V}$, changes the effective refractive index experienced by an optical field $\boldsymbol{E\omega}$. This can be used for phase and amplitude modulation, as mentioned in 2.5.4. Additionally, the term also contains the terms for Second Harmonic Generation (SHG) by the frequencies $e^{\pm i2\omega_1 t}, e^{\pm i2\omega_2 t}$, Sum Frequency Generation (SFG) $e^{\pm i(\omega_1+\omega_2)t}$, and Difference Frequency Generation (DFG) $e^{\pm i(\omega_1-\omega_2)t}$, meaning that the *polarization of the crystal* oscillates at frequencies not present in the original fields. The strength of these interactions depend on value of the $\chi^{(2)}_{ijk}(\omega_n+\omega_m,\omega_n,\omega_m)$, which in general depend on the frequencies of the input and relative orientation of their electric fields with respect to the medium. For the next step in the derivation, we need to describe the coherent interaction of the polarization of the crystal with the electric fields.

For further derivation[38] of the electric field in a lossless, nonmagnetic and nonlinear dielectric, one needs to find solutions to the equation

$$\nabla^2 \boldsymbol{E} + \frac{\boldsymbol{\epsilon}_r}{c^2}\frac{\partial^2 \boldsymbol{E}}{\partial t^2} = -\mu_0 \frac{\partial^2 \boldsymbol{P}^{(2)}}{\partial t^2} \tag{2.33}$$

with μ_0 the permeability, c the speed of light and $\boldsymbol{\epsilon}_r$ the (frequency dependent) dielectric tensor (for isotropic media the refractive index $n = \sqrt{|\boldsymbol{\epsilon}|}$). This is a form of the wave equation, derived from Maxwell's equations, where the nonlinear polarization vector $\boldsymbol{P}$ acts as a source term. Deriving solutions to this equation is beyond the scope of this work and can be found in Ref. [38], so here we focus on the solutions of three fields $\omega_1, \omega_2, \omega_3 = \omega_1 + \omega_2$ of the form $E_m(z,t) = A_m(z)e^{i(k_m z - \omega_m t)} + c.c.$, which are co-propagating plane waves along the z-axis, with slowly varying amplitudes $A_m(z)$.

The solutions for their amplitudes are given by the coupled mode equations[38]

$$\frac{dA_1(z)}{dz} = -i\kappa_1 A_2^*(z)A_3(z)e^{-i\Delta k z} \tag{2.34}$$

$$\frac{dA_2(z)}{dz} = -i\kappa_2 A_1^*(z)A_3(z)e^{-i\Delta k z} \tag{2.35}$$

$$\frac{dA_3(z)}{dz} = -i\kappa_3 A_1(z)A_2(z)e^{i\Delta k z}, \tag{2.36}$$

for the coupling constants $\kappa_m \propto d_{eff} \propto \frac{\chi^{(2)}_{ijk}}{2}$. The parameter d_{eff} is called the effective nonlinear coefficient, which is a material specific property and can be calculated from the propagation and polarization directions of all three fields, given by the relation in equation 2.32. We introduced the refractive index $n(\omega_m,...) \equiv n_m$ that belongs to the wave m (which can depend on quantities other than ω_m such as temperature). The value k_m is then given by the dispersion relation $c|\boldsymbol{k}_m| = n_m\omega_m$. The relation 2.35 describes

the change of the complex amplitude A_2 along the material, which depends on the two other complex amplitudes of the other fields A_1, A_3, and a phase term $e^{\pm i\Delta kz}$, with

$$\Delta k = k_3 - k_1 - k_2 \tag{2.37}$$

which is the wavevector mismatch. In general, k_m (and hence Δk) can be a vector in $3D$ space, but for the processes in this work we restrict ourselves to co-linear fields in the $\hat{z}$ direction. All second-order nonlinear effects can be described using this set of equations. In the next section we will describe how to engineer a system such that this process happens *efficiently*.

2.3.2. PHASEMATCHING

Whether or not a second-order nonlinear effect to occurs efficiently, depends on the wavevector mismatch 2.37. To illustrate this, we can find the intensity after propagation through a medium of length L by integrating 2.35 over z (as derived in [38])

$$A_2(L) = -i\kappa_2 A_1^* A_3 \int_{z=0}^{L} e^{-i\Delta kz} = -i\kappa_2 A_1^* A_3 \frac{e^{-i\Delta kz} - 1}{-i\Delta k}, \tag{2.38}$$

and taking the squared modulus

$$I_2(L) = |A_2(L)|^2 \sim (\kappa_2 |A_1||A_3|)^2 L^2 \,\mathrm{sinc}^2\left(\frac{\Delta kL}{2}\right). \tag{2.39}$$

where we have assumed that the amplitudes A_1, A_3 are constant* over the length of the medium. Achieving maximal efficiency is only possible for

$$\Delta k = 0, \tag{2.40}$$

which is called the *phasematching* condition, and the intensity drops off quickly for $\Delta k \neq 0$, see Fig.2.3a. Together with the energy conservation condition

$$\hbar\omega_3 = \hbar\omega_1 + \hbar\omega_2, \tag{2.41}$$

they are the two conditions that need to be satisfied for the the nonlinear process to occur. In general it is not easy to satisfy both of these conditions at once. Using that $\lambda = \frac{2\pi c}{\omega}$ and filling Eq. 2.41 into Eq. 2.37 we find

$$\Delta k = \frac{1}{c}\big(n_3\omega_3 - n_1\omega_1 - n_2\omega_2\big) = \frac{1}{c}\big((n_3 - n_1)\omega_1 + (n_3 - n_2)\omega_2\big). \tag{2.42}$$

If the relation between refractive index and frequency is monotonically increasing[40], this dispersion is called *normal*, which is the case for a lot of (relatively simple) dispersive media. This gives $n_3 > n_1, n_2$, and hence Eq. 2.42 is always positive. One way to look at this is that the waves at different frequencies travel at different velocities inside the medium, and after a certain length $\frac{\pi}{\Delta k}$ are completely out of phase. This can be seen for

*For the strong pump field E_1 this holds, but the single-photons E_3 are depleted if the process is efficient. The full derivation for the case $\frac{dA_3}{dz} \neq 0$ we refer to [38]

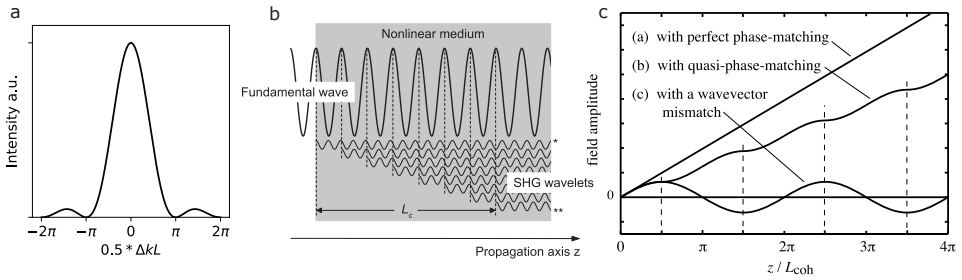

Figure 2.3: a) Visualization of the dependence of field intensity on the wavevector mismatch (Eq. 2.39). The $sinc^2$ quickly drops off for nonzero wavevectormismatch. b) Intuitive picture of why the phasematching matters, with Second Harmonic Generation as an example. The wavelets generated by the nonlinear Polarization travel at a different speed through the medium, and after a distance L_c are out of phase. Therefore destructive interference prevents buildup of the electric field, image adapted from [37] c) By satisfying the phasematching condition 2.40, coherent buildup of the wavelets can lead to an output field. For critical(perfect) phasematching Δk is zero throughout the propagation (a), while for quasi phasematching the periodic inversion of d_{eff} improves the build up(b) compared to the non-phasematched case (c). Images a,b adapted from [38].

the case of second harmonic generation (SHG) in Fig.2.3b, where an input field at frequency ω generates smaller fields via the nonlinear polarization of the medium along its path at frequency 2ω, that travel faster, e.g. $\Delta k \neq 0$, and after a distance $L = 2L_c = \frac{\pi}{\Delta k}$ the generated fields destructively interfere. The many techniques to overcome this challenge are the groundwork of nonlinear optics experiment and devices, and it entails finding a configuration of frequencies and material properties that satisfy both conditions at once. Two of these techniques are especially relevant for this work, called Critical phasematching (CPM) and Quasi phasematching (QPM). CPM satisfies the conditions by using a material where the refractive index not only depends on the frequency, but also the polarization of the light inside the crystal (and temperature of the crystal, but we will discuss this later). This property is called birefringence, and therefore this is sometimes also called Birefringent phasematchig. QPM is uses manufacturing or manipulation techniques to periodically invert one of the crystal axis, and therefore the *sign* of the d_{eff}. Choosing the period of this inversion can compensate for nonzero wavevector mismatch. We will now give a brief discussion of both types of phasematching, where we take the QFC processes used in Chapters 3 and 6 as an example. This process is DFG of single-photons at the visible wavelength ($\frac{2\pi c}{\omega_3}$ =637 nm), to the telecom L-band ($\frac{2\pi c}{\omega_2}$ =1587 nm) using a strong classical pump ($\frac{2\pi c}{\omega_1}$ =1064 nm).

CRITICAL PHASEMATCHING

There are two main types of birefringent materials, uniaxial and biaxial[†]. In a uniaxial crystal, there is a single direction $\hat{c}$ defined by the crystal structure, called the optical axis. For light traveling in direction $\boldsymbol{k}$, if the polarization is in the plane containing $\hat{c}$ and $\boldsymbol{k}$ it is called extra-ordinary, and if its orthogonal to this plane it is called ordinary. The

[†]In the context Type I and II phasematching usually there is one ordinary and one (orthogonal) extraordinary polarization for the three fields, where a single angle is tuned to perform the phasematching to change the extraordinary refractive index, and we can treat a biaxial crystal effectively as a uniaxial crystal.

Table 2.1: Types of phasematching for birefringent crystals.

	Positive ($\bar{n_e} - n_o > 0$)	Negative ($\bar{n_e} - n_o < 0$)
Type I	$n_3^o\omega_3 = n_1^e\omega_1 + n_2^e\omega_2$	$n_3^o\omega_3 = n_1^o\omega_1 + n_2^o\omega_2$
Type II	$n_3^o\omega_3 = n_1^o\omega_1 + n_2^e\omega_2$	$n_3^e\omega_3 = n_1^e\omega_1 + n_2^o\omega_2$

refractive index for the ordinary polarization n_o is independent of propagation direction, but for the extraordinary polarization it is given by

$$\frac{1}{n_e(\theta)^2} = \frac{\sin^2\theta}{\bar{n_e}^2} + \frac{\cos^2\theta}{n_o^2}, \tag{2.43}$$

where $\bar{n_e}$ is the principle value of the extraordinair refractive index, and θ the angle between the direction of propagation $\boldsymbol{k}$ and the optical axis $\hat{c}$. In the case where $\bar{n_e} - n_o > (<) 0$ the birefringence is postive (negative). Considering the normal dispersion, this gives four types of possible phasematching, given in the table 2.1.

When varying this angle $\theta \in [0, \frac{\pi}{2}]$ on can vary n_e of the full range of $[n_o, \bar{n_e}]$. It is this *tunability* that gives flexibility to phasematch for a given set of frequencies. In general it is preferred to have a normal incidence of the fields on the entry and exit facet of the crystal. We can achieve this by doing careful calculations on how the surface is to be cut with a certain angle to the crystal orientation. Only small angle variations are then needed to fine-tune the phasematching. In practice, it is difficult to tune this angle to the level at which the wavevector mismatch is completely zero. We can therefore use the fact that the birefringence is temperature dependent to tune it to an even finer degree. The resulting phasematching shows a continuous increase of the field amplitude over the length of the crystal, see Fig. 2.3c.

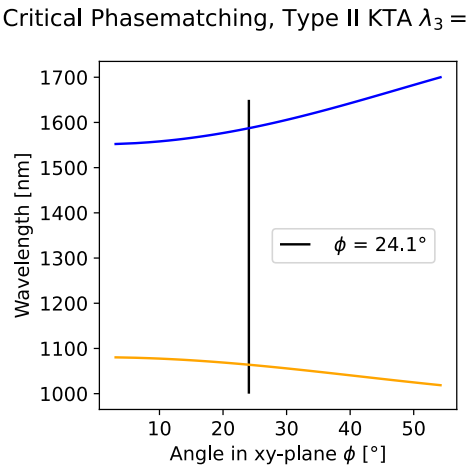

Figure 2.4: Coloured lines show the wavelengths for which DFG is phasematched using Type II CPM in a KTA crystal, with orange (blue) being the pump (idler) field. At the calculated angle of 24.1° the wavelengths correspond to λ_3 =637 nm, λ_2 =1064 nm and λ_3 =1587 nm (vertical line).

The QFC used in Delft in the experiment in Chapter 6 is critically phasematched, using a birefringent (negative, biaxial) and nonlinear material called $KTiOAsO_4$ (KTA). We can use the Sellmeier[40] equations (empirically determined formulae for the dispersion) for this material[41] to calculate the refractive indices and therefore the wavevectormismatch Δk. For this we need to know the type of phasematching used (Type II, so ω_3 is extraordinary, tab. 2.1), and the orientation of the crystal with respect to the beams ($\theta = 90°, \phi \approx 30°$ (varied)). We can use the software package *SNLO* (available here to calculate the expected phasematching conditions when varying the angle ϕ, effectively

solving Eq. 2.37 using Eq. 2.43. This is shown in Fig. 2.4, where the expected phase-matching angle is 23.1°, close to the crystal cut of $\phi \approx 30°$. Note that the simulation software did not include the temperature effects, which are significant for this material, and this was taken into account in the design of the QFC (but outside the scope of this example). More details will be shown in the later section 2.4.3.

There are a few downsides to using CPM. Firstly, some materials that are have a high nonlinear coefficients exhibit no birefringence, making them unsuited for this approach. Secondly, for the materials that are both birefringent and have high nonlinear coefficients in the direction of propagation is fully determined by the phasematching, while from the perspective of having the maximal nonlinear coefficient d_{eff} other directions/polarizations might give an order of magnitude higher values. Second, the extraordinary polarized beam experiences an effect called walk-off: the direction of the energy propagation is no longer aligned with $\boldsymbol{k}$. This makes the ordinary and extraordinary beams move apart inside the crystal, limiting the effective interaction length, and putting a lower limit on the beam-waists of the light. This also prohibits the used of structures such as waveguides to confine the light, which can greatly boost the efficiency by virtue of higher field intensities, see Eq. 2.39. This makes it difficult to achieve high internal conversion efficiencies at moderate powers (<1 W) and crystal lengths (<10 cm). A lot of these downside are eliminated when Quasi phasematching is performed.

QUASI PHASEMATCHING

Introduced after the realization of CPM, QPM gets rid of most of the issues previously mentioned via clever material engineering. For a given nonlinear interaction there is a characteristic distance over which the wavelets get out of phase, and by inverting the d_{eff} after that exact distance, the phase contribution gets flipped and enhances the signal. Repeating this over the full length of the crystal L, making repeating blocks of opposite d_{eff} with period $\Lambda = 2L_{coh}$, the amplitude keeps building up, see Fig.2.3. The phasematching conditions and nonlinear configuration for this configuration, called QPM to the first order, is given by[38]

$$\Delta k_\Lambda = k_3 - k_1 - k_2 - \frac{2\pi}{\Lambda} \tag{2.44}$$

$$d_\Lambda = \frac{2}{\pi} d_{eff} \tag{2.45}$$

which now depends on the flipping period Λ. This extra degree of tuneability gives the freedom to choose both the material, polarization and propagation directions that give the highest nonlinear coefficients for a given set of $\omega_1, \omega_2, \omega_3$, given that is possible to engineer the domains accurately. The real breakthrough for this technique came when a method for the growth of Lithiumniobate (LN), a nonlinear material previously used with CPM, with these varying domains was developed.

This freedom allows using materials that are not birefringent and to use so called Type-0 phasematching where all fields are polarized in the same direction, e.g. $n_3^o\omega_3 = n_1^o\omega_1 + n_2^o\omega_2$. This has the benefit of having no walkoff in the propagation through the crystal, allowing for the usage of waveguides for increased mode overlap and intensity. It also allows for the usage of the propagation direction with the highest nonlinear

coefficient, where for example in LN d_{31} =4.35 pmV^{-1} is generally used for CPM, now d_{33} =27 pmV^{-1} can be accessed.

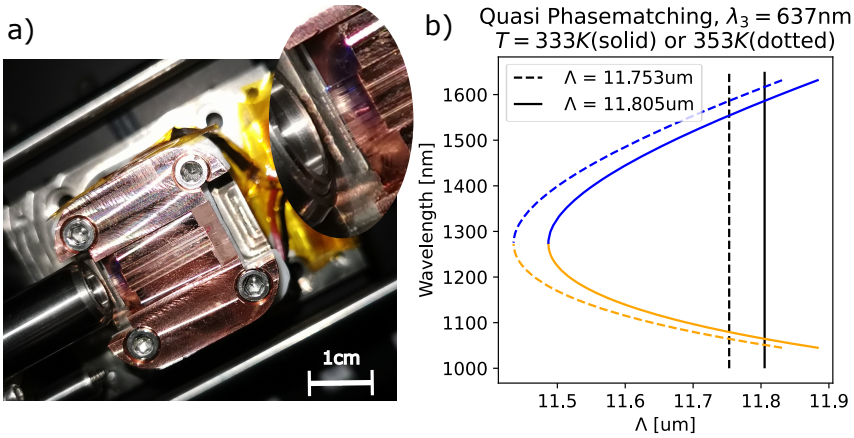

Figure 2.5: **Quasi Phasematching crystal.**a) Photo of ppLN crystal (transparent) on copper heatsink, with lens aiming at input facet. Zoom in shows front of crystal, with waveguides visible as lines in crystal. b) Wavelengths for which DFG is phasematched using Type 0 QPM in a LN crystal. Coloured lines show the phasematching curve for the pump (orange) and idler (blue) fields, for two typical temperatures (60°C (solid) and 80°C (dashed)). This leads to the optimal QPM period Λ of 11.753 µm and 11.805 µm (vertical lines) to phasematch λ_3 =637 nm, λ_2 =1064 nm and λ_1 =1587 nm, highlighting the tunability of the phasematching process.

To give an idea of the length scale of the modulation of d_{eff} we can calculate the phasematching condition 2.44 for our application of downconversion of single-photons at the visible wavelength ($\frac{2\pi c}{\omega_3}$ =637 nm), to the telecom L-band ($\frac{2\pi c}{\omega_2}$ =1587 nm) using a strong classical pump ($\frac{2\pi c}{\omega_1}$ =1064 nm). We use the fact the LN has a flat cut facets, and the phasematching is of Type-0. By using a software package *SNLO* (available here we can calculate which Λ is needed. The result is shown in Fig. 2.5b), where we have plotted the phasematching curves for two different temperatures of the crystal. This shows that the period is about 11.4 µm, where an accuracy below 10 nm is needed to accurately match the target wavelengths. The vertical lines indicate where the two lower wavelengths match the input of 637 nm. The difference between the curves, visible as the different starting points of the phasematching and trajectories followed, shows that also for QPM the temperature of the crystal can be used to finetune the phasematching condition. This is not due to the change in birefringence (as all waves have the same polarization), but actually the expansion/contraction of the crystal and hence the period Λ, changing the $\frac{2\pi}{\Lambda}$ in Eq. 2.44. In general, a single crystal can be manufactured with waveguides on top that all have a slightly different poling period, increasing the chance of a well phasematched system within a temperature range (see Fig. 2.5b)), given the manufacturing imperfections.

In practice, one can order these types of crystals from companies such as NTT (see here) or AdvR (here). There are even solutions where the crystal is already packaged with input/output fibers, and thermistors/heaters for active temperature tuning. They can also include waveguides in the material, which are basically μm-scale features on the

surface of the crystal, that have a different refractive index than the surrounding material. These create a better confinement of the optical fields in the crystal, and allow for close to unity internal conversion efficiencies at moderate pump powers (200 mW). These waveguides, together with the periodic poling, create variations in the phase-matching, and allow for unwanted processes to be slightly phasematched. These unwanted processes can be Spontaneous Parametric Down-Conversion (SPDC) processes, that could generate single photons at the target wavelength. We will discuss this in the next sections

2.4. QUANTUM FREQUENCY CONVERSION: PRACTICAL CONSIDERATIONS

In the last section we have discussed the basic theory behind nonlineair processes such as DFG, and provided some basic calculations in how one can realize the conditions for efficient conversion. In the following section we will discuss some of the practical considerations for the specific process of downconverting single-photons from NV-centers (as used in Chapters 3 and 6, but are also applicable or other emitters in the visible, such as the ones used to convert a photon state compatible with a rare-earth ion memory to match an NV-center in Chapter4. In partical, we further investigate the noise photons that are added in the QPM approach, and introduce a novel design that suffers from orders of magnitude lower noise, used in Chapter 6). The converters used in Chapter 4 however do not suffer from excess noise because of favourable wavelength selection, as will also be clear from the following sections.

2.4.1. CONVERSION OF SINGLE PHOTONS*

$$\lambda_P < \lambda_{out} \text{ for } \lambda_{in} < \frac{\lambda_{out}}{2} \text{ (“short-wavelength pumped”)} \tag{2.46}$$

$$\lambda_P > \lambda_{out} \text{ for } \lambda_{in} > \frac{\lambda_{out}}{2} \text{ (“long-wavelength pumped”)} \tag{2.47}$$

The internal conversion efficiency η_{int} of a QFC can in principle reach unity, values exceeding 70 % [42] were previously demonstrated for a down-conversion setup from λ^{NV} to the telecom L-band. η_{int} equals the rate of generated photons at λ_{out} behind the QFC divided by the rate of photons at λ_{in} incident to the QFC and corrected for all losses and the energy difference between the photons at the different wavelengths. Most significant losses are introduced by the required spectral filters and the free-space to single-mode coupling when the fields enter the waveguide and subsequently a single-mode optical fiber for long-range transmission, limiting the total device efficiency (i. e., external efficiency) of demonstrated QFCs to below 60 % [43, 44].

2.4.2. EXCESS NOISE IN PERIODIALLY POLED SYSTEMS*

In state-of-the-art devices, periodically poled NLM with waveguiding structures are used. While efficient conversion with low pump power is possible due to the confinement of the interacting waves, random duty-cycle (RDC) errors in the spatial parame-

ters of periodicity and waveguide result in elevated efficiency of the SPDC noise process which can be larger by orders of magnitude than for a birefringently phasematched configuration [45, 46]. This process was theoretically investigated in [47]. For a statistical deviation σ_l from the mean period length l, the rate of SPDC noise photons additionally generated by the existence of RDC-errors, n_{SPDC}^{RDC}, is described by:

$$n_{SPDC}^{RDC} = \frac{N_{pm}}{N_D}\left(1 - e^{-\frac{\pi^2\sigma_l^2}{2l^2}}\right) \tag{2.48}$$

N_{pm} denotes the rate of converted photons in perfectly phase matched conditions ($\Delta k = 0$) for the wavelength combination of the noise-generation process (1064 nm→1589 nm+3220 nm) and N_D equals the number of domains. This effect can be reduced by reducing the RDC-errors of periodically poled materials. In a QFC incorporating a periodically poled bulk crystal without waveguide confinement, a significant reduction by roughly a factor of five was achieved [42]. To further reduce this effect, the poling quality of NLM must be improved, which implies higher manufacturing costs. Even in the ideal case of zero RDC-errors, the rate of SPDC-generated noise will remain non-zero due to the non-vanishing efficiency of off-phase matched conversion.

To investigate the rate of SPDC-generated noise without the effect of RDC-errors, one can use a monocrystalline NLM, i.e., implementing birefringent phasematching. With a variety of those materials being available at low cost, a significant reduction of noise photons may be available without excessive cost demand. In case of birefringent phasematching, the conversion efficiency of a three-wave mixing process in a NLM of length L at the low-gain limit is proportional to

$$\mu_c \propto \operatorname{sinc}\left(\frac{\Delta k\, L}{2}\right)^2 \tag{2.49}$$

with the phase mismatch Δk (see also sec. 2.3.2). To confirm the applicability of Eq. 2.48 to the case of the SPDC-generated photons, one must calculate the gain-factor and phase-mismatch for the respective experimental conditions. In the case investigated here, high pump powers are present in the NLM, but the phase mismatch for the SPDC process is large. Hence, the low-gain approximation remains valid for this case. The explicit calculation is presented in section 2.4.5.

Therefore, if Raman-noise can be neglected and the material parameters are chosen to result in a large phase mismatch and thus strongly suppressed efficiency of the SPDC-process, the noise generated by quantum frequency converters may be reduced to negligible levels. Note, that spectral filtering will always remain a requirement for low-noise conversion, since the amplitudes of both Raman-scattering and SPDC strongly vary with the wavelength of the generated photons. While the applicability of the semi-classical approximation to the single-photon level is arguable, we assume that the average rate of SPDC-generated noise photons will be in similar orders of magnitude when quantum effects are considered. An alternative approach to circumvent high rates of noise is a two-step conversion scheme with an intermediate conversion to the near infrared [48], i.e., realizing a long-wavelength pumped QFC from the visible range, which adds losses and increases complexity.

In this work, we investigate a single stage QFC scheme for the conversion of photons emitted by Nitrogen-vacancy centers (NV-centers) at $\lambda^{NV} = \lambda_{in}$ =637.24 nm to λ_{out} =1589 nm, resulting in a short-wavelength pumped configuration (λ_P =1064 nm). In current generation short-wavelength pumped periodically-poled Lithium Niobate (ppLN) based QFCs with waveguided interaction (ppLN waveguide QFC), the spectral density of noise photons (NSD) introduced to the transmission channel per time interval equals 250 $s^{-1}\,pm^{-1}$ (2100 $s^{-1}\,GHz^{-1}$)[49]. In a recent work, an improvement by a factor of five was demonstrated with a QFC based on a ppKTP crystal without a waveguide in a passive enhancement cavity (cavity-assisted ppKTP QFC), where a NSD of 45 $s^{-1}\,pm^{-1}$ at an external conversion efficiency of 33 % was demonstrated [42], confirming that noise can be decreased by making use of higher-quality periodically-poled materials. However, further work must be conducted. For a strictest possible bandwidth of 50 MHz (limited by the bandwidth of the down-converted photons), the ppLN waveguide QFC (cavity-assisted ppKTP QFC) therefore adds error counts with a rate of approximately 100 s^{-1} (20 s^{-1}). Since dark-count rates of single-photon detectors can be below 10 s^{-1}, the QFC is the main source of noise events, thus limiting the achievable fidelity of entanglement generation. Our experiment shown in Chapter 3 involves two state-of-the-art NV-center nodes combined with waveguide-based ppLN QFCs highlight the need for low noise solutions. In this interference experiment, the average SNR after ultra-narrow spectral and time filtering was approximately 15, with the major noise contribution by the QFCs. Without any improvements in noise reduction, the usage of the single-click protocol for entanglement-generation[16, 50] intrinsically reduces the signal brightness (i.e., the bright state population of the NV-center) to limit the protocol error of double photon events. At a modestly reduced signal-brightness (10 %), this would result in a SNR of 1.5 (3 in case of cavity-assisted ppKTP QFC), prohibiting entanglement generation.

In the following section, we demonstrate that a conversion scheme in birefringent phasematching configuration enables highly efficient conversion with smaller noise counts than in any other configuration for the wavelength combination investigated here. The overall device efficiency is as high as in state-of-the-art QFCs, while reducing the number of noise counts by more than two orders of magnitude compared to a ppLN waveguide QFC and by a factor of 20 compared to a cavity-assisted ppKTP QFC.

2.4.3. NOISE REDUCED APPROACH (NORA) CONCEPT*

In state-of-the-art devices, periodically poled crystals with waveguiding structures are used because they enable high conversion efficiency with low-power pump lasers. At the same time, high rates of noise photons are introduced. We propose a TWM scheme without the use of a periodically poled material and waveguiding structures, i.e., TWM in a monocrystalline bulk material. This approach requires birefringent phase matching for efficient conversion, which requires orthogonal polarization of the interacting waves. For most NLM, the effective nonlinearity is smaller, if the phasematching condition is met in Type-I or Type-II configuration compared to the effective nonlinearity in Type-0 configuration in the case of quasi phasematching in pp-NLM. To overcome this challenge, larger pump laser intensities are required, which can be achieved by resonantly enhancing the pump laser power in an optical cavity. Relying on active stabilization of

the cavity, which can be accomplished with low-cost electronic components, enables maintaining efficient conversion while the pump wavelength is tuned, resulting in a tunable output wavelength. Since the central wavelength of photons emitted by NV-center qubits can drift by up to 10 MHz, a tunable QFC output wavelength is required to maintain indistinguishable telecom photons. Whereas similar setups have been proposed for QFC [42, 51, 52] and photon-pair generation [53], they incorporate periodically-poled crystals and passively stabilized cavities to achieve the required efficiency.

Here monocrystalline KTA is chosen as the NLM, exhibiting a broad transparency range between 0.5 to 3.5 µm [54] and high threshold to laser-induced damage. The phase matching condition is met in type-II configuration, i.e., the high-intensity pump field and the converted telecom photons have perpendicular polarization. Numerical simulations are performed to approximate the required laser power and crystal length for efficient conversion. With this scheme, an internal conversion efficiency as high as 80 % can be reached. With pump laser power up to 400 W available for the experiments, an internal efficiency of approximately 60 % is expected. Since due to the free-space interaction no single-mode waveguide coupling (which can result in losses up to 40 % [55, 56] is required, the overall device efficiency is expected to reach similar values as in waveguide-based setups with larger internal conversion efficiency.

2.4.4. NORA DESIGN*

The experimental setup is depicted in Fig. 2.6. The 30 mm-long NLM KTA is placed in a bow-tie cavity (length 46 cm) consisting of three HR-coated mirrors (R_{HR} =99.95 %) and one coupling mirror (R_{in} =99 %), in which the incident (coupled) pump power is enhanced by a factor of 40 (60). Two cavity mirrors have a ROC of 100 mm, resulting in a focus diameter of roughly 100 µm inside the NLM.

An amplified fiber laser (NKT ADJUSTIK Y10 and BOOSTIK Y10) provides up to 9 W pump power with a tuning range of 160 GHz. To maintain resonant enhancement at any time, one cavity mirror is mounted to a piezoelectric actuator. A feedback loop implementing the Hänsch-Couillaud locking scheme [57] provides an error signal. Further components are half-wavelength (quarter-wavelength) retardation plates (HWP, QWP) rotating the polarization state of the two input fields and various elements (Telescopes, collimation lens (CL), focusing lens (FL)) for efficient coupling of the fields into the cavity and single-mode optical fiber, respectively. To reduce the coupling of any stray-light or residual pump light into the optical fiber, the converted light is filtered spectrally by several band-pass and edge-pass filters (BP, optical density of 20 at 1064 nm). The type-II phasematching condition is met at a crystal orientation of $\Theta \approx 90°, \Phi \approx 30°$ and a crystal temperature 130 °C, where Θ equals the angle between the propagating light and the crystal's z-axis and Φ being the angle between the propagating light and the crystal's x-axis measured in the x-y plane. A precise measurement of the angles was not possible due to the limited space between mirrors and crystal.

In this configuration, the phase-mismatch of the SPDC process (1064 nm→1589 nm+3220 nm) Δk_{SPDC} is in the order of $10^5\,\mathrm{m}^{-1}$, while the gain factor Γ is in the order of $10^1\,\mathrm{m}^{-1}$. The numbers are calculated with the refractive indices of KTA taken from [41]. Therefore, the low-gain approximation of Eq. 2.48 is valid.

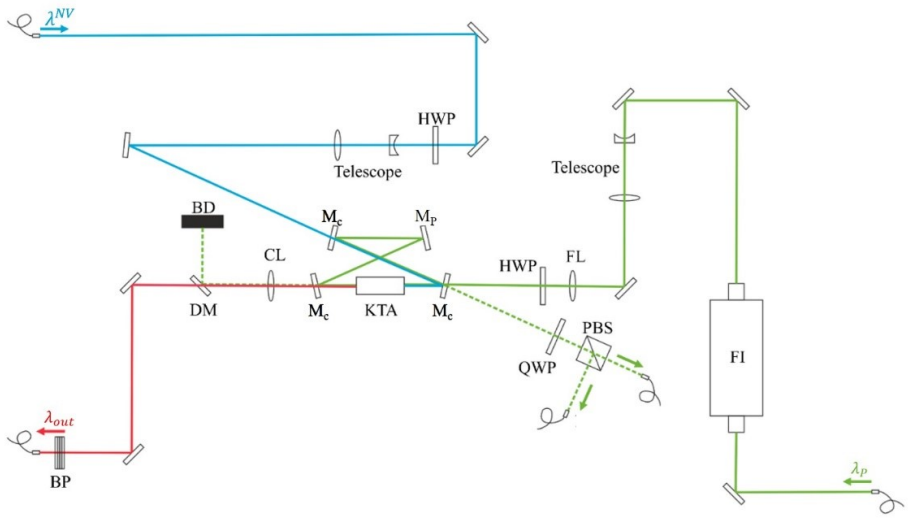

Figure 2.6: **Schematic drawing of the QFC setup.** The enhancement cavity consists of three mirrors (MC) and one which is mounted to a piezoelectric actor to control the cavity length (MP). The nonlinear crystal (KTA) is placed such that the cavity mode's focus is centered inside of it. At the device's signal input/output and pump input, the interacting waves are coupled from free space to fiber or vice versa, indicated by the respective arrow. The solid blue (green, red) lines indicate the beam path of 637 nm (1064 nm, 1589 nm) light, whereas dashed lines denote reflected light and leakages from the cavity, which are either used to implement the cavity control via the Hänsch-Couillaud method or to be filtered from the output field by a dichroic mirror (DM) and further long-pass and band-pass filters (BP). The converted light is coupled to a single-mode fiber behind the BP. Additional components are a Faraday-isolator (FI), half-waveplates (HWP), a quarter-waveplate (QWP), focusing and collimation lens (FL, CL), a polarizing beam splitter (PBS) and a beam dump (BD).

2.4.5. NORA PERFORMANCE*

The performance of the QFC is quantified by the pump-power dependent rate of telecom photons in the output channel divided by the rate of visible photons in the input channel. This figure is called conversion efficiency and takes the following form:

$$\eta_c(P) = \eta_{max} \sin\left(L\sqrt{\alpha_{QFC} P}\right)^2 \tag{2.50}$$

where η_{max} equals the maximum conversion efficiency including all losses, L is the length of the NLM and α_{QFC} is the device-specific normalized power efficiency in the low-gain limit [58]. We measure both the internal conversion efficiency, providing general information on the efficiency of the external enhancement cavity approach and the external conversion efficiency to allow for a comparison to different devices independent of filter setups and losses at optical elements. We demonstrate that the internal efficiency can reach similar values compared to waveguide based QFCs, while the overall losses at optical elements in the device can be significantly smaller. The measurement is conducted with an attenuated cw laser of the same wavelength as the NV-center emission (Toptica DLC DL PRO HP 637, linewidth 300 kHz). The converted power P_{out} is measured behind the dichroic mirror (DM) and behind the single-mode fiber respec-

tively. The pump power in the cavity is calculated by measuring a portion transmitted at one of the cavity mirrors and correcting for the transmission. All error bars and accuracies given in this work are the 1σ-interval calculated by combining both statistical deviations and systematic accuracies. The measured ratio of output power to input power is corrected for the wavelength ratio, yielding the photon rate ratio (i.e., conversion efficiency).

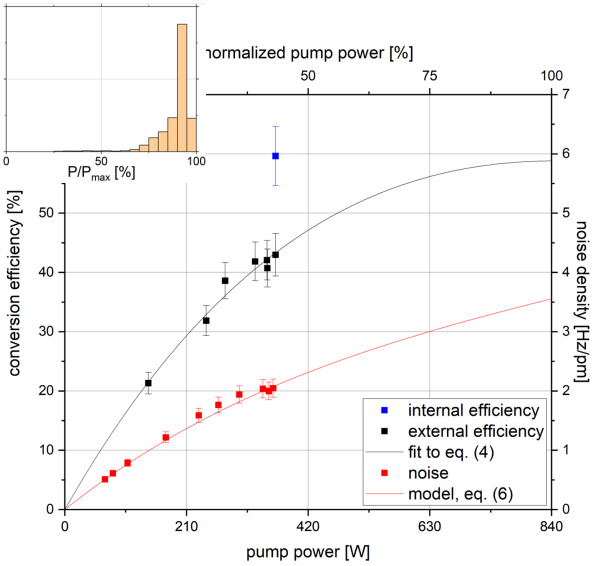

Figure 2.7: **QFC-performance in dependency of the circulating pump power.** The absolute pump power is measured with a relative accuracy of 10 %, which is omitted for clarity. Conversion efficiency: Depicted are both the measurement results for the external and internal efficiency (black and blue squares) and the result of a fit to equation 2.50 (black line). Noise density: Depicted are the noise counts normalized to the Bandpass' bandwidth (red squares) as well as the model given in equation (6) (red line). Inset: Histogram of the circulating pump power normalized to the maximum value P_{max} while tuning the center wavelength by 80 GHz over 4 min.

The conversion efficiency is measured while sweeping the circulating pump power (see 2.7), exhibiting the expected behavior from equation 2.50. A maximum internal conversion efficiency of 60(5) % is measured at a circulating pump power of 360(40) W. Behind the filter stack (transmission T_{BP} =90 %, bandwidth (FWHM) $\Delta\lambda$ =3.14(7) nm, center-wavelength $\lambda_{BP} = \lambda_{out}$) and after coupling to a single-mode optical fiber (SMF28, coupling efficiency η_{FC} =80(6) %), the external conversion efficiency is measured to equal 43(5) %. To identify the maximum internal efficiency, the data is fitted to Eq. 2.50, yielding a maximum value of 80(10) % at a pump power of 840(80) W and a normalized power efficiency ofα_{QFC} = 3.3(6) $\mathrm{W}^{-1}\,\mathrm{m}^{-2}$. Therefore, a maximum external conversion efficiency of 59(9) % can be extrapolated. The pump power (peak intensity) is limited to 360 W (9 $\mathrm{kW\,cm}^{-2}$) during the experiment by the limited enhancement factor of 60 and imperfect coupling efficiency of pump light to the cavity (≈70 %). With the damage threshold of KTA being in the order of 1 $\mathrm{GW\,cm}^{-2}$ [59], it is possible to further optimize the enhancement cavity to enable maximum efficiency.

An investigation of the stability of the circulating pump power while sweeping the pump wavelength with a speed of 0.33 GHz s^{-1} reveals a relative power stability of 10 % (see inset of Fig. 2.7) which demonstrates the feasibility to maintain a constant output wavelength when the device is operated with photons emitted from NV-center qubits. Note, that this tuning speed is determined by the pump laser. It is much larger than required for the typical drift of λ^{NV} (10 MHz min^{-1}).

To determine the rate of noise photons introduced by the QFC, the single-mode optical fiber from the QFC's output is connected to a single-photon detector while pump light is circulating in the cavity and the input beam is blocked. Every detection event recorded can therefore be attributed to either a detector dark count, black-body radiation, stray light, or noise processes in the NLM, e.g., SPDC or Raman-scattering of a pump photon. To isolate the pump-induced noise from the constant noise floor resulting from detector dark-counts and black-body radiation, measurements are conducted with (without) enabled pump light, respectively, while the crystal oven is operating.

The noise counts per second N are measured with a superconducting-nanowire single-photon detector (SNSPD, Quantum OPUS One, η_{SNSPD} =70(5) %, dark counts n_{dc} =12.4(2) s^{-1}). The results are furthermore normalized to the bandwidth of the filter stack, assuming white noise (i.e., $\frac{dn}{d\lambda} = const.$) in this interval:

$$\frac{dn}{d\lambda} = \frac{N}{\eta_{SNSPD}\Delta\lambda_{BP}} \tag{2.51}$$

In this setup, an absolute rate of noise events smaller or equal to 4500 s^{-1} is recorded. Correcting for the detector efficiency and normalizing to the filter bandwidth (see Eq. 2.51) yields a noise spectral density in the order of single counts per picometer, which is two orders of magnitude smaller than in the former record low-noise QFC setup for NV-center emission based on a ppLN waveguide at an external (internal) efficiency of 17 % (65 %) [49]. The noise density (averaged over 30 s) while sweeping the pump power is depicted in Fig.2.7. The rate of pump-induced noise increases linearly for small pump powers, as it is expected for spontaneous processes [48]. A linear fit to the first three data points yields a non-zero offset of 60(50) s^{-1}, which is attributed to detector dark-counts and black-body radiation originating from the crystal oven which is operated at elevated temperatures. For high pump powers (> 40%$\hat{P}$), a deviation from this linear dependency is observed. This deviation is attributed to the increasing probability to up-convert a noise photon from λ_{out} to λ_{in} with increasing pump power, effectively reducing the noise rate at λ_{out} . Following the expression given in [56], we find:

$$\frac{dn}{d\lambda} = \frac{\alpha_N P}{\eta_{SNSPD}\Delta\lambda_{BP}}\left(1 - \frac{\eta_{max}}{2} + \frac{\sin\left(2L\sqrt{\alpha_{QFC}P}\right)}{4L\sqrt{\alpha_{QFC}P}}\right) \tag{2.52}$$

with α_N =0.0079(2) s^{-1} pm^{-1} W^{-1} being the internal noise generation coefficient, which equals the slope of the linear approximation at low pump power. The resulting curve (see Figure 2.7, red line) well fits the measurement result. To analyze, if Raman-scattering or SPDC is the leading noise generation process in this configuration, further measurements must be conducted. The maximum noise density introduced by the QFC equals 2.0(2) s^{-1} pm^{-1} (17(2) s^{-1} GHz^{-1}) at a pump power of 360(40) W. At a pump power

840(80) W with an expected maximum internal efficiency of 80 %, the noise density is extrapolated to 3.6 $s^{-1}\,pm^{-1}$ (30 $s^{-1}\,GHz^{-1}$).

To summarize the part about Quantum Frequency Conversion section, we have given a short introduction into the field of nonlinear optics, and derived the coupled mode equations 2.35 for a general nonlinear process. We identified the key conditions to satisfy for this process to happen efficiently, called the energy conservation 2.41 and phasematching 2.40. We introduced two ways how to satisfy these conditions, and used them to calculate the required tuning parameters for the converters used in Chapters Chapters 3 and 6. We then discussed the source of additional noisephotons generated by Quasi-phasematching, and introduced a new, low-noise design for the downconversion of NV center photons to the telecom L band, which improved the SNR significantly in the experiment performed in Chapter 6.

2.5. PHASE STABILIZATION METHODS

In this section we discuss some of the methods use to perform the measurement, manipulation and stabilization of the relative phase between two optical fields. Considering this is a very broad topic, ranging from the encoding of classical information in the phase of an optical signal called phase-shift keying (PSK) or using interferometry to measure tiny displacements (such as LIGO[60]) so this description is not meant to be exhaustive by any means. It is meant to provide a basic understanding of the concept of interference in order to understand the phase stabilization techniques employed for entanglement generation, described in the later Chapters. First we describe the concept of interference, then the methods to generate and process the information coming from this interference, and finally the different was how to feedback this information to achieve stabilization. Finally we provide a brief overview of previous experiments using phase stabilization techniques for entanglement generation between matter qubits/solid-state nodes and highlight the important differences with this work.

2.5.1. OPTICAL DETECTION AND INTERFERENCE

In this section we discuss the two types of interference, homodyne and heterodyne, by considering two optical waves propagating in a single spacial dimension with perfect spatial mode and polarization overlap. We can use equation 2.30 to write down the electric field component of optical waves, simplifying to one spatial dimension z as

$$E(z,t) = Ae^{i(kz-2\pi f t+\theta)} + A^* e^{-i(kz-2\pi f t+\theta)}, \tag{2.53}$$

with A the amplitude, $k = \frac{2\pi}{\lambda} = \frac{2\pi f}{c}$ the wavenumber, $f = \frac{\omega}{2\pi}$ the frequency and θ the initial phase respectively, which are all constants in time and space. The variables z, t denote space and time. Let us first consider how we can measure and electric field like this.

DETECTORS OF LIGHT

All common detectors of light, such as avalanche photodiodes, measure the time-averaged, slow-varying electric field intensity and can not sense the 100 THz oscillations of the electric field. The output is usually in the form of an DC/AC current, where they

can measure the fluctuations in the intensity of the light field at frequency between 0 and 1 GHz. More concretely, given an electric field E, detectors have a response given by

$$I = \left\langle E(z,t)E(z,t) \right\rangle = \left\langle 2AA^* + AAe^{2i(kz-2\pi ft+\theta)} + A^*A^*e^{-2i(kz-2\pi ft+\theta)} \right\rangle, \tag{2.54}$$

where $\langle x \rangle$ denotes the time-average of x. Due to the fast oscillating terms, this simplifies to $2A^2$ when A is real. In general, A can be time-dependent, and its that time dependence that the detector senses.

Any realistic measurement apparatus will suffer from noise, which can negatively effect the ability to measure the signal accurately. Two of the most relevant noise sources for measuring optical signals are thermal or Nyquist noise[61] due to the thermal motion of electrons, shot-noise[62] due to the Poissonian nature of electrons and photons. Both of these noise sources are white noise sources, meaning that they are frequency independent.

A key metric how well a given signal can be detected is the Signal-to-noise ratio $SNR = \frac{Signal}{Total\ Noise}$, that can depend on many factors such as detector sensitivity, filter bandwidth, excess noise added and time-averaging. Common for photodetectors is the Noise-equivalent power (NEP), defined as the *optical input power* need to reach a SNR of 1 in 0.5 Hz of integration. Some photodiodes can reach NEPs of 1 to 0.1 pW/$\sqrt{\text{Hz}}$, which roughly means they can measure oscillations of an optical field on the order of 1 pW after on second of integration. For single-photon detectors such as Single-Photon Avalanchediodes (SPADs) or Superconducting Nanowire Singlephoton Detectors (SNSPD), the 'NEP' is extremely low and equivalent to the half the darkcounts per second.

Interference effects occur when two waves are superimposed in space and time, which can be achieved with an equal beamsplitter with input modes 1,2 and output modes 3,4. For sake of simplicity, lets assume we have placed the detectors used to measure the optical field at the convenient location of $z = 0$, and drop the spatial dependence in further derivations. We can measure the intensity of the combined light field in the output arms 3,4 with a measurement apparatus. In the most general case, the output intensities $I_{3,4}$ are given by

$$I_3 = \left\langle (E_1(t) + E_2(t))\,(E_1(t) + E_2(t)) \right\rangle \tag{2.55}$$

$$I_4 = \left\langle (E_1(t) - E_2(t))\,(E_1(t) - E_2(t)) \right\rangle \tag{2.56}$$

where the $+/-$ sign is due to the beamsplitter imprinting a 0°, (180°) phase on transmission (reflection) of a wave. We can write out the cross terms and use 2.54 to simplify the terms:

$$\langle E_1(t)E_1(t)\rangle = 2A_1^2 = I_1 \tag{2.57}$$

$$\langle E_2(t)E_2(t)\rangle = 2A_2^2 = I_2 \tag{2.58}$$

$$\pm\langle E_1(t)E_2(t)\rangle = \pm A_1A_2\left(e^{\phi_1(t)+\phi(t)_2} + e^{-(\phi_1(t)+\phi_2(t))} + e^{\phi_1(t)-\phi_2(t)} + e^{-(\phi_1(t)+\phi_2(t))}\right) \tag{2.59}$$

where $\phi_n(t)$ is the time dependent phase. Realizing that the fast oscillating term $\phi_1(t) + \phi_2(t) \sim f_1 + f_2$ drops out again from the time-averaging of the electric field, and using

that $2\cos\phi = e^{i\phi} + e^{-i\phi}$ we can write

$$I_{3,4} = I_1 + I_2 \pm 2\sqrt{I_1 I_2}\left(\cos\left(\phi_1(t) - \phi_2(t)\right)\right) \tag{2.60}$$

which has the terms of the individual intensities and a term with dependence on both amplitudes, the frequency and the phases of the incoming waves. How this last term behaves is the most important aspect of the interference and two different scenarios can be found: homodyne and heterodyne interference. For homodyne interference the two input fields have the same frequency, $f_1 = f_2$, a while for heterodyne interference they differ $f_1 \neq f_2$.

HOMODYNE

For homodyne interference the frequencies of the optical fields are equal, e.g. $f_1 = f_2$, and therefore simplify Eq. 2.60 as follows:

$$I_{3,4} = I_1 + I_2 \pm 2\sqrt{I_1 I_2}\cos\left(\Delta\theta\right) \tag{2.61}$$

where we define $\Delta\theta = \theta_1 - \theta_2$ the phase difference between the incoming waves, and the frequency f dropped out of the equation. This shows that the **intensity** of the light in the outputs 3 and 4 depends on the **phase difference** $\Delta\theta$ of the inputs 1 and 2. A photodetector that can measure the DC component of the intensity has to be used, because under stabilization $\Delta\theta$ can become small/constant. Only if the intensities of the input fields I_1, I_2 are known, one can recover the phase difference up $\Delta\theta$ by measuring the intensities in the arms $3,4$ and taking the difference between the two outputs

$$4\sqrt{I_1 I_2}\cos\Delta\theta = \hat{I}_3 - \hat{I}_4 \tag{2.62}$$

$$\Delta\theta = \pm\arccos\frac{\hat{I}_3 - \hat{I}_4}{4\sqrt{I_1 I_2}} \tag{2.63}$$

with $\hat{I}_n$ the measured power in arm n. Due to the symmetry of the cosine, one can only recover the value of $\Delta\theta$ up to a minus sign. For large variations of $\Delta\theta$ the error-signal deviates significantly form the real phase difference. This makes this method of measuring the relative phase between two optical fields less reliable, and sensitive to power fluctuations of the input fields. One can however stabilize the relative optical phase by choosing a smart stabilization point of $\Delta\theta = \pm\frac{\pi}{2}$, which corresponds to having equal powers in both outputs, and removes the sensitivity of the measurement to the input powers.

In the case where the input powers are very unequal, e.g. $I_2 \ll I_1$, the signal can be dominated by the constant term I_1.The shot-noise per unit time is proportional to $\sqrt{I_1}$, and usually dominates the measurement error of the measurement $\hat{I}_n$ in each of the modes $3,4$. Since the recovery of the phase depends on the difference between two detectors in each arm (see Eq. 2.62), this also dominates the error in the measured value for $\Delta\theta$. For this situation, increasing the power in the input mode 1 would **not** improve in the SNR. However, when increasing the measurement time by a factor M, the the SNR improves by a factor of $\sqrt{M}$, because the the signal increases with a factor of M, but the shot-noise only with a factor of $\sqrt{M}$.

HETERODYNE

For heterodyne interference, the input fields can be a difference frequencies, and we substitute $f_1 - f_2 = \Delta f$ and Eq. 2.60 becomes:

$$I_{3,4} = I_1 + I_2 \pm 2\sqrt{I_1 I_2}\cos(2\pi\Delta f\, t + \Delta\theta) \tag{2.64}$$

where $\Delta\theta$ is the initial phase difference of the fields. We now have the situation where the intensity in the outputs is oscillating in time and the **phase** of this oscillation is now the **phase difference** $\Delta\theta$ of the input fields. Now, to recover the relative phase the intensities of the input fields is no longer needed, given that one knows the frequency difference Δf sufficiently well. With this frequency being known beforehand, and can be used to accurately recover $\Delta\theta$ from the measured signal.

An important practical distinction in the measurement of the phase $\Delta\theta$ is that in principle one can use the intensity measurement of a single arm to recover the phase. Furthermore, because this signal is oscillating at the frequency Δf, and AC coupled photodetector such as a balanced photodiode can be used, that (ideally) is not sensitive to the DC components I_1 and I_2. Considering the same scenario as above where I_2 is small, providing more power in mode 1 can now be used to boost the SNR of the measured interference. This is because now the noise of the measurement $\hat{I}_3 \sim 2\sqrt{I_1 I_2}$ scales as $\sim I_1^{\frac{1}{4}}$, hence a factor M increase of the input power will lead to an improved SNR by a factor $\frac{\sqrt{M}}{M^{\frac{1}{4}}} = \sqrt{M}$. Usually the non-idealities of the balanced photodiode such as imperfect rejection of the DC component and saturation of the amplification will lead to an optimal power for the inputs. Typical frequency differences Δf are in the 1 to 500 MHz regime, where analog signal processing techniques such as spectral filtering, amplification and mixing are readily available.

2.5.2. ERROR-SIGNAL PROCESSING METHODS

Now that we have described the two different methods to generate an electrical signal that contains the relative phase information of two optical fields, we can discuss the different ways we can process this into an error-signal ready to be used for feedback. There are two main methods of doing the electrical error-signal processing: digital and analog.

DIGITAL PROCESSING

Digital signal processing is the sampling of the electrical signal into a stream of digital values, and subsequent processing on a digital processor. This sampling is usually done by an Analog-to-Digital Converter (ADC), which has a digitization speed given in Hz and a digitization depth, usually given in the number of bits. Typical ADCs used are specialized cards for the Adwin, or USB digital scopes such as the AnalogDiscovery2. Once the signal is digitized, one can perform operations such as time-averaging, filtering and PID control all on the same digital device. It has the advantage of being very flexible, were quick changes to filter- and control parameters can be changed via programming.

The downsides are that the process of digitization introduces extra noise sources such as quantization errors and non-linearity of the ADC, and jitter due to the finite

accuracy of the digital clock. Furthermore, the delays (~5 µs) introduced by these processing steps can significantly slow down the time between the measurement of the error signal and the eventual feedback, especially when non real-time devices are used. For feedback tasks where a high bandwidth (e.g. fast feedback) is needed digital processing is usually avoided.

ANALOG PROCESSING

Analog processing does not involve the sampling of the error-signal to the digital realm, but uses analog components such as spectral filters, mixers and amplifiers to implement the processing tasks. The benefits are that one can introduce the lowest amount of delay, and thus the highest bandwidth possible for the feedback. The downsides are that the design, testing and operation of analog signal processing circuits is usually much more difficult and time-consuming than digital counterparts. Also effects such as crosstalk an non-ideality of components can be very difficult to deal with.

For highly demanding and specialized systems, the performance gain is needed in order to reach thresholds needed for proper operation of the system. This is also the case for some of the stabilization tasks used in Chapters 5 and 6. We therefore explain some of the important components and there function.

2.5.3. PROCESSING COMPONENTS

The components we want to describe here are the passive frequency mixer, phase-frequency detector, phase-gain detector and servo controller. They all play a crucial role in the processing of electrical signal in all subsequent Chapters.

PASSIVE FREQUENCY MIXER

A passive frequency mixer is a electronic circuit build of passive component with two inputs, usually the Radio Frequency (RF) and Local oscillator (LO), and one output called Intermediate Frequency (IF), see Fig. 2.8a. These names reveal its historic usage in Radio receivers and transmitters, where an incoming Radio signal would be transformed using a Locally generated signal, to produce a signal at and Intermediate frequency. An ideal mixers takes the input signals, and produces the product of the two signals on the output (IF). In general, the output of a mixer contains the $product$ signal of the RF and LO inputs with a conversion loss, plus leakage a the combination of the RF and LO (or both) superimposed, which are called a double balanced, single balanced or unbalanced mixer.

A passive mixer can be used to recover the relative optical phase from the heterodyne errors signal in Eq. 2.64. In order for this to work, it is important that the LO is *coherent*, e.g. with the same phase and frequency Δf with control signal that is used for generating the frequency difference between the optical fields. In practice this is usually done by splitting a single (microwave) signal, where one part is used for the frequency offset using an Acousto-optical modulator (AOM) on one of the input fields, and the other part is used as LO in the error-signal processing. This can be more challenging when the physical location where the frequency offset is being applied is far away from the location where the error-signal is generated.

Provided we can satisfy the requirement for the *LO*, when we input the (AC component of the) error-signal on the RF port, and the local oscillator on *LO*, we get the following signal on the output:

$$V_{IF} \propto 2\sqrt{I_1 I_2}\cos(2\pi\Delta f\, t + \Delta\theta)\cos(2\pi f_{LO} t) = \sqrt{I_1 I_2}\left(\cos(2\pi(\Delta f - f_{LO})t + \Delta\theta) + \cos(2\pi(\Delta f + f_{LO})t + \Delta\theta)\right) \quad (2.65)$$

where the first term reduces to a the constant $\cos(\Delta\theta)$ when $f_{LO} = \Delta f$, and the second term oscillates at frequency $2\Delta f$. By using adequate low-pass filtering, cutting off the high frequency components, the output is now proportional to the Cosine of the relative optical phase difference $\Delta\theta$, see Fig. 2.8b. That means, as with the homodyne detection, for large variations of $\Delta\theta$ the error-signal deviates significantly form the ideal linear response. Additionally, the amplitude of the signal determines the gain of the feedback, which could make the feedback unstable when the input powers I_1, I_2 change. These things combined make it far from and ideal phase measurement, but still a cheap and useful way to lock the system around a zero-crossing. They are used in the local phase stabilization in Chapters 5 and 6.

What is more challenging however is when the frequency difference between the *RF* and the *LO* input becomes large, e.g. $|f_{LO} - \Delta f|$ becomes large. Due to the periodic sinusoidal nature of the error-signal, the time-average is zero, and contains no information about whether the difference in frequency is positive or negative. This means you can not feedback on this error signal, and there is no way to establish stabilization. Luckily there are more sophisticated ways of extracting the information out of the error-signal, which we will discuss now.

PHASE-FREQUENCY DETECTOR

The phase-frequency detector is a more complex and active electronic device, that can perform the same task of recovering the phase of an *RF* field compared to a local oscillator, plus some useful additional features. To fully explain its functionality would require too much background, so we restrict our self to discussing the input/output relation.

The device again has two inputs, *RF* and *LO*, but now it has two outputs, called Up (UP) and Down (DN). The difference UP-DN that is low-pass filtered is the error-signal of interest, see Fig. 2.9a. It uses the rising edges of the *RF* and *LO* to turn on two separate

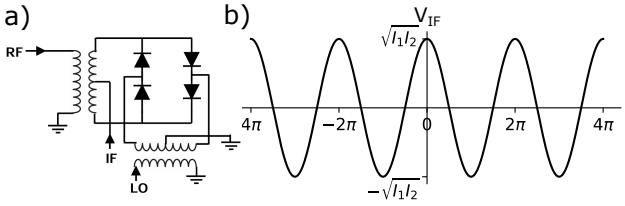

Figure 2.8: **Passive frequency mixer.** a) Electrical schematic of a doubly balanced passive frequency mixer, with the two inputs *RF* and *LO*, and the output IF shown. Adapted from [63] b) The typical output (V_{IF} vs. $\Delta\theta$ see 2.65) of a passive mixer when $\Delta f = f_{LO}$. The sinusoidal response has a mean value of 0, and is only linear for small regions around $m\pi$, $m = 1, 2, 3, ...$

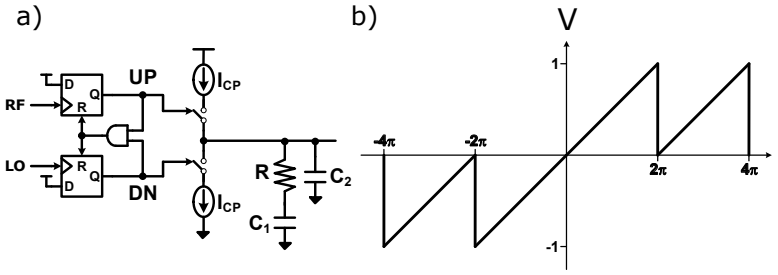

Figure 2.9: **Phase-frequency detector.** a) Electrical schematic of a phase-frequency detector. The two inputs *RF* and *LO* are connected to flip-flops that get activated on the rising edges, and reset using a comparator on their output. The flip-flops activate currents that increase/decrease the signal on the output, which is lowpass fileterd. Image adapted from [64]. b) The typical voltage response (V_{out} vs. $\Delta\theta$) of the PFD, showing a linear response on the range $\Delta\theta \in [-2\pi, 2\pi]$, and a negative (positive) mean value for a large negative (positive) $\Delta\theta$. Additionally, the scaling is not dependent on the input powers of *RF* and *LO*.

flip-flops that control a current. When the two flip-flops are both ON, as detected by a comparator, they get reset to the OFF state. When the *RF* rising edges arrive *before* the rising edge of the *LO*, the UP signal spends more time in the ON state than the DN, and the output is positive (e.g. a positive phase offset). When the *RF* rising edges arrive *after* the *LO*, the DN signal spends more time in the ON state and the output is negative (e.g. a negative phase offset). Taking the average of this signal using some low-pass filtering, we creates a linear error signal over the phase range of $[-2\pi, 2\pi]$, that is independent of the amplitude of the input signals, see Fig. 2.9b.

Furthermore, we can see that for *increasing* positive phase differences, the output is always positive. This can be interpreted as that the *RF* has more rising edges per time interval than *LO*, e.g. the frequency is higher. The opposite effect happens for more negative phase differences, where an always negative output is produced (Fig. 2.9b). So for significant frequency differences, the *average* output voltage can be used to bring the *RF* closer to the *LO*. This allows the feedback to operate on a much larger frequency range, while having a linear response to the phase when the frequencies are equal. This make the phase-frequency detector better suited for phase stabilization tasks where large differences can occur. This phase detector is used in the fast phase synchronization and frequency lock used in Chapters 3, 5 and 6 to allow for the measurement and subsequent feedback of these larger frequency differences.

PHASE-GAIN DETECTOR

Another type of phase detector is the phase-gain detector, which is an active circuit used to measure the phase and relative phase *and amplitude*. It can be used to measure the power of a signal *RF* relative to an input power *LO*, see Fig. 2.10.

The crucial component in this device is the so-called demodulating logarithmic amplifier, that *demodulates* e.g. looks at the amplitude-envelope, and has a logarithmic response to envelope variations. The logarithmic response is achieved by cascading many amplifiers to a small input signal, each of which the output is clipped to 1 V. Each of the outputs of the chain are also rectified and summed, and form the output of the logarithmic amplifier, Fig. 2.10b). By setting the gain of each amplifier to 20 dB, each step

of 1 V that saturates represents a 10 dB of *power* gain. The phase-gain detector uses two demodulating logarithmic amplifiers and subtracts the output of the *LO* from the *RF*, giving a relative measure of the two powers, Fig. 2.10c). The phase response of the phase-gain detector is less sophisticated as the phase-frequency detector, as it uses a simple passive mixer, Fig. 2.10d). However, by using the limiting amplifier output of each of the demodulating logarithmic amplifiers, the phase response is insensitive to input power fluctuations. Usually it is possible to provide a steady power in the *LO* arm, and by choosing it at a sufficient strength allows for the accurate measurement of the *RF* power. This detector is used in Chapter 6 to measured the amplitude of the AC signal coming from a photodiode. The light on the photodiode passed through a polarizer, so by maximizing the amplitude we can control the polarization.

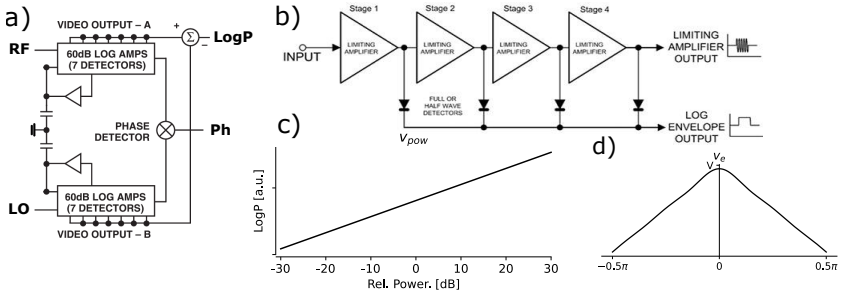

Figure 2.10: **Phase-gain detector.** a) Electrical schematic of a phase-gain detector, where the *RF* and *LO* inputs are each 'demodulated' by a separate logarithmic amplifier. Their outputs are compared and generate the output LogP. b) Workings of a demodulating logarithmic amplifier, where the outpout of several 20 dB gain stages is combined to form the LogP output. The last output is also routed to a passive frequency mixer, and is used to generate a phase signal. Images adapted from [65]. c) Typical output LogP, where the *RF* power can change by several orders of magnitude, resulting in a linear change of the V_{LogP}. d) The phase response, resulting from the mixing of the saturated outputs of the logarithmic amplifiers on a passive frequency mixer.

SERVO CONTROLLER

The last component that we discuss is the servo controller. These devices take the error-signals generated by the devices mentioned above, and performs various tasks to turn the electrical signal into an appropriate feedback signal that can drive the device that is performing the feedback. These tasks can be separated into three stages, pre-amplification stage, filter stage, and post-amplification stage. Of these three, the filter stage is the most import, as this decides the relation between the error-signal and the feedback. The servo adds a degree of flexibility in designing an analog feedback loop, where there are many parts of the system that influence the relation between error and feedback signals. In principle we can see the servo controller as an analogue PID controller that can be easily adjusted and fine tuned. The detailed design these filters is a large and very active field on its own, and out of the scope of this thesis.

In principle it is possible to calculate the electrical response of each component, cable and connector, and add components such as low-/high-/band-pass filters and amplifiers, such that the desired system response is realized for optimal feedback. In reality

this is however nearly impossible, as every component has some uncertainty in its specifications. The servo controller allows for a degree of tunability of the frequency response of the system, by changing the frequency cut-offs and amplification gain in the filter stage via knobs and switches on a device. The pre- and post-amplification stages are are tuned independent, such that the error-signal always properly serves as input, and the output signal always matches to the specs of the actuator, independent of filter settings. It therefore provides the flexibility needed to in-situ tune the feedback response of the analog system, allowing for fine-tuning of the feedback whilst maintaining the high feedback bandwidth of analog systems. These devices are extensively used in Chapters 3, 5 and 6 where they process the error signals of the stabilization tasks.

2.5.4. FEEDBACK METHODS

Now that we have discussed the generation and processing of the electrical signals involved in the stabilization of the relative phase between two optical fields, the last step is to apply the feedback signal onto the optical fields using an actuator. In the context of phase stabilization for entanglement generation, the phase actuators often act on light that is at the single-photon level. Additional losses due to the actuator are therefore an important consideration, as well as the feedback range and bandwidth. For more mature systems complexity and costs are also important parameters, but for experimental demonstrations they are usually not a priority.

The stabilization task is to minimize the phase-difference between two optical fields, where one field can be thought of as being 'constant' or a reference, and the phase of the other field has to be brought to to that phase reference. Figure 2.11 shows a simplified picture of this task, where at $t = 0$ the two fields are completely out of phase. One can then change a property of the field, e.q. its frequency or its phase, to bring them into phase at $t = 1$. This can be done with different actuators which we discuss now, but in some sense they are equivalent.

PHASE MODULATION

The most straightforward way to adjust the relative phase between two optical fields is to place a phase modulator in one of the paths. Figure 2.11c shows the effect bringing two fields in phase using a direct change of the phase. The two fields that were previously out of phase, are perfectly in phase after the feedback is complete. There are various ways with one can modulate the phase of an optical field directly, which can be achieved by changing:

- The length of the optical path taken by the light
- The refractive index of the material which the field propagates through
- The phase of a wave that is interfering with the optical field

Changing the optical path can be achieved by e.g. reflecting the light off a movable mirror, of which the position can be adjusted on the order of the wavelength of light, or guiding the light through a fiber that can be stretched/contracted mechanically. These methods are low-loss, and relatively easy to implement optically. As these systems are

mechanical, they are however limited in feedback range (typ. $\leq 1\,\text{mm} \approx 2\pi\times 2000\,\text{rad}$ depending on the wavelength) and bandwitch (typ. $\leq 50\,\text{kHz}$), and need high-voltage, high-frequency driving circuits to operate.

Another option is to keep the length of the optical path constant, but change the refractive index with for instance the *electro-optical* effect. For various materials such as Lithium niobate (LN) or beta-barium borate (BBO) the refractive index can be changed by applying an electric field via electrodes on the surface of the material, see Eq. 2.32 and [39]. By guiding the light through this material (~10 cm), a full 2π phase shift can already be achieved with less then 10 V. Because there are no moving parts, these modulators can be extremely high bandwidth ≥50 GHz, mainly limited by the driving electronics. The downsides of this approach is the moderate insertion loss ~3 dB, the small tuning range of only a couple of full periods, as well as the significant electronics overhead.

Another option is to modulate the phase of a wave that is interacting with the optical field already. Many optical components such Acousto-Optical modulators or deflectors (AOM or AOD) are based on the scattering of optical fields with with sound waves inside a material[39]. These devices are commonly found in the quantum optics experiments, where they are used to steer or attenuate lightfields. The acoustic waves in the material are usually generated using radio-frequency waves ω_{RF} ~100 MHz driving a piezo-electric transducer, that modulate the density (and there for dielectric constant) of the material. This forms an effective grating, and the higher order modes of the resulting optical field exit the material at an angle from the unaffected beam. These can then be selected using a spatial filter. The frequency of the first order mode is offset by $\pm\omega_{RF}$, and the phase $\pm\theta_{RF}$. By controlling the phase of the RF field applied (via an electronic phase modulator) the phase of the optical field is changed as well. The modulation is then limited by the electronic phase modulator, which can be high bandwidth (≥1 GHz at moderate cost.

All of these techniques run into a problem when there are (small) frequency differences between the two optical fields: sooner or later you reach the end of the feedback range because the continuous adjustments needed, and you need to reset your feedback loop/actuator.

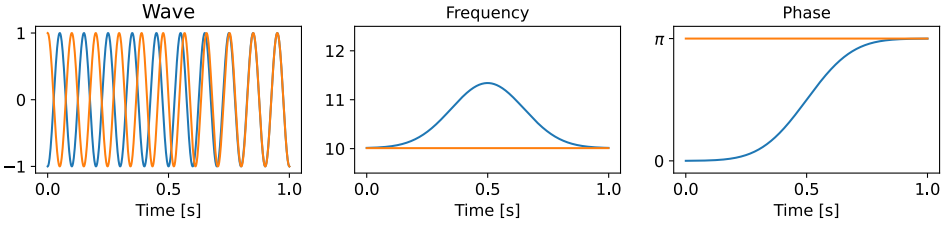

Figure 2.11: **Stabilizing the relative phase between two waves.**a) Two waves with frequency 10 Hz are completely out of phase at $t = 0$. After the feedback on the blue wave, at $t = 1$ they are completely in phase. b) Plotting the frequency $\frac{d\phi}{dt}$ shows a change of instantaneous frequency. The difference between the integral of both signals is exaclty the phase difference π c) Plotting the phase $\phi - 10t$ shows the changing phase of the wave where feedback is acting on, and the constant phase profile of the other. This shows the relation of the feedback methods

FREQUENCY MODULATION

Another method of changing the optical phase is by temporarily changing the frequency of the field (the inverse, changing the frequency by modulating the optical phase, can also be done, called serrodyne modulation [66]). This equivalence can be seen in Fig. 2.11b), where a change in frequency can be seen when the phase-ramp starts. This means that equivalent to the phase modulator, we could have used a frequency modulator instead. There are various ways of changing the frequency of a light field, for instance by changing:

- the controls of the light source (laser)
- the frequency of a wave that is interfering with the optical field
- the phase under a continuous phase-ramp (serrodyne modulation)

In a lab scenario, where all the equipment is localized in one location, the feedback signal could be applied direct to the light source. The exact actuators and specifications however are heavily dependent on the type of laser itself. Another approach is already mention before, where the optical field interacts with an acoustic wave in a material. Because the first order diffraction is used, the frequency shift of the optical field depends on the frequency of the radio frequency applied. This frequency can be easily controlled using a Voltage Controlled Oscillator (VCO) or via fast digital techniques.

The benefit of this approach is that any *step-change* in optical phase difference, can be compensated in a way where the feedback signal returns to the centre of the range (0), as seen in Fig. 2.11b). We call this *endless* feedback, where phase jumps can not lead to reaching the end of the feedback range. For small frequency differences between the optical fields, a step in frequency will compensate for this. What is limiting this type of feedback is the operating bandwidth of the acousto-optic modulators have, based on the method of selecting the first-order mode and rejecting the zeroth-order. This typically has a bandwidth of $\leq$5 MHz before significant losses start to occur. One downside of this method of feedback is that is is difficult to pause due to non-idealities in the frequency modulation actuator that result in an error that builds up over time. This limits how long the feedback can be paused. This method of feedback is used extensively in the Chapters 5 and 6 where their effectiveness is described in more detail.

Together all these components form the basis for phase stabilization of optical fields. We will now discuss some historical experiments that utilized phase stabilization in the context of entanglement generation, and will highlight some of the choice made in their design.

2.5.5. PREVIOUS EXPERIMENTS USING PHASE STABILIZATION

One of the first examples of successful entanglement generation using the single-click protocol introduced earlier is between two atoms in the same trap[67].The two atoms emit indistinguishable photons, that take separate paths to a detector. The separation between the atoms ($\ll$1 cm) is was carefully chosen to guarantee the same phase imprinted by the excitation laser. A distant and movable mirror is used to control the phase of one of those paths, to make it arrive with a deterministic phase with respect to the

other path. The light used during the cooling of the atoms generates the error signal for this control, allowing for repeated generation of the same entangled state.

The generation of spatially separated solid state nodes was first shown with quantum dots[68] and soon after with NV-centers[29]. The experimental lay-out for these experiments are very similar, where an in-fiber beampslitter splits an excitation laser, each arm goes to a cryostat housing the quantum node where there is a probabilistic photon emission, and a second in-fiber beamsplitter combines the two paths the single photons, followed by detection in single-photon detectors. This forms an Mach-Zehnder interferometer, which allows for a straight-forward definition of the relative optical phase. The phase was measured using the count rates of the same single-photon detectors that was used for the entanglement generation. The quantum dot experiment used both a fast electro-optic modulator, as well as a piezo-controlled reflector for fast and slow phase feedback respectively. The early NV-center experiment used only a fiber-stretcher controlled by a digital micro-controller to stabilize the phase, which limited the locking speed to ~10 ms and thus unable to compensate for fast phase drifts present in the system.

An improved design of the phase-stabilization was used in a series of groundbreaking experiments, realizing a multi-node quantum network with solid-state nodes[16, 30]. It introduced the concept of breaking up the setup in multiple stabilization schemes, and tailoring the design of the signal generation, processing and feedback for each of the individual parts. For example at each node, part of the experiment was stabilized an error-signal in a heterodyne scheme measured by a fast-photodiode, and used movable mirror on a piezo mount. These improvements allowed the weak signal to be boosted by a separate high-power optical path, and the faster actuator increased the feedback bandwidth significantly. The remaining stabilization was done with the same homodyne measurement of the optical phase in the single photon detectors and the fiber stretcher. This approach resulted in faster locking speeds (~ 10 to 100 µs) and low residual phase error (σ =15 to 30°) (see Supplement of [16] for more information).

The work in Chapter 5 extends on this base of previous knowledge, by making the phase stabilization design compatible with deployed fiber networks, large node separation and enabling the usage of individual excitation lasers on the nodes. It describes in-depth the addition of another independent stabilization scheme, that operates at a higher bandwidth (>200 kHz), in order to remove additional phase noise introduced by the linewidth of the excitation laser. Furthermore, we use a heterodyne method to generate an error signal using the SNSPDs, which removes the sensitivity to power fluctuations, and allows for arbitrary setpoints of the relative optical phase in the midpoint.

2.6. EXPERIMENTAL SET-UP

In this last section we broadly discuss the lay-out of the optics, electronics and software of the set-ups used in the upcoming chapters. For a more detailed description we refer to the supplementary information that accompanies some of the chapters.

2.6.1. OPTICS

The optics used for all experiments in this work can be broadly described as a combination of continuous wave lasers in the power range of20 to 8000 mW, and with frequencies 515 to 1588 nm. The lasers are modulated by in-fiber AOMs (On/Off ratios 50 dB, often 2 per optical path) for sufficient extinction and control of the optical powers over many orders of magnitude. The fields in the visible spectrum used for NV-center control with powers 1 nW to 1000 nW) are then combined using an in-fiber colour combiner (custom OZ-optics) and delivered to the Quantum Device through a home-built con-focal microscope setup. The custom objective stage houses a microscope objective (Olympus 100x 0.9NA) movable by using three closed-loop PI piezo stages, giving ≈ nanometer control. The emission from the NV center is then guided out of the cryostat via the same objective, and the PSB is filtered out using a dichroic and detected using an microscope objective coupling into a multi-mode fiber (50 µm core diameter). The ZPL is separated from the resonant excitation using a cross-polarization technique[25], implemented by a set of quarter- and half-wave plates (Lamdba Research Optics 0-th order for 633 nm) and a plate polariser (60 dB PER). Motorized mirror mounts allow for remote optimization of the ZPL light into a single-mode fiber, the output of which can guided to either an APD for local measurement, or the QFCs for conversion to the telecom L band.

2.6.2. ELECTRONICS

The nature of the experiments conducted in this work require decision making and electronic control, ranging from slow feedback loops on the timescale of seconds to the real-time logic needed for heralding at the nano-second timescale.

At the highest level we have computers running a typical operating system such as Linux to control all the devices in the network. We program our experiments and all supporting tasks such as Graphical User Interfaces (GUI) in Python 3.x, and use it to write the data coming from various devices to disk. Slow optimization and calibrations are executed and stored using these systems to keep track of changes in e.g. laser power and objective stage position. The next level of control is a time-deterministic microcontroller (Jäger ADwin-Pro II T12) that is in charge of signals that need to be controlled deterministically and at the microsecond level. Examples of these processes are the counting of photons during illumination with a microsecond long laser pulse and the logic of the Charge-Resonance check [16] to keep the NV center on resonance during experiments. It also handles the communication of the readiness of the nodes during entanglement generation. The lowest and most time-critical level of control is done by an Arbitrary Waveform Generator (AWG) (Zurich Instruments HDAWG), to provide real-time waveform generation and pulse sequences. It has a sample rate of $2.4 GSa/s = 0.41667^{-1}$ ns, allowing for the accurate spacing of or optical and microwave control pulses. The AWG also handles the real-time heralding signal that is used as input to decide the feedforward to process the detection pattern in Chapter 6.

2.6.3. SOFTWARE

As mentioned before we use software based on the Quantum Measurement Infrastructure [69] (QMI), a Python 3 framework for controlling laboratory equipment. We use this

framework to build up Python 3 scripts that are used to perform and analyse the experiments throughout this work and control tasks that handle processes that are ongoing in the background (stabilization of lasers, monitoring of phase/power etc). It allows us to control all experimental equipment over the network, irrespective whether they are interfaced using USB, RS232 or Ethernet. This makes it possible to scale up the amount of equipment in the network whilst still being able to control everything from a single location, which is crucial for operating deployed hardware.

REFERENCES

[1] J. Geus *et al.*, *Low-noise short-wavelength pumped frequency down-conversion for quantum frequency converters,* Optica Open (2023), 10.1364/opticaopen.23684502.v1.

[2] W. Pfaff, *Quantum measurement and entanglement of spin quantum bits in diamond,* Ph.D. Thesis, TUDelft (2013).

[3] H. Bernien *et al.*, *Heralded entanglement between solid-state qubits separated by three metres,* Nature **497**, 86–90 (2013).

[4] M. Ruf, N. H. Wan, H. Choi, D. Englund and R. Hanson, *Quantum networks based on color centers in diamond,* Journal of Applied Physics **130**, 070901 (2021).

[5] N. Kalb, *Diamond-based quantum networks with multi-qubit nodes,* Ph.D. Thesis, TUDelft (2018).

[6] D. Riedel *et al.*, *Deterministic enhancement of coherent photon generation from a nitrogen-vacancy center in ultrapure diamond,* Phys. Rev. X **7**, 031040 (2017).

[7] P. Tamarat *et al.*, *Spin-flip and spin-conserving optical transitions of the nitrogen-vacancy centre in diamond,* New Journal of Physics **10**, 045004 (2008).

[8] M. L. Goldman *et al.*, *Phonon-induced population dynamics and intersystem crossing in nitrogen-vacancy centers,* Phys. Rev. Lett. **114**, 145502 (2015).

[9] T. van der Sar, *Quantum control of single spins and single photons in diamond,* Ph.D. Thesis, TUDelft (2012).

[10] L. Robledo *et al.*, *High-fidelity projective read-out of a solid-state spin quantum register,* Nature **477**, 574 (2011).

[11] P. Tamarat *et al.*, *Stark shift control of single optical centers in diamond,* Phys. Rev. Lett. **97**, 083002 (2006).

[12] L. C. Bassett, F. J. Heremans, C. G. Yale, B. B. Buckley and D. D. Awschalom, *Electrical tuning of single nitrogen-vacancy center optical transitions enhanced by photoinduced fields,* Phys. Rev. Lett. **107**, 266403 (2011).

[13] M. W. Doherty *et al.*, *The nitrogen-vacancy colour centre in diamond,* Physics Reports **528**, 1–45 (2013).

[14] C. Bradley, *Order from disorder: Control of multi-qubit spin registers in diamond,* Ph.D. Thesis, TUDelft (2021).

[15] L. M. K. Vandersypen and I. L. Chuang, *Nmr techniques for quantum control and computation,* Rev. Mod. Phys. **76**, 1037 (2005).

[16] M. Pompili *et al.*, *Realization of a multinode quantum network of remote solid-state qubits,* Science **372**, 259–264 (2021).

[17] M. H. Abobeih *et al., One-second coherence for a single electron spin coupled to a multi-qubit nuclear-spin environment,* Nature Communications **9**, 2552 (2018).

[18] A. Jarmola, V. M. Acosta, K. Jensen, S. Chemerisov and D. Budker, *Temperature- and magnetic-field-dependent longitudinal spin relaxation in nitrogen-vacancy ensembles in diamond,* Phys. Rev. Lett. **108**, 197601 (2012).

[19] G. de Lange, Z. H. Wang, D. Ristè, V. V. Dobrovitski and R. Hanson, *Universal dynamical decoupling of a single solid-state spin from a spin bath,* Science **330**, 60–63 (2010).

[20] G. Waldherr *et al., Quantum error correction in a solid-state hybrid spin register,* Nature **506**, 204–207 (2014).

[21] T. Nakazato *et al., Quantum error correction of spin quantum memories in diamond under a zero magnetic field,* Communications Physics **5** (2022), 10.1038/s42005-022-00875-6.

[22] T. H. Taminiau, J. Cramer, T. van der Sar, V. V. Dobrovitski and R. Hanson, *Universal control and error correction in multi-qubit spin registers in diamond,* Nature Nanotechnology **9**, 171–176 (2014).

[23] J. Cramer *et al., Repeated quantum error correction on a continuously encoded qubit by real-time feedback,* Nature Communications **7** (2016), 10.1038/ncomms11526.

[24] C. E. Bradley *et al., A ten-qubit solid-state spin register with quantum memory up to one minute,* Phys. Rev. X **9**, 031045 (2019).

[25] H. Bernien *et al., Heralded entanglement between solid-state qubits separated by three metres,* Nature **497**, 86 (2013), number: 7447 Publisher: Nature Publishing Group.

[26] W. Pfaff *et al., Unconditional quantum teleportation between distant solid-state quantum bits,* Science **345**, 532–535 (2014).

[27] B. Hensen *et al., Loophole-free bell inequality violation using electron spins separated by 1.3 kilometres,* Nature **526**, 682 (2015).

[28] N. Kalb *et al., Entanglement distillation between solid-state quantum network nodes,* Science **356**, 928–932 (2017).

[29] P. C. Humphreys *et al., Deterministic delivery of remote entanglement on a quantum network,* Nature **558**, 268 (2018).

[30] S. L. N. Hermans *et al., Qubit teleportation between non-neighbouring nodes in a quantum network,* Nature **605**, 663 (2022).

[31] C. K. Hong, Z. Y. Ou and L. Mandel, *Measurement of subpicosecond time intervals between two photons by interference,* Phys. Rev. Lett. **59**, 2044 (1987).

[32] S. D. Barrett and P. Kok, *Efficient high-fidelity quantum computation using matter qubits and linear optics,* Physical Review A **71**, 060310 (2005).

[33] C. Cabrillo, J. I. Cirac, P. García-Fernández and P. Zoller, *Creation of entangled states of distant atoms by interference,* Physical Review A **59**, 1025–1033 (1999).

[34] S. Bose, P. L. Knight, M. B. Plenio and V. Vedral, *Proposal for Teleportation of an Atomic State via Cavity Decay,* Physical Review Letters **83**, 5158 (1999).

[35] C. Granade, J. Combes and D. G. Cory, *Practical bayesian tomography,* New Journal of Physics **18**, 033024 (2016).

[36] C. Granade *et al.*, *Qinfer: Statistical inference software for quantum applications,* Quantum **1**, 5 (2017).

[37] S. Zaske, *Quantum frequency down-conversion of single photons in nonlinear optical waveguides,* (2013).

[38] R. Boyd and D. Prato, *Nonlinear Optics* (Elsevier Science, 2008).

[39] R. Kaltenbaek, *Photonics ii- lectures,* University Lecture (2020).

[40] W. Sellmeier, *Ueber die durch die aetherschwingungen erregten mitschwingungen der körpertheilchen und deren rückwirkung auf die ersteren, besonders zur erklärung der dispersion und ihrer anomalien,* Annalen der Physik **223**, 386–403 (1872).

[41] K. Kato and N. Umemura, *Sellmeier and thermo-optic dispersion formulas for ktioaso4,* in *Conference on Lasers and Electro-Optics/International Quantum Electronics Conference and Photonic Applications Systems Technologies* (Optica Publishing Group, 2004) p. CThT35.

[42] F. Mann, H. M. Chrzanowski, F. Gewers, M. Placke and S. Ramelow, *Low-noise quantum frequency conversion in a monolithic cavity with bulk periodically poled potassium titanyl phosphate,* Phys. Rev. Appl. **20**, 054010 (2023).

[43] T. van Leent *et al.*, *Entangling single atoms over 33 km telecom fibre,* Nature **607**, 69 (2022).

[44] P. S. Kuo *et al.*, *Reducing noise in single-photon-level frequency conversion,* Optics Letters **38**, 1310 (2013).

[45] J. S. Pelc, C. R. Phillips, D. Chang, C. Langrock and M. M. Fejer, *Efficiency pedestal in quasi-phase-matching devices with random duty-cycle errors,* Optics Letters **36**, 864 (2011).

[46] C. R. Phillips, J. S. Pelc and M. M. Fejer, *Parametric processes in quasi-phasematching gratings with random duty cycle errors,* Journal of the Optical Society of America B **30**, 982 (2013).

[47] J. S. Pelc, C. Langrock, Q. Zhang and M. M. Fejer, *Influence of domain disorder on parametric noise in quasi-phase-matched quantum frequency converters,* Optics Letters **35**, 2804 (2010).

[48] J. Pelc, C. Langrock, Q. Zhang and M. Fejer, *Influence of domain disorder on parametric noise in quasi-phase-matched quantum frequency converters,* Optics letters **35**, 2804 (2010).

[49] A. Dréau, A. Tchebotareva, A. E. Mahdaoui, C. Bonato and R. Hanson, *Quantum frequency conversion of single photons from a nitrogen-vacancy center in diamond to telecommunication wavelengths,* Phys. Rev. Appl. **9**, 064031 (2018).

[50] S. L. N. Hermans *et al.*, *Entangling remote qubits using the single-photon protocol: an in-depth theoretical and experimental study,* New Journal of Physics **25**, 013011 (2023).

[51] R. Ikuta, T. Kobayashi, T. Yamazaki, N. Imoto and T. Yamamoto, *Cavity-enhanced broadband photonic rabi oscillation,* Physical Review A **103** (2021), 10.1103/physreva.103.033709.

[52] C. E. Vollmer *et al., Quantum up-conversion of squeezed vacuum states from 1550 to 532 nm,* Phys. Rev. Lett. **112**, 073602 (2014).

[53] E. Arenskötter *et al., Telecom quantum photonic interface for a 40ca+ single-ion quantum memory,* npj Quantum Information **9** (2023), 10.1038/s41534-023-00701-z.

[54] G. Hansson, H. Karlsson, S. Wang and F. Laurell, *Transmission measurements in ktp and isomorphic compounds,* Applied Optics **39**, 5058 (2000).

[55] B. Albrecht, P. Farrera, X. Fernandez-Gonzalvo, M. Cristiani and H. de Riedmatten, *A waveguide frequency converter connecting rubidium-based quantum memories to the telecom c-band,* Nature Communications **5** (2014), 10.1038/ncomms4376.

[56] N. Maring, D. Lago-Rivera, A. Lenhard, G. Heinze and H. de Riedmatten, *Quantum frequency conversion of memory-compatible single photons from 606nm to the telecom c-band,* Optica **5**, 507 (2018).

[57] T. Hansch and B. Couillaud, *Laser frequency stabilization by polarization spectroscopy of a reflecting reference cavity,* Optics Communications **35**, 441–444 (1980).

[58] R. V. Roussev, C. Langrock, J. R. Kurz and M. M. Fejer, *Periodically poled lithium niobate waveguide sum-frequency generator for efficient single-photon detection at communication wavelengths,* Optics Letters **29**, 1518 (2004).

[59] V. G. Dmitriev, G. G. Gurzadyan and D. N. Nikogosyan, *Handbook of Nonlinear Optical Crystals* (Springer Berlin Heidelberg, 1999).

[60] B. Abbott *et al., Observation of gravitational waves from a binary black hole merger,* Physical Review Letters **116** (2016), 10.1103/physrevlett.116.061102.

[61] H. Nyquist, *Thermal agitation of electric charge in conductors,* Physical Review **32**, 110–113 (1928).

[62] W. Schottky, *Über spontane stromschwankungen in verschiedenen elektrizitätsleitern,* Annalen der Physik **362**, 541–567 (1918).

[63] A. Devices, *Chapter iv, rf components, active and passive mixers,* ADI 2006 RF Seminar (2006).

[64] S. Palermo, *Ecen620: Network theory broadband circuit design,* University Lecture (2023).

[65] E. Nash, *Ask the applications engineer-28: Logarithmic amplifiers explained,* .

[66] R. Kohlhaas *et al.*, *Robust laser frequency stabilization by serrodyne modulation,* Optics Letters **37**, 1005 (2012).

[67] L. Slodička *et al.*, *Atom-atom entanglement by single-photon detection,* Physical Review Letters **110**, 083603 (2013).

[68] R. Stockill *et al.*, *Phase-Tuned Entangled State Generation between Distant Spin Qubits,* Physical Review Letters **119**, 010503 (2017), publisher: American Physical Society.

[69] I. T. Raa *et al.*, *QMI - Quantum Measurement Infrastructure, a Python 3 framework for controlling laboratory equipment,* (2023).

3

TELECOM-BAND QUANTUM INTERFERENCE OF FREQUENCY-CONVERTED PHOTONS FROM REMOTE DETUNED NV CENTERS

Plans are worthless but planning is everything

Dwight D. Eisenhower

A. J. Stolk*, K. L. van der Enden*, M.-C. Roehsner, A. Teepe, S.O.F. Faes, C.E. Bradley, S. Cadot, J. van Rantwijk, I. te Raa, R.A.J. Hagen, A.L. Verlaan, J.J.B. Biemond, A. Khorev, R. Vollmer, M. Markham, A. M. Edmonds, J.P.J. Morits, T.H.T. Taminiau, E.J. van Zwet, and R. Hanson

Here we report the interference of photons emitted by remote, spectrally detuned NV center-based network nodes, using quantum frequency conversion to the telecom L-band. We find a visibility of 0.79 ± 0.03 *and an indistinguishability between converted NV photons around* 0.9 *over the full range of the emission duration, confirming the removal of the spectral information present. Our approach implements fully separated and independent control over the nodes, time-multiplexing of control and quantum signals, and active feedback to stabilize the output frequency. Our results demonstrate a working principle that can be readily employed on other platforms and shows a clear path towards generating metropolitan scale, solid-state entanglement over deployed telecom fibers.*

The results of this chapter have been published in PRX Quantum **3**, 020359 (2022) [1].

* These authors contributed equally to this work.

3.1. INTRODUCTION

A future quantum internet [2, 3], built using quantum processor nodes connected via optical channels, promises applications such as secure communication, distributed quantum computation, and enhanced sensing [4–6]. In recent years, the generation of entanglement between remote processor nodes has been realized with ions and atoms [7–10], Nitrogen-Vacancy (NV) centers in diamond [11, 12], and quantum dots [13, 14]. Moreover, other platforms such as rare-earth doped crystals [15–17], atom-cloud based memories [18, 19], and mechanical resonators [20] have been used to explore distributed entangled states.

Central to commonly used remote entanglement generation protocols [7, 9–14] is the propagation and interference of single photons that are entangled with stationary qubits in the nodes. Scaling these schemes to many nodes and to long distances poses two main challenges. First, any source of distinguishability between the emitted photons needs to be removed to generate high-fidelity entangled states. Especially for solid-state emitters, this requirement is difficult to meet for a large number of nodes due to variations in the local environment of the emitters. Second, for long-distance connections photon loss in fibers is a dominant factor determining the rate at which the entanglement generation succeeds. Leading platforms for realizing processor nodes [10, 21–25] in a future quantum network have natural emission frequencies in the visible spectrum; fiber losses at these frequencies hinder scaling beyond a few kilometers.

In this work, we show that both challenges can be addressed simultaneously by converting the coherent single-photon emission from NV centers (637 nm) to a single target wavelength in the Telecom L-band (1565-1625 nm) (Fig. 3.1a). Using the pump lasers to compensate for local detuning and using active stabilization of the frequency of the converted field, we are able to decouple the natural emission wavelength of the emitters from the wavelength used for propagation and interference and build fully independent, modular quantum nodes. We demonstrate that this method enables the removal of spectral offsets over a broad frequency range (>3 GHz). Moreover, the chosen interference wavelength has low propagation losses over commercially available optical fibers, making it suitable for long-range single-photon transmission.

We validate our approach by measuring quantum interference [26] between telecom photons that are frequency converted from the emission of two remote NV-centers that are detuned by more than 100 linewidths. By comparing the data to a detailed model we extract both the major noise sources and the underlying indistinguishability of the converted NV photons.

3.2. INDEPENDENT QUANTUM NETWORK NODES

We employ two independently operated quantum network nodes separated by a few meters on different optical tables. The nodes are connected to a midpoint located in two separate 19-inch racks. The relevant elements are depicted in Fig. 3.1c. Each node operates a single diamond NV center as stationary qubit, hosted in a closed-cycle cryostat at $T \approx 4K$. The relevant energy levels and optical transitions of the NV qubit are depicted in Fig. 3.1b. The spin reset transition is used for spin initialization into $m_s = 0$ (fidelity

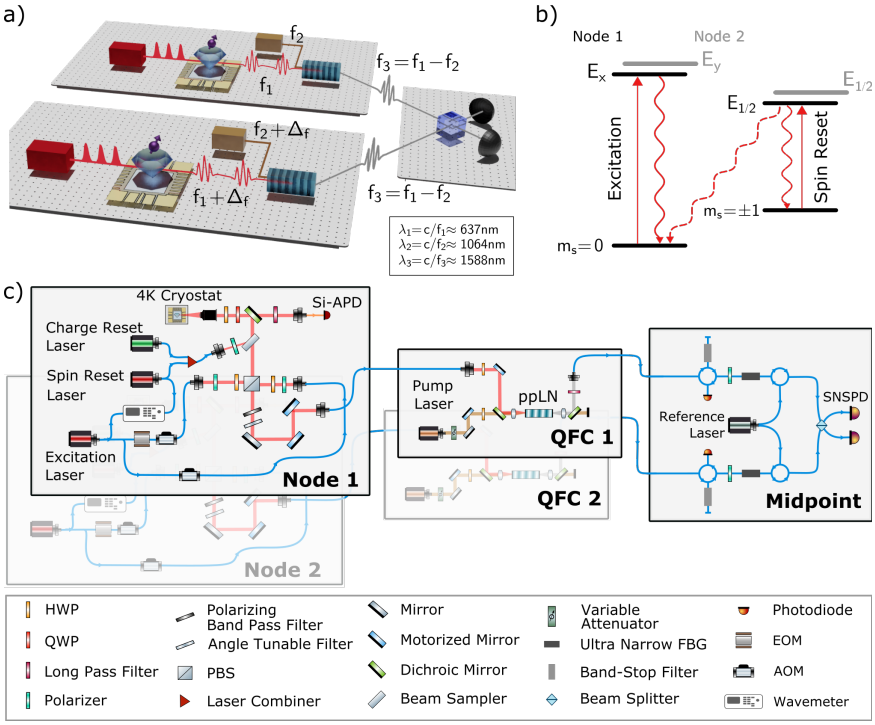

Figure 3.1: **Lay-out of the two independent network nodes and the midpoint.** a) Schematic of the main components of the set-up. Pulses excite the NV center, which emits single photons through spontaneous decay. The photons are converted to telecom wavelength and guided towards a midpoint placed in the neighboring lab, where they interfere on a beamsplitter (see Sec. 3.7.1 for more details on optics). b) NV center level structure showing the spin levels in the ground state and the relevant optical transitions. The optical transitions of the two nodes have different energies due to local variations in strain (see text). c) Detailed schematic showing the optics used for full operation of the system. The nodes are identical, and no hardware is shared between the systems. Each node has a set of charge reset, spin reset and excitation laser, which are modulated, combined and focused via a high NA objective onto the NV center. The Phonon side-band (PSB) (Zero-phonon line (ZPL)) emission from the NV center is filtered using frequency (polarization) filtering and coupled into a multi (single-) mode fiber. The PSB emission is measured locally on an APD, while the ZPL emission is sent to the QFC module. Stabilization light is split off from the excitation path, and brought into the single-photon path via a polarizing beamsplitter. The QFC module contains remotely controllable optics to align the input, pump and converted fields to the waveguide on the ppLN crystal that converts both the single-photons and stabilization light. Polarization maintaining (PM) fibers transport the photons to a midpoint where the single photons are filtered and separated from the stabilization light using a combination of in-fibre filters. The single photons interfere on a beamsplitter and are measured by SNSPDs, while the stabilization light interferes with the reference laser and is measured on a photodiode.

> 0.99). We use the transition to the $E_{x/y}$ excited state to generate single photons: a coherent optical π-pulse (≈2 ns) brings the NV center to the excited state, followed by spontaneous emission (lifetime ≈12 ns [27, 28]). Both setups employ their own lasers and optical components that deliver and collect light to the NV center.

The nodes are equipped with a (nominally identical) Quantum Frequency Conversion (QFC) module. Here the light at 637 nm is converted to 1588 nm via a single-step Difference Frequency Generation (DFG) process. This process has previously been shown to preserve entanglement between the photon and an NV center qubit [29]. The QFC modules are based on waveguides in a periodically poled Lithium Niobate crystal (ppLN), where the large non-linear coefficient facilitates conversion of single photons using a strong 1064 nm pump field. Various remotely controllable components allow for the remote and automated optimization of the QFC modules. While this single-step conversion has the upside of using a prevalent commercially available pump laser, it has the challenge of introducing spontaneous parametric down-conversion noise at the target wavelength by the pump laser due to imperfections in the crystal domains [30].

After free-space filtering to remove the bright pump light, the frequency-converted light is guided to a central midpoint. In the midpoint, a series of filters separate photons at the target wavelength from stabilization light and filter out noise photons. To achieve a high suppression of any broad-band background light, we use a two-step filtering process. First, we use a reflection off a narrow Band-Stop filter of 0.35 nm, followed by transmission through an ultra-narrow (FWHM of ~50 MHz) Fiber Bragg Grating (abbreviated with UNF). The filters are connected via circulators, and an in-fiber polarizer is used to ensure optimal performance of the UNF (Fig. 3.1B). After filtering, we interfere the two paths using a 50 : 50 beam splitter, and detect the photons using single-photon superconducting nanowire detectors (SNSPDs).

3.3. REALIZING SPECTRAL STABILITY VIA FEEDBACK

For solid-state emitters, the local environment can influence the emission properties directly via electric, magnetic or strain fields. For instance, for NV centers in nominally low-strain samples the local strain environment can shift the emission frequency by more than 1000 times the linewidth [31]. While direct tuning of emission wavelength is in principle possible on several platforms, e.g. by strain [32], via static electric fields [11, 14], or by using Raman tuned emission for emitters embedded in a cavity [33, 34], the range of tunability is generally limited. Also, direct tuning brings additional complexities in the device fabrication and can add significant experimental overhead.

We show that we can use the QFC process to remove the spectral offset between the NV emission without the need for direct tuning of the optical transition. An analogous scheme has recently been used on spectrally distinct quantum dots [35, 36]; a key difference is that the NV center host diamond also contains a long-lived matter qubit[37] and can function as a processing node in a quantum network [24]. Using resonant excitation spectroscopy we find the optical transition frequency used for single-photon generation at each node (Fig. 3.2a). We observe that these transition frequencies are separated by approximately 3 GHz (about 100 natural linewidths), as shown in Fig. 3.2B.

To bring the NV photons to the same target frequency, we realize a scheme that locks

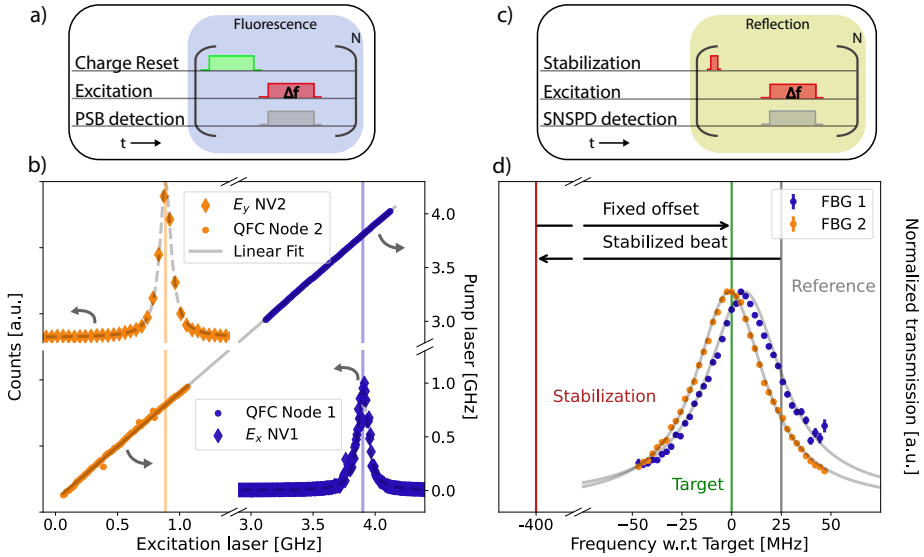

Figure 3.2: **Removing spectral offset using conversion.** a) Fluorescence measurement sequence used in b). A charge reset pulse is followed by repeated resonant excitation, during which fluorescence in the PSB is monitored. b) Resonant excitation spectra at Node 1 (Node 2) shown in blue (orange) diamonds, revealing the frequencies of the optical transitions (vertical lines) used for photon generation. The horizontal axis shows the optical excitation frequency with respect to a 470.477 THz offset. Grey dotted lines are Lorentzian fits. The right vertical axis shows the frequency of the QFC pump with respect to a 281.635 THz offset. Blue and orange dots show the QFC pump laser frequency when the stabilization is active. Solid grey line is linear fit. c) Pulse schematic for measuring the transmission through the ultra-narrow filter (UNF) shown in d). Reflections from the excitation light off the sample surface, which follow the same path as the resonant NV emission, are converted to the target telecom frequency and measured on the SNSPDs. The excitation frequency is swept by modulating the AOM frequency (see Fig. 3.1c). Transmission data is corrected for the frequency dependence of the losses in the AOMs. d) Layout of relevant laser frequencies and transmission data of the ultra-narrow filters (UNF). The UNF transmissions (blue and orange dots) are actively stabilized via their temperature to half transmission of the reference laser (grey vertical line). The stabilization light (red vertical line) is detuned from the target (green vertical line) and therefore reflected off the UNF (see main text).

the pump laser at each node to the frequency difference between the excitation laser at that node (and hence the NV emission frequency) and a joint Telecom reference laser at the midpoint. To achieve this lock, we use a split-off of the excitation laser, offset in frequency by a fixed 400 MHz, as stabilization light (see Fig. 3.2D). We propagate this stabilization light through the same frequency-conversion path as the NV photons. Due to the frequency offset, the stabilization light is reflected at the UNF, travelling backwards towards the first circulator where it exits (see Fig. 3.1c). Light from the joint reference laser is inserted at the second circulator, from where it propagates in opposite direction through the transmission flank of the UNF, also exiting on the first circulator. Here, the interference with the stabilization light is measured on a photo diode yielding the error signal for the lock (see Sec. 3.7.1). We close the loop by applying feedback to the pump laser, imprinting the same frequency shift on both the single photons and stabilization light. By transmitting the reference laser 25 MHz detuned from the transmission peak of

the second ultra narrow filter, the DC amplitude on the same photo diode serves as an error signal for active temperature stabilization of the UNF. Typical transmission profiles of the temperature-stabilized UNFs and the respective light-field frequencies are shown in Fig. 3.2d. The small deviation from ideal peak transmission at the target frequency is due to unaccounted background voltage of the photo diode and the slight difference in FWHM of the two UNFs. The remaining thermal drifts of about 1 MHz have only a minor (~1%) effect on the transmission (see Sec. 3.7.1). Note that the part of the reference light that is reflected off the ultra-narrow filter exits the circulator towards the SNSPDs and thus needs to be taken into account when designing the experimental sequence (see next section).

We verify our frequency locking by sweeping the excitation laser and monitoring the resulting pump laser frequency in Fig. 3.2b. We observe the expected linear relationship: a change in excitation laser frequency is precisely compensated by the pump laser frequency to always yield the same target frequency across the full tuning range. A linear fit yields the target frequency of (1587.5298 ± 0.0001) nm. This data demonstrates the ability of our frequency-locked down-conversion system to robustly compensate for a wide range of detunings.

3.4. PHOTON GENERATION AT THE TARGET TELECOM WAVELENGTH

We now turn to the generation of single telecom photons by the nodes as used for the measurement of two-photon quantum interference at the midpoint. The measurement sequence involves four stages (see Fig. 3.3), which are synchronized across the nodes by a fixed electronic "heartbeat" every 200 µs. This heartbeat is derived from a GPS-disciplined atomic clock positioned in the midpoint, which is distributed over telecom fibers via the White Rabbit Precision Time Protocol [38]. The first 2.5 µs following each heartbeat are used for the error signal generation for the frequency lock. This scheme allows the frequency lock to operate without knowledge of the state of the nodes, which reduces the complexity and rounds of communication needed. Moreover, it enables the autonomous operation of each of the nodes, using their own independent hardware to control the NV center and generate single photons.

In the first stage of the measurement sequence, a Charge-Resonance (CR) check is performed at each node to ensure that the NV centers are in the correct charge state and their transitions are on resonance with their respective spin reset and excitation lasers [11, 39]. In case a CR check fails, a charge reset laser pulse is applied and a new CR check is started; this protocol is repeated until success. Importantly, the CR check can be run in parallel with the frequency locking as the stabilization light for the lock does not reach the NV center nor the local PSB detectors; hence the CR checks can run independently of the heartbeat. The second phase starts once the CR check is passed on a node, where a digital trigger from the micro-controller signals the readiness to the other node. After the readiness of both nodes has been communicated, the heartbeat at which they move to the third stage is agreed upon (Fig. 3.3a and Sec. 3.7.1 for timings and more information).

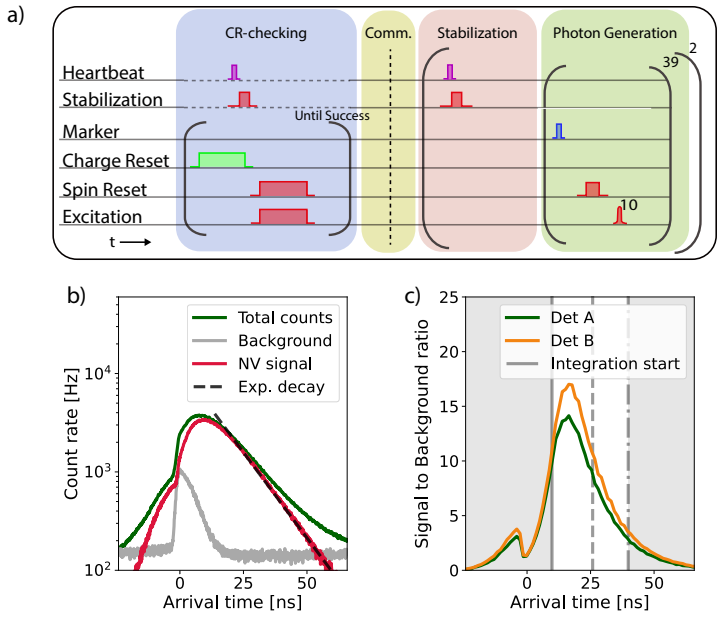

Figure 3.3: **Generating single-photons using a fixed heartbeat.** (a) Measurement sequence for synchronized generation of single-photons using a distributed heartbeat. For detailed timing see Sec. 3.7.1. (b) Histogram of SNSPD counts in a single excitation round, averaged over $\approx 2.8 \times 10^{11}$ repetitions and analyzed in 80 ps bins. The measured count rate (green) is a combination of background (grey) and NV fluorescence (red), which is calculated by subtracting the background from the total counts. The dotted line depicts exponential decay with 12.5 ns lifetime and serves as a guide to the eye. The NV signal before time 0, the peak of the excitation pulse, is due to the non-perfect extinction ratio of the devices generating the optical excitation pulse. The background data was taken continuously over 24 hours to include any drifts that occur over the same timescale as the signal data. (c) Signal-to-background ratio for both detectors as calculated from data in (b) (solid lines). The solid vertical grey line shows the start of our chosen detection window, whereas the dashed (dash-dotted) line shows the end for the data shown in Fig. 3.4a (Fig. 3.4b). The difference between the two curves is due to non-equal detector performances.

The third stage of the measurement sequence is used for the time-multiplexed frequency stabilization, as described above. In the fourth stage, we repeatedly apply a block consisting of a spin reset pulse (1.5 µs) followed by 10 optical π-pulses, ideally generating a train of 10 NV photons. A time-tagged digital signal marks the times at which the photon generation takes place. This block is repeated 39 times per heartbeat period. After two heartbeat periods, the system returns to the first stage (CR checks). Note that during the third and fourth stage, time-multiplexing the operations on the NV center and the error signal generation for the frequency lock is critical as the stabilization light and the reference light both leak into the single-photon detection path.

We analyze the resulting telecom photon detection rate in Fig. 3.3b (green line). We show the events observed in a single detector, aggregated over all single excitation rounds and both nodes. We denote $t = 0$ as the relative time of excitation. A sharp increase in count rate is observed when the ≈2 ns-wide optical π-pulse starts, followed by a slower decay dominated by spontaneous emission of the NV centers.

A data set displaying only the noise counts and the counts due to leakage of the excitation π-pulse (grey line) is independently generated by detuning the excitation laser by 1 GHz. The observed uniform background consists of intrinsic detector darkcounts (5 Hz per detector), counts induced by detector blinding from leaked reference and stabilization light (35 Hz per detector), and SPDC photons from the QFCs (≈150 Hz per detector). The leakage of the excitation π-pulse reflected off the sample is clearly visible. By subtracting this background from the data, we isolate the frequency-converted NV signal (red) displaying the characteristic exponential decay.

In remote entanglement experiments, the effect of noise counts can be mitigated by defining a heralding detection time window: only photon counts in this window are taken as valid entanglement heralding events [11]. In general, setting the heralding window involves a trade-off between high signal-to-background and thus high fidelity (favouring shorter windows) and success rate (favouring longer windows). In Fig. 3.3c we plot the signal-to-background ratio (SBR) for the two detectors as a function of photon detection time. The SBR is bounded on one side by the leaked excitation pulse and on the other side by the NV signal approaching the uniform background. For the analysis of the two-photon interference visibility (Fig. 3.4a), we apply a detection window in which the average SBR exceeds 10 (Fig. 3.3c, up to dashed line). For a more detailed comparison of our model to the data (Fig. 3.4b) we use an extended window (up to dash-dot line). In order to maintain the same SBR throughout the experiment, we employ a system of automatic optimization based on the live monitoring and processing of the single photon detection events (see Sec. 3.7.1).

3.5. TWO-PHOTON QUANTUM INTERFERENCE

Next we investigate the distinguishability of the photons emitted by the two nodes by analyzing their quantum interference. For two fully indistinguishable photons impinging on the input ports of a balanced beam splitter, quantum interference leads to vanishing probability to detect one photon in each output port [26], while for fully distinguishable photons this probability is 0.5 [40, 41]. From the (properly normalized) coincidence counts in the two detectors we can thus extract the distinguishability of the photons.

Figure 3.4a) shows the measured coincident detections between the two output arms without any background subtraction. Each excitation round is treated as a “detection bin” in which a photon can arrive. We analyze the coincidences per block of 10 excitation pulses, defined as a click in both detectors in the same or two different detection bins. This leads to a maximum detection absolute bin difference of 9 and a coincidence probability increasing linearly towards 0 bin difference. We overlay the data with a model based on independently determined parameters, treating the photons as completely distinguishable (Sec. 3.7.1). For the non-zero bin differences, in which the NV photons are fully distinguishable by their arrival time difference of at least 10x the lifetime, the model shows excellent agreement with the measured coincidences. In stark contrast, we observe a strong reduction in measured coincidences compared to the model for the zero bin difference. This drop in coincidences when the photons arrive in the same bin is the hallmark of two-photon quantum interference and forms the main result of this work.

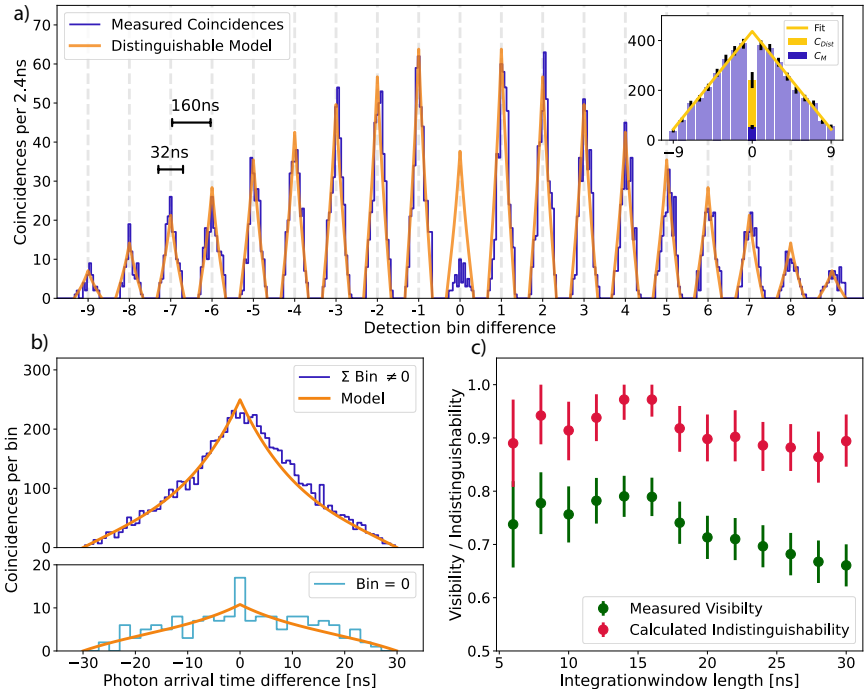

Figure 3.4: **Two-photon quantum interference at telecom wavelength.** a) Histogram of measured coincidences (blue) for the analyzed time-bins, overlaid with a model assuming distinguishable photons (orange), based on independently determined parameters. Histogram binsize is 2.4 ns. Vertical lines depict the time-origin of each detection bin difference. Horizontal scale bars show the relevant timescales in and between the detection bin difference. Inset: extraction of the interference visibility, corrected for the imbalance of measured photons per excitation of the two nodes, using a linear fit to the total counts per bin difference (see text). b) Histogram showing temporal shape of the non-zero (zero) bin difference coincidences shown at the top (bottom) panel. We overlay the data with the same model (see Sec. 3.7.1), taking into account brightness and background rates and indistinguishability of converted NV photons of 0.9 (see c)). Binsize for top (bottom) panel is 0.8 ns (2 ns) c) Measured visibility and extracted indistinguishability of converted NV photons for varying window length. Errorbars for visibility/indistinguishability are 1σ/68% confidence interval. Green (blue) circled points indicate data corresponding to the window length shown in Fig. 3.4a (Fig. 3.4b).

The observed visibility is defined as $V = 1 - \frac{C_M}{C_{Dist}}$, with C_M the measured number of coincidences, and C_{Dist} the coincidences we would have measured at zero bin difference in case the photons were completely distinguishable. In the inset of Fig. 3.4a we show the method of extracting the visibility. First we use a linear fit to the total distinguishable coincidences per detection bin difference to get C_E, the extrapolated coincidences for 0 bin difference. From this value we extract C_{Dist}, by correcting for the imbalanced emission rates (see Sec. 3.7.1). The resulting visibility is $V = 0.79 \pm 0.03$, which is well above the classical bound of 0.5 [40, 41], proving the successful demonstration of quantum interference of single photons in the telecom L-band.

A more detailed picture of the temporal shape of the coincidences allows us to test our model with more precision (Fig. 3.4b). The accumulated coincidences for non-zero

bin difference (top panel) show a characteristic shape dominated by the exponential decay of the NV emission. The data is well described by our model that takes into account the temporal shape of the NV-NV, background-NV and background-background coincidence contributions (derivation in Sec. 3.7.1). The temporal histogram of coincidences within the same bin (bottom panel) shows a good match with the temporal shape predicted by our model. In particular, we observe no reduction of coincidences at 0 time delay, consistent with the visibility being limited by background counts rather than frequency differences between emitted photons [42, 43].

With our knowledge of the background and signal rates we can extract the degree of indistinguishability of the emission coming from our NV centers. We perform a Monte-Carlo simulation of our dataset using the independently determined parameters and apply Bayesian inference to find the most likely value of the indistinguishability, given our measured result (see Sec. 3.7.1).

In Fig. 3.4c we plot the visibility and the extracted photon indistinguishability for increasing detection time window lengths. While the visibility drops for longer windows consistent with the decreasing signal-to-background ratio, the indistinguishability of the NV photons remains high around 0.9. We note that this latter value is similar to values found for NV-NV two-photon quantum interference without frequency conversion [12], confirming that our conversion scheme including the frequency stabilization to a single target wavelength preserves the original photon indistinguishability, and enables solid-state entanglement generation via entanglement swapping.

3.6. CONCLUSION AND OUTLOOK

We have shown quantum interference of single photons emitted by spectrally distinct NV centers, by converting them to the same telecom wavelength. We have demonstrated an actively stabilized Quantum Frequency Conversion scheme using Difference Frequency Generation on fully independent nodes. The design and implementation allow for the scheme to be used at large distances. Furthermore, the techniques can be readily transferred to other quantum emitters in the visible regime with minimal adaptations to the conversion optics and control schemes used.

Future improvements to our system can increase the performance in multiple ways. First, adapting our optical design to prevent detector blinding by the stabilization light can lower the detector contribution to the background counts to the design level of 5 Hz. Second, a different approach [44] to the QFC technique based on a bulk crystal may remove the (currently dominating) SPDC background noise due to poling irregularities. Third, the signal level of collected coherent photons from the NV centers could be improved significantly by use of an open microcavity [45, 46]. In particular, achieving a fraction of coherent emission of 46% as reported in Ref. [45] would raise the signal-to-background ratio above 200. Finally, by extending the hardware we can stabilize the optical phase of the single photons emitted by the NV centers, enabling entanglement generation upon heralding of a single photon [24].

By combining the protocols demonstrated here with established spin-photon entangling operations and photon heralding at the midpoint [11, 12], remote NV centers can be projected in an entangled state via telecom photons. Owing to the low propagation

loss of these photons and extendable control scheme, our results pave the way for entanglement between solid-state qubits over deployed fiber at metropolitan scale.

3.7. SUPPLEMENTARY INFORMATION

3.7.1. OPTICAL SET-UP

Our experiments are performed using two nominally identical quantum network nodes. Each node houses a Nitrogen-Vacancy (NV) center in a high-purity type-IIa chemical-vapor-deposition diamond cut along the ⟨111⟩ crystal orientation (Element Six). Both samples have a natural abundance of carbon isotopes. Fabrication of solid immersion lenses and an anti-reflection coating on the diamond samples enhances the photon-collection efficiencies from the NV centers. The ground-state spin levels are split using a small permanent magnetic field aligned with the NV axis of ≈ 30 G.

Experimental equipment used for each node is summarized in Tab. 3.1. Node 1 and 2 are in the same laboratory, around 7 m apart. The optical fibers that connect Node 1 and 2 with the first midpoint 19" rack containing the filters are PM fibers of 3 m and 10 m long, respectively. After the filters, both are connected to the beamsplitter and subsequently the SNSPDs in a separate 19" rack in the room next door with 10 m long PM fibers.

Details of the optical lay-out of the free-space and in-fibre optics used are shown in figure 3.1B. For initialization in the correct charge and spin state, we use a combination of off-resonant (515 nm) and resonant (637 nm) excitation respectively. Both lasers are combined using in-fibre optics, and coupled into the free-space part using a beam sampler optimized for transmission. For single-photon generation, we use a second resonant laser tuned to a spin-preserving transition. Both resonant lasers are stabilized using a wave meter. The main part of the excitation light passes electro- and acoustic-optical modulation (EOM and AOM) for fast switching, and is coupled into the free-space path using a central polarizing beam splitter (Thorlabs). Combined, this light is guided to the high NA microscope objective (Olympus 100x 0.9NA) using a dichroic mirror (DM) (Semrock), after which the polarization is set at an optimum for cross-polarization. The second part of the excitation laser is sent to a separate set of AOMs that provide an offset in frequency to form the stabilization light and coupled in on the opposite side of the central PBS. The main purpose of this light is to provide a fixed frequency reference of the single photons generated by the excitation light, and its purpose can be extended to stabilize the phase of the relevant phases for entanglement generation [24, 47].

Emission from the NV-centre propagates backwards through the set-up, where the phonon side-band (PSB) is separated from the main path using the DM, filtered by additional long-pass filters (Semrock) and coupled into a multi-node fibre to be detected locally by an APD (LaserComponents). During the measurement, detection in this path is used for live monitoring and diagnostic purposes. The resonantly emitted photons in the zero-phonon line (ZPL) are guided to the central PBS, separated from the excitation light based on polarization (Thorlabs), and filtered using a band pass filter (Semrock). We use a deformable mirror and a set of motorized mirrors to couple in both the single photons and frequency control light simultaneously into the same PM SMF. Using these components, we can periodically optimize the coupling remotely, greatly improv-

ing the long-term performance and remote operation capabilities. By coupling into a fibre, we can decouple the alignment of the free-space optics from the QFC optics, simplifying the set-up and allowing for easy exchange of different QFC modules (full details of equipment list in Tab. 3.1 and 3.2.

Table 3.1: Experimental equipment used in the two nodes.

Equipment name	Part name/number
Cryostat	Montana Instruments Cryostation S50
Positioners	Microscope objective on 3x PI E-873
Micro-controller	Jäger ADwin-Pro II T12
Arbitrary Waveform Gen. *AWG*	Zürich Instruments HDAWG-8
Excitation laser	Toptica DL pro 637 nm
Spin reset laser	Toptica DL pro 637 nm
Charge reset laser	Cobolt 06-01 515 nm
Reference laser	NKT Photonics Koheras ADJUSTIK E15 PM FM
EOM	Jenaoptik AM635b
AOM	Gooch and Housego Fibre Q 637nm
AOM Driver	Time Base DIM-3000
APD	Laser Component COUNT-10
SNSPDs	Quantum Opus 00-NPD-1588-HDE

Table 3.2: QFC equipment used in the two nodes.

Equipment name	Part name/number
Pump laser	NKT Photonics 1064 nm Koheras ADJUSTIK Y10
Pump laser amplifier	NKT Photonics Koheras BOOSTIK HP
Non-linear Crystal	Custom ppLN crystal NTT
Remote Piezo mirrors	Newport AG-M100n

3.7.2. OVERVIEW OF TIMING ELECTRONICS

Interfering photons emitted by two NV centres with high fidelity places strict requirements on the arrival time and thus the generation time of the single photons. Future long distances between our nodes prevent us from using a single waveform generator to meet these requirements, and a more scalable approach is needed, which we have employed for the current experiment. The lay-out is shown in figure 3.5 (full equipment in 3.4), showing how a single GPS disciplined clock is shared across the nodes via White-Rabbit enabled switches. The resulting synchronization pulses are then coherently split and distributed to the devices requiring timing synchronization. The microcontrollers EVENT cycles are externally triggered by a 1 MHz pulse. The AWG sequencers are referenced externally by the 10 MHz. Furthermore, the waveform generation inside the AWG is triggered using the 5 kHz heartbeat, after which the AWG sequencer can realize a sub

nanosecond delay. Together, this allows for the long range synchronization of the experimental sequence with a jitter of 100 ps.

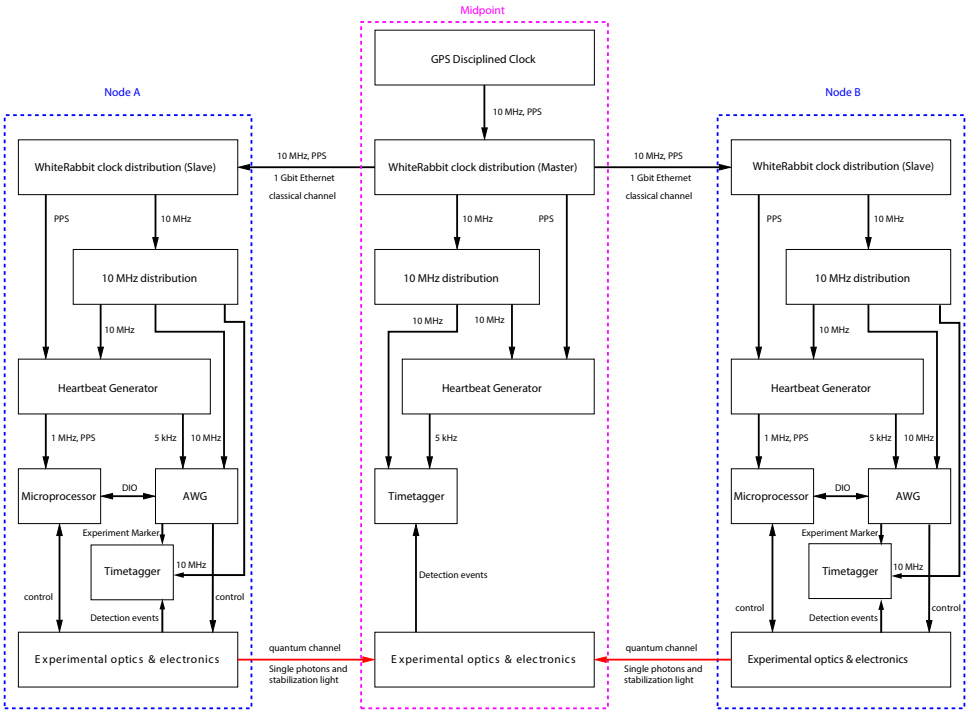

Figure 3.5: Schematic overview of hardware to synchronize events across the experiment. All connections that distribute the critical timing signals are propagated over telecom fibres on a dedicated fibre. The data that is generated by the timetaggers is sent over the network to a single PC that processes the data. Both the raw and processed data are stored to disk.

For future experiments, the heartbeat can be adjusted by changing the settings of the heartbeat generator. This would allow to run the frequency stabilization at a higher rate needed for the higher feedback bandwidth for phase-locking of two remote excitation lasers.

3.7.3. OVERVIEW EXPERIMENTAL SEQUENCE.

The experimental sequence is given in more detail in Fig. 3.6. The CR-check procedure contains a bright off-resonant charge reset pulse to probabilistically re-ionize the NV centre into the negative charge state. We then verify that the lasers are resonant with the right transitions by monitoring the fluorescence during excitation with both the spin reset and excitation laser. The counts during this interval are compared to a threshold determined before the experiment. If past this threshold, we assume to be on resonance and in the right charge state. This procedure is repeated until success, and has a typical

passing rate of 5 – 10%, taking on average 1.5 ms[39]. The amount of experimental sequences per CR-checking round is a balance between ionization to the NV^0 state during the sequence and data rate. At the start of each CR-check we find the NV centres to be ionized in about 10% of the cases per node.

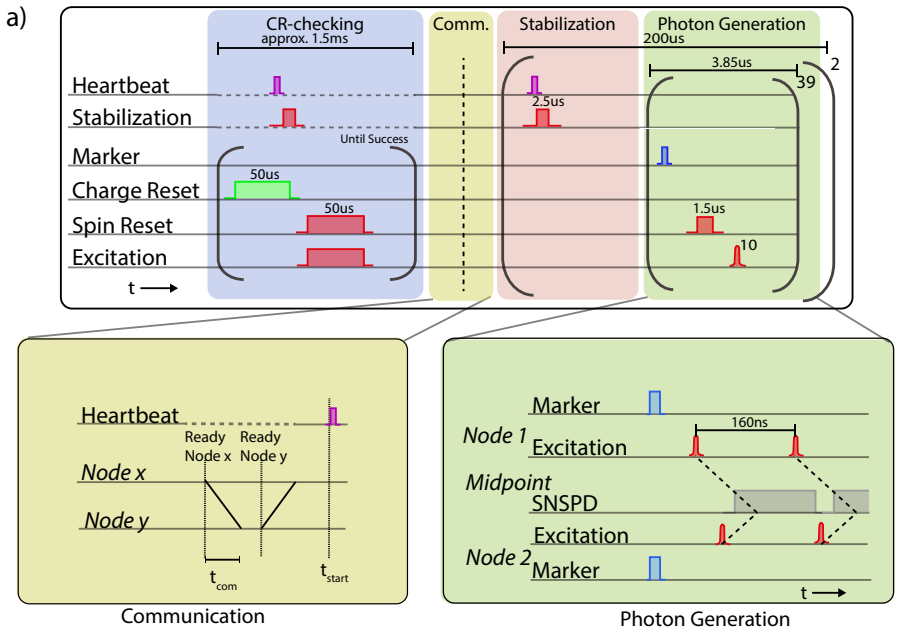

Figure 3.6: . Schematic showing pulses played during the experiment. The timescale is indicated above the pulses and sequence stages. The communication step (bottom left) is symmetric whether node1 or node2 succeeds first in passing the CR check. The heartbeat where the next stage is started is shown. Using the Marker signals, the corresponding coincidence windows in the SNSPDs in the midpoint can be calculated.

The communication between the nodes signalling the ready state is done by exchanging a digital trigger between the micro-controllers in charge of the CR-check process. By using the predetermined travel time of the communication, each microcontroller can calculate the next available starting time upon receiving the digital trigger of the opposite node. Using this information it triggers the AWG in advance of that heartbeat, reliably triggering the AWGs that switch to playing the waveforms that generate the optical pulses needed for photon generation. During the live analysis of the data, the experiment markers are used to signal the generation of single photons. These markers are in sync with the heartbeat present on the midpoint, and allow for the faithful recovery of the single photon events. Future improvements can be made by actively heralding the arrival of photons in the midpoint, conditioned on receiving the experiment signal.

3.7.4. DATA COLLECTION AND PROCESSING

The data taken shown in Fig. 3.3 and Fig. 3.4 was taken over the course of 17 days. To allow for long-duration remote experiments, we operate the set-ups with minimal manual in-situ intervention, and employ a multitude of automatic calibrations. We determined the amount of data to collect by using previous measurements of coincidence rates and targeting an approximate statistical errorbar of 3% on the measured visibility.

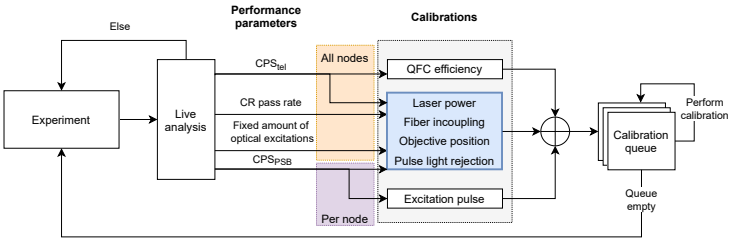

Figure 3.7: Schematic visualization of the automated calibration framework. At fixed intervals of NV excitation attempts, we perform live an analysis of several variables that triggers specific calibrations per node or on all nodes. The order in which the possible calibrations are performed in the queue is the same as the order in which they are shown in the schematic, reading from top to bottom.

The data was collected in batches of ≈ 24 hours, during which the set-up was operating fully autonomously. Remote monitoring was made possible by live viewing in a Grafana dashboard showing performance and environmental data pushed to a database. Live warnings of parameters that went outside pre-defined ranges provided 24/7 warnings, and the possibility to manually intervene remotely. After each block of 24 hours, manual routine inspections were done to check the sample and set-up status. As an example of the benefits of this system, the interference data was collected over a period of 17 days, of which 78% of the wallclock time under autonomous operation of the complete system, during which no human operator actively controlled the experiment.

3.7.5. DATA PROCESSING

We employ various data processing steps during the experiment. First, all the raw data generated by the Adwin counting modules describing the result of the CR-checking process on the nodes is written to disk every ≈ 2 of minutes, and a next block of measurements is started. Simultaneously the stream of time tags of all synchronizations (heartbeat and experiment marker), and all SNSPD events outside of the blinding window, are tagged using 80 ps bins, and saved to disk on dedicated node PCs every couple of seconds, totalling to ≈ 1.2Tb of uncompressed data.

Because performing the analysis on large amounts of raw data is challenging, we employ live processing that generates significantly smaller files. This processing stores only the photon events that might be of interest for further analysis, by looking at the time bins where converted single photons from the nodes are expected to arrive in the midpoint (see Fig. 3.6). The data stored when an event occurs is given in Tab. 3.5, which can be extracted from the combined stream of timetagged events from all 3 timetaggers. One experiment marker can have more than one event (e.g. coincidences). The size of this

dataset is less than 0.5% of the raw data generated, making it much more manageable.

While analyzing the coincidence data we noticed that some blocks contain many events that happen at time intervals much shorter than the dead time of our detectors (20 ns). We suspect that these events are due to (yet unexplained) resonances in the biasing electronics of the SNSPDs. To filter out these events we ignore blocks of measurements in which more than 2 detection events have happened in a single 160 ns window for both the SNSPDs. We can give an upper bound on how many events we would expect of this kind based on our signal rate by taking the maximum singles detection rate in Fig. 3.3b (3000 Hz) for the full duration of the 160 ns. Then, the probability of having more than 2 counts in both nanowires simultaneously is given by $P(C>2)^2$ with

$$P(C>2) = 1 - P(C=0) - P(C=1) - P(C=2) \tag{3.1}$$

the chance of having more than 2 counts in one nanowire. For the amount of repetitions of our experiment ($282226000000 \approx 2.8 * 10^{11}$), we thus conservatively expect 0.015 of these occurrences. When applying this filter we remove ≈ 36 blocks which equates to 0.05% of the total data.

3.7.6. AUTOMATED CALIBRATIONS

Keeping multiple nodes at their pre-calibrated performance level in parallel requires an automated calibration framework, in which several setup-specific calibrations can be performed both in parallel and successively, where the order of calibrations is conditional on setup specific inter-dependencies. After a constant amount of optical excitations, each node's performance is evaluated against several parameters that are indicative for the NV photon emission, conversion and collection rate per node, listed below in Sec. 3.7.7. Every parameter has a specific threshold chosen to reflect the manually calibrated performance level at the time of initialization of each dataset taken per day. A visual representation of the automated calibration framework is shown in Fig. 3.7. Violation of the pre-calibrated parameter thresholds triggers adding specific calibrations to the 'calibration queue', where the calibrations are ordered by setup specific inter-dependencies and subsequently executed, parallelizing calibrations on nodes as much as possible.

Every individual calibration that will block the optical path output of the QFC temporarily freezes the frequency lock's feedback loop for the duration of the calibration, schematically shown in Fig. 3.8. We require this when calibrating the QFC efficiency with path-blocking flip-in power meters, as well as using a diagnostic flip-in mirror to measure NV excitation resonant laser light and photons coupling in to the QFC. The lock feedback loop is resumed after every such a calibration to ensure the locking feedback scheme can keep up with longer term drifts of the locking beat frequency.

3.7.7. EVALUATED PERFORMANCE PARAMETERS

- **Count-per-shot of PSB photons ($\mathbf{CPS_{PSB}}$)**: The amount of photon detections in the PSB per excitation attempt contains information on how well we address the relevant transition with the optical excitation pulse. A reduction in CPS_{PSB} can

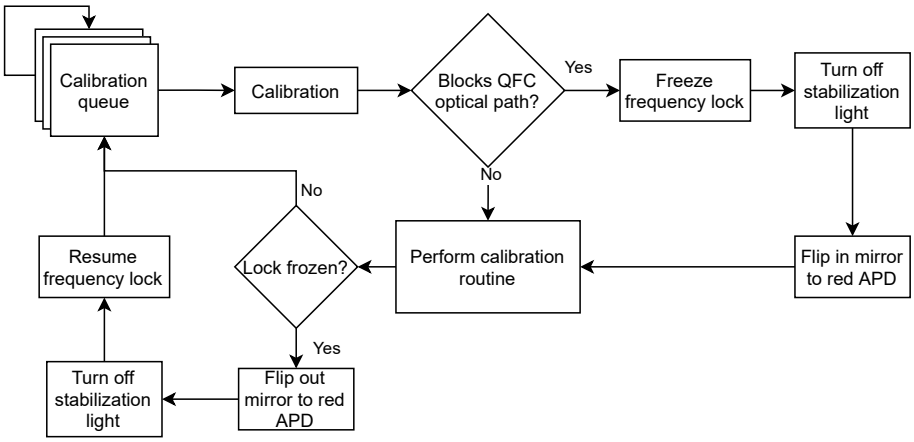

Figure 3.8: Schematic showing the decision logic deciding if the frequency lock should be frozen before performing a calibration routine. To ensure proper handoff of setup-equipment control, the stabilization light is always turned off before any calibration is started whilst freezing the feedback, if this calibration will block the optical path going through the QFC. Resuming of the lock is an exact reversal of this process, where the stabilization light has to be turned on before the lock's feedback loop is resumed, otherwise no locking beat will be generated.

thus trigger all available node-related calibrations, including re-calibration of the power of the excitation pulse, but only of the specific node on which this is detected.

- **Average CR-check passing rate**: Indicative of the stability of optical addressability of the NV center's transitions.
- **Fixed amount of optical excitations**: Recalibration of each node is performed regardless of performance thresholds after a fixed amount of attempts, both for logging purposes of small drifts as well as certainty about bringing the setup to a well calibrated known state, mitigating any drifts we could not observe while the experiment is live.
- **Count-per-shot of telecom photons from NV excitation ($\mathbf{CPS_{tel}}$)**: The amount of single telecom photons incident on the SNSPD detectors per excitation attempt show a performance of the entire node: the entire optical path the single photons traverse until detection at the SNSPD detectors. This also includes the intrinsic performance of the QFC, which is calibrated separately.

These measurements also enable us to collect the data crucial for the further analysis of the two-photon quantum interference: the probability of detecting a photon from Node 1 or 2 in detector A and B and the rate of background counts detected in detector A and B. An overview of the average value and standard deviation per measurement dataset is shown in Fig. 3.10. How these values are used for further calculations is explained in the next section.

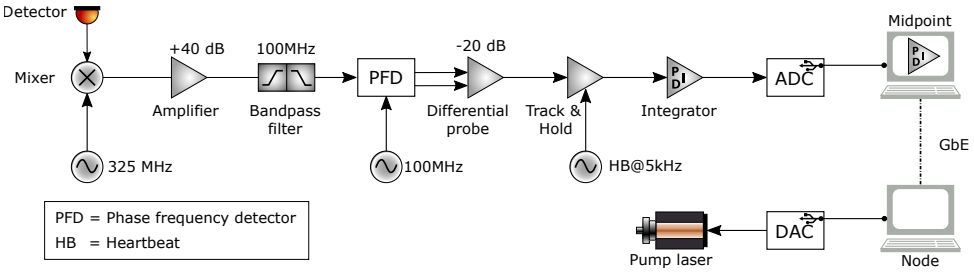

Figure 3.9: Schematic of frequency lock hardware for one arm of the two-node setup. The optical beat is down-mixed with 325 MHz and then further processed using standard electronics components. The feedback loop is closed using a pair of ADC/DAC over a Gigabit Ethernet connection, resulting in a feedback rate of ~ 500 Hz.

3.7.8. MODEL OF COINCIDENCE PROBABILITIES

In this section we will give details on the model used to calculate the expected coincidence probabilities assuming both completely distinguishable photons and (partially) indistinguishable photons with an indistinguishability η. We collect coincidences in 19 distinct difference bins (-9 ... 9) which are generated as follows: Once both nodes have indicated their ready-state we perform 10 pulsed excitations. This results in 10 consecutive time windows in which we can detect single photons emitted from the NV centers. For each detected photon we are looking for photon coincidences (i.e. events for which also the other detector clicked). We consider coincidence events where both photons were detected in the same time window (these coincidences are shown in the zero-difference bin) as well as photon detections in different time windows. Depending on the difference in time window number we assign these coincidences to one of the 19 possible bin number differences, numbered from −9 to 9, as shown in Fig. 3.4a of the main text. Due to the finite number of time windows, the probability of detecting a coincidence decreases for higher bin number differences. The probability of detecting a coincidence for any given bin number difference is thus given by $P_{det} = sP_{coinc}$ with the scaling factor $s = 10 - |bin|$ where bin is the bin number difference. The probability of detecting a coincidence is:

$$P_{coinc} = P_{NVNV} + P_{NVDC} + P_{DCDC} \tag{3.2}$$

where P_{NVNV} is the probability of a coincidence between two photons emitted by an NV center, P_{NVDC} is the probability of a coincidence between an NV emitted photon and a dark count (or other noise or background count) and P_{DCDC} is the probability of a coincidence between two dark counts.

For the non-zero bin number differences these probabilities are given by

$$P_{NVNV} = p_{1A}p_{2B} + p_{1B}p_{2A} + p_{1A}p_{1B} + p_{2A}p_{2B} \tag{3.3}$$

$$P_{NVDC} = p_{DC_A}(p_{1B} + p_{2B}) + p_{DC_B}(p_{1A} + p_{2A}) \tag{3.4}$$

$$P_{DCDC} = p_{DC_A}p_{DC_B} \tag{3.5}$$

where $p_{1(2)A(B)}$ is the probability of a photon emitted by node 1 (2) to be detected in detector A (B) and $p_{DC_{A(B)}}$ is the probability of a dark count in detector A (B). All these

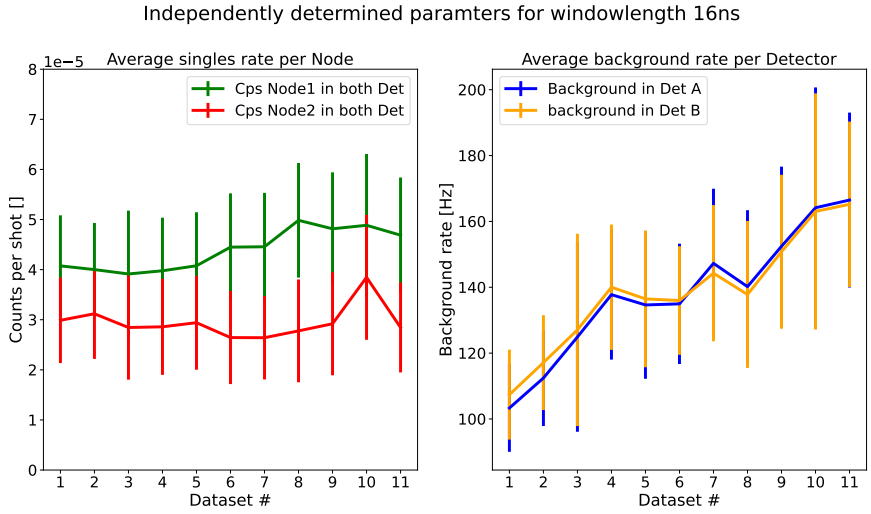

Figure 3.10: Average of the independently measured parameters for one of the analyzed integration windows. Individual data sets are about 24 hours of measurement. The error-bar on the values is the standard error of the mean. For each datapoint,the parameter is measured during at approximately 2 minute intervals. The signal rate is calculated in the fluorescence window after the excitation as shown in figure 3.3. The average background rate is calculated using data in between the pulses, far away from the optical excitation and fluorescence. These parameters can be calculated for the different windowlengths using the same dataset. The rise of the background counts during the experiment is currently not understood.

parameters are measured during the experiment by having excitation rounds from only a single node interleaved with the normal excitation rounds.

As the single emitter nature of our NV center does not permit two photons from the same NV within one time window (up to a small probability of double excitation which we neglect in this model), in the zero bin number difference P_{NVNV} reduces to the following expression:

$$P_{NVNV,0bin} = (p_{1A}p_{2B} + p_{1B}p_{2A})(1-\eta) \tag{3.6}$$

while P_{NVDC} and P_{DCDC} remain the same. Here η is the indistinguishability, which represents the reduction of the probability of getting an coincidence from NV contributions. This single parameter in our model takes into account the possible sources of distinguishibility such as spectral/temporal offset and polarization differences.

3.7.9. CALCULATING THE VISIBILITY WITH UNBALANCED EMITTERS

We define Visibility using the ratio between coincidence counts in the case that photons are fully distinguishable C_{dist} and coincidence counts we measured, C_M.

$$V = 1 - \frac{C_M}{C_{dist}} \tag{3.7}$$

We can directly extract C_M from our experiment, as it corresponds to the measured coincidences in the zero-difference bin. In our model, it is given by filling in Eq. 3.6 and 3.3

into Eq. 3.2:

$$P_M = (p_{1A}p_{2B} + p_{1B}p_{2A})(1-\eta) + p_{DC_A}(p_{1B} + p_{2B}) + p_{DC_B}(p_{1A} + p_{2A}) + p_{DC_A}p_{DC_B} \quad (3.8)$$

However, we do not have such direct access to C_{dist}. To extract C_{dist} from measured parameters we fit the number of coincidences in the non-zero bins using a linear fit (as shown in Figure 4 of the main text), and use this to extrapolate the value in the zero-bin, which we will call C_E. This extrapolation will overestimate the coincidences we would get in the zero bin number difference for perfectly distinguishable photons as the non zero bin number differences also include coincidences of photons emitted from the same NV, a case that does not occur in the zero bin number difference. To determine the necessary correction we compare the probability of a coincidence in the zero bin number difference for $\eta = 0$

$$P_{dist} = (p_{1A}p_{2B} + p_{1B}p_{2A}) + p_{DC_A}(p_{1B} + p_{2B}) + p_{DC_B}(p_{1A} + p_{2A}) + p_{DC_A}p_{DC_B} \quad (3.9)$$

with P_E, the probability for an extrapolated zero-bin using the fit of the non-zero bins

$$P_E = (p_{1A}p_{2B}+p_{1B}p_{2A})+(p_{1A}p_{1B}+p_{2A}p_{2B})+p_{DC_A}(p_{1B}+p_{2B})+p_{DC_B}(p_{1A}+p_{2A})+p_{DC_A}p_{DC_B} \quad (3.10)$$

Resulting in the following correction for the C_E, where we use $C_E = P_E N_{attempt}$

$$C_{dist} = C_E - (p_{1A}p_{1B} + p_{2A}p_{2B})N_{attempt} \quad (3.11)$$

Here we have used the number of experimental attempts $N_{attempt}$ (i.e. the number of excitation pulses sent to the NV center over the course of the entire experiment). We note that in case the used beamsplitter is strongly imbalanced this would also affect the number of coincidences in the zero bin number difference. In particular, our determined indistinguishability would be scaled by an additional correction factor to $\eta(1-\frac{(R-T)^2}{(R^2+T^2)})$ with the beam splitter reflectivity R and transmitivity T. Using the specified values of our beam splitter $R = 0.496$ and $T = 0.504$, we find that this effect is on the order of $\eta(1-10^{-4})$ and we therefore neglect it in our model.

3.7.10. MODEL OF TEMPORAL SHAPE OF DISTINGUISHABLE COINCIDENCES

The analysis of the measured coincidences with respect to their arrival time difference holds a vast amount of information of the (relative) emitter properties. In our case, it is difficult to extract detailed information about the NV centres from the measured coincidences in the zero-difference bin as the vast majority of these coincidences involves background counts. We can, however, model the different temporal shape of the three contributions as mentioned in 3.2 in the non-zero difference bins. Analogous to Kambs [43] we start by writing down the photon wave-packets of the individual events. The single photon wave function an NV-centre from spontaneous emission (ignoring any spectral and phase information) is given by

$$\phi_{NV}(t) = \frac{1}{\sqrt{\tau(e^{\frac{-T_{start}}{\tau}} - e^{\frac{-T_{end}}{\tau}})}} e^{-\frac{t}{2\tau}} H(t - T_{start})(1 - H(t - T_{end})) \quad (3.12)$$

where τ =12.5 ns the lifetime of the excited state. We can define $W(t) \equiv H(t - T_{start})(1 - H(t - T_{end})$ to be the selected window with start(end) time $T_{start}(T_{end})$ both larger than 0. $H(t)$ is the Heaviside step function. Here we have chosen $t = 0$ to be the moment the infinitely short optical excitation would have arrived in the detector as the start of the exponentially decaying wave-packet. We now assume that both NV centres have the same excited state lifetime, and the beamsplitter ratio to be perfect. The joint detection probability is given by:

$$P_{joint}(t, \Delta t) = \frac{1}{4}|\phi_i(t+\Delta t)\phi_j(t) - \phi_j(t+\Delta t)\phi_i(t)|^2 \tag{3.13}$$

A background photon at the beamsplitter is modeled as a process that has a uniform probability density in time:

$$P_{DC}(t) = \frac{1}{(T_{end} - T_{start})} W(t) \tag{3.14}$$

Here we assume that the contribution of background noise is constant in time, which is a good approximation for the darkcounts of the detector and SPDC noise coming from the QFC process. For the excitation pulse leakage this approximation does not hold, but we assume this error to be small if we limit the amount of pulse light in our analysis window. For completely distinguishable events the interference term in the joint detection probability drops out, and it simplifies to:

$$P^{dist}_{joint}(t, \Delta t) = \frac{1}{4}(P_i(t+\Delta t)P_j(t) + P_j(t+\Delta t)P_i(t)) \tag{3.15}$$

with $P_i(t) = |\phi_i(t)|^2$. To obtain the second order cross-correlation function we integrate over the detection times of the single photons. The NV-NV contribution is therefore given by:

$$\mathcal{G}^{(2)}_{NVNV}(\Delta t) = \int_{-\infty}^{\infty} \frac{1}{4}\, 2P_{NV}(t')P_{NV}(t'+\Delta t)dt' = \tag{3.16}$$

$$\frac{1}{2\tau^2(e^{\frac{-T_{start}}{\tau}} - e^{\frac{-T_{end}}{\tau}})^2} \int_{-\infty}^{\infty} e^{-\frac{t'}{\tau}} e^{-\frac{t'+\Delta t}{\tau}} W(t')W(t'+\Delta t)dt' \tag{3.17}$$

We can solve this integral by breaking it up for positive and negative Δt, and absorbing the Heavisides accordingly in the integration limits. For $\Delta t > 0$ we get:

$$\frac{1}{2\tau^2(e^{\frac{-T_{start}}{\tau}} - e^{\frac{-T_{end}}{\tau}})^2} \int_{T_{start}}^{T_{end}-\Delta t} (e^{-\frac{t'}{\tau}} e^{-\frac{t'+\Delta t}{\tau}})\, dt' = \frac{1}{4\tau(e^{\frac{-T_{start}}{\tau}} - e^{\frac{-T_{end}}{\tau}})^2} (-e^{\frac{-2T_{end}-\Delta t}{\tau}} + e^{\frac{-2T_{start}+\Delta t}{\tau}}) \tag{3.18}$$

For $\Delta t < 0$ we get:

$$\frac{1}{2\tau^2(e^{\frac{-T_{start}}{\tau}} - e^{\frac{-T_{end}}{\tau}})^2} \int_{T_{start}-\Delta t}^{T_{end}} (e^{-\frac{t'}{2\tau}} e^{-\frac{t'+\Delta t}{2\tau}})\, dt' = \frac{1}{4\tau(e^{\frac{-T_{start}}{\tau}} - e^{\frac{-T_{end}}{\tau}})^2} (-e^{\frac{-2T_{end}+\Delta t}{\tau}} + e^{\frac{-2T_{start}-\Delta t}{\tau}}) \tag{3.19}$$

which, after combining both, arrive at the expression for $\Delta t \in [-(T_{end}-T_{start}), T_{end}-T_{start}]$:

$$\mathcal{G}_{NVNV}(\Delta t) = \frac{1}{4\tau(e^{\frac{-T_{start}}{\tau}} - e^{\frac{-T_{end}}{\tau}})^2}(e^{\frac{2T_{start}+|\Delta t|}{\tau}} - e^{\frac{2T_{end}-|\Delta t|}{\tau}}) \tag{3.20}$$

As a sanity check, we can integrate $\mathcal{G}_{NVNV}(\Delta t)$ over the interval $[-(T_{end} - T_{start}), T_{end} - T_{start}]$, to get the overall probability to get a coincidence in our window:

$$\int_{-(T_{end}-T_{start})}^{T_{end}-T_{start}} \mathcal{G}_{NVNV}(\Delta t)\, d\Delta t \tag{3.21}$$

which, by separately integrating the for negative and positive Δt results in

$$\frac{1}{4\tau(e^{\frac{-T_{start}}{\tau}} - e^{\frac{-T_{end}}{\tau}})^2}\tau\left((e^{\frac{-T_{start}}{\tau}} - e^{\frac{-T_{end}}{\tau}})^2 + (e^{\frac{-T_{start}}{\tau}} - e^{\frac{-T_{end}}{\tau}})^2\right) = \frac{1}{2} \tag{3.22}$$

This is what we would expect for two completely distinguishable photons.

Following the same approach, we can calculate the integral for the NV-DC as

$$\mathcal{G}^{(2)}_{NVDC}(\Delta t) = \int_{T_{start}}^{T_{end}} \frac{1}{4}(P_{NV}(t'+\Delta t)P_{DC}(t') + P_{DC}(t'+\Delta t)P_{NV}(t'))\, dt' = \tag{3.23}$$

$$\frac{e^{\frac{-T_{start}}{\tau}} - e^{-\frac{T_{end}-|\Delta t|}{\tau}} + e^{-\frac{T_{start}+|\Delta t|}{\tau}} - e^{\frac{-T_{end}}{\tau}}}{4\tau(T_{end}-T_{start})(e^{\frac{-T_{start}}{\tau}} - e^{\frac{-T_{end}}{\tau}})} \tag{3.24}$$

For the DC-DC contribution we get

$$\mathcal{G}^{(2)}_{DCDC}(\Delta t) = \int_{T_{start}}^{T_{end}} \frac{1}{4}(P_{DC}(t'+\Delta t)P_{DC}(t') + P_{DC}(t'+\Delta t)P_{DC}(t'))\, dt' = \frac{(T_{end}-T_{start})-|\Delta t|}{2(T_{end}-T_{start})^2} \tag{3.25}$$

that both integrate to $\frac{1}{2}$ over the coincidence window.

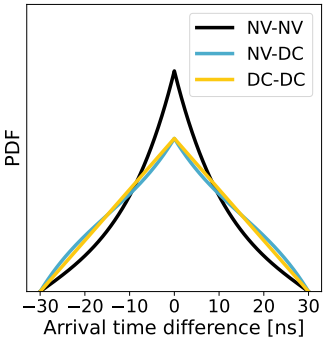

Figure 3.11: Temporal shape of the three contributions of our model explained in section 3.7.8 and 3.7.10.

Figure 3.11 shows the shapes of these cross-correlation functions for the different contributions of coincidences in the experiment. The difference between NV-DC and DC-DC contributions is minimal, but the NV-NV shape is clearly distinguishable from the noise sources. The plot in Fig. 3.4b in the main text is a weighted sum of the three shapes. The weights of for the different contributions are calculated using Eq. 3.3- 3.5 and the data shown in Fig. 3.10. For the numerical values of input parameters used see Tab. 3.6 For the indistinguishable case,

we use the same temporal shape as the distinguishable, and scale the amplitude with $1-\eta$. This is a valid approximation where polarization difference are the dominant contribution with respect to any temporal or spectral effects.

3.7.11. MONTE-CARLO BASED DERIVATION OF INDISTINGUISHABILITY USING BAYESIAN INFERENCE

As a next step we use our model to derive an expression for the indistinguishablity η. Due to the stochastic nature of the coincidences observed in our measurement, the calculation of the indistinguishability using standard error propagation like the variance formula can lead to non-physical results for the indistinguishability being in its confidence interval. We prevent this by using Bayesian Inference to find a more accurate confidence interval. In words, we want to know the most likely indistinguishability η_{opt}, given the set of measured coincidences C_M and C_E. Equations 3.8 and 3.10 and the number of attempts $N_{attempts}$ give us a direct way of calculating C_M and C_E, based on $p_{1(2)A(B)}$, $p_{DC_{A(B)}}$ (denoted $\bar{\theta}$ in short) and η as described in 3.7.8. The strategy is then to simulate many realizations of our experiment with η_i the only free parameter, via a Monte-Carlo simulation. We then use the outcomes of these simulations to calculate the likelihood of a certain η, given our measured C_M and C_E via Bayes rule:

$$P(\eta,\bar{\theta}|\bar{M}) = \frac{P(\bar{M}|\eta,\bar{\theta})P(\eta,\bar{\theta})}{P(\bar{M})} = \frac{P(\bar{M}|\bar{\theta},\eta)P(\eta,\bar{\theta})}{\sum_i P(\bar{M}|\bar{\theta},\eta_i)P(\eta_i,\bar{\theta})} \tag{3.26}$$

where $P(a|b)$ is the probability of a given b, $\bar{M}$ is the observed measurement outcomes C_M and C_E, and $\bar{\theta}$ the vector containing the parameters that fully describe our experiment. $P(\eta,\bar{\theta})$ is the probability of the set of parameters *before* our measurement, the so called prior. The only unknown parameter is η, for which we take a uniform distribution on the interval $[0,1]$, to reflect the assumption of no prior knowledge. All the other parameters θ_j in $\bar{\theta}$ are assumed to be normally distributed, with the mean and variance determined by the independent samples during the measurement, see previous section 3.7.4 and 3.10.

Algorithm 1 Monte-Carlo simulation routine to find likelyhood of η_i, based on the inputs $\bar{\theta}$ and $\bar{M}$

for η_i in $[0\ldots1]$ **do**
  for θ_j in $\bar{\theta}$ **do**
    Draw N times input parameters $\theta_{\mathbf{n}}$ from $\mathcal{N}(\mu_j, \sigma_j^2)$
    Calculate N values for P_E^n and P_M^n according to eq. S8 and S10
  end for
  for n in $[0, 1, \ldots, N]$ **do**
    Draw K realizations of the measurement outcomes
    $C_E^{Sim} = Poisson(P_E^n * N_{attempts})$ and $C_N^{Sim} = Poisson(P_M^n * N_{attempts})$
    Store C_E^{Sim} and C_M^{Sim} in array
  end for
  Calculate fraction $\frac{\sum[(C_E^{Sim}=C_E)\wedge(C_M^{Sim}=C_M)]}{N*K}$, which is equal to $P(\bar{M}|\eta,\bar{\theta})$
  Calculate likelyhood of η_i using eq. S23 and store the value.
end for

The algorithm to calculate the posterior distribution of η for a given set of $\bar{\theta}$ and $\bar{M}$ is given in algorithm 1. It captures both the uncertainty in the input parameters $\bar{\theta}$, as well as the statistical fluctuations introduced by the stochastic nature of measuring a rate of coincidences. In our case, the uniform chosen prior means that the normalized likelyhood function produced by the algorithm is directly the probability density function (pdf) for the left hand side of Eq. 3.26. The pdf's for the calculated indistinguishability of the data shown in Fig. 3.4a and b are shown in Fig. 3.12. Here we can clearly see the asymmetry of the calculated distributions, and their cut-off at the maximum of 1. To report this likelyhood as a single value with 'errorbars', we chose the maximum of the likelyhood to be our datapoint, and calculate a symmetric 68% confidence interval around the most likely η. For the datapoints where the most likely indistinguishibility is closest to 1, a symmetric confidence interval, with 34% of the probability on either side can not be taken, and asymmetric intervals are used.

3.7.12. SNSPD BLINDING INDUCED BACKGROUND

The current lay-out of the in-fibre optics guides the reflected part of the reference light through the same port of the circulator as the single-photons. Therefore the power is aimed directly at the nanowires of the SNSPDs, blinding the dectectors. Additionally, because of the beamsplitter in front of the detectors, the reference light reflected from both UNFs interferes, making the output power oscillate in time. To prevent latching, the manufacturer placed anti-latching shunt resistors in the circuits to prevent the loss of photon counting over timescales of >milliseconds.

However, during the early investigation of the time multiplexing of frequency stabilization with single photon generation, we noticed a blinding-power dependent elevated darkcount rate, persisting long (>10 µs after the end of the blinding pulse. By scanning the incident power on one of the nanowires in a controlled manner (Fig. 3.13, we can see a clear power dependence of this effect. We reduce the additional background counts to a constant manageable level of 30 Hz by moving our single photon generation by ≈45 µs,

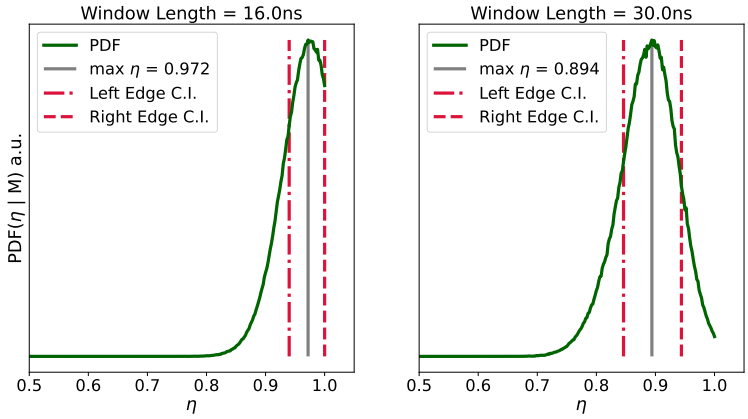

Figure 3.12: Probability density functions generated by the Monte-Carlo simulations, used for the calculation of the indistinguishability shown in the main text and figure3.4. A clear optimum is seen for both the distributions. The asymmetric confidence intervals are the result of the distribution being close to 1, as shown by the distribution for the left figure.

and optimizing the reference light power in-situ. Further improvement to the in-fibre optics that reduce the backpropagated power through the FBG and active attenuation shielding the detectors can be employed in the future to remove this background contribution.

3.7.13. UNF STABILITY

The UNFs are enclosed in an well-isolated box, with a heating pad and thermometer, temperature controlled by a Team Wavelength TC5. This controller provides ~0.1 mK control of the temperature setpoint. Due to non-homogeneous distribution of temperature inside the box and fluctuating temperature gradients coming from outside the box, with a fixed temperature setpoint we observe significant drift of the UNF frequency if not actively stabilized to a target frequency.

The UNFs are frequency stabilized by measuring the power incident on the detector (Thorlabs PDB482C-AC) that measures the frequency lock beat, extracted as a voltage from a monitoring port of the detector. We stabilize the temperature controller setpoint of the UNF to the relative half-of-maximum transmission point. We calibrate the maximally measured power through each individual UNF by temperature-sweeping them, effectively changing the position of the filters in frequency space. In this calibration, there is no correction for the noise incident on or coming from the detector. After calibration, we feedback the measured transmission power back to the temperature setpoint of the temperature controller of the UNF with a software implemented PI-control loop.

3.7.14. TRANSMISSION STABILITY

Due to inherent inaccuracies in the active stabilization described above, a spread of transmission powers of the UNFs with respect to their setpoint at the relative half-of-

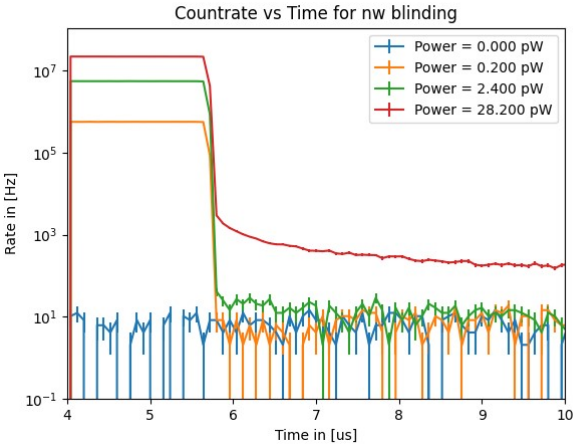

Figure 3.13: Rate of measured events after a bright blinding pulse in the superconducting nano-wire single photon detectors. After the bright pulse we measure an elevated background level as compared to no blinding pulse applied. This effect persists for tens of microseconds, forcing us to delay the single photon generation by more than 45 µs with respect to the frequency stabilization measurement. The optimal powers used during the experiment is not shown, and was optimized in-situ.

maximum transmission point is observed. This occurs due to the limitation in accuracy of the actual temperature control at the filter and other drifts of fixed in-fiber components in the path that passes through the UNF. Such a drift in frequency of the UNF maximum transmission point results in a reduction of NV photon transmission probability, however the NV conversion target frequency is unaffected. To determine the exact UNF frequency shift with respect to the setpoint, we start with the Cauchy-distribution fit in Fig. 3.2d of the transmission power T of the reference laser through the filter with respect to frequency f:

$$T(f) = \frac{I}{1+\left(\frac{(f-f_0)}{\gamma}\right)^2} + B, \tag{3.27}$$

where f_0 is the location of the filter, 2γ the filter FWHM and I and B a relative scaling factor and offset to background, respectively. We can relate the offset from the half-of-maximum transmission point to a frequency shift on this characteristic shape of the filter by rewriting the above function to be a function of transmission

$$f = f_0 - \gamma\sqrt{-1+\frac{I}{(T(I+B)-B)}}, \tag{3.28}$$

obtaining f by using the filter-specific fit parameters obtained from Eq. 3.27.

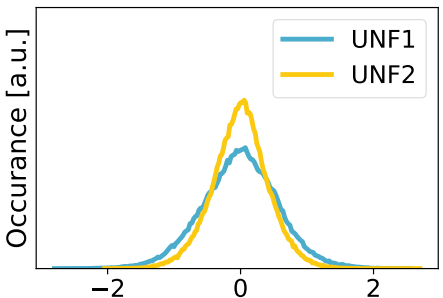

The root-minus solution is chosen according to the boundary condition that appropriately reflects the direction of

change in frequency for a change in transmission power. With Eq. 3.28 we can convert a representative stabilized 70 h set of second-interval transmission power data to a relative shift in frequency of the filter with respect to the the half-of-maximum transmission point, in the assumption that all transmission power drift is due to the shift in UNF frequency. The transmission power is not corrected for any other drifts of in-fiber components between the power-stabilized reference laser emission and detection at the beat detector. The residual frequency instability for both filters is shown in Fig. 3.14.

3.7.15. NV PHOTON TRANSMISSION

From this frequency instability we can calculate the change in average transmission probability of converted photons emitted from the NV center through the UNFs. The emitted NV photons with natural linewidth of $2\gamma_{\mathrm{NV}} \approx 12.7\,\mathrm{MHz}$ [27] have a frequency distribution as the Cauchy distribution

$$P(f) = \frac{1}{\pi\gamma_{\mathrm{NV}}\left(1+\left(\frac{(f-f_{NV})}{\gamma_{\mathrm{NV}}}\right)^2\right)}, \tag{3.29}$$

where f_{NV} is the frequency of our target wavelength (see Fig. 3.2). We can treat the UNFs as frequency dependent transmission devices, i.e. the Cauchy fit parameters used for Fig. 3.2D can be used to construct the *probability* of transmission $T_{\mathrm{p}}(f)$ of an incident photon by setting $I = 1, B = 0$ in Eq. 3.27, resulting in $T(f = f_0) = 1$. The probability of the NV photon transmitting through the UNF filter is then

$$P_{\mathrm{t}} = \int_{-\infty}^{\infty} P(f)\, T_{\mathrm{p}}(f)\, df. \tag{3.30}$$

Using the above equation we can calculate the relative change in transmission probability from each UNF's fitted parameters and all frequencies $f_0 \pm 1\,\mathrm{MHz}$, the interval where almost all of the occurrences of the measured filter shift are located. Using numerical methods to approximate the above integral we find that the total transmission of the NV photon is reduced to $\approx 75\%$(UNF1) and $\approx 77\%$ (UNF2) with the filters at the half-of-maximum transmission setpoint, excluding any losses incurred in the physical implementation. For the UNF stability data shown in Fig. 3.14 we obtain a transmission change of at most $\approx 1.5\%$(UNF1) and $\approx 0.4\%$ (UNF2) for $f_0 \pm 1\,\mathrm{MHz}$ that would solely be ascribable to the frequency shift of the UNFs.

Table 3.3: Frequency lock hardware

Equipment name	Part name/number
Balanced photodetector	Thorlabs PDB482C-AC
Mixer	MiniCircuits ZX05-1l+
Amplifier	Femto DHPVA-201
Bandpass filter	MiniCircuits SBP-100+
Downmix signal generator 325 MHz	AnaPico APSin6010
Beat reference generator 100 MHz	AnaPico APSin6010
Phase-Frequency-Detector	AnalogDevices HMC3716LP4E
Differential probe	Pintek DP-60HS
Track & Hold	Texas Instruments OPA1S2384
Integrator	NewFocus LB1005
ADC, DAC	Analog Discovery 2

Table 3.4: Timing Hardware

Equipment name	Part name/number
GPS-disciplined clock	Stanford Research Systems FS752
Frequency Distribution, between nodes (10MHz, PPS)	OPNT WRS-3/18 White Rabbit Switch
Frequency Distribution, local (10MHz)	Pulse Research Lab PRL-4110
Heartbeat Generator	Tektronix AFG 31022
Micro-controller	Jäger ADwin-Pro II T12
Arbitrary Waveform Generator (AWG)	Zürich Instruments HDAWG-8
Time Tagger	PicoQuant MultiHarp 150 4N

Table 3.5: Entry in filtered dataset

Field name	Field description	Field data-type
trigger index	Experiment Marker index preceding event in midpoint	uint64
node1 trigger timestamp	Absolute timestamp of corresponding Experiment marker on node1	uint64
node2 trigger timestamp	Absolute timestamp of corresponding Experiment marker on node2	uint64
detection bin index	Index of detection bin this event is detected in	uint32
detA counts	Number of counts measured by nanowire A for this event	uint16
detB counts	Number of counts measured by nanowire B for this event	uint16
detA relative timestamp	Timestamp w.r.t. the start of detection bin of first count measured in nanowire A	int32
detB relative timestamp	Timestamp w.r.t. the start of detection bin of first count measured in nanowire B	int32

Table 3.6: Numerical values of inputs to calculation and simulations

Wind. L. [ns]	p_1 [10^{-5}]	p_2 [10^{-5}]	p_{DC_A} [10^{-6}]	p_{DC_B} [10^{-6}]	C_M	C_{dist}
6	2.1 ± 0.4	1.4 ± 0.4	0.84 ± 0.1	0.84 ± 0.1	13 ± 4	92.37 ± 0.32
8	2.7 ± 0.4	1.8 ± 0.4	1.12 ± 0.15	1.12 ± 0.13	19 ± 4	154.7 ± 0.4
10	3.2 ± 0.4	2.1 ± 0.4	1.40 ± 0.19	1.40 ± 0.17	30 ± 5	221.7 ± 0.5
12	3.7 ± 0.4	2.4 ± 0.4	1.67 ± 0.22	1.68 ± 0.20	37 ± 6	297.9 ± 0.6
14	4.1 ± 0.4	2.7 ± 0.4	1.95 ± 0.26	1.96 ± 0.23	44 ± 7	367.6 ± 0.6
16	4.4 ± 0.4	2.9 ± 0.4	2.23 ± 0.30	2.24 ± 0.27	53 ± 7	436.9 ± 0.7
18	4.7 ± 0.4	3.1 ± 0.4	2.51 ± 0.34	2.52 ± 0.30	74 ± 9	496.5 ± 0.7
20	5.0 ± 0.4	3.2 ± 0.4	2.8 ± 0.4	2.79 ± 0.33	93 ± 10	558.9 ± 0.8
22	5.2 ± 0.4	3.4 ± 0.4	3.1 ± 0.4	3.1 ± 0.4	103 ± 10	611.1 ± 0.8
24	5.4 ± 0.4	3.5 ± 0.4	3.3 ± 0.4	3.4 ± 0.4	118 ± 11	662.9 ± 0.9
26	5.5 ± 0.4	3.6 ± 0.4	3.6 ± 0.5	3.6 ± 0.4	133 ± 12	708.5 ± 0.9
28	5.7 ± 0.4	3.7 ± 0.4	3.9 ± 0.5	3.9 ± 0.5	148 ± 12	749.5 ± 0.9
30	5.8 ± 0.4	3.7 ± 0.4	4.2 ± 0.6	4.2 ± 0.5	159 ± 13	785.7 ± 0.9

REFERENCES

[1] A. J. Stolk *et al.*, *Telecom-Band Quantum Interference of Frequency-Converted Photons from Remote Detuned NV Centers,* PRX Quantum **3**, 020359 (2022).

[2] H. J. Kimble, *The quantum internet,* Nature **453**, 1023 (2008), number: 7198 Publisher: Nature Publishing Group.

[3] S. Wehner, D. Elkouss and R. Hanson, *Quantum internet: A vision for the road ahead,* Science **362** (2018), 10.1126/science.aam9288, publisher: American Association for the Advancement of Science Section: Review.

[4] A. Ekert and R. Renner, *The ultimate physical limits of privacy,* Nature **507**, 443 (2014), number: 7493 Publisher: Nature Publishing Group.

[5] L. Jiang, J. M. Taylor, A. S. Sørensen and M. D. Lukin, *Distributed quantum computation based on small quantum registers,* Physical Review A **76**, 062323 (2007), publisher: American Physical Society.

[6] D. Gottesman, T. Jennewein and S. Croke, *Longer-Baseline Telescopes Using Quantum Repeaters,* Physical Review Letters **109**, 070503 (2012), publisher: American Physical Society.

[7] D. L. Moehring *et al.*, *Entanglement of single-atom quantum bits at a distance,* Nature **449**, 68 (2007), number: 7158 Publisher: Nature Publishing Group.

[8] S. Ritter *et al.*, *An elementary quantum network of single atoms in optical cavities,* Nature **484**, 195 (2012), number: 7393 Publisher: Nature Publishing Group.

[9] J. Hofmann *et al.*, *Heralded Entanglement Between Widely Separated Atoms,* Science **337**, 72 (2012), publisher: American Association for the Advancement of Science Section: Report.

[10] L. Stephenson *et al.*, *High-Rate, High-Fidelity Entanglement of Qubits Across an Elementary Quantum Network,* Physical Review Letters **124**, 110501 (2020), publisher: American Physical Society.

[11] H. Bernien *et al.*, *Heralded entanglement between solid-state qubits separated by three metres,* Nature **497**, 86 (2013), number: 7447 Publisher: Nature Publishing Group.

[12] P. C. Humphreys *et al.*, *Deterministic delivery of remote entanglement on a quantum network,* Nature **558**, 268 (2018), number: 7709 Publisher: Nature Publishing Group.

[13] A. Delteil *et al.*, *Generation of heralded entanglement between distant hole spins,* Nature Physics **12**, 218 (2016), number: 3 Publisher: Nature Publishing Group.

[14] R. Stockill *et al.*, *Phase-Tuned Entangled State Generation between Distant Spin Qubits,* Physical Review Letters **119**, 010503 (2017), publisher: American Physical Society.

[15] I. Usmani *et al.*, *Heralded quantum entanglement between two crystals,* Nature Photonics **6**, 234 (2012).

[16] M. l. G. Puigibert *et al.*, *Entanglement and nonlocality between disparate solid-state quantum memories mediated by photons,* Phys. Rev. Research **2**, 013039 (2020).

[17] D. Lago-Rivera, S. Grandi, J. V. Rakonjac, A. Seri and H. de Riedmatten, *Telecom-heralded entanglement between multimode solid-state quantum memories,* Nature **594**, 37 (2021).

[18] C. W. Chou *et al.*, *Measurement-induced entanglement for excitation stored in remote atomic ensembles,* Nature **438**, 828 (2005).

[19] Y. Yu *et al.*, *Entanglement of two quantum memories via fibres over dozens of kilometres,* Nature **578**, 240 (2020).

[20] R. Riedinger *et al.*, *Non-classical correlations between single photons and phonons from a mechanical oscillator,* Nature **530**, 313 (2016).

[21] D. Hucul *et al.*, *Modular entanglement of atomic qubits using photons and phonons,* Nature Physics **11**, 37 (2015).

[22] V. Krutyanskiy *et al.*, *Light-matter entanglement over 50 km of optical fibre,* npj Quantum Information **5**, 72 (2019).

[23] S. Daiss *et al.*, *A quantum-logic gate between distant quantum-network modules,* Science **371**, 614–617 (2021).

[24] M. Pompili *et al.*, *Realization of a multinode quantum network of remote solid-state qubits,* Science **372**, 259–264 (2021).

[25] T. van Leent *et al.*, *Entangling single atoms over 33 km telecom fibre,* (2022).

[26] C. K. Hong, Z. Y. Ou and L. Mandel, *Measurement of subpicosecond time intervals between two photons by interference,* Phys. Rev. Lett. **59**, 2044 (1987).

[27] M. L. Goldman *et al.*, *State-selective intersystem crossing in nitrogen-vacancy centers,* Phys. Rev. B **91**, 165201 (2015).

[28] N. Kalb, P. C. Humphreys, J. J. Slim and R. Hanson, *Dephasing mechanisms of diamond-based nuclear-spin memories for quantum networks,* Phys. Rev. A **97**, 062330 (2018).

[29] A. Tchebotareva *et al.*, *Entanglement between a diamond spin qubit and a photonic time-bin qubit at telecom wavelength,* Phys. Rev. Lett. **123**, 063601 (2019).

[30] J. Pelc, C. Langrock, Q. Zhang and M. Fejer, *Influence of domain disorder on parametric noise in quasi-phase-matched quantum frequency converters,* Optics letters **35**, 2804 (2010).

[31] M. Ruf *et al., Optically coherent nitrogen-vacancy centers in micrometer-thin etched diamond membranes,* Nano Letters **19**, 3987 (2019).

[32] S. Meesala *et al., Strain engineering of the silicon-vacancy center in diamond,* Phys. Rev. B **97**, 205444 (2018).

[33] A. Sipahigil *et al., An integrated diamond nanophotonics platform for quantum-optical networks,* Science **354**, 847 (2016), https://www.science.org/doi/pdf/10.1126/science.aah6875 .

[34] S. Sun *et al., Cavity-enhanced raman emission from a single color center in a solid,* Phys. Rev. Lett. **121**, 083601 (2018).

[35] J. H. Weber *et al., Two-photon interference in the telecom c-band after frequency conversion of photons from remote quantum emitters,* Nature Nanotechnology **14**, 23 (2019).

[36] X. You *et al., Quantum interference between independent solid-state single-photon sources separated by 300 km fiber,* (2021), arXiv:2106.15545 [quant-ph], arXiv:2106.15545 [quant-ph] .

[37] C. E. Bradley *et al., A ten-qubit solid-state spin register with quantum memory up to one minute,* Phys. Rev. X **9**, 031045 (2019).

[38] E. F. Dierikx *et al., White rabbit precision time protocol on long-distance fiber links,* IEEE Transactions on Ultrasonics, Ferroelectrics, and Frequency Control **63**, 945 (2016).

[39] L. Robledo *et al., High-fidelity projective read-out of a solid-state spin quantum register,* Nature **477**, 574 (2011).

[40] H. Paul, *Interference between independent photons,* Rev. Mod. Phys. **58**, 209 (1986).

[41] F. Bouchard *et al., Two-photon interference: the hong–ou–mandel effect,* Reports on Progress in Physics **84**, 012402 (2021).

[42] T. Legero, T. Wilk, A. Kuhn and G. Rempe, *Time-resolved two-photon quantum interference,* Applied Physics B **77**, 797 (2003).

[43] B. Kambs and C. Becher, *Limitations on the indistinguishability of photons from remote solid state sources,* New Journal of Physics **20**, 115003 (2018).

[44] J. F. Geus *et al., Frequency down-conversion for efficient, low-noise quantum frequency converters,* in *Quantum Computing, Communication, and Simulation II*, Vol. 12015, edited by P. R. Hemmer and A. L. Migdall, International Society for Optics and Photonics (SPIE, 2022) pp. 24 – 29.

[45] D. Riedel *et al., Deterministic enhancement of coherent photon generation from a nitrogen-vacancy center in ultrapure diamond,* Phys. Rev. X **7**, 031040 (2017).

[46] M. Ruf, M. Weaver, S. van Dam and R. Hanson, *Resonant excitation and purcell enhancement of coherent nitrogen-vacancy centers coupled to a fabry-perot microcavity,* Phys. Rev. Applied **15**, 024049 (2021).

[47] R. Hanson, N. Kalb, P. Humphreys and E. van Zwet, *Photon exchange based quantum network and method of operating such a network,* (2020), h04B.

4

QUBIT TELEPORTATION BETWEEN A MEMORY-COMPATIBLE PHOTONIC TIME-BIN QUBIT AND A SOLID-STATE QUANTUM NETWORK NODE

In Hilbert space no one can hear you scream

Person on X (formerly known as Twitter)

M. Iuliano*, M.-C. Slater*, A. J. Stolk, M. J. Weaver, T. Chakraborty, E. Loukiantchenko, G. C. do Amaral, N. Alfasi, M. O. Sholkina, W. Tittel, R. Hanson

We report on a quantum interface linking a diamond NV center quantum network node and 795 nm *photonic time-bin qubits compatible with Thulium and Rubidium quantum memories. The interface makes use of two-stage low-noise quantum frequency conversion and waveform shaping to match temporal and spectral photon profiles. Two-photon quantum interference shows high indistinguishability between converted* 795 nm *photons and the native NV center photons. We use the interface to demonstrate quantum teleportation including real-time feedforward from an unbiased set of* 795 nm *photonic qubit input states to the NV center spin qubit, achieving a teleportation fidelity well above the classical bound. This proof-of-concept experiment shows the feasibility of interconnecting different quantum network hardware.*

The results of this chapter are accepted for publication in npj Quantum Information.

* Equally contributing authors.

4.1. INTRODUCTION

The future quantum internet will leverage the principles of quantum mechanics for ultra-secure communication, enhanced sensing, and distributed quantum computing [1, 2]. Progress in the past decade has led to pioneering experiments on different components of such a network [3–7]. For instance, entanglement generation between separated quantum memory systems based on atomic ensembles has recently been reported [8, 9] and the first multi-node network of rudimentary quantum processors has been realized inside the lab [10, 11]. As different hardware platforms may be optimized for different network tasks, realizing interfaces that enable quantum information transfer between heterogeneous devices is a key challenge.

Here, we report on a proof-of-concept demonstration of a quantum interface between a diamond NV center qubit [12, 13] and photonic time-bin qubits at 795 nm that are compatible with Thulium-based solid-state memories [14–16] and Rubidium-based atomic gas memories [17–20]. Such an interface conceptually corresponds to future quantum Internet scenarios such as connecting remote qubit processors via a repeater chain [21] or realizing remote state preparation on a quantum computing server from a photonic client [22]. We validate the quantum nature of the interface by performing quantum teleportation [23, 24] of 795 nm time-bin qubits into the NV center spin qubit with state fidelity beating the classical bound.

4.1.1. A QUANTUM INTERFACE BETWEEN HETEROGENEOUS DEVICES

A major challenge for linking heterogeneous quantum network hardware is the matching of their corresponding photonic qubits. Many leading hardware platforms for quantum memories and quantum network nodes are based on atom-like systems [25, 26]. The properties of the photonic interface of these platforms, such as temporal profile and wavelength of emitted photons, are therefore largely determined by the atomic properties and vary significantly among the different platforms. Our approach to bridging these differences is depicted in the schematic of our interface in Fig.4.1.

The interface converts the input 795 nm photonic time-bin qubit to match the properties of the NV center photon. In parallel, entanglement is generated between the spin state of the NV center and the temporal mode of a single emitted photon. Then, the converted 795 nm photon and the NV photon are interfered on a beam-splitter. Subsequent detection of the photons in different time bins constitutes a Bell state measurement that teleports the original 795 nm time-bin qubit state to the NV spin qubit. Real-time feedforward of the Bell-state measurement outcome and application of the corresponding correction gate on the NV spin qubit completes the action of the interface.

For this interface to function with high fidelity, it is crucial that the converted 795 nm photons are indistinguishable from the NV center photons. In particular, the 795 nm photons need to match the NV photons' 637 nm wavelength, polarization and exponential temporal profile set by NV's 12 ns optical lifetime. In this proof-of-concept work, we create photonic time-bin qubits at 795 nm from weak coherent states by using an intensity modulator and a phase modulator. We calibrate the intensity modulator to mimic the NV photon's temporal profile within a 30ns time window. The photonic states obtained through this method are compatible with the storage and retrieval

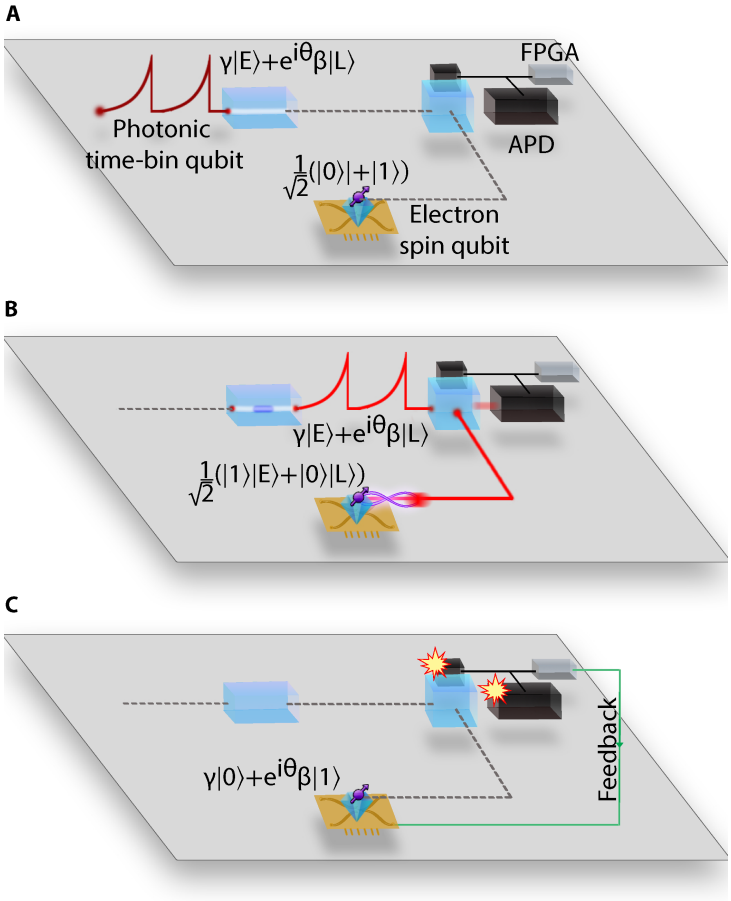

Figure 4.1: **Overview of the quantum interface between** 795 nm **photonic time-bin qubits and an NV center processing node.** The interface consists of a low-noise two-step frequency conversion module including a frequency stabilization module, an interference station containing a balanced beam splitter with output ports connected to avalanche photodiodes (APDs), and an FPGA for real-time feedback. The interface can be visualized in three steps: a) a 795 nm time-bin qubit with a temporal shape matching the spontaneous emission profile of the NV center is sent to the input of the interface. The NV spin qubit is prepared in a balanced superposition state. b) The 795 nm photonic qubit is converted to 637 nm, while the NV center generates a 637 nm photonic time-bin qubit entangled with the spin qubit. The generation of the 795 nm photonic qubit is timed to ensure maximum overlap at the beam splitter with the NV center photonic qubit. (c) Upon detecting one photon in each time bin, feedback of the correct phase flip to the NV spin qubit of the NV completes the state teleportation. For the experiments reported in this paper, we employed the NV qubit setup, called “Alice", described in Refs. [10, 11], that includes a micro-controller unit (MCU) and a fast waveform generator (AWG).

from Thulium-doped solid-state quantum memories [27] as well as Rubidium-gas-based quantum memories [28, 29]. These platforms are capable of multiplexing by storage and retrieval of multiple photonic modes in different degrees of freedom [26, 30], and therefore have attracted interest for quantum repeater applications [31].

To achieve wavelength indistinguishability, we employ a low-noise two-stage quantum frequency conversion process [32], depicted in Fig.4.2a. In the first step, the 795 nm shaped weak-coherent state is overlapped with a 1064 nm pump laser and coupled into a temperature-stabilized periodically-poled Lithium Niobate (ppLN) waveguide crystal, generating 455 nm light via a sum-frequency conversion process with conversion efficiency of 32% (Fig.4.2b), measured free-space to free-space between the output of the input fiber and before the coupling into the output fiber. Subsequently, the 455 nm light is down-converted to 637 nm using a 1596 nm pump laser, with conversion efficiency of 22%. At the output of each ppLN crystal we include dichroic mirrors and filters to remove residual unconverted light and pump light. The overall process efficiency including in- and outcoupling from fibers and filtering is 3%, which is sufficient for the current proof-of-concept but should be further improved in future designs. Importantly, having both pump lasers red-detuned from the signal photons results in a negligible amount of added noise in the conversion stages, obtaining a signal-to-noise ratio≥1250, when only the conversion setup is considered. To ensure that the converted light precisely matches the NV photon frequency, despite unavoidable component drifts, the frequency of converted 795 nm light is locked to the NV excitation laser light. To this end, an identical two-stage conversion setup is employed with 1 mW at the input derived from the same 795 nm source (Fig. 4.2a). Details on the frequency locking procedure and the employed electronics are discussed in the Supplementary Information. The resulting spread of the beat signal is 75 kHz, pushing the corresponding contribution to teleportation infidelity well below 1% (see below).

4.2. RESULTS

4.2.1. TWO-PHOTON QUANTUM INTERFERENCE BETWEEN CONVERTED 795 nm PHOTONS AND NV CENTER PHOTONS

To investigate the degree of indistinguishability of the NV photons and the converted 795 nm photons, we perform a two-photon quantum interference (TPQI) experiment, also known as Hong-Ou-Mandel interference. Perfectly indistinguishable photons interfering on a balanced beam-splitter show bosonic coalescence leading to zero probability of detecting photons in both output ports of the beam-splitter [33]. In such an experiment, on one side we employ the NV center in its negatively charged state NV^-. The ground state of NV^- is a spin-1 system whose spin sublevels are split by the zero-field splitting and the applied magnetic field of 25.3 mT [12]. We employ the m_S= 0 (-1) spin state as the $|0\rangle$ ($|1\rangle$) qubit state. The NV optical transitions are spin-dependent, allowing for spin-selective optical excitation and photon emission. In the current work, we use the cycling transition $|0\rangle \rightarrow |g\rangle$, where $|g\rangle$ represent the $|E_x\rangle$ excited state. In the TPQI experiment, the NV center can be modeled as a single-photon source parametrized by the probability of a photon detection per optical excitation p_{NV} (counts per shot).

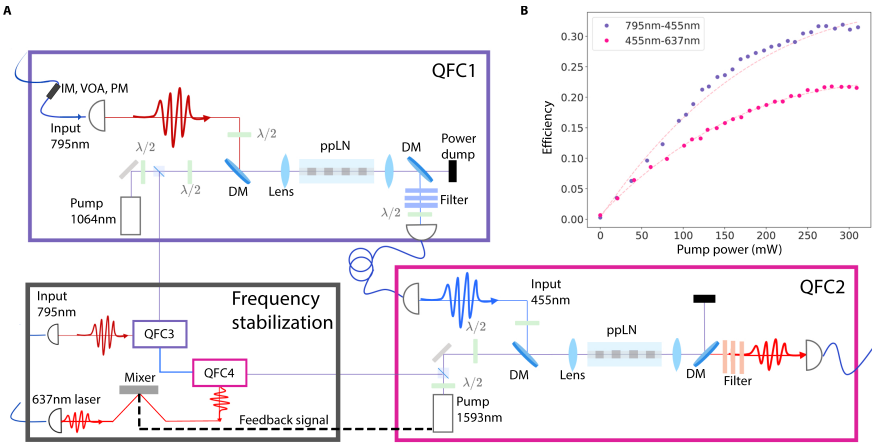

Figure 4.2: **Quantum frequency conversion setup.** a) Overview of the frequency conversion setup. To generate converted weak-coherent states at 637 nm, the input light at 795 nm undergoes two-step frequency conversion (QFC1 and QFC2), after passing through an intensity modulator (IM) to obtain the typical decay time-shape of the NV spontaneous emission, a variable optical attenuator (VOA) to manipulate the mean photon number, and a phase modulator (PM) for imprinting a phase on the time-bin qubits (only for quantum teleportation experiments). At the output of each conversion step, a dichroic mirror (DM) and a set of filters suppress residual unconverted light and pump light. A copy of the two-step frequency conversion setup (QFC3 and QFC4) is used for frequency stabilization. A higher power tap-off from the 795 nm laser is converted and the resulting 637 nm light is mixed with the light coming from the excitation laser of the NV. An error signal is computed and fed back to the frequency modulator of the 1593nm pump laser to match the converted light to the excitation wavelength of the NV. b) Measured efficiency for each step of the conversion while sweeping the power of the corresponding pump laser. The dashed lines represent the respective fit of the data points to a saturation curve, to extrapolate the optimal pump power. The relative error on each data point is 1%.

On the other side, the 795 nm photonic states constitute a multi-photon source, featuring Poissonian photon statistics. Up to the second order, the emission can be approximated through the mean-photon number $|\alpha|^2$ as $|\alpha|^2 + 1/2|\alpha|^4$ [34]. The consequences of having two photonic sources with different statistics are discussed in detail in Sec. 4.5.

In Fig.4.3a, the experimental sequence for the TPQI experiment is depicted. In the first step, a Charge-Resonance (CR) check is performed [35], which ensures that the NV center is in the correct charge state (namely, NV^-) and the lasers are on resonance with the relevant NV transitions. When the CR check threshold is satisfied, the actual TPQI experiment is triggered. Two trains of 10 optical π-pulses each, which we define as 10 different bins, are sent to the NV, which leads to 20 possible emission windows (10 per train). Each train is preceded by an optical spin-reset pulse that prepares the NV in the $|0\rangle$ state. In parallel, two trains of 10 decay-shaped pulses each are sent from the 795 nm laser. The mean-photon number can be manipuleted via a variable optical attenuator (VOA). As illustrated in Fig.4.3a, the first train of pulses constitutes the indistinguishable sequence, with the two photonic states overlapping in time on the beam splitter. The second train is the distinguishable sequence: each 795 nm photonic state is delayed by 50ns with respect to the corresponding NV photon, rendering the photons fully distinguishable. The sequence of two trains is repeated 100 times before returning to the CR

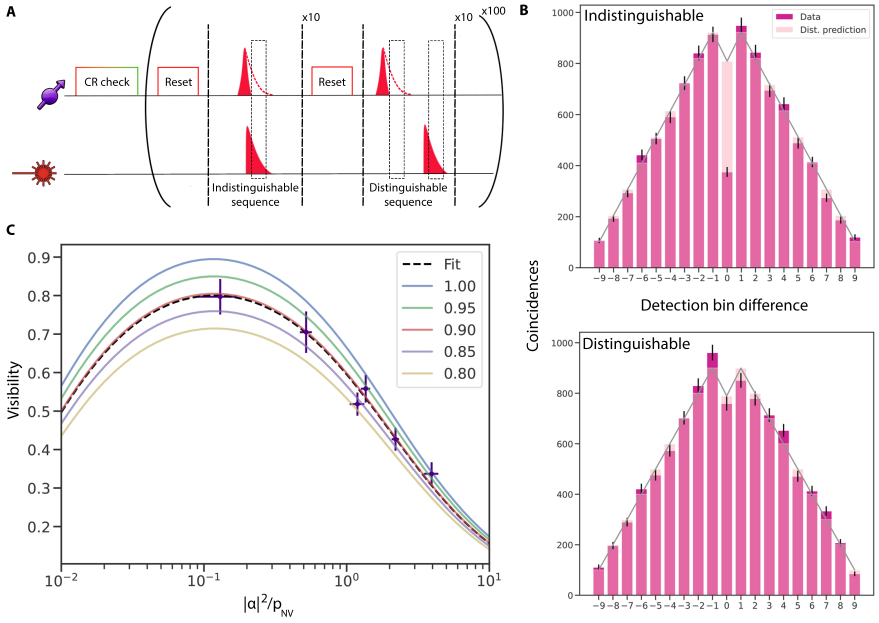

Figure 4.3: **Two-photon quantum interference.** a) Experimental sequence for the two-photon quantum interference experiment. The top line refers to the NV, while the bottom refers to the 795 nm weak-coherent state. b) Histograms of the coincident clicks in the two sequences (magenta) for the ratio $x = |\alpha|^2/p_{NV}$ of 1.19±0.14. Each bar of the histograms represents coincident clicks in the two detectors within 30ns windows for all the possible combinations of a given time bin difference. As a reference, we also include, in both histograms, the expected coincidences in the case of perfectly distinguishable photons (in pink). In both diagrams, the grey line connects the expected values of the distinguishable prediction. In the distinguishable case, we consider two pulse windows: one around the NV photons and one around the converted 795 nm photonic states. Therefore, the histogram contains the contribution of coincident clicks for three possible cases: coincident clicks in the NV window, in the converted 795 nm window and in the combined windows. c) Extracted visibility for different values of x. The values are fitted according to the visibility model included in Sec. 4.5. The dashed line represents the fit result, corresponding to indistinguishability of 0.895±0.019, while the colored lines represent our model of the visibility for different values of indistinguishability.

check. The next CR check validates both the previous TPQI sequence and, in case the threshold is satisfied, directly triggers the next sequence. In case the validation round of CR check fails, the experiment iteration is discarded in the analysis, while the CR check is repeated until success to trigger the next experiment iteration. The emitted photons from both sides impinge on a 50:50 in-fiber beam splitter, whose output ports are connected to two single-photon detectors. A timetagger registers the detection times of the photons in the two output ports, enabling the reconstruction of the histograms in Fig. 4.3b. Each bin of the histogram counts the number of coincident clicks

From the histograms in Fig.4.3b we extract the visibility V=1-$\frac{p_{ind}}{p_{dist}}$, where p_{ind} (p_{dist}) is the probability of a coincidence detection if the photons are indistinguishable (distinguishable) in the 0-bin difference. Taking into account that the photonic states follow different statistics and introducing the indistinguishability η, the visibility can be ex-

pressed as

$$V = \frac{\eta x}{\frac{1}{2}g^{(2)}(0) + \frac{1}{2}x^2 + x + \frac{2p_{noise}(1+x)}{p_{NV}} + \frac{2p_{noise}^2}{p_{NV}^2}} \tag{4.1}$$

(see 4.6.1 for the derivation), where x is the ratio $|\alpha|^2/p_{NV}$ and p_{noise} is the probability of a background (noise) click per 30 ns window in one detector.

By performing this TPQI experiment and extracting the visibility for 6 different values of x, we can reconstruct the visibility function as shown in Fig.4.3c. We also plot the expected visibility function, using the independently measured values for the NV $g^{(2)}$ of 0.011±0.004 and p_{NV} of (5.76±0.20)e^{-4}, for several values of η. The value of p_{noise} is discussed in Sec. 4.5. We observe that the data follows the model closely over the full range. From a fit to the data we obtain the indistinguishability η=(0.895±0.019), showing that we have matched all the relevant degrees of freedom of the two photonic states to a high level. The limited indistinguishability can be due to a residual mismatch between the temporal profile of the NV photons and the 795 nm photons, as well as an imperfect coherence of the NV photons, that from previous NV-NV TPQI experiments showed limited indistinguishability of 0.9 [10].

4.2.2. QUBIT TELEPORTATION FROM A 795 nm PHOTONIC TIME-BIN QUBIT TO THE NV CENTER SPIN QUBIT

Having established the high indistinguishability of the photonic states involved, we exploit the interface to perform quantum teleportation of 795 nm time-bin qubits to the NV electron spin qubit, as illustrated in the diagram in Fig.4.4a. Real-time feed-forward is included to complete the teleportation, enabling the correction of phase-flipped outcomes in the Bell-state measurement and delivery of the teleported state “alive".

The 795 nm time-bin qubit is constituted by an early and late weak-coherent state separated by 300 ns and generated in the same way as in the TPQI experiment. Additionally, we include a phase modulator (PM) to manipulate the phase difference between the early and late temporal modes. The resulting qubit state is therefore in the general form of$\gamma|E\rangle + e^{i\theta}\beta|L\rangle)$ with $|E\rangle$ ($|L\rangle$) denoting the early (late) time bin. For this experiment, we prepare time-bin qubits in an unbiased set of states (the cardinal states) that we indicate as: $|Z\rangle$, $|-Z\rangle$, $|X\rangle$, $|-X\rangle$, $|Y\rangle$, $|-Y\rangle$, referring to their position on the Bloch sphere.

On the NV's side, the electron spin qubit is optically initialized in $|0\rangle$. A microwave $\pi/2$ rotation along $\hat{x}$ axis of the Bloch sphere brings the qubit into a balanced superposition state. An optical π-pulse excites the NV's population in $|0\rangle$, enabling the spontaneous emission of a photon in the early time bin. Subsequently, the electron spin goes through a microwave π rotation along $\hat{y}$ axis, and another optical π- pulse enables the NV to spontaneously emit the late time-bin photon. The resulting NV-photon entangled state is $1/\sqrt{2}(|1\rangle|E\rangle \pm |0\rangle|L\rangle)$. Throughout the teleportation experiment we keep the ratio $|\alpha|^2/p_{NV}$ constant at 1.20±0.24 by regular recalibration.

The converted 795 nm photonic state and the NV photon interfere on the balanced beam splitter, erasing the which-path information. Successful teleportation is heralded by the detection of a photon in each of the two time-bins. We can discriminate between the Bell states $|\Psi^+\rangle$ and $|\Psi^-\rangle$ by the double-click pattern: two clicks on the same detec-

tor for $|\Psi^+\rangle$ and two clicks on two different detectors for $|\Psi^-\rangle$. The valid detector clicks are detected by an FPGA in a 50ns window around the corresponding photons' time of arrival. In data analysis, we further shorten the valid teleportation time window to 20ns for an improved signal-to-noise ratio. The teleportation sequence is repeated for a maximum of 50 times before going back to the CR check.

When the FPGA detects a valid click pattern, it sends a two-bit message to the AWG. The AWG jumps out from the teleportation attempt sequence (Fig.4.4a) and starts the feedback and tomography sequence for the electron spin state. This sequence is composed of an XY4 dynamical decoupling sequence [36] followed by a basis selection pulse for the tomography. The latter is selected in real-time, taking the detector click pattern into account by applying a phase-flip correction when necessary. Finally, a single-shot readout of the NV spin qubit is performed. Throughout the measurement, a set of automated measurement and calibration routines detect anomalies in the converted frequency and in the reset frequency, declaring those datasets as failed when the required parameters are not met (more details in Sec. 4.5). In Fig. 4.4b, the results for the telepor-

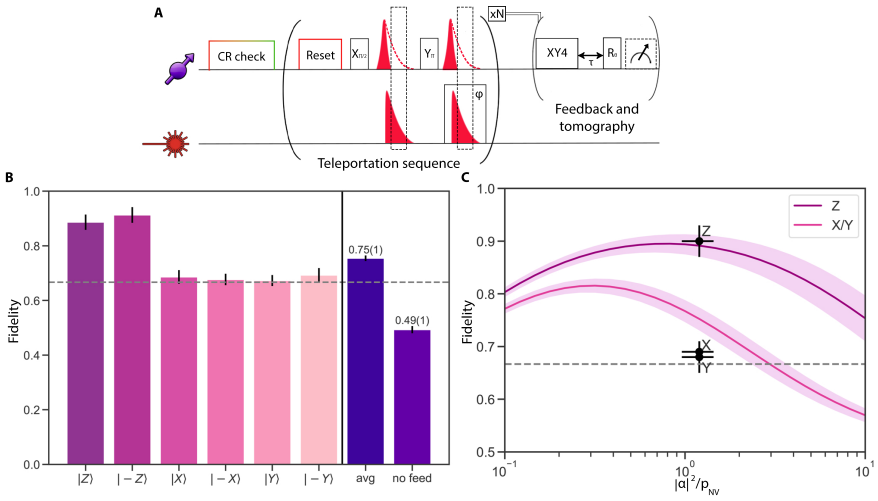

Figure 4.4: **Quantum teleportation of a time-bin qubit into the electron spin of the NV center.** a) Experimental sequence. After passing the CR check, the AWG plays the teleportation sequence as described in the main text. Such a sequence is played N times. The timeout for the teleportation sequence is set to 50 repetitions, after which the NV center goes back to CR check. If a valid click pattern is detected by the FPGA in the Bell-state measurement, the AWG jumps out from the teleportation sequence and starts the feedback and tomography sequence. This sequence contains an XY4 set of pulses, where the first pulse is played after a time τ with respect to the $\pi/2$ rotation pulse in the teleportation sequence. The value τ is a multiple of the Larmor period of the electron spin, optimized taking into account the effects of the spin bath. After the XY4 sequence, the base selection pulse is played taking into account the input state and the Bell-state measurement outcome. Finally, the tomography single-shot readout of the NV electron spin is performed at the MCU level. b) Histogram showing the individual fidelities per each cardinal state, as well as the average and the resulting fidelity when no feedback operations are applied to the NV electron spin qubit. The results are corrected for tomography errors, but not for preparation errors. c) Simulation curves based on the model described in Sec. 4.5. The data points in black represent the average fidelity for the states along the three axes of the Bloch sphere. The dashed line indicates the corrected classical bound.

tation of the six cardinal states are reported together with the average state fidelity. The average fidelity is obtained as F_{avg}=1/3$\bar{Z}$+1/3$\bar{X}$+1/3$\bar{Y}$, where $\bar{Z}$, $\bar{X}$, $\bar{Y}$ represent the average fidelity along the respective axis. The resulting fidelity of (75.5 ± 1.0)%. is well above the classical bound, which is set taking into account the use of a multi-photon source (see SI). Additionally, we also calculate the average fidelity for the equatorial states in the absence of feed-forward. In this case, the fidelity is consistent with a fully mixed state, confirming the critical role of feedback in the teleportation protocol. In the measured fidelities, we also filter based on the CR check's validation.

In Fig.4.4c we report the comparison between the measured fidelities and the predicted values of our model as a function of the ratio $|\alpha|^2/\mathrm{p}_{NV}$. The model includes the effect from leakage of the intensity modulator, resulting in a preparation error for the Z states of around 4%. More details on the simulated curves are included in Sec. 4.5. The small discrepancy between the X and Y data points and the simulation may be due to errors not captured by the model. On one side, the model does not consider imperfections in the microwave pulses that implement the NV quantum gates, which we estimate to cause an accumulated error below 1.5%. On the time-bin qubit side, our model does not take into account phase errors due to imperfections in the fast phase modulation, which affect the preparation of the X and Y states but not Z. Correcting for the input photonic qubit preparation errors yields a best estimate for the teleportation fidelity of (78.3 ± 0.9)%.

4.3. DISCUSSION

We have benchmarked a photonic interface between 795 nm converted time-bin qubits and an NV center-based quantum processor. The time-bin qubits are compatible with Thulium-doped crystals employed for quantum memories as well as Rubidium gas quantum memories. The interface exhibits a high photon indistinguishability, thanks to a low-noise two-step quantum frequency conversion setup, that leads to beating the classical bound for the quantum teleportation protocol, together with the capabilities of the NV center as quantum processor, which shows long coherence time and a reliable optical interface. Additionally, the implementation of control scripts made the setup to be operable at distance and for long periods. Our results demonstrate the realization of interfaces between heterogeneous platforms that constitute the building-blocks of the future Quantum Internet. The interface presented in this work is versatile, as the methods and results presented can be transferred to platforms with similar functionalities. Hence, further improvements can be targeted at several aspects, like application field, experimental rate and bandwidth matching. Some examples might include the use of actual quantum memories that can be synchronized with the photon emission from the NV center, along with the integration of NV centers into optical cavities [37] for higher photon rate. Another possibility is the use of different color center defects in diamonds, like the group-IV, that promise higher photon emission rates and the possibility of integration into nanophotonic structures [38–41]. Other promising quantum processor platforms might include defect centers in SiC [42], Si [43] and optical quantum dots [44, 45]. Additionally, higher efficiency frequency conversion setups to telecom wavelengths [46, 47] can be employed to convert the photons emitted from both parties,

leading towards the real-case scenario of quantum networks over long distances.

4.4. METHODS

4.4.1. FIDELITY CALCULATION

The fidelity for each teleported state is calculated as $F = (1 + \frac{R_{\langle i|i\rangle} - R_{\langle j|i\rangle}}{R_{\langle i|i\rangle} + R_{\langle j|i\rangle}})/2$, given that we prepared the time-bin qubit in the state $|i\rangle$ and we measure in the state $|i\rangle$ and in its orthogonal state $|j\rangle$. The quantity $R_{\langle|\rangle}$ represents the tomography-related single-shot readout outcome, including the correction for known errors (see Supplementary of [10]).

4.5. SUPPLEMENTARY INFORMATION

4.5.1. FREQUENCY LOCKING

To ensure indistinguishability in frequency between the converted weak coherent states and the zero phonon line emission of the NV we apply an active frequency locking scheme outlined in Fig.4.5. We use two additional frequency converters (QFC3 and QFC4) which convert a continuous wave tap-off from the 795 nm laser to light at 637 nm. We interfere this light on a balanced beamsplitter with light from the laser that excites the NV center. This excitation light passes through an AOM before reaching the NV center, which shifts the frequency by 200 MHz. Thus, we stabilize the frequency of the converted light to a fixed frequency offset of 200 MHz. We detect the light in the two output ports of the beamsplitter (BS) using a balanced photodiode, the output of which feeds, together with a 200 MHz reference, that comes from the driving frequency of the AOM, into a custom control box based on a HMC3716 Digital Phase Frequency Detector. This control box generates an error signal which we use to adapt the frequency of our telecom pump laser.

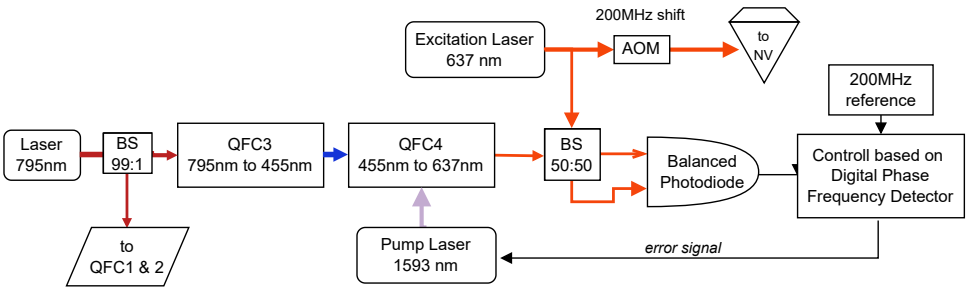

Figure 4.5: Outline of the frequency locking scheme. The converted light and the excitation laser light interfere on a balanced beam-splitter. The signal from the two output ports is detected by a balanced photodiode. A custom and homemade Digital Phase Frequency Detector box generates an error signal that is used by the frequency modulator of the pump laser to correct the second step of the frequency conversion.

4.6. TELEPORTATION PROTOCOL

In this section we report step-by-step the general evolution of the total system.

- Initialization: on the time-bin qubit side, we prepare the general state $\gamma|E\rangle + e^{i\theta}\beta|L\rangle$. For the NV center, we initialize the electron spin in a superposition state: $1/\sqrt{2}(|0\rangle + |1\rangle)$. The state after the double optical excitation of the NV is $\frac{1}{\sqrt{2}}(|1\rangle|E_{NV}\rangle + |0\rangle|L_{NV}\rangle)$. Therefore the total state of the system is the following: $(\gamma|E\rangle + e^{i\theta}\beta|L\rangle)\frac{1}{\sqrt{2}}(|1\rangle|E_{NV}\rangle + |0\rangle|L_{NV}\rangle)$
- Bell-state measurement: given that the photons are indistinguishable, when they impinge on the beam-splitter, we erase the which-path information and the Hong-Ou-Mandel effect holds. The beam-splitter entangles the photons coming from the two platforms. We post-select on events where the detectors clicked in both the early and late time-bin (same detector or different ones), namely we project into the state: $\frac{1}{\sqrt{2}}(|E\rangle|L\rangle \pm |L\rangle|E\rangle)$.
- Real-time feed-forward: To retrieve the correct state on the electron spin qubit's side, a feed-forward operation, based on the outcome of the Bell-state measurement, is necessary. The two different click pattern reflect a phase difference of π between the two output ports. Therefore, in case of a click pattern where early and late photons are detected in two different detectors, an extra π rotation is fed back in real-time to the electron spin qubit.

4.6.1. MODEL OF EXPECTED TPQI VISIBILITY

In this section we will give details on our model to predict the Two Photon Quantum Interference (TPQI) Visibility. We base this model on a similar one presented in [48]. We will derive the expected TPQI visibility as a function of p_{NV}, the NV emission probability and $|\alpha|^2$ the mean photon number of the weak coherent state.

We start by defining the visibility as

$$V = 1 - \frac{p_{ind}}{p_{dist}} \tag{4.2}$$

with p_{ind} (p_{dist}) the probability of a coincidence detection if the photons are indistinguishable (distinguishable). We will assume the probability of 3-photon events to be negligible and thus p_{ind} consists of four contributions

$$p_{ind} = p_{2nv} + p_{2wcs} + p_{nv,wcs} + p_{bg}, \tag{4.3}$$

where p_{2nv} is the probability of detecting 2 NV photons, p_{2wcs} is the probability of detecting 2 photons from the weak coherent state, $p_{nv,wcs}$ is the probability of detecting one NV photon and one weak coherent state photon and p_{bg} is the probability of detecting a coincidence where one click is originated from the background noise. Here, the probability of detecting 2 photons in the NV detection window is given by

$$p_{2nv} = \frac{1}{4}p_{NV}^2 g^{(2)} \tag{4.4}$$

The autocorrelation coefficient $g^{(2)}$ of the NV can be determined separately during the distinguishable sequence of the TPQI experiment by calculating the ratio of a coincidence event p_{coinc} between the two detectors $D1$ and $D2$ and the individual probabilities of a detector click $p_{D1(2)} = 0.5 p_{NV}$, $g^{(2)} = \frac{p_{coinc}}{p_{D1} p_{D2}}$.

Secondly, the probability of detecting two photons originating from the weak coherent state is given by $p_{2wcs} = \frac{1}{4}|\alpha|^4$. Furthermore, the probability of a coincidence originating from one photon entering on each side of the beam splitter depends on the indistinguishability η of the photons

$$p_{nv,wcs} = (1-\eta)\frac{p_{NV}|\alpha|^2}{2} \tag{4.5}$$

and finally the probability of a coincidence where a noise count is involved is given by

$$p_{bg} = p_{noise}(|\alpha|^2 + p_{NV} + p_{noise}) \tag{4.6}$$

with p_{noise}, the probability of a single background (noise) click in one detector per time window. Thus, p_{ind} becomes

$$p_{ind} = \frac{1}{4}p_{NV}^2 g^{(2)} + \frac{1}{4}|\alpha|^4 + (1-\eta)\frac{p_{NV}|\alpha|^2}{2} + p_{noise}(|\alpha|^2 + p_{NV} + p_{noise}) \tag{4.7}$$

For perfectly distinguishable photons ($\eta = 0$) we obtain

$$p_{dist} = \frac{1}{4}p_{NV}^2 g^{(2)} + \frac{1}{4}|\alpha|^4 + \frac{p_{NV}|\alpha|^2}{2} + p_{noise}(|\alpha|^2 + p_{NV} + p_{noise}) \tag{4.8}$$

This then leads to

$$V = 1 - \frac{p_{ind}}{p_{dist}} = 1 - \frac{\frac{1}{4}p_{NV}^2 g^{(2)} + \frac{1}{4}|\alpha|^4 + (1-\eta)\frac{p_{NV}|\alpha|^2}{2} + p_{noise}(|\alpha|^2 + p_{NV} + p_{noise})}{\frac{1}{4}p_{NV}^2 g^{(2)} + \frac{1}{4}|\alpha|^4 + \frac{p_{NV}|\alpha|^2}{2} + p_{noise}(|\alpha|^2 + p_{NV} + p_{noise})} \tag{4.9}$$

or

$$V = \frac{\eta p_{NV}|\alpha|^2}{\frac{1}{2}p_{NV}^2 g^{(2)} + \frac{1}{2}|\alpha|^4 + p_{NV}|\alpha|^2 + 2p_{noise}(|\alpha|^2 + p_{NV} + p_{noise})} \tag{4.10}$$

Finally, we can re-write the Visibility as a function of the ratio x between $|\alpha|^2$ and p_{NV}, with $x = |\alpha|^2 / p_{NV}$ as follows

$$V = \frac{\eta x}{\frac{1}{2}g^{(2)} + \frac{1}{2}x^2 + x + \frac{2p_{noise}(1+x)}{p_{NV}} + \frac{2p_{noise}^2}{p_{NV}^2}} \tag{4.11}$$

which we use to fit the data shown in Fig.4.3 of the main text.

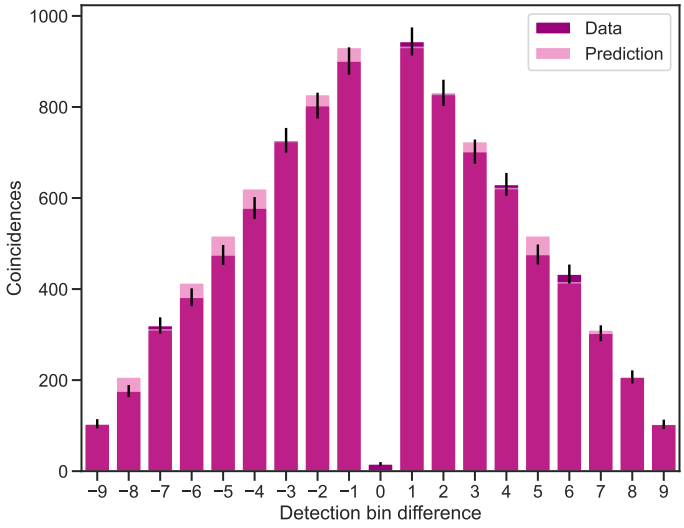

Figure 4.6: Autocorrelation function of the NV center. The magenta bins represent the data collected during the TPQI experiment for all the measured ratios. The pink bins, instead, represent the expected coincidences when assuming a perfect single-photon source. The resulting $g^{(2)}$ value corrected for noise is 0.011 ± 0.004.

4.6.2. MODEL OF EXPECTED TELEPORTATION FIDELITY

In this section we will derive the model we used to predict the Fidelity of the teleported state. We start by defining the input states and measurements and then continue to discuss the different emission patterns that can lead to a valid heralding event and how they affect the final fidelity we can expect to observe.

The state to be teleported will be denoted as $|\Psi_A\rangle$ and is prepared in either the early time bin $|E\rangle$, the late time bin $|L\rangle$ or an equal superposition of the two. The set of states prepared for teleportation are the two states on the poles of the Bloch-sphere

$$|+Z\rangle = |E\rangle \tag{4.12}$$
$$|-Z\rangle = |L\rangle \tag{4.13}$$
$$\tag{4.14}$$

as well as the four equatorial states

$$|\pm X\rangle = \frac{1}{\sqrt{2}}(|E\rangle \pm |L\rangle) \tag{4.15}$$
$$|\pm Y\rangle = \frac{1}{\sqrt{2}}(|E\rangle \pm i|L\rangle) \tag{4.16}$$
$$\tag{4.17}$$

. Due to imperfections in the preparation, the polar states cannot be prepared perfectly. Still, there is a probability of leakage light emission in the orthogonal time bin which we will consider in our model. The electron spin qubit of the NV center and the emitted photon are prepared in the joint state

$$|\Phi\rangle_B = \frac{1}{\sqrt{2}}(|1\rangle|E\rangle + |0\rangle|L\rangle) \tag{4.18}$$

where $|0\rangle$ ($|1\rangle$) denotes the bright (dark) state of the spin qubit (see main text).

The Bell-state measurement, required for teleportation consists of interfering the two photonic states on a balanced beam splitter and post-selecting events where a detection event happened both in the early and late time-bin (either in the same or in different detectors). This corresponds to projection onto the states:

$$|\Psi^{\pm}\rangle = \frac{1}{\sqrt{2}}(|E\rangle|L\rangle \pm |L\rangle|E\rangle) \tag{4.19}$$

where the sign is determined by the detection pattern. As neither of the photon sources emits perfect single-photon states, we have to consider several distinct emission cases that can lead to an accepted heralding signal and how these affect the resulting quantum state. Due to the low emission probability, we neglect all terms in which more than two photons are emitted from any side as well as the case where both sides emit two photons. We will start by defining the different probabilities of occurrence for different photon numbers. For the weak coherent state we have:

$$P_0^w = e^{-\mu} \tag{4.20}$$
$$P_1^w = e^{-\mu}\mu \tag{4.21}$$
$$P_2^w = e^{-\mu}\frac{\mu^2}{2} \tag{4.22}$$
$$\tag{4.23}$$

with P_i^w the probability of emission of i photons from a weak coherent state with mean photon number μ.

The probability of collecting i photons from the NV-center is given by P_i^{NV}

$$P_0^{NV} = (1 - p_{NV}) \tag{4.24}$$
$$P_1^{NV} = p_{NV}(1 - p_{de}) \tag{4.25}$$
$$P_2^{NV} = p_{NV}p_{de} \tag{4.26}$$
$$\tag{4.27}$$

where p_{de} denotes the double excitation probability of the NV-center. We now write out these individual contributions as non-normalized density matrices ρ_{ij} with their respective probability of occurrence $P_i^{NV}P_j^w$ for the different numbers of photons emitted from the NV center (i) and from the weak coherent state (j) as well as contributions in which (at least) one click was triggered by a background (or noise) count. For the case where the weak coherent state is prepared in a pole state ($\pm|Z\rangle$) we also consider the

probability of emitting k unwanted or leaked photons in the state orthogonal to the desired one which are denoted as $P_k^{w\perp}$. In the following we use the simplified notation P_{ijk} for $P_i^{NV}P_j^{w}P_k^{w\perp}$ or P_{ij} for $P_i^{NV}P_j^{w}$. The probability of one or two background or noise photons contributing to a valid trigger event is, for the pole states, given by

$$P_{bg}^{pole} = 2p_{noise}(2p_{noise}P_{000} + P_{010} + P_{100} + P_{001}) \tag{4.28}$$

and for the equatorial states by

$$P_{bg}^{eq} = 2p_{noise}(2p_{noise}P_{00} + P_{10} + P_{01}) \tag{4.29}$$

Where p_{noise} is the probability of a background or noise detection per detector and time bin and we have limited the background contributions we consider to a maximum of two emitted photons. For the teleportation experiment, the measured p_{noise} per detector is $(5.5\pm0.2)e^{-6}$.

Now we will consider the non-normalized density matrix contributions corresponding to these probabilities of occurrence. They are non-normalized as not all detection patterns are considered valid trigger events and we will post-select on these valid heralding events. In writing down these contributions and their probabilities of yielding a valid heralding event, we will have to differentiate between teleporting the pole-states ($|\pm Z\rangle$) from the states in the equatorial plane of the Bloch-sphere ($|\pm X\rangle$ and $|\pm Y\rangle$), which we will mark as ρ^{pole} and ρ^{eq}. For the desired case of one emitted NV photon and one photon emitted from the weak coherent state we can write

$$\rho_{11}^{pole} = \frac{P_{110}}{2}|\Psi_A\rangle\langle\Psi_A| + \frac{P_{101}}{2}|\Psi_A^{\perp}\rangle\langle\Psi_A^{\perp}| \tag{4.30}$$

$$\rho_{11}^{eq} = P_{11}(\frac{\eta}{2}|\Psi_A\rangle\langle\Psi_A| + \frac{(1-\eta)}{2}\mathbb{I}) \tag{4.31}$$

The factor $\frac{1}{2}$ takes into account the fact that we could project on any of the four Bell-states but we can only unambiguously discern two of them and thus, only these two will lead to an accepted heralding pattern. The difference between the pole and the equatorial states is due to the fact that in the case of the pole states we profit from the classical correlations in the system, while for the equatorial states we will only obtain the desired result if the photons from the two sources interfere.

In the case of a double emission from the weak coherent state and no NV photon, there will only be a valid trigger event for a pole state if the double emission happened in the form of one photon from the desired time bin and one in the orthogonal one, and there can as well be a valid trigger in case of an equatorial state which will lead to

$$\rho_{02}^{pole} = P_{011}\mathbb{I} \tag{4.32}$$

$$\rho_{02}^{eq} = \frac{P_{02}}{2}\mathbb{I} \tag{4.33}$$

We will omit the case in which one photon was emitted from the NV center but two from the weak coherent state due to it's low probability of occurrence for the mean photon numbers used in the experiment.

Finally, for the case of two NV photons and one from the weak coherent state we get

$$\rho_{21}^{pole} = \frac{P_{210}}{4}|\Psi_A\rangle\langle\Psi_A| + \frac{P_{201}}{4}|\Psi_A^{\perp}\rangle\langle\Psi_A^{\perp}| \tag{4.34}$$

$$\rho_{21}^{eq} = \frac{P_{21}}{4}\mathbb{I} \tag{4.35}$$

When teleporting pole states the final density matrix becomes

$$\rho^{pole} = \frac{\frac{1}{2}P_{110} + \frac{1}{4}P_{210}}{N}|\Psi_A\rangle\langle\Psi_A| + \frac{\frac{1}{2}P_{101} + \frac{1}{4}P_{201}}{N}|\Psi_A^{\perp}\rangle\langle\Psi_A^{\perp}| + \frac{P_{011} + P_{bg}^{pole}}{N}\mathbb{I} \tag{4.36}$$

with

$$N = \frac{P_{110} + P_{101}}{2} + \frac{P_{210} + P_{201}}{4} + P_{011} + P_{bg}^{pole} \tag{4.37}$$

Thus, we can calculate the expected fidelity to be

$$F^{pole} = \frac{P_{110} + \frac{1}{2}P_{210} + P_{011} + P_{bg}^{pole}}{2N} \tag{4.38}$$

For the equatorial states we obtain

$$\rho^{eq} = \frac{\eta P_{11}}{2N}|\Psi_A\rangle\langle\Psi_A| + \frac{(1-\eta)P_{11} + P_{02} + P_{21} + 2P_{bg}^{eq}}{2N}\mathbb{I} \tag{4.39}$$

with

$$N = \frac{P_{11} + P_{02}}{2} + \frac{P_{21}}{4} + P_{bg}^{eq}, \tag{4.40}$$

thus, the Fidelity is given as

$$F^{eq} = \frac{1}{2N}\left(\frac{P_{11}(1+\eta) + P_{02} + P_{21}}{2} + P_{bg}^{eq}\right) \tag{4.41}$$

4.6.3. CLASSICAL BOUND WHEN TELEPORTING WITH WEAK COHERENT STATES

When comparing our experimentally achieved teleportation fidelity with the classical bound of $\frac{2}{3}$, this bound is derived using the optimal classical strategy when using single photons to encode qubits [49]. In the case of qubits encoded in weak coherent states, however, a classical strategy might use the higher photon number contributions of that

state to achieve a higher probability of success. One can calculate the maximally achievable Fidelity for a classical strategy as shown in [50] as

$$F_{max}(|\alpha|^2) = \sum_{N\geq 1} F_{MP}(N)\frac{p(|\alpha|^2,N)}{1-p(|\alpha|^2,0)} \tag{4.42}$$

where N is the number of photons per pulse, p describes the poissonian distribution of photon numbers

$$p(|\alpha|^2,N) = \frac{|\alpha|^{2N}}{N!}e^{-|\alpha|^2} \tag{4.43}$$

and

$$F_{MP}(N) = \frac{N+1}{N+2} \tag{4.44}$$

is the maximum achievable fidelity for a state with a fixed amount of photons N. For the parameters of our teleportation experiment we can now calculate the maximum achievable fidelity for a classical strategy as follows: During the teleportation experiment we had an average NV emission probability of $p_{NV} = (4.50 \pm 0.9)e^{-4}$ and a ratio $\frac{|\alpha|^2}{p_{NV}} = 1.20 \pm 0.24$. It is noteworthy that, with respect to the TPQI experiment, a degradation of the p_{NV} parameter occurred, as well as lower CR check counts were encountered. The reason for the lowered photon emission of the NV might be due to a fault in our cryostat that led to ice formation inside the sample chamber. Despite that, the setup was stable in the new configuration and the experiment was executed remotely. At the same time, the intensity modulator employed for the generation of the time-bin qubits showed higher leakage, leading to a generally increased noise probability. Using the upper bound of this ratio between mean photon number and p_{NV} (and thus $|\alpha|^2 = 6.50e^{-4}$) the maximally achievable fidelity for a classical strategy would be $F_{max} = 0.666694$. As we can see, due to the low mean photon numbers used in our experiment, the correction is minimal but should be considered in implementations with higher mean photon numbers.

4.6.4. NOISE CHARACTERIZATION

In this section, we report on the characterization of the noise sources that are involved in the experiments.

To obtain the dark count rates of the detector, we block the ZPL collection path of the NV and the output of the QFC2. This results in a mean noise rate of (11.7±5.6)Hz. The contribution of the pump lasers for the two-step frequency conversion is measured by keeping the ZPL path closed and blocking the 795 nm input of the QFC1. The rate in this case is (12.3±5.6)Hz, showing that our conversion setup is low noise, if compared with the rate obtained when no conversion setup was involved. To characterize the noise contribution of the weak-coherent state in the NV center window (particularly relevant in the distinguishable sequence of the TPQI experiment), we block the ZPL path of the NV center and we sweep the voltage applied to the variable optical attenuator, namely we manipulate the mean-photon number of the weak-coherent state. We play

the distinguishable sequence of the TPQI experiment, collecting the counts in the time window where the NV center pulse is supposed to be. The results are illustrated in Fig.4.7.

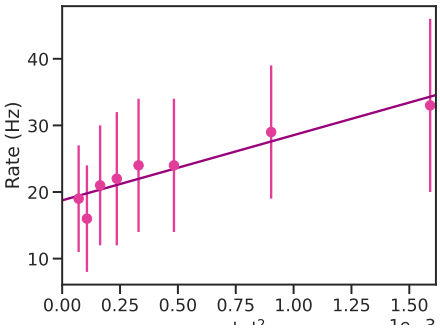

Figure 4.7: Noise characterization of the weak coherent state. By sweeping the voltage applied to the VOA, the mean-photon number changes. We assume a linear model for the noise count rate vs. the mean-photon number. The result of the linear fit is used in the calculation of the p_{noise} term in Eq. 4.9, thus affecting the visibility of the TPQI experiment.

Lastly, we check the noise contribution coming from the NV setup. We block the output of the QFC2 setup and we open the ZPL path. We repeat the distinguishable sequence, collecting counts in the weak-coherent state window. The rate is (12.8 ± 5.4)Hz, which is comparable with the rate measured above for the detector dark counts and the pump noise. We can therefore conclude that the main source of noise comes from the preparation of the weak coherent state, particularly the combination of the intensity modulator, whose bias voltage needs to be optimized throughout the measurement, and the variable optical attenuator. However, this noise source is relevant only in the distinguishable sequence of the TPQI experiment, while in the indistinguishable one, we can consider as p_{noise} the constant background noise given by the detectors and the conversion setup. For the teleportation experiment, the noise rate increased to (275±10)Hz due to equipment degradation, as discussed above.

4.6.5. PHASE MODULATOR CHARACTERIZATION AND STABILITY

To characterize the phase modulator, namely to identify V_π and $V_{\pi/2}$, we build a Mach-Zehnder-type interferometer at 795 nm. In particular, the input of the QFC1 from main text, the shaped pulses, is connected to a 50:50 in-fiber beam splitter. The two output arms of such a beam splitter are 2m long fibers, and on one of the two arms, we include the phase modulator device we want to characterize. The two arms impinge on a second in-fiber 50:50 beam splitter, whose output ports are connected to two APDs. The voltage source for the phase modulator is one of the wave channels of the AWG, whose output has an amplitude between ±5V.

We send a pulse to the interferometer, encountering a phase shift due to the phase modulator, and we register, through the time-tagger at the detectors, the counts per shot for the two pulses. We repeat this experiment while sweeping the voltage applied to the phase modulator, reconstructing the plot in Fig.4.8a for the two detectors.

The data collected for the two detectors are jointly fit to the following curves:

$$A_1 \sin\left(\frac{s \cdot cps_{det_1}}{2} + o\right) + c_1$$

$$A_2 \cos\left(\frac{s \cdot cps_{det2}}{2} + o\right) + c_2$$

From the fit of the s parameter, it is possible to estimate V_π (and $V_{\pi/2}$) as $|\pi/s|$ (and $|\pi/(2s)|$).

At this point, we repeat the measurement and the data fit more times over a time span of 15h. In Fig.4.8b we report the estimation of $V_{\pi/2}$ and V_π over time, resulting in an average of (2.601±0.002)V and (5.202±0.004)V. These values are then used to make the time bin qubits in the several cardinal states. The results in Fig.4.8b also show the stability of these values, confirming the reproducibility. Given that V_π exceeds the maximum amplitude that the HDAWG can provide, we use a phase modulator pulse per bin for this case.

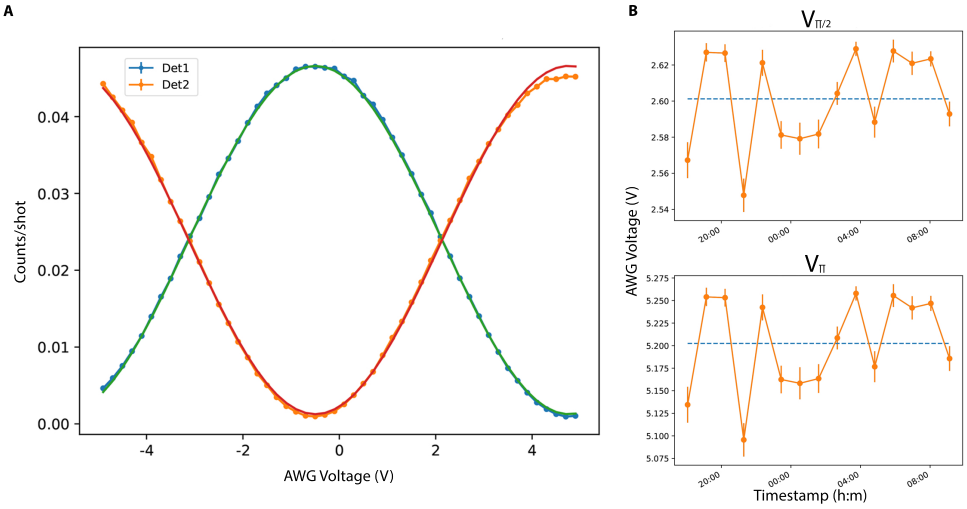

Figure 4.8: a) Data fit to extract the values of V_π and $V_{\pi/2}$. The solid lines represent the fitted curve per detector. b) Stability measurement for V_π and $V_{\pi/2}$. The dashed lines represent the average value.

4.6.6. DEVICES AND EXPERIMENTAL MONITORING

As stated in the main text, the NV setup is “Alice" of [10, 11]. However, some devices have been replaced. In particular, in this work we employed the Zurich Instruments HDAWG as an arbitrary waveform generator, and the PicoQuant MultiHarp as timetagger. All the other devices remained unchanged.

The experiments, both the TPQI and the teleportation, were running remotely, at a distance of up to 7745km between the scientists and the setup. This shows that the setup is robust over time and automated experimental monitoring is crucial. Here we report the list of automatization routines that have been implemented using the software environment in Ref.[51].

- For the TPQI experiment only: auto-relocking system for the 795 nm laser. During the TPQI experiment, the 795 nm laser wavelength was locked to an external cavity. A homemade background program detects when the laser frequency drifts and

about to go out of lock and adjusts the piezo voltage of the laser to bring the desired spectral mode back. For the teleportation experiment, the laser was locked to a wavemeter with a constant PID loop running to keep the desired wavelength. It is important to notice that the wavelength of the 795 nm laser did not change between the two experiments, as the same wavemeter was monitoring the wavelength during the TPQI experiment.

- The system is automatically calibrated over time. In particular, the calibration is targeted at the laser power, the position of the NV with respect to the objective, in such a way as to maximize the fluorescence under the excitation using green light in the Phonon-Side Band (PSB). Small drifts in the optics of the NV setup are compensated by a Python-controlled deformable mirror that is included in the Zero-Phonon Line (ZPL) path. The calibration maximizes the fluorescence in the ZPL when the green light is on. A system of automated waveplates minimizes the leakage of pulse light in the ZPL. The bias voltage of the EOM for the NV optical π-pulses and of the intensity modulator for the 795 nm pulses is also optimized during the experiments to minimize leakage.

- A set of control scripts checks for frequency shifts of converted light and all the lasers involved with "real-time" data filtering. In particular, when the control scripts detect an anomaly in one of the frequencies monitored via the wavemeter, a flag is raised and the ongoing measurement is tagged as failed and discarded.

- For teleportation experiment only: calibration of the ratio mean-photon number/counts per shot of the NV every 5 datasets taken. The variable optical attenuator is controlled via the Micro-Controller Unit (MCU). In this way, it is also possible to compensate for drifts in the mean-photon number as well as in the conversion setup that might cause lower efficiency during the experiment.

The experimental rate of teleportation, including the overhead time due to the experimental monitoring and calculated after time-filtering (as discussed in the main text) is ~0.6mHz.

REFERENCES

[1] H. J. Kimble, *The quantum internet,* Nature **453**, 1023 (2008).

[2] S. Wehner, D. Elkouss and R. Hanson, *Quantum internet: A vision for the road ahead,* Science **362**, eaam9288 (2018).

[3] E. Togan *et al.*, *Quantum entanglement between an optical photon and a solid-state spin qubit,* Nature **466**, 730 (2010).

[4] P. Lodahl, *Quantum-dot based photonic quantum networks,* Quantum Science and Technology **3**, 013001 (2017).

[5] M. Bock *et al.*, *High-fidelity entanglement between a trapped ion and a telecom photon via quantum frequency conversion,* Nature Communications **9**, 1998 (2018).

[6] M. Ruf, N. H. Wan, H. Choi, D. Englund and R. Hanson, *Quantum networks based on color centers in diamond,* Journal of Applied Physics **130**, 070901 (2021).

[7] P.-J. Stas *et al.*, *Robust multi-qubit quantum network node with integrated error detection,* Science **378**, 557–560 (2022).

[8] D. Lago-Rivera, J. V. Rakonjac, S. Grandi and H. d. Riedmatten, *Long distance multiplexed quantum teleportation from a telecom photon to a solid-state qubit,* Nature Communications **14**, 1889 (2023).

[9] J.-L. Liu *et al.*, *Creation of memory–memory entanglement in a metropolitan quantum network,* Nature **629**, 579–585 (2024).

[10] M. Pompili *et al.*, *Realization of a multinode quantum network of remote solid-state qubits,* Science **372**, 259–264 (2021).

[11] S. L. N. Hermans *et al.*, *Qubit teleportation between non-neighbouring nodes in a quantum network,* Nature **605**, 663 (2022).

[12] M. W. Doherty *et al.*, *The nitrogen-vacancy colour centre in diamond,* Physics Reports **528**, 1–45 (2013).

[13] L. Childress and R. Hanson, *Diamond NV centers for quantum computing and quantum networks,* MRS Bulletin **38**, 134 (2013).

[14] C. Thiel, N. Sinclair, W. Tittel and R. Cone, *Tm3+:Y3Ga5O12 Materials for Spectrally Multiplexed Quantum Memories,* Physical Review Letters **113**, 160501 (2014).

[15] N. Sinclair *et al.*, *Proposal and proof-of-principle demonstration of non-destructive detection of photonic qubits using a Tm:LiNbO3 waveguide,* Nature Communications **7**, 13454 (2016).

[16] M. F. Askarani *et al.*, *Long-Lived Solid-State Optical Memory for High-Rate Quantum Repeaters,* Physical Review Letters **127**, 220502 (2021).

[17] Y.-W. Cho *et al.*, *Highly efficient optical quantum memory with long coherence time in cold atoms,* Optica **3**, 100 (2016).

[18] R. Zhao *et al.*, *Long-lived quantum memory,* Nature Physics **5**, 100 (2009), number: 2 Publisher: Nature Publishing Group.

[19] W. Rosenfeld, S. Berner, J. Volz, M. Weber and H. Weinfurter, *Remote Preparation of an Atomic Quantum Memory,* Physical Review Letters **98**, 050504 (2007).

[20] L. Heller, P. Farrera, G. Heinze and H. de Riedmatten, *Cold-Atom Temporally Multiplexed Quantum Memory with Cavity-Enhanced Noise Suppression,* Physical Review Letters **124**, 210504 (2020).

[21] K. Azuma *et al.*, *Quantum repeaters: From quantum networks to the quantum internet,* Reviews of Modern Physics **95**, 045006 (2023).

[22] P. Drmota *et al.*, *Robust Quantum Memory in a Trapped-Ion Quantum Network Node,* Physical Review Letters **130**, 090803 (2023).

[23] C. H. Bennett *et al.*, *Teleporting an unknown quantum state via dual classical and Einstein-Podolsky-Rosen channels,* Physical Review Letters **70**, 1895 (1993).

[24] D. Bouwmeester *et al.*, *Experimental quantum teleportation,* Nature **390**, 575 (1997).

[25] K. Heshami *et al.*, *Quantum memories: emerging applications and recent advances,* Journal of Modern Optics **63**, 2005 (2016).

[26] Y. Lei *et al.*, *Quantum optical memory for entanglement distribution,* Optica **10**, 1511 (2023).

[27] M. Afzelius, C. Simon, H. de Riedmatten and N. Gisin, *Multimode quantum memory based on atomic frequency combs,* Physical Review A **79**, 052329 (2009).

[28] J. P. Covey, H. Weinfurter and H. Bernien, *Quantum networks with neutral atom processing nodes,* npj Quantum Information **9**, 1 (2023).

[29] M. Lipka, M. Mazelanik, A. Leszczyński, W. Wasilewski and M. Parniak, *Massively-multiplexed generation of Bell-type entanglement using a quantum memory,* Communications Physics **4**, 1 (2021).

[30] F. Bussieres *et al.*, *Prospective applications of optical quantum memories,* Journal of Modern Optics **60**, 1519 (2013).

[31] N. Sangouard, C. Simon, H. de Riedmatten and N. Gisin, *Quantum repeaters based on atomic ensembles and linear optics,* Reviews of Modern Physics **83**, 33 (2011).

[32] P. Kumar, *Quantum frequency conversion,* Optics Letters **15**, 1476 (1990).

[33] C. K. Hong, Z. Y. Ou and L. Mandel, *Measurement of subpicosecond time intervals between two photons by interference,* Phys. Rev. Lett. **59**, 2044 (1987).

[34] R. Loudon, *The Quantum Theory of Light* (Clarendon Press, 1983).

[35] H. Bernien *et al.*, *Heralded entanglement between solid-state qubits separated by three metres,* Nature **497**, 86–90 (2013).

[36] Z.-H. Wang, G. de Lange, D. Ristè, R. Hanson and V. V. Dobrovitski, *Comparison of dynamical decoupling protocols for a nitrogen-vacancy center in diamond,* Physical Review B **85**, 155204 (2012).

[37] M. Ruf, M. Weaver, S. van Dam and R. Hanson, *Resonant excitation and purcell enhancement of coherent nitrogen-vacancy centers coupled to a fabry-perot microcavity,* Phys. Rev. Applied **15**, 024049 (2021).

[38] C. Hepp *et al.*, *Electronic Structure of the Silicon Vacancy Color Center in Diamond,* Physical Review Letters **112**, 036405 (2014).

[39] M. Bhaskar *et al.*, *Quantum Nonlinear Optics with a Germanium-Vacancy Color Center in a Nanoscale Diamond Waveguide,* Physical Review Letters **118**, 223603 (2017).

[40] C. Nguyen *et al.*, *Quantum Network Nodes Based on Diamond Qubits with an Efficient Nanophotonic Interface,* Physical Review Letters **123**, 183602 (2019).

[41] A. E. Rugar *et al.*, *Quantum Photonic Interface for Tin-Vacancy Centers in Diamond,* Physical Review X **11**, 031021 (2021).

[42] D. M. Lukin, M. A. Guidry and J. Vučković, *Integrated Quantum Photonics with Silicon Carbide: Challenges and Prospects,* PRX Quantum **1**, 020102 (2020).

[43] D. B. Higginbottom *et al.*, *Optical observation of single spins in silicon,* Nature **607**, 266 (2022).

[44] P. Lodahl, *Quantum-dot based photonic quantum networks,* Quantum Science and Technology **3**, 013001 (2017).

[45] S. Liu *et al.*, *Violation of Bell inequality by photon scattering on a two-level emitter,* (2023).

[46] M. Schäfer, B. Kambs, D. Herrmann, T. Bauer and C. Becher, *Two-stage, low noise quantum frequency conversion of single photons from silicon-vacancy centers in diamond to the telecom c-band,* Advanced Quantum Technologies , 2300228 (2023), https://onlinelibrary.wiley.com/doi/pdf/10.1002/qute.202300228 .

[47] E. Bersin *et al.*, *Telecom networking with a diamond quantum memory,* PRX Quantum **5** (2024), 10.1103/prxquantum.5.010303.

[48] A. Padrón-Brito, J. Lowinski, P. Farrera, K. Theophilo and H. de Riedmatten, *Probing the indistinguishability of single photons generated by Rydberg atomic ensembles,* Physical Review Research **3**, 033287 (2021).

[49] S. Massar and S. Popescu, *Optimal Extraction of Information from Finite Quantum Ensembles,* Physical Review Letters **74**, 1259 (1995).

[50] H. P. Specht *et al.*, *A single-atom quantum memory,* Nature **473**, 190 (2011).

[51] I. T. Raa *et al., QMI - Quantum Measurement Infrastructure, a Python 3 framework for controlling laboratory equipment,* (2023).

5

EXTENDABLE OPTICAL PHASE SYNCHRONIZATION OF REMOTE AND INDEPENDENT QUANTUM NETWORK NODES OVER DEPLOYED FIBERS

Politics can affect things locally and temporarily, but technology can affect things globally and permanently

Lyn Alden

A. J. Stolk, J. J. B. Biemond, K. L. van der Enden, L. van Dooren, E. J. van Zwet, and R. Hanson

In this paper we present a phase synchronization scheme for a metropolitan quantum network, operating in the low-loss telecom L-band. To overcome various challenges such as communication delays and optical power limitations, the scheme consists of multiple tasks that are individually stabilized. We characterize each task, identify the main noise sources, motivate the design choices and describe the synchronization schemes. The performance of each of the tasks is quantified by a transfer-function measurement that investigates the frequency response and feedback bandwidth. Finally we investigate the resulting optical phase stability of the fully deployed system over a continuous period of 10 hours, reporting a short-term stability standard deviation of $\sigma \approx 30\,\mathrm{deg}$ *and a long-term stability of the average optical phase to within a few degrees. The scheme presented served as a key enabling technology for an NV-center based metropolitan quantum link. This scheme is of interest for other quantum network platforms that benefit from an extendable and telecom compatible phase synchronization solution.*

The results of this chapter are under preparation for submission

5.1. INTRODUCTION

Quantum networks [1] hold the promise to revolutionize the way people exchange information. A central task of a quantum network is the generation of entanglement between (end-)nodes, in which the entanglement can be stored, manipulated and processed [2]. In general, protocols to generate entanglement between stationary qubits involve the emission, transmission and joint measurement of flying qubits, encoded in a photon state, see Fig. 5.1a. A common configuration envisioned for a future large scale quantum internet is the combination of nodes, which house the stationary qubits, and midpoints, where the flying qubit from different nodes are sent to. These nodes are connected via deployed telecom fiber to midpoints, that provide synchronization, interference and detection tasks, see Fig. 5.1b.

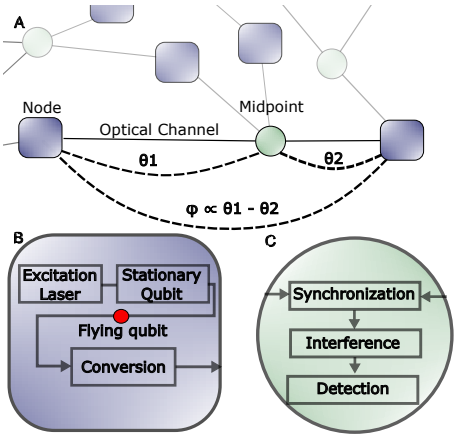

Figure 5.1: **Schematic overview of elements in a Quantum Network. A)** Many nodes can be connected by sending flying qubits over optical channels towards a central midpoint. The optical path from excitation in the node, to detection in the midpoint, gives rise to an optical phase, θ. When using the Fock-state encoding of the flying qubit for entanglement generation, the resulting entangled state phase ϕ is proportional to the difference between the optical phases. B) Elements needed to generate entanglement between stationary qubits, via the exchange of flying qubits. If the flying qubits are photons not compatible with deployed infrastructure, frequency conversion can be used to significantly lower the propagation losses. C) Upon arrival in the midpoint, the phase of the incoming photonic qubits needs to be stabilized, after which they can be interfered and subsequently detected. The outcome of this detection heralds entanglement between the stationary qubits in the nodes.

Photon loss in the connecting fibers decreases the rate at which entanglement between the nodes is generated, with the exact scaling depending on the photonic qubit encoding used. For example, for frequency encoding [3], polarization encoding [4–8], and time-bin encoding [9–12], the entangling rate scales linearly with the photon transmission η between the nodes. In contrast, for photonic encoding using number states (0 or 1 photon) [13, 14] the rate scales favourably with $\sqrt{\eta}$, yielding significantly higher rates in the typical scenario of substantial photon loss (i.e. for $\eta \ll 1$). However, with this encoding the resulting entangled state phase ϕ is proportional to the optical phase difference between the two paths to the midpoint (θ_1 and θ_2, see Fig. 5.1a), leading to the additional experimental requirement that this optical phase difference at the time of interference in the midpoint needs to be known [*].

If the phase deviates from the chosen setpoint by $\delta\phi$, the maximum fidelity achievable is given by $F(\delta\phi) = \frac{1}{2}(1+\cos(\delta\phi))$. In a larger network, the single photons are originating from multiple sources at distant locations, where the

[*]For time-bin encoding the entangled state phase is dependent on the optical phase difference picked up between the two time bins. Thus, optical phase stability is required only on this timescale which is typically below 500ns [10, 12, 15]

phase is affected at many length- and time-scales. Any attempt to stabilize this phase needs to take into account unwanted light from either conversion or the synchronization methods used, that degrade the fidelity of the entangled state. This puts stringent requirements on any classical stabilization light co-propagating with the quantum channel.

Entanglement generation using photonic number state encoding, hereafter called single-click protocol, has been demonstrated in atoms [16], (hole-)spins in semiconductors [17, 18], ensemble-based quantum memories [19, 20], and between single rare-earth ions in cavities [21]. Specifically, the implementation of this protocol on the Nitrogen Vacancy (NV-) center in diamond [22] resulted in orders of magnitude faster entanglement generation than the preceding experiments on the same platform that used time-bin encoding [10, 15, 23]. This allowed for the extension to a multi-node network on which distributed quantum protocols can be realized [24, 25]. So far these experiments have not dealt with the additional requirements of large separation between nodes or telecom compatibility, allowing them to simplify their design. Our approach forms an essential part of a metropolitan quantum link realized in the Netherlands, where solid-state entanglement is generated between two NV-based quantum nodes using 25 km of deployed telecom fiber, which we discuss in Ch. 6.

A key challenge for the implementation of the single-click protocol for entanglement generation over large distances are the strict requirements on the optical phase stability. Large physical separation between the end nodes adds even more complexity to the system, as fast fluctuation of the optical phase can only be synchronized by using high-bandwidth feedback, where the propagation-delay of information exchange between locations becomes potentially problematic. Furthermore, directly sharing of optical phase references between the nodes beforehand becomes challenging when the distance between the nodes becomes larger and the excitation lasers are in in the visible wavelengths. The duration of this stability is demanded for the full duration of the time it takes to analyze (or in the future, end-user protocol runtime) the entangled state that is being generated. A robust, extendable and highly synchronized solution is therefore a key enabler for future quantum networks at scale.

In this work we propose, implement and verify an optical phase synchronization scheme between remote and independent quantum nodes operating in the telecom band. The structure of the paper is as follows. In the following section we provide the broader scope in which our phase synchronization scheme is developed and the challenges it is aiming to solve. In the section after that, we provide a full system overview and provide information on the various noise sources that occur in the system. We describe the division of the full system into smaller synchronization tasks, which are subsequently individually described, where the control-layout, noise spectrum and feedback performance are discussed. We then verify the synchronization of the full system at work using measurements of the optical phase between the nodes deployed in the network. Finally we conclude by highlighting the benefits of our scheme, as well as give an outlook on broader applications and further improvements.

5.2. PHASE-STABILIZATION FOR NV-CENTER ENTANGLEMENT.

The NV center is an optically active defect in a diamond lattice, of which the electronic spin state forms the basis of many previous demonstrations of solid-state entanglement generation in a network [10, 15, 24]. The entanglement generation can be briefly described in three steps: (1) the generation of single photons by resonant excitation and spontaneous emission, (2) the collection, possible frequency conversion, and propagation towards a central beamsplitter, and (3) a measurement of a single photon. The schematic in the top of Fig. 5.2 shows the important optical components needed to perform the entanglement generation.

Single-photons are generated by carving short (1.5 ns FWHM) optical pulses from a tap-off from a continuous laser. This excitation light is routed to the NV-center housed in a 4 K cryostat via in-fiber and free-space optics. Spin-selective, resonant excitation followed by spontaneous emission, generates single photons emitted by the NV-center (Fig. 5.2a, left). Around 3% of the photon-emission is not accompanied by a phonon emission, the so called Zero-Phonon line (ZPL). These photons are coherent with the laser field used for excitation, and are entangled with the spin-state of the NV-center. The ZPL photons are collected into a single-mode fiber, and guided to a Quantum Frequency Converter (QFC), similar to previous work [26, 27], that maintains the entanglement between the photon and the NV spin [28].

In the QFC process, the single-photons are mixed with a high-power pump (1064 nm) inside a non-linear medium, which is phase-matched for a Difference Frequency Generation process (Fig.5.2a). This converts the single photons from the original 637 nm to 1588 nm in the telecom L-band. This process is crucial to reduce propagation losses, and also serves as a method to remove any frequency difference between the different NV-centers used for entanglement generation. For more details see previous experiments [29].

After the frequency conversion, the single-photons propagate over the deployed fibers towards a central location called the midpoint, shown in Fig. 5.2a on the right. There the incoming photons are spectrally filtered via transmission through an Ultra-narrow Filter (UNF, FWHM 50 MHz), and guided to an in-fiber beamsplitter, where the modes of the two nodes interfere. At this point, the relative optical phase is crucial for the entanglement generation when using the single click protocol. The resulting modes behind the beamsplitter are measured using Superconducting Nanowire Single Photon Detectors (SNSPDs), that perform a photonic Bell-state measurement on the combined photon mode. The outcome of this measurement heralds the spin-state of the NV-centers in an entangled state.

For this configuration of a qubit platform we highlight a few specific challenges of synchronizing the optical phase.

Firstly, the free-space and in-fiber optics is sensitive to resonances when placed on an optical table together with a closed-cycle cryostat inducing vibrations, showing up as phase noise on the single photon field. Depending on the mechanical frequencies and stability, a moderate feedback bandwidth is needed to get rid of these fluctuations. Furthermore, careful design of the optics should be done to limit these mechanical vibrations, to reduce the phase-noise that is present due to this effect.

Second, the optical path that requires phase-synchronization is inherently optically connected with a two-level quantum system on one end, and sensitive single-photon detectors on the other end. This constrains the optical powers that can be used for the phase synchronization, and makes the design of the whole system more complex. For instance, unwanted reflections at fiber to fiber connectors or free-space to matter interfaces can lead to crosstalk between the synchronization tasks and entanglement generation. The careful balancing of optical powers and illumination times of light that is incident on the NV-center, as well as the extra shielding of the SNSPDs with Variable Optical Attenuators (VOAs) are additions to allow for a more stable optical phase without reducing the coherence of the NV-center or blinding of the SNSPDs.

Third, when using optical fibers over large distance, the thermal expansion can introduce variations that expand the fiber in the same direction for days. Because we only stabilize the relative phase, large drift in fiber length introduces many phase-slips of 2π, which results in a non-negligible difference between the stabilized phase and optical phase of interest, see 5.9.4. This is due to the fact that the stabilization light propagates over the long fiber with slightly different frequency than the photons with which we generate entanglement. In our case, when using an offset of 400 MHz, residual phase error $\Delta\theta$ is $\Delta\theta = M\ 360\ (\frac{f_{NV}-f_{stab}}{f_{stab}}) = M\ 7.6\times10^{-4}$ degrees, where M is the number of phaseslips. For deployed fibers of kilometers long, many centimeters of expansion/contraction occurs on the timescale of days, corresponding to millions of phaseslips. This makes it significant for continuous operation of entanglement generating networks over large fiber networks. Fourth, propagating high power optical pulses over long fibers can create a significant background at the single photon level both due to double Rayleigh scattering [30], and via interfaces such as connectors and splices. This puts limits on the shot-noise limited feedback bandwidth one can achieve using this classical light, without inducing more background photons in the SNSPDs.

In the following section we discuss our approaches to tackle all these challenges, given the boundary conditions as discussed in the previous sections. We identify three subtasks that can be synchronized independently, resulting in the synchronization of the relative phase of the single-photon fields between two NV-center nodes.

5.3. SYSTEM OVERVIEW AND NOISE SOURCES

An overview of the optical layout that enables synchronization is shown in Fig. 5.2b. The strategy to divide the phase synchronization for NV-based networks in multiple subtasks was first divised and implemented in Ref. [24], which we extend in this work to suit the additional challenges of telecom operation and large node separation. In this section we identify those sub tasks, showing which optical paths are used where error-signals are generated and subsequently what actuator is used to achieve the synchronization. In Fig. 5.3 we describe the synchronization subtasks in more detail, giving an overview of the individual components used.

To achieve the ultimate goal of synchronizing the ZPL photons coming from different nodes, an additional light field is added on both nodes, enabling optical phase synchronization at higher optical powers. This stabilization light is generated at both nodes from the same laser that also excites the NV, and is offset in frequency using a similar set

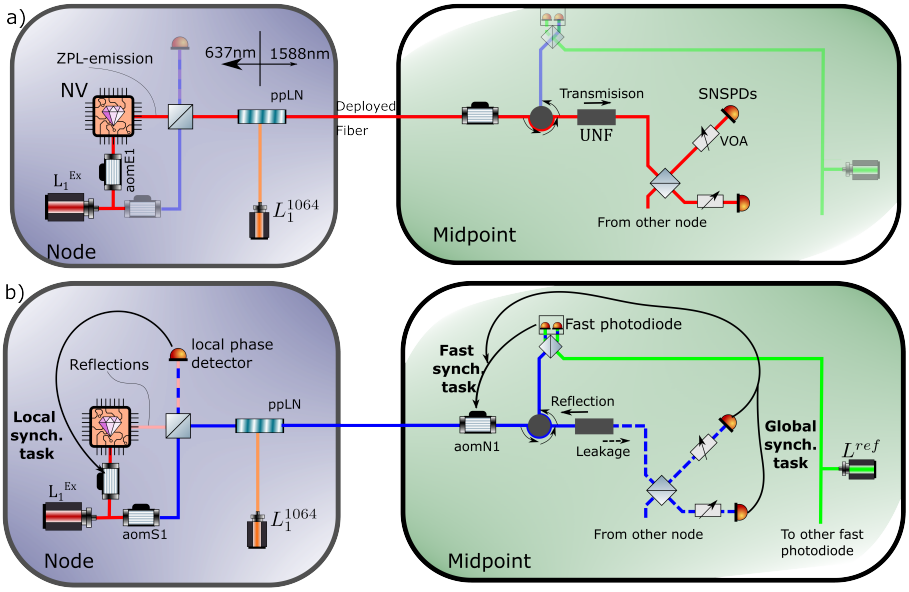

Figure 5.2: **Schematic of optical lay-out with sources, detectors and optical phase actuators. a)** Optical paths for entanglement generation. At the node light from the excitation laser (red) excites the NV center, yielding single photons at the ZPL wavelength (in red) through spontaneous emission which are converted and routed to the midpoint. There the single photons are passed through an AOM and an ultra-narrow FBG (UNF) for spectral filtering. Overlapping the incoming photon with the photon from the other node on a central beamsplitter, they are measured using SNSPDs. As described in the main text, the relative phase at this beamsplitter is crucial in the entanglement generation. **b)** The lay-out of the phase synchronization schemes to achieve the synchronized phase at the beamsplitter in the midpoint. The laser used for excitation of the NV-center is split and offset in frequency to generate stabiliation light (in blue). In addition reflections of the excitation light (shown pink) coming from the diamond surface, are generated which guided to the 'local phase detector', interfering with part of the stabilization light. This error signal is used to feedback the local synchronization task. The stabilization light is also converted and sent to the midpoint, following the same optical path as the single-photons. There the stabilization light co-propagates with the single photons until it hits the UNF in the rejection band, where most of the stabilization is reflected and routed towards the fast photo-diode, ultimately interfering at the 'fast detector' with light from a reference laser (green). This error signal is used to synchronize the fast task. Leakage stabilization light passes through the FBG (blue dotted line) and reaches the central beamsplitter at the midpoint and the SNSPDs. Similarly, light from Node 2 arrives at the midpoint to arrive at the same beamsplitter, interfering with the light from Node 1. This beat can be measured by the SNSPDs, and the error signal is used to stabilize the global synchronization task.

of AOMs. This stabilization light is optically overlapped with light coming from the cryostat using a beamsplitter on the node, where the majority is transmitted and overlaps with the reflections coming from the diamond chip. This reflection is used to synchronize the ZPL light to the stabilization light via a local interferometer in the node, see Fig. 5.2b, left. This interferometer stabilization, called the local synchronization task, is discussed in Section 5.4, and effectively makes the stabilization light a good phase reference coherent with the ZPL light. The part of the stabilization light that does not go to the local photodiode, propagates via the same fiber as the ZPL photons, via the QFC to the midpoint. Fast phase disturbances in the fiber and phase noise from the excitation and

pump lasers are now present on both the stabilization light and ZPL light. The stabilization light is separated from the ZPL using a spectral filter due to the frequency offset of 400 MHz. The stabilization light is synchronised to light from a telecom reference laser by means of frequency modulation by of an AOM driver. We do this by generating an error signal on a balanced photodetector, as shown in Fig. 5.2b. This is called the fast synchronization lock and is described in more detail in Section 5.5.

Finally, the SNSPDs are used to assess the optical powers of the stabilization light to each detector, generating a single-photon detector based detection scheme for interference measurement. The error signal is generated using stabilization light that is leaking through the spectral filter at both arms, and meets on the central beampslitter connecting the two arms, see Fig. 5.2b. This measurement is inherently of low bandwidth, limited by the low powers used, and the SNSPDs' maximum count rate of $1\,\mathrm{MC\,s^{-1}}$. Higher bandwidths would demand lower integration times, and introduce too high shotnoise. Based on this phase measurement, the setpoint of the fast synchronization task at node 1 is altered. This allows the synchronization of the stabilization light combining from the two nodes, closing the synchronization scheme. As length variations (caused e.g. by temperature variations) over the long deployed fiber will generate non-negligible phase variations between light at the ZPL and stabilization frequency, this length variation is measured and the frequency-induced phase variation is compensated. Using this compensation, synchronization between ZPL light from both nodes is achieved, cf. Section 5.6.

Hence, 3 distinct synchronization tasks have been identified. Each of these synchronization tasks are performed using heterodyne phase measurements, and are described in more detail in the following three sections. An overview of the three tasks and their description, including noise sources, heterodyne frequency and feedback bandwidth is shown in Table 5.1. A full theoretical description of the synchronization tasks, underlying assumptions and the conditions that must be met for them to function is given in Sec. 5.9.

Synchronization task	**Light sources generating error signal and used actuator**	**Distortions and dominant frequency range**	**Heterodyne frequency**	0 dB **feedback bandwidth**
Local synchronization at the node	Reflected excitation light from Quantum Device and stabilization light measured on photodiode. Feedback implemented on AOM of excitation light.	• mechanical vibrations of objective lens w.r.t sample, 10 Hz-5 kHz • thermal drift of free space/fiber optics <1 Hz	400 MHz ±750 Hz	3 kHz
Fast synchronization at the midpoint	Stabilization light of selected node and reference light, measured on fast detector. Feedback via AOM acting on both the stabilization light and single photons. Actuator desaturation is done via the pumplaser of QFC.	• thermal effects on deployed fiber <10 Hz • mechanical vibrations of deployed fiber 1 Hz-5 kHz • phase noise in excitation laser, pumplaser and reference laser 1 kHz-50 kHz	215 MHz +0/-1500 Hz	224 kHz
Global synchronization at the midpoint	Stabilization light of node 1 and 2 measured on SNSPDs. Compensation through the setpoint of the fast synchronization loop from node 1.	• thermal drift at midpoint <10 Hz	1500 Hz	~50 Hz

Table 5.1: Summary of synchronization tasks.

5.4. LOCAL SYNCHRONIZATION AT THE NODE

The local synchronization tasks consists of ensuring that the reflected excitation light from the Quantum Device is phase-synchronized to the stabilization light. In this manner, we also ensure phase synchronization between the ZPL photons and the stabilization light. Namely, the ZPL light emitted at the NV center is phase-synchronous with the excitation light as they run over the same optical path[†]. The reflected excitation light is separated from the ZPL light based on polarisation using a free space beamsplitter. The stabilization light enters the system at the other input, after which we use a set of birefringent α-Bariumborate (αBBO) crystals to maximize the complex overlap between the orthogonally polarized reflected beam and the stabilization light. These crystals can correct for static differences in tip-tilt and translation errors between the stabilization and reflected light. After this optimization, we project both beams in a common polarization mode using a polarizer, and measure a sufficient interference signal using a photodiode. After demodulation, an analogue proportional controller with roll-off filter is used to generate a frequency-modulating signal for the AOM driver of AOME1, see Fig. 5.2.

To assess the performance of this control loop, a *linear* system identification experiment is performed for each of the synchronization tasks, as show in Fig. 5.3a. Within

[†]There is a small optical path difference between the emitter location and light reflected off the diamond surface, which can be kept constant via spatial optimization of the microcsope objective.

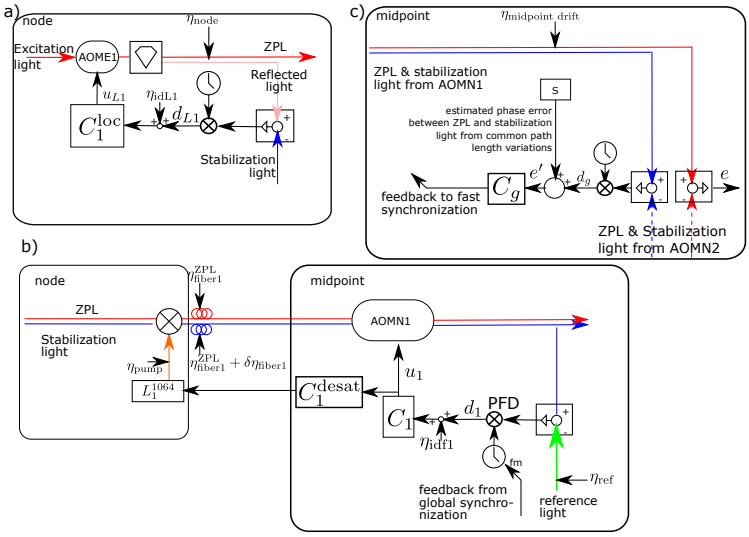

Figure 5.3: **Control scheme including main distortions. a) Local synchronization.** At the nodes, light exciting the NV is modulated using AOME1, where the controller C_1^{loc} applies a frequency modulation of the sine generator driving the AOM. This modulation depends on the heterodyne measurement of the beat between reflected and stabilization light at a balanced detector. Main noise sources are the phase noise of the excitation laser and mechanical vibrations and drift that are not shared by the stabilization light and the ZPL light (η_{node}). **b) Fast synchronization.** Subsequently, ZPL and stabilization light are frequency-converted by mixing with a 1064nm-pumplaser, and this light travels from both nodes to the midpoint. The stabilization light is separated from the ZPL light and interferes on a balanced detector with the reference laser, where the demodulation is performed with a Phase Frequency Detector (PFD). The PFD output is fed to a synchronization controller C_1 which modulates the ZPL and stabilization light with AOMN1. This fast controller suppresses mechanical distortions $\eta_{\text{fiber}}^{\text{ZPL}}$ shared between ZPL and stabilization light and phase noise from the excitation- and pumplaser, i.e. $\eta_{\text{excitation}}$ and η_{pump}. A varying setpoint to the fast synchronization task on node 1 is supplied by the global synchronization task. **c) Global synchronization**. The phase error between stabilization light at the SNSPDs is measured to suppress phase drifts $\eta_{\text{midpoint drift}}$ in the optical paths at the midpoint between reference laser and fast detectors, as well as between the fast detectors and the SNSPDs. This heterodyne measurement uses the SNSPD count rates as error signal. The global controller C updates the setpoint of the fast synchronization task of node 1. Since larger length variations will occur over the deployed fiber, a phase error will be introduced between ZPL and stabilization light, which is estimated using fiber-length measurements and compensated through S. Homodyne interference between ZPL light also is measured using the SNSPDs. The interference between ZPL light (red) is used in the entanglement generation process, and the error e directly reduces the maximum fidelity thereof.

each synchronization task we can identify a 'plant'. The plant is defined as the combination of the processing and actuation of the error signals (e.g. d_{L1} to u_{L1}). It consists of the actions of the frequency-modulation of a digital clock, amplification to drive the AOM, interference detection and demodulation of the electrical signal. While the frequency shifting behaviour of the AOM and subsequent demodulation via an analogue diode-based double balanced mixer are in practice nonlinear, we assume a linear input-output behaviour of the plant, which matches our observations.

To identify this subsystem[‡] in series with the controller we use a commonly used technique of injecting an additional but known broadband noise signal on the actuator (η_{idL1} and η_{idL1} in Fig. 5.3a. By measuring the resulting output with the feedback on and off and comparing them we can calculate important performance parameters such as the open-loop transfer function of the plant. We can also record the spectral densities of the residual phase noise. For more information see Sec. 5.9.

We show the result of this analysis for the local synchronization task in Fig. 5.4. It shows that a bandwidth of ~3 kHz is obtained[§], where the gain reaches a value of ~ 0.5 in Fig. 5.4a. The free-running Power Spectral Density (PSD) shown in Fig. 5.4b (orange) has the features of slow drifts below 10 Hz, as well as mechanical resonances between 100 Hz to 1000 Hz. By integrating the PSD when the controller is enabled (Fig. 5.4b, blue), we reach a cumulative phase error of 12° RMS, as shown in Fig. 5.4c.

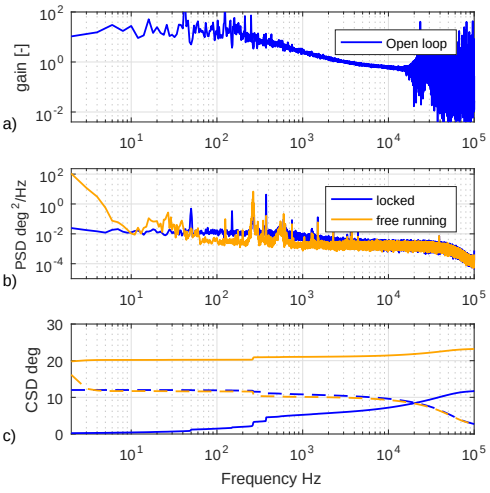

Figure 5.4: **Performance of local synchronization task**. a) Identified linear dynamical relation between control output u_{L1} and demodulation output d_{L1} (demodulated around DC as used as control input), called plant. b) Power Spectral Density and c) Cumulative and Inverse Cumulative Spectral Density of residual phase error without additional noise injection.

[‡]In contrast to the final operation, the stabilization light is constantly available, i.e. the 2.5 µs 'dark' periods every 10 µs period are avoided for the identification experiments.

[§]To define the synchronization bandwidth, we use the 0dB point of the open loop dynamics, given by the controller and plant of the system.

5.5. FAST SYNCHRONIZATION AT THE MIDPOINT

Both fast synchronization loops at the midpoint have the goal to synchronize the stabilization light of the nodes to light of the same reference laser which is located in the midpoint, see Section 5.3 and Fig. 5.3, and have the same design for both arms coming from Node 1 and Node 2, and we discuss the workings in the context of Node 1. After conversion and subsequent arrival in the midpoint, stabilization light of the node and reference light interfere and is measured with a balanced photodetector, demodulated using a phase frequency detector (PFD) and then passed to an analog controller $C1$ of proportional-integral type. The output of this controller is then used for frequency modulation of the AOM AOMN1. To limit the frequency-modulation range of this AOM to avoid reduced optical transmission, de-saturation is required, which is performed via additional feedback to the pump laser frequency back at the node. This control signal is sent over an User Datagram Protocol (UDP) connection (update frequency 500 Hz) from the midpoint to the node.

To identify the synchronization performance, we used the same techniques as outlined for the local synchronization task. The resulting open-loop transfer function is identified and shown in Fig. 5.5a. It shows that a 220 kHz control bandwidth is achieved. By integrating the 'locked' PSD of the residual phase noise (Fig. 5.5b), we find the cumulative phase error of 21° RMS, as shown in Fig. 5.5c. The achieved bandwidth is realized by the short distance between error-signal generation and actuation, and fast servo control for error signal processing. Spectral data of the recorded signals is shown in Fig. 5.8a.

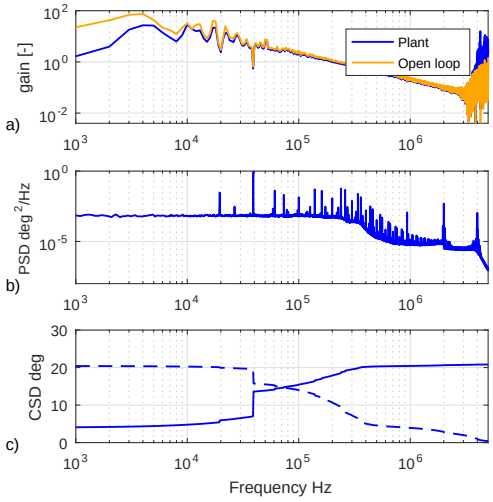

Figure 5.5: **Performance of fast synchronization task.** a) Identified linear dynamical relation between control output u_1 and demodulation output d_1 (demodulated around DC as used as control input), called plant, and between control input and demodulation output, i.e. the open-loop behaviour. b) Power Spectral Density and c) Cumulative and Inverse Cumulative Spectral Density of residual phase error.

5.6. GLOBAL SYNCHRONIZATION

The global synchronizing feedback is required to suppress low-frequent phase drifts in the optical paths at the midpoint between reference laser and fast detectors, as well as between the fast detectors and the SNSPDs, schematically depicted in Fig. 5.3. A heterodyne phase error measurement is obtained from the SNSPD measurement by converting the single-photon count rate to well-defined pulses using an analog pulse stretcher, subtracting both pulse signals and lowpass-filtering the result. Employing a small frequency offset between the stabilization light between the nodes, we can detect a heterodyne beat at 1500 Hz, still below the relatively low bandwidth of the error signal generated with the SNSPDs, while making the measurement insensitive to power fluctuations (see Table 5.1 for details). The error signal is processed and fed back by changing the setpoint of one of the fast synchronization scheme by an amount determined by controller C', which affects the phase shift introduce by AOMN1, cf. [31]. A proportional controller is used in this setup.

We compensate the expected phase differences between stabilization and ZPL light over the deployed fibers (i.e., $\delta\eta_{\text{fiber1}}$ and $\delta\eta_{\text{fiber2}}$, which will occur due to the optical frequency mismatch, combined with length variations over these fibers (see also 5.9.3). Exploiting the measurement of these length variations using roundtrip-time measurements, estimates $\tilde{\delta}\eta_{\text{fiber1}}$ and $\tilde{\delta}\eta_{\text{fiber2}}$ are obtained in subsystem S in Fig. 5.3, cf. [32].

The performance of the global synchronization is illustrated in Fig. 5.6, where the spectrum with and without this feedback is shown. The dominant noise-sources are below 10 Hz, as seen in the unlocked PSD of the phase noise in Fig. 5.6. This is because all high-frequency noise is removed by the fast synchronization task, and only slow drifts remain. This controller yields a cumulative phase error of 8° RMS, as shown in Fig. 5.6c.

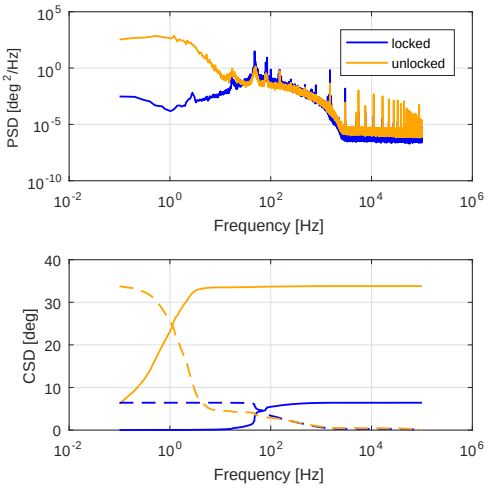

Figure 5.6: **Performance of global phase synchronization**. Power Spectral Density (top) and Cumulative and Inverse Cumulative Spectral Density (bottom) of residual phase error.

5.7. SYNCHRONIZATION OF REMOTE NODES.

We now measure the performance of the complete system when all the synchronization tasks are active. We evaluate the system by measuring the phase error e between the excitation lasers of the both nodes, see Fig. 5.3c. The system is deployed at three locations in the Netherlands, where the nodes are separated by ≈10 km, connected to the midpoint by 10 km and 15 km of fiber between the cities The Hague and Delft respectively. This configuration is has been used to generate entanglement over this link in Chapter 6.

We assess the optical performance by using classical light fields reflected off the diamond surface, which should result in homodyne interference, and allows us to access the relative optical phase between the nodes. This light originates in the nodes and travels the same optical path as the ZPL photons (which are coherent with this light), up to a small propagation through the diamond sample. The intensity of this reflected light can be adjusted on the nodes (>1 kC s^{-1}), allowing for quick integration times and high signal-to-noise ratio in the SNSPDs. We conduct this measurement under identical conditions as an entanglement generation experiment. This means that the powers of the optical fields, both reflected and direct, and their on/off modulation are done in the way one does during entanglement generation. The reflected laser pulses are located at the same location in the sequence as where the optical excitation would be, making the phase measured in this experiment a good metric for the expected performance.

The interference and subsequent measurement by the SNSPDs of this reflected light is show in Fig. 5.7a, with clear interference shown in the region where the light fields overlap in time. The contrast of this interference can be corrected for imbalance of the incident power, and by sweeping the phase setpoint a full fringe can be taken (Fig. 5.7b). Fitting these fringes with a single cosine $I = \frac{1 \pm C\cos(\phi+\phi_0)}{2}$, we can retrieve the contrast C and setpoint ϕ_0 of the synchronised system. By assuming that the loss of contrast C is solely due to a normally distributed residual phase error, we calculate its standard deviation from the contrast which is $\sigma_{measured}$ =35.5°. This matches well with the expected residual phase noise, which would be the quadratic sum of all five independent synchronization tasks: $\sigma_{total} = \sqrt{2\sigma^2_{local} + 2\sigma^2_{fast} + \sigma^2_{global}}$ =34.9°. By repeating this measurement and recording both contrast and setpoint, we can characterize the long-term behaviour of the phase synchronization system (Fig. 5.7c. We find that the phase synchronization is stable over a time-span of more than ten hours, showing a high contrast. The long term drift (Fig. 5.7d of the phase setpoint is almost completely explained by the offset in phase due to the combination of the frequency offset and long fiber length variation, that was calculated but not compensated in this test. The resulting phase setpoint distribution is shown in the bottom right of Fig 5.7, showing a sharp distribution around a setpoint of 0°.

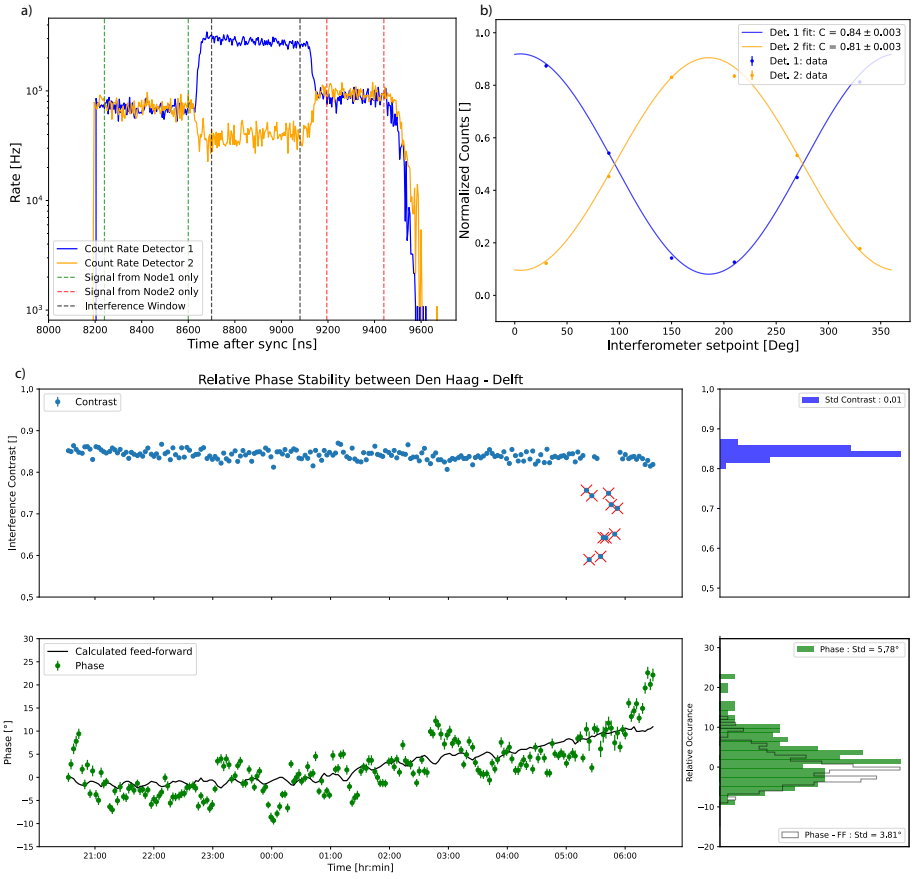

Figure 5.7: **Performance of the total system performing phase synchronisation. a)** Interference of reflections of the excitation lasers from the diamond chip from, as measured by the SNSPDs in the midpoint. The blue (orange) line indicate the rate of photons incident on the first (second) detector. The shaded indicate regions in time where only light from Node1 (green) or Node2 (red) is present show no interference. In the overlapping region (grey), the light interferes and is directed to predominantly one detector, indicating interference of the weak laser fields. **b)** By sweeping the local oscillator of the global synchronization task in 5.3c, we change the setpoint of the interference, directing light into one or the other detector, as show by change of preferred direction to detector 1 (blue) or 2 (orange). By correcting the count rates for imbalance, we can fit these oscillations with a single cosine, recovering the relative phase of the excitation lasers of the two nodes. The non-perfect contrast of this oscillation represent the residual phase noise in the system at timescales below the measurement time (≈seconds). **c)** Measurement of the relative optical phase between the paths coming from Delft and Den Haag over a timespan of ten hours. We measure a constant average contrast over the full duration of more than 200 measurement, with the exception of a group of 10 measurements. These were the result of one of the excitation lasers lasing multi-mode, as picked up a separate monitoring scope. **d** The measured relative phase shows a small drift over this time-frame, without the compensation for phase slips due to large fiber drifts (green, see 5.9.3). Plotting the calculated the calculated feed-forward based on the round-trip time between the two nodes and the midpoint shows the correlation. When taking this feed-forward into accounts, the resulting spread standard deviation of the phase setpoint is below 4° over the course 10 hours (white histogram).

5.8. CONCLUSION AND OUTLOOK

We have designed, built and evaluated an extendable phase synchronization scheme to enable entanglement generation between solid-state emitters, compatible with the telecom L band and large node separation. The phase synchronization is achieved between two independent excitation lasers, which are integrated in an NV-center quantum network node, connected over deployed fibers. The introduction of stabilization light allows to generate reliable phase measurements with low shotnoise and enable the ability to guide the stabilization light to an alternative detector. Therefore we can use two distinct feedback loops at the midpoint, to compensate both the high-frequent distortions via a balanced photodetector but also compensate the low-frequent distortions using the SNSPDs, achieving synchronization at the central beamsplitter where the single-photon paths of two distant nodes interfere. The separation of the overall synchronization task and tailoring the control schemes to the specific noise present allow us to realize high-performing synchronization using independent excitation lasers and at a metropolitan scale node separation. By making the synchronization tasks robust against drifts of optical power and compensating for large fiberlength variations, phase stability sufficient for entanglement generation is achieved for more than 10 hours.

Our implementation has a few distinct advantages. First, our method only requires the distribution of a phase reference in the RF domain, e.g. 10 MHz, over the network. This can be done over deployed fiber using the White Rabbit [33] protocol, and is easily distributed locally via amplified buffers. Second, due to the choice of AOMs as feedback actuators and additional offloading on the pump laser of the QFC, the system has both a fast step response, and the feedback range is only limited by the QFC conversion bandwidth. Additionally, the achieved feedback bandwidth lowers the requirements on the linewidth of our lasers used on the nodes, simplifying their design and avoiding complex optical reference distribution. Furthermore, the design allows the reduction of the optical intensity of signals that could interfere with the entanglement generation, by using heterodyne schemes. This boosts the signal-to-noise ratio of the generated error signal, and at the same time limits the crosstalk with the quantum system and single-photon emission.

This scheme also allows for scaling the number of nodes in the network. The most straightforward way of scaling would be in a star pattern, as all the incoming nodes could be continuously synchronized with the same optical reference. To establish a connection between two nodes, one has to switch the incoming photons to the same beamsplitter. With the appropriate feedback speed one can make the newly switched paths phase-stable before the photons arrive from the remote nodes. A similar approach can be taken on a line-configuration with multiple midpoints if the frequency difference between the optical references used at each midpoint can be kept reasonably small, below the feedback bandwidth of the fast synchronization.

Further improvements can be made for the local and fast subtasks, which we will discuss starting with the local synchronization task. Currently the fully analog and integral nature via feedback on an AOM causes a high gain at low frequencies. This means that it is sensitive to small analog input offsets to this AOM when the errorsignal generation is paused. This results in the reduction of the free-evolution time, the time that the phase

stays synchronised without feedback. Using a proportional feedback or a fast digital controller could circumvent this. The residual phase noise present in the fast synchronization could be reduced in a number of ways. Excitation lasers with less phase-noise would lead to a direct improvement of the performance. Additionally, more in-depth tuning of the control to the noise-spectrum measured could deal more effectively with the noise. Further investigations into the exact noise spectrum and more complex control techniques could further enhance the performance of the fast synchronization.

As a conclusive demonstration of the system we recently used it to generate heralded entanglement between two NV-centers over deployed metropolitan fiber. Here the phase synchronization was time-multiplexed with the emission of single-photons by the NV-centers. We believe that this scheme can form the basis for many future implementations in developing large-scale entanglement over deployed fiber networks, which we discuss in the following Chapter.

5.9. SUPPLEMENTARY INFORMATION

5.9.1. SYSTEM IDENTIFICATION DETAILS.

We injected additional noise at the location shown in Fig. 5.3 while the control loop is active and measured the signals u_{L1} and the demodulated output d_{L1} of the local synchronization loop. Throughout the paper, these measured interference powers $x(t_i), i = 1,\ldots,N$, are analysed by subsequently taking the Hilbert transform to compute the phase of the resulting analytical signal [34]. Additionally we can plot the spectral content measured during the identification experiments. This is done with using Welch's averaged periodogram method [35], and is shown in Fig. 5.8. We repeat this analysis for the fast synchronization loop, injecting noise, monitoring the signals and demodulated output, and perform the analysis. The spectral content of the measurements are show in Fig. 5.8, with the analysis in the main text.

For the global synchronization task injecting noise posed a challenge, and we therefore only measured the residual phase error under open/closed loop conditions.

5.9.2. THEORETICAL DESCRIPTION OF SYNCHRONIZATION RESULT

Here we give a theoretical description of the phase synchronization scheme, and determine the conditions that must hold for the phase synchronization to succeed. We start off by describing some definitions and assumptions underlying the analysis and provide a schematic that includes all relevant fields and optical paths. This allows us to define the central stabilization task we want to achieve, and how we achieve it by breaking up the task into smaller synchronization tasks.

5.9.3. DEFINITIONS AND ASSUMPTIONS.

We make the following definitions and assumptions in the derivation of the phase conditions:

- In propagating the fields we treat them all as monochromatic plane waves that propagate along the optical axis, the $\hat{z}$ direction. We can therefore write the com-

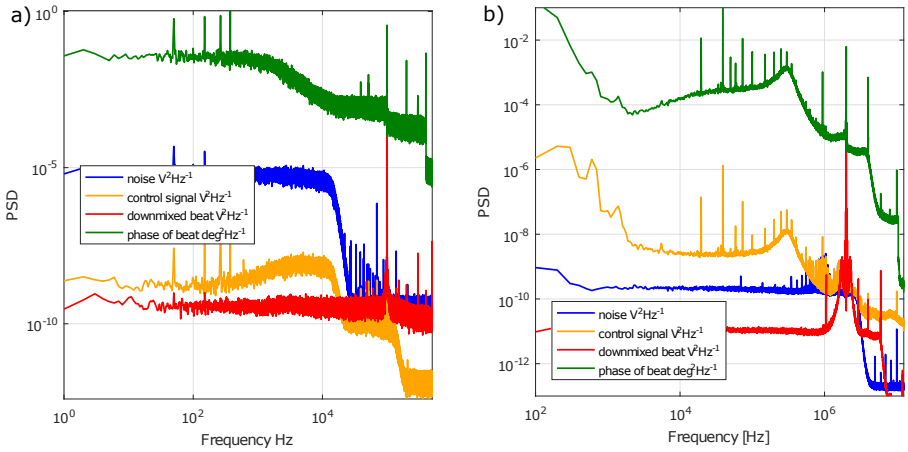

Figure 5.8: **System identification of synchronization tasks.**a) Power Spectral Density of noise injected before the controller η_{idL1}, control output signal u_{L1}, measured beat signal m_{L1} (analoguely downmixed to 100 kHz), and phase error on this signal, respectively, for the local synchronization task. b) Power Spectral Density of noise injected before the controller η_{idf1}, control output signal $u1$, measured beat signal $m1$ (analoguely downmixed to 2 MHz), and phase error on this signal, respectively, for the fast synchronization task.

plex wavefunction of a field with frequency f_i in a medium with refractive index n_l depending on time t and space z as

$$U(z,t) = Ae^{j\phi_i} = Ae^{j(\omega_i t - k_i z)} \tag{5.1}$$

with A being a constant, $\omega_i = 2\pi f_i$ and $k_i = \frac{n\,\omega_i}{c}$ with c the speed of light in vacuum and n the refactive index. We ignore all effects of a varying spatial intensity distribution or curvature of the wavefront in free space.

- We treat reflection and transmission through the Ultra-narrow filter as having no impact on the phase, an assumption that is true if the central frequency is kept stable, and the reflection is far away from the resonance of the filter.

- We assume that the change in refractive index for small frequency differences (<1 GHz) or temperature variations are negligible.

- All clocks (RF sources as references in the synchronization) used in the scheme are coherent with each other. This is realized by providing a 10 MHz External Reference to each of the signal generators, and finding clock settings that minimize any non-idealities in the signal generation of the devices used.

We make extensive use of heterodyne interference, which is the interference of two fields of different frequencies. When measuring the intensity of this field with a photodiode, the combined field intensity is described as

$$I = |U_1 + U_2|^2 = |U_1|^2 + |U_2|^2 + U_1^* U_2 + U_1 U_2^* \tag{5.2}$$

Filling in two plane waves of equal amplitude $\sqrt{I_0}$ at the start of the lasers, but different frequencies and initial phase, we get

$$I(t) = 2I_0 + 2I_0 \cos\big((\omega_2 - \omega_1)t + \frac{n}{c}(\omega_1 D_1 - \omega_2 D_2) + (\theta_2 - \theta_1)\big), \tag{5.3}$$

where THz-frequencies are dropped. The intensity is varying in time with the difference of the two frequencies of the original waves (called a beat), with change of the distances D_1 and D_2, and with a phase given by the initial phases of the two fields. This allows us to use the photodiode to generate an error signal that contains both the difference frequency $\omega_1 - \omega_2 = \Delta\omega$ and the relative phase of the two optical waves. By choosing the frequency difference of the two optical fields in the RF regime (<1 GHz), we can use RF-generators, mixers, amplifiers and filters to stabilize this errorsignal. This synchronizes the two fields, and adjusts for frequency variations, drifts of the distances to the point of interference, and phase jumps due to the linewidth of the laser. This is the underlying principle to stabilize the relative optical phase of two optical fields, at a certain location in space.

5

It is useful to give a proper definition of what we mean when we say two phases are synchronized. When two optical fields in a task are *synchronized*, it means that at a specific point in space z_s, the two fields $U_1(z_s, t)$ and $U_2(z_s, t)$ have a phase relation that can be written as

$$\big(Arg(U_1(z_s,t)) - Arg(U_2(z_s,t))\big) - \omega_{clock}\, t \equiv \eta(t) \tag{5.4}$$

with ω_{clock} the clock frequency of the RF-source used in the signal processing and $\eta(t) - \mu \ll \pi$ the residual phase error and μ a constant. For sampling frequencies much smaller than the feedback bandwidth (and therefore slower than phase residuals), these samples are independent of their evaluation time $t_i, \imath = 0, 1, 2, ...$, and thus follow a probability distribution with constant parameters in time, i.e.

$$\eta(t_i) \in \mathcal{N}(\mu, \sigma),\ i = 0, 1, 2, ..., \tag{5.5}$$

where, for small angles, $\mathcal{N}$ is a normal distributed variable with mean μ and standard deviation σ. Experimentally we can choose $\mu \in [0, 2\pi]$ by changing the clock setpoint used for the stabilization, and $\sigma \ll \pi$ gives the performance of the synchronization: smaller σ indicates better synchronization performance. For the special case where $\omega_{clock} = 0$, or when one has access to a source coherent with the clock, one can sample the distribution $\mathcal{N}$. For entanglement generation experiments this conditions holds, where the sampling occurs at the measurement of a single-photon every couple of seconds.

5.9.4. ERRORS DUE TO LARGE LENGTH VARIATIONS

Suppose we have two coherent, co-propagating fields U_1 and U_2 with different frequencies ω_1, ω_2, on a long fiber with length L. The first field is (perfectly) synchronized at the end of the fiber $z = L$ with a phase actuator that works **on both** U_1 and U_2, with the phase setpoint $\theta_{Ref} := \frac{nL\omega_1}{c}$. The phase that the field U_2 has at $z = L$ is than given as

$$\varphi_2\big|_{z=L} = \frac{nL\omega_2}{c} = \theta_{Ref} + \frac{n\,L(\omega_2 - \omega_1)}{c} = \theta_{Ref} + \frac{n\,L(\omega_2 - \omega_1)}{c}, \tag{5.6}$$

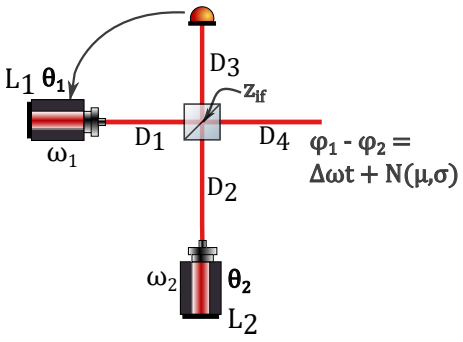

Figure 5.9: **Phase synchronization.** An example of two independent sources 1 and 2, being synchronized by using an interference measurement on one output D_3 of a beamsplitter, traveling further via D_4. The interference location z_{if} is the point on the beamsplitter where the beams meet. Depending on the setpoint and performance of the synchronization task, the relative phase $\phi_1 - \phi_2$ can be written as a time dependent term, plus a normal distribution $\mathcal{N}$ with mean μ and standard deviation σ that do not depend on time.

which is at a constant offset of θ_{ref}. This means the synchronization task of U_1 is also synchronizing U_2, it is no longer varying in time, albeit at a constant offset. If now the fiber expands to length $L+\Delta L$, the synchronization tasks aims for phase $\varphi_1\big|_{z=L+\Delta L} \rightarrow \theta_{Ref}$. Hence,

$$\varphi_2\big|_{z=L+\Delta L} = \frac{n\,(L+\Delta L)\omega_2}{c} = \frac{n\,(L+\Delta L)\omega_1}{c} + \frac{n\,(L+\Delta L)(\omega_2-\omega_1)}{c} \tag{5.7}$$

$$= \theta_{Ref} + \frac{n\,L(\omega_2-\omega_1)}{c} + \frac{n\,\Delta L(\omega_2-\omega_1)}{c} \tag{5.8}$$

$$= \frac{n\,L\omega_2}{c} + \theta_{err}(\Delta L), \tag{5.9}$$

with $\theta_{err}(\Delta L) = \frac{n\,\Delta L(\omega_2-\omega_1)}{c}$ an additional term, indicating the phase of U_2 has moved with respect to its original position at L, and is no longer synchronized. therefore we have to be careful in exchanging phase terms of fields that are co-propagating and synchronized over long fibers, but at slightly different frequencies. Using the numbers in our system, $\Delta\omega = 2\pi\times 400\,\text{MHz}$, and a ΔL of 2 cm expansion of the fiber would result in a $\theta_{err}(0.02)$ of 10° of phase error. Given the low thermal expansion coefficient of silica of $\frac{dL}{dT} = 5.5\times10^{-}7\text{m}\,\text{K}^{-1}$, this effect only happens when large fiber lengths and temperature drifts are involved. In the main text, Fig. 5.7 shows a measurement of this effect, where the value calculated using our accurate timing hardware matches the value measured by the phase interference well.

For a full overview of all the optical fields used, we refer to Table 5.2 that gives the typical central frequency, linewidth and powers. In Fig. 5.10 we show the division of the connection of one node to the midpoint into separate optical paths, used in the derivation of the phase synchronization requirements. These sections ($D1$, $D4$, $D5$ and $D7$) form a continuous path between the excitation laser L^{Ex} and the central beamsplitter in the midpoint where the relevant interference takes place, plus additional sections that

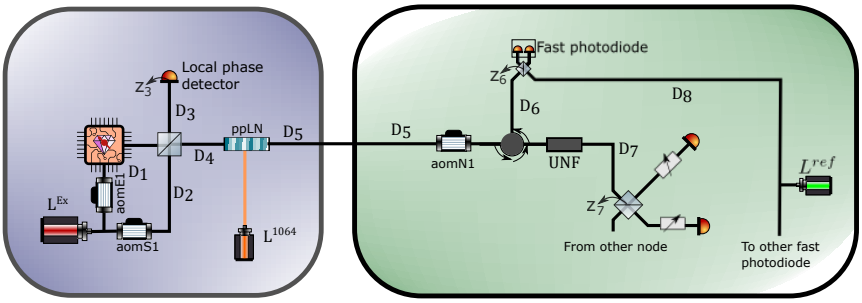

Figure 5.10: **Schematic showing the division of optical paths in the system, used for deriving the synchronization tasks.** The main synchronization task, and the subdivision of local, fast and global synchronization tasks is given in the main text Fig. 5.2

are needed to describe the individual synchronization tasks ($D2$, $D3$, $D6$ and $D8$). A short description, typical distances and extra information is given in Table 5.3.

Optical field	NV emission	Excitation	Reflections	Stabilization	Leakage Stab.	QFC Pump	Reference
Typ. Freq. [GHz]	470450	470450	470450	470450.4	470450.4	281759	188691
Typ. Linewidth [kHz]	12.3e3	~10	~10	~10	~10	<20	<0.1
Power in Local PD	Single photons	~5uW	~1nW	~5uW	-	-	-
Power in Midpoint	Single photons	-	<1pW	~30nW	Single Photons	-	~5mW

Table 5.2: Overview of optical fields.

5.9.5. CENTRAL SYNCHRONIZATION TASK

We define the central synchronization task as achieving a stable phase between the photon emission on each node, measured at the location of the central beamsplitter in the midpoint, denoted z_7 in Fig. 5.10. This is the central requirement for entanglement generation via the single-click protocol, as discussed in the main text. To simplify things, we will first derive the stability of the relative phase between the two excitation lasers on each node, as measured in the central beamsplitter in the midpoint, and then argue that the single photon emission is coherent with this field (see Sec. 5.9.13).

The time-dependent relative phase at the central beamsplitter can be written as

$$\eta(t) = \phi(t, z_7)^A - \phi(t, z_7)^B \tag{5.10}$$

where $\phi(t, z_7)^i$ is the phase of the field coming from node i at the location of the central beamsplitter z_7. When all the synchronization tasks are active, the error $\eta(t)$ will be small ($\ll \pi$), and under probabilistic entanglement generation samples this time-dependent phase is sampled, and the errors form a distribution $\mathcal{N}_{Tot}$.

Section	Description	Length [m]	Dominant noise source
D_1	Excitation path, from laser, via AOM, objective and diamond chip to local central beamsplitter	10	Objective stage/vibrations and laser phase noise
D_2	Local stabilization light path, from laser, via AOM, free-space optics, to local central beamsplitter	10	Fibre optics/vibrations
D_3	Local central beamsplitter to local phase projection (Polarizing BS)	2	Long term optics drift/birefringent optics
D_4	Local central beamsplitter, via free-space optics, to QFC crystal	2	-
D_5	QFC crystal, via deployed fibers, through EPC, AOM to Ultra-narrow filter	>10e3	Thermal expansion/environmental vibrations
D_6	Backwards reflection off UNF, to BS at fast detector	2	Vibrations/loose fibers
D_7	Transmission through UNF, towards central beamsplitter in midpoint	2	Vibrations/loose fibers
D_8	Reference laser, via fibers, to BS at fast detector	2	Vibrations/loose fibers

Table 5.3: Overview and description of optical paths.

We can write $\phi(t, z_7)$ by following the fields through the setup as shown in the main text Fig. 5.2. It is given by

$$\phi(t, z_7) = \theta_{Ex} + \frac{n\omega_{Ex}}{c}(D_1 + D_4) - \theta_{1064} + \frac{n'\omega'_{Ex}}{c}(D_5 + D_7) + \omega'_{Ex}t, \tag{5.11}$$

where ω_{Ex} the frequency of the excitation laser, $\theta_{Ex/1064}$ are the phases of the excitation and QFC pump laser respectively. The $'$ denotes the fact that the field has been converted, meaning $\omega'_{Ex} = \omega_{Ex} - \omega_{1064}$. For the other node to the midpoint we can write an identical equation, containing the same but uncorrelated terms. In order to synchronize these two fields, we need to get rid of the terms that are varying rapidly in time (see Tab. 5.3). The next step is to fill in the synchronization conditions guaranteed by the synchronization tasks realized in the setup.

5.9.6. LOCAL SYNCHRONIZATION TASK

The local synchronization task synchronizes the relative phase of the light coming from two paths consisting of $D_1 + D_3$, and $D_2 + D_3$, both starting at the excitation laser and ending at detector z_3. In the path $D_2 + D_3$, the AOM shifts the light in frequency with 400 MHz±750 Hz. Due to the two paths being different polarization states of the light, the actual interference happens after projection into the same state by a polarizer, and subsequent detection by the detector after travelling D_3, which we denote as z_3, see Fig. 5.2b and Fig. 5.10. The synchronization error is given by the equation

$$\eta_{loc}(t) = \phi^A(t, z_3) - \phi^B(t, z_3) - \omega_{loc}t,$$

and can be written out as

$$\omega_{Loc}t + \eta_{loc}(t) = \left(\theta_{Ex} + \frac{n\omega_{Ex}}{c}(D_1 + D_3) + \omega_{Ex}t\right) - \left(\theta_S + \frac{n\omega_S}{c}(D_2 + D_3) + \omega_S t\right) \tag{5.12}$$

with θ_{Ex} the phase due to the finite linewidth of the Excitation laser, and ω_S the frequency of the stabilization light and $\omega_{loc} = \omega_{Ex} - \omega_S$ the frequency and θ_{loc} the phase of

the clock used as reference. By ensuring that $D_1 - D_2$ is well within the coherence length of the excitation laser, we can write $\theta_{Ex} = \theta_S$. The remaining terms are slowly varying in time with respect to the feedback bandwidth, as shown in the main text 5.4. The performance parameter σ_{loc} is also given there. We can also write 5.12 in a different form that makes it easier to use in future derivation as

$$\theta_{Ex} + \frac{n\omega_{Ex}}{c} D_1 = \theta_S + \frac{n\omega_S}{c} D_2 + \frac{n(\omega_S - \omega_{Ex})}{c} D_3 + \eta_{loc}(t), \tag{5.13}$$

5.9.7. FAST SYNCHRONIZATION TASK

The next synchronization task we describe is the fast synchronization task. This consist of again two arms, A and B, that meet at the point z_6. Path A is from the excitation laser, via the stabilization split-off (D_2), through the QFC (D_4), over the long deployed fiber (D_5), through the AOM at the midpoint, reflected by the UNF (D_6) to reach z_6. Path B is from the Reference laser directly to z_6 (via D_8), see Fig. 5.2b and Fig. 5.10. We can again define the synchronization error for this task as

$$\eta(t)_{fast} = (\phi^A(t, z_6) - \phi^B(t, z_6)) - \omega_{fast}(t),$$

and filling in the terms we find

$$\omega_{fast} t + \eta_{fast}(t) = \left(\theta_S + \frac{n\omega_S}{c}(D_2 + D_4) - \theta_{1064} + \frac{n'\omega'_S}{c}(D_5 + D_6) + \omega'_S t\right) - \left(\theta_{Ref} + \frac{n\, D_8\, \omega_{Ref}}{c} + \omega_{Ref} t\right) \tag{5.14}$$

Where $\omega_{fast} = \omega'_S - \omega_{Ref}$ is the frequency and θ_{loc} the phase of the reference clock used in the fast lock (see Fig. 5.3b). Again, in order for this synchronization to work, we need to have fast enough feedback with respect to the noise present. Because this equation contains the three phase term due to the linewidth of the lasers ($\theta_{Ex/1064/Ref}$), of which θ_{Ex} is by far the dominant (see Table 5.2). For long fibers, the term containing the long fibers (D_5) can also induce fast phase fluctuations. We show that we can ensure these conditions in the main text, Fig. 5.5, and give the performance parameter σ_{fast}. We can rewrite 5.14 to a more useful form as

$$\theta_S + \frac{n\omega_S}{c}(D_2 + D_4) - \theta_{1064} + \frac{n'\omega'_S}{c} D_5 + \omega'_S t = -\frac{n'\omega'_S}{c} D_6 + \omega_{fast} t + \eta_{fast}(t) + \theta_{Ref} + \frac{n\, D_8\, \omega_{Ref}}{c} \tag{5.15}$$

5.9.8. GLOBAL SYNCHRONIZATION TASK

The final synchronization task is the global synchronization, which is the final task that closes the feedback system between the two distant nodes. It takes as input two arms, A and B, that interfere at the point z_7, the central beamsplitter. The fields that are interfering is stabilization light that is leaking *through* the UNF in each arm. This is light

that came from the same location as in the fast synchronization task 5.14, but is now travelling towards the SNSPDs. We can write the optical phase coming from node A/B as

$$\phi^{A/B}(t,z_7) = \theta_{Ex} + \frac{n\omega_S^{A/B}}{c}(D_2^{A/B} + D_4^{A/B}) - \theta_{1064} + \frac{n'\,\omega_S^{'A/B}}{c}(D_5^{A/B} + D_7^{A/B}) + \omega_S^{'A/B}\,t \quad (5.16)$$

We described in the main text that the global synchronization task only needs a small bandwidth (1000 Hz) to be realized. However, equation 5.16 contains many fast terms, such as the laser linewidth of the Excitation laser. Therefore the global synchronization can only be realized once the fast synchronization condition is met. This becomes apparent when we filling in 5.15 in 5.16, giving:

$$\phi^{A/B}(t,z_7) = \eta_{fast}(t) + \theta_{Ref} + \frac{n\,D_8^{A/B}\,\omega_{Ref}}{c} + \frac{n'\,\omega_S^{'A/B}}{c}(D_7^{A/B} - D_6^{A/B}) + \omega_S^{'A/B}\,t \quad (5.17)$$

and using that to write down synchronization task error for the global lock:

$$\eta(t)_{glob} = \left(\phi^A(t,z_7) - \phi^B(t,z_7)\right) - \omega_{glob}(t) - \theta_{glob}(t) \quad (5.18)$$

which, when grouping similar terms pairwise, becomes

$$\eta(t)_{glob} = \eta_{fast}^A(t) - \eta_{fast}^B(t) + \quad (5.19)$$

$$\theta_{Ref}^A - \theta_{Ref}^B + \frac{n\,(D_8^A - D_8^B)\,\omega_{Ref}}{c} + \quad (5.20)$$

$$\frac{n'\,\omega_S^{'A}}{c}(D_7^A - D_6^A) - \frac{n'\,\omega_S^{'B}}{c}(D_7^B - D_6^B) + \quad (5.21)$$

$$(\omega_S^{'A} - \omega_S^{'B})\,t - \theta_{glob}(t) \quad (5.22)$$

where the super-script$^{A/B}$ denotes the field coming from node 1/2 and $\omega_{glob} = (\omega_S^{'A} - \omega_S^{'B})$ the frequency and θ_{glob} the phase of the clock used as reference in the global synchronization (see Fig. 5.3c). We will go over this equation term by term. The first line of the equation are the residual terms from the fast synchronization tasks $\eta_{fast}^{A/B}(t)$, which are the residuals of the fast lock, and therefore too fast for the global synchronization to provide any feedback on. That is why they also appear on the other side of the equation, as they remain an error source in the system. The second line is the phase contribution due to the linewidth of the reference laser and optical path of the delivery of the laser to the fast photo-diodes. By using the same length fibers ($D_8^A \sim D_8^B$) we can minimize both the effect of fiber drifts, as well as the effect of the Reference laser linewidth. The third line of equation 5.19 shows two terms that are dependent on the distance from the UNF to the two points (fast photo-diode z_6 and central beamsplitter z_7) of interference. These are more difficult to keep equal, and is best practice to keep these fibers in the same optical rack such that they share vibrations/temperature fluctuations. We can also identify the synchronization error of the global synchronization *by itself* by excluding

the fast errors and writing as

$$\eta_{glob}(t) = \theta^{A}_{Ref} - \theta^{B}_{Ref} + \frac{n\,(D^{A}_{8} - D^{B}_{8})\,\omega_{Ref}}{c} + \frac{n'\,\omega'^{A}_{S}}{c}(D^{A}_{7} - D^{A}_{6}) - \frac{n'\,\omega'^{B}_{S}}{c}(D^{B}_{7} - D^{B}_{6}) - \omega_{glob}\,t \tag{5.23}$$

Now that we have discussed all three different synchronization tasks and described their synchronization task error, we can go back go to 5.10 and fill in the synchronization conditions.

5.9.9. SUBSTITUTION LOCAL SYNCHRONIZATION

We start with equation 5.11 and fill in the local synchronization condition in the form of Eq. 5.13 to get

$$\phi(t, z_7) = \theta_S + \frac{n\omega_S}{c} D_2 + \eta_{loc}(t) + \frac{n(\omega_S - \omega_{Ex})}{c} D_3 + \frac{n\omega_{Ex}}{c} D_4 - \theta_{1064} + \frac{n'\omega'_{Ex}}{c}(D_5 + D_7) + \omega'_{Ex}\,t \tag{5.24}$$

where the term $\frac{n(\omega_S - \omega_{Ex})}{c} D_3 = \theta_{err}(\Delta D_3)$ is due to the fact that the interference for the local synchronization happens at a distance D_3 away from where the stabilization light ω_S is split off (local beamsplitter). The phase is therefore sensitive to expansion/contraction of D_3, albeit with only the frequency difference of $\omega_S - \omega_{Ex}$. Therefore drifts of D_3 are minimized by making the distance short and housed in a temperature stabilized environment and can be considered constant.

5.9.10. SUBSTITUTION FAST SYNCHRONIZATION

In order to fill in the fast synchronization task into eq. 5.24, we need to substitute all the terms containing ω_{Ex} with ω_S. These fields are co-propagating from the local beamsplitter towards the QFC (D_4) and onward. Because the local synchronization ensure their mutual coherence at the local beamsplitter, and ω_S is stabilized in the midpoint at the fast photodiode, we can follow the substitution method as outlined in Section 5.9.4, taking into account the expected fiber drifts. The terms containing ω_{Ex} contain the distances D_4, D_5 and D_7. We remark that the drifts in $\theta(\Delta D_4)$ and $\theta(\Delta D_7)$ are negligible when the (fiber) lengths are short($\approx$10 m) and will be considered constant and left out, however $\theta(\Delta D_5)$ can be significant due to the length of D_5 (see Table 5.3). Completing the substitution gives us:

$$\begin{aligned}\phi(t, z_7) = \theta_S + \frac{n\omega_S}{c}(D_2 + D_4) + \theta_{err}(\Delta D_3, \omega_{loc}) + \eta_{loc}(t) - \\ \theta_{1064} + \frac{n'\omega'_S}{c}(D_5 + D_7) + \theta_{err}(\Delta D_5, \omega_{loc}) + (\omega'_S + \omega_{loc})\,t\end{aligned} \tag{5.25}$$

where we have added the error term $\theta_{err}(\Delta D_5, \omega_{loc})$ accordingly. We can now recognize the terms of the fast synchronization task, and filling in the form of eq. 5.15 we arrive at the expression

$$\phi(t, z_7) = \eta_{loc}(t) + \eta_{fast}(t) + \theta_{err}(\Delta D_5, \omega_{loc}) + \theta_{Ref} + \frac{n\,\omega_{Ref}}{c} D_8 + \frac{n'\omega'_S}{c}(D_7 - D_6) + (\omega_{fast} + \omega_{loc})\,t \tag{5.26}$$

5.9.11. SUBSTITUTION GLOBAL SYNCHRONIZATION

We can now fill in eq. 5.26 into 5.10, and use the global synchronization condition (the last four terms of this expression are precisely one half of the global synchronization condition 5.23), to simplify it into its final form:

$$\eta(t) = \eta^{A}_{loc}(t) + \eta^{A}_{fast}(t) - \eta^{B}_{loc}(t)) + \eta^{B}_{fast}(t) + \tag{5.27}$$

$$\theta^{A}_{err}(\Delta D_5, \omega_{loc}) - \theta^{B}_{err}(\Delta D_5, \omega_{loc}) + \tag{5.28}$$

$$\Omega_{tot}\, t + \eta_{glob}(t) \tag{5.29}$$

The first line is the performance of the local and fast synchronization task $\eta^{A/B}_{loc/fast}(t)$ of the two nodes, the second line the error due to the expansion/contraction of the long fibers $\theta^{A/B}_{err}(D_5)$. The last line is the global synchronization task performance $\eta_{glob}(t)$, and a time dependent term $\Omega_{tot}\ t$, where $\Omega_{tot} = (\omega^{A}_{fast} + \omega^{A}_{loc}) - (\omega^{B}_{fast} + \omega^{B}_{loc})$. All the other terms in this equation are either not dependent on time, or we have discussed ways to minimize their effects over longer time duration. The only thing left is then to choose the right frequencies of all the synchronization tasks such that the time dependence of the phase is removed, e.g. $\Omega_{tot} = 0$, with only small variations of $\eta(t)$ remaining in the system.

5.9.12. SELECTION OF CLOCK FREQUENCIES

As described in the main text, the condition $\Omega_{tot} = 0$ is not the only requirement for the frequencies at which the synchronization tasks operate. Due to shot-noise limitations of the SNSPDs, $\omega'^{A}_{S} - \omega'^{B}_{S} = \omega_{glob}$ can realistically not exceed 10 kHz, and in order for the feedback bandwidth of the fast synchronization to be fast enough, a high ω_{fast} is needed. The additional requirement of $\omega'^{A}_{Ex} = \omega'^{B}_{Ex}$ to generate indistinguishable photons, while the natural frequency $\omega^{A}_{Ex} - \omega^{B}_{Ex} > 1$ GHz can be far detuned, adds to the complexity. The flexibility in choosing ω_{1064} on each of the nodes separately deals with this requirement, and shifts both the excitation and stabilization light equally. Considering other experimental details outside the scope of this work regarding the temperature stabilization of the FBGs, we arrive on the choice of frequencies as presented in Table 5.1. Setting $\omega^{A/B}_{loc} = 400e6 \mp 750$Hz and $\omega^{A}_{fast} = 215001500$Hz and $\omega^{B}_{fast} = 215000000$Hz. With these values, the remaining frequency difference between the excitation lasers is:

$$\Omega_{tot} = (215001500 + 399999250) - (215000000 + 400000750) = 0 \tag{5.30}$$

Additionally, this gives us $\omega_{glob} = 1500$Hz, which lies well within the bandwidth of the SNSPDs.

5.9.13. CONCLUSION

We can now return to the central synchronization condition 5.10 and make the following claim. Given that the conditions

1. Both nodes have the local phase synchronization active (5.12),
2. The midpoint synchronizes the Stabilization light to the Reference laser (5.14),

3. The Stabilization light of the nodes is synchronized to each other(5.19),
4. The known error $\theta_{err}^{A/B}(\Delta D_5)$ is calculated and compensated by adjusting the phase of the clock used for reference in the global synchronizaiton.
5. The phase is sampled at a frequency below the frequency of the noise (5.5),
6. The measured residual phase noise in each of the synchronization tasks can be considered independent,

hold we can consider the excitation lasers to be synchronized. Condition six is valid due to the fact that the local synchronization task feedback is done on the excitation laser AOM, and therefore not affected by the synchronization in the midpoint. Additionally the residual phase noise of the fast synchronization is practically zero below the bandwidth of the global synchronization task, see Fig. 5.5 and 5.6, making them independent. Given these conditions, then the sampling of the error $\eta(t)$ from Eq. 5.27 of the phase between the excitation lasers of each node arriving at the central beamsplitter in the midpoint can be written as:

$$\mathcal{N}_{tot}(\mu_{tot},\sigma_{tot}) + \theta_{offset} \tag{5.31}$$

$$\mu_{tot} = \mu_{loc}^{A} + \mu_{loc}^{B} + \mu_{fast}^{A} + \mu_{fast}^{B} + \mu_{glob} \tag{5.32}$$

$$\sigma_{tot} = \sqrt{(\sigma_{loc}^{A})^2 + (\sigma_{loc}^{B})^2 + (\sigma_{fast}^{A})^2 + (\sigma_{fast}^{B})^2 + (\sigma_{glob})^2} \tag{5.33}$$

where $\mathcal{N}_{tot}(\mu_{tot},\sigma_{tot})$ is the distribution of the total phase error, and $\mathcal{N}_{i}^{A/B}(\mu_i,\sigma_i)$ the mean and standard deviation of resulting distributions of the sampling of the individual synchronization task errors. The value θ_{offset} is a term that contains all the constant phase terms in this derivation. This is the central result of the derivation, and provides the full description of the total synchronization. This result is also experimentally verified in Fig. 5.7, by measuring the interference of the excitation lasers at the central beamsplitter. The measurement involves the changing of the phase of the RF-clock used for the global synchronization, therefore changing μ_{global}. The measured phase of the oscillation of Fig. 5.7b is the true 'phase setpoint' of the optical interference of the excitation lasers. The relation between μ_{global} and this phase setpoint is difficult to calculate due to the constant terms neglected in this derivation, currently denoted as θ_{offset}. It can however be measured relatively quickly and consistently, as Fig. 5.7c shows over the duration of 10 h, showing that its long-term drift is dominated by the terms mentioned in Section 5.9.134.

5.10. RELATION BETWEEN OPTICAL PHASE AND ENTANGLED STATE PHASE

The main result of this work shows the stabilization of the optical phase between two remote nodes over telecom fiber. The light with which we show this stability is reflected of the diamond chip, and follows the same optical path towards the midpoint and central beamsplitter. However, during the entanglement generation, the Excitation light is actually:

1. propagating ≈10 µm into the diamond,
2. excitation the Nitrogen Vacancy-center resonantly and subsequent emission of a single photon through spontaneous emission,
3. that propagates ≈10 µm back out of the diamond.

All steps add an additional phase to the optical field that is now a single photon. These factors introduce fixed offsets between the phase investigated in this work, and need to be calibrated using a separate experiment. therefore, a stable optical phase is necessary but not sufficient to generate entanglement between two distant NV-center electron spins. Any drifts in these parameters would change the entangled state phase, and therefore the correlations between the spin states. These processes can be considered constant in time given the following conditions:

1. The path taken towards the NV center is constant in time
2. The path taken from the NV center towards the collection is constant in time and a single spatial mode with well-defined phase.
3. The spontaneous emission process is coherent with the exciting field

Both (1) and (2) are realized by making sure the relative position of the microscope objective used to address the NV center and the diamond sample is stationary during the entanglement generation. Furthermore, if the objective is moved during the operation, a check of the entangled state phase has to be done again. The relative microscope and sample location is one of the limiting factors in keeping a constant entangled state phase. The spontaneous emission is found to be coherent with the excitation field [36], and, because of the short ≈1 ns excitation pulse used, even in the presence of small detunings with the emitter.

REFERENCES

[1] H. J. Kimble, *The quantum internet,* Nature **453**, 1023 (2008), number: 7198 Publisher: Nature Publishing Group.

[2] S. Wehner, D. Elkouss and R. Hanson, *Quantum internet: A vision for the road ahead,* Science **362** (2018), 10.1126/science.aam9288, publisher: American Association for the Advancement of Science Section: Review.

[3] D. L. Moehring *et al.*, *Entanglement of single-atom quantum bits at a distance,* Nature **449**, 68 (2007), number: 7158 Publisher: Nature Publishing Group.

[4] S. Ritter *et al.*, *An elementary quantum network of single atoms in optical cavities,* Nature **484**, 195 (2012), number: 7393 Publisher: Nature Publishing Group.

[5] J. Hofmann *et al.*, *Heralded Entanglement Between Widely Separated Atoms,* Science **337**, 72 (2012), publisher: American Association for the Advancement of Science Section: Report.

[6] L. Stephenson *et al.*, *High-Rate, High-Fidelity Entanglement of Qubits Across an Elementary Quantum Network,* Physical Review Letters **124**, 110501 (2020), publisher: American Physical Society.

[7] S. Daiss *et al.*, *A quantum-logic gate between distant quantum-network modules,* Science **371**, 614–617 (2021).

[8] V. Krutyanskiy *et al.*, *Entanglement of trapped-ion qubits separated by 230 meters,* Phys. Rev. Lett. **130**, 050803 (2023).

[9] S. D. Barrett and P. Kok, *Efficient high-fidelity quantum computation using matter qubits and linear optics,* Physical Review A **71**, 060310 (2005).

[10] B. Hensen *et al.*, *Loophole-free bell inequality violation using electron spins separated by 1.3 kilometres,* Nature **526**, 682 (2015).

[11] A. Narla *et al.*, *Robust concurrent remote entanglement between two superconducting qubits,* Physical Review X **6**, 031036 (2016).

[12] C. M. Knaut *et al.*, *Entanglement of nanophotonic quantum memory nodes in a telecom network,* Nature **629**, 573–578 (2024).

[13] C. Cabrillo, J. I. Cirac, P. García-Fernández and P. Zoller, *Creation of entangled states of distant atoms by interference,* Physical Review A **59**, 1025–1033 (1999).

[14] S. Bose, P. L. Knight, M. B. Plenio and V. Vedral, *Proposal for teleportation of an atomic state via cavity decay,* Physical Review Letters **83**, 5158–5161 (1999).

[15] H. Bernien *et al.*, *Heralded entanglement between solid-state qubits separated by three metres,* Nature **497**, 86 (2013), number: 7447 Publisher: Nature Publishing Group.

[16] L. Slodička *et al.*, *Atom-atom entanglement by single-photon detection,* Physical Review Letters **110**, 083603 (2013).

[17] A. Delteil *et al.*, *Generation of heralded entanglement between distant hole spins,* Nature Physics **12**, 218–223 (2016).

[18] R. Stockill *et al.*, *Phase-Tuned Entangled State Generation between Distant Spin Qubits,* Physical Review Letters **119**, 010503 (2017), publisher: American Physical Society.

[19] D. Lago-Rivera, S. Grandi, J. V. Rakonjac, A. Seri and H. de Riedmatten, *Telecom-heralded entanglement between multimode solid-state quantum memories,* Nature **594**, 37 (2021).

[20] J.-L. Liu *et al.*, *Creation of memory–memory entanglement in a metropolitan quantum network,* Nature **629**, 579–585 (2024).

[21] A. Ruskuc *et al.*, *Scalable multipartite entanglement of remote rare-earth ion qubits,* (2024).

[22] P. C. Humphreys *et al.*, *Deterministic delivery of remote entanglement on a quantum network,* Nature **558**, 268 (2018).

[23] W. Pfaff *et al.*, *Unconditional quantum teleportation between distant solid-state quantum bits,* Science **345**, 532–535 (2014).

[24] M. Pompili *et al.*, *Realization of a multinode quantum network of remote solid-state qubits,* Science **372**, 259–264 (2021).

[25] S. L. N. Hermans *et al.*, *Qubit teleportation between non-neighbouring nodes in a quantum network,* Nature **605**, 663–668 (2022).

[26] A. Dréau, A. Tchebotareva, A. E. Mahdaoui, C. Bonato and R. Hanson, *Quantum frequency conversion of single photons from a nitrogen-vacancy center in diamond to telecommunication wavelengths,* Physical Review Applied **9**, 064031 (2018).

[27] J. Geus *et al.*, *Low-noise short-wavelength pumped frequency down-conversion for quantum frequency converters,* Optica Open (2023), 10.1364/opticaopen.23684502.v1.

[28] A. Tchebotareva *et al.*, *Entanglement between a diamond spin qubit and a photonic time-bin qubit at telecom wavelength,* Phys. Rev. Lett. **123**, 063601 (2019).

[29] A. J. Stolk *et al.*, *Telecom-band quantum interference of frequency-converted photons from remote detuned nv centers,* PRX Quantum **3**, 020359 (2022).

[30] J.-P. Chen *et al.*, *Sending-or-not-sending with independent lasers: Secure twin-field quantum key distribution over 509 km,* Phys. Rev. Lett. **124**, 070501 (2020).

[31] J. J. B. Biemond, A. J. Stolk, K. L. van der Enden, E. J. van Zwet and A. J. H. Meskers, *Controlled synchronisation at bandwidths beyond the limit of direct synchronisation error measurement,* Patent pending (2023).

[32] J. J. B. Biemond *et al.*, *Estimation method of phase difference between two optical channels induced by optical latency variations,* Patent pending (2023).

[33] E. F. Dierikx *et al.*, *White rabbit precision time protocol on long-distance fiber links,* IEEE Transactions on Ultrasonics, Ferroelectrics, and Frequency Control **63**, 945 (2016).

[34] A. Matsuki, H. Kori and R. Kopayashi, *An extended Hilbert transform method for reconstructing the phase from an oscillatory signal,* Scientific Reports **13** (2023).

[35] P. Welch, *The use of fast fourier transform for the estimation of power spectra: A method based on time averaging over short, modified periodograms,* IEEE Transactions on Audio and Electroacoustics **15**, 70–73 (1967).

[36] C. R. Stroud, *Quantum-electrodynamic treatment of spontaneous emission in the presence of an applied field,* Physical Review A **3**, 1044–1052 (1971).

6

METROPOLITAN-SCALE HERALDED ENTANGLEMENT OF SOLID-STATE QUBITS

If you want to go fast go alone, if you want to go far go together

Disputed Author

A.J. Stolk*, K.L. van der Enden*, M.-C. Slater, I. te Raa-Derckx, P. Botma, J. van Rantwijk, J.J.B. Biemond, R.A.J. Hagen, R.W. Herfst, W.D. Koek, A.J.H. Meskers, R. Vollmer, E.J. van Zwet, M. Markham, A.M. Edmonds, J.F. Geus, F. Elsen, B. Jungbluth, C. Haefner, C. Tresp, J. Stuhler, S. Ritter, R. Hanson

[1]

A key challenge towards future quantum internet technology is connecting quantum processors at metropolitan scale. Here, we report on heralded entanglement between two independently operated quantum network nodes separated by 10km. The two nodes hosting diamond spin qubits are linked with a midpoint station via 25km of deployed optical fiber. We minimize the effects of fiber photon loss by quantum frequency conversion of the qubit-native photons to the telecom L-band and by embedding the link in an extensible phase-stabilized architecture enabling the use of the loss-resilient single-click entangling protocol. By capitalizing on the full heralding capabilities of the network link in combination with real-time feedback logic on the long-lived qubits, we demonstrate the delivery of a predefined entangled state on the nodes irrespective of the heralding detection pattern. Addressing key scaling challenges and being compatible with different qubit systems, our architecture establishes a generic platform for exploring metropolitan-scale quantum networks.

The results of this chapter have been published in Science Advances **10** eadp6442(2024)
*These authors contributed equally to this work.

6.1. INTRODUCTION

Future quantum networks distributing entanglement between distant quantum processors [2, 3] hold the promise of enabling novel applications in communication, computing, sensing, and fundamental science [4–7]. Over the past decades a range of experiments on different qubit platforms have demonstrated the rudimentary capabilities of quantum networks at short distances including photon-mediated entanglement generation [8–14]. These short-range qubit networks are useful for testing of improved hardware [15], developing a quantum network control stack [16] and for exploring quantum network protocols in a lab setting [17–19].

The next major challenge is to develop quantum network systems capable of generating, storing and processing quantum information on metropolitan scales. Such systems face several new requirements. First, the large physical distance, the consequential substantial communication times and need for scalability demand that the network nodes operate fully independently. Second, as the optical fibers connecting nodes will extend for tens of kilometers, photon loss becomes a critical parameter that must be mitigated. Third, as advanced network applications require the heralded delivery of shared entangled states ready for further use, the qubit systems must be able to store quantum information for extended times and the network system must be capable of applying real-time feedback to the qubits upon successful entanglement generation.

Recent qubit experiments have shown promising progress towards the latter two criteria, including the integration with efficient quantum frequency converters [20–25], demonstration of long coherence times on qubit systems that can be extended into multi-qubit registers [26, 27] and entanglement generation between nearby qubits via tens of kilometers of optical fiber [28, 29]. In parallel, experiments on ensemble-based quantum memories have pioneered notable advances on the first two criteria [30–33].

Here, we report on the realization of a deployed quantum link between two solid-state qubit nodes separated by 10 km matching all three criteria. The two network nodes are combined with a midpoint heralding station via 25 km of deployed fiber, with all relevant classic and quantum signals propagating over the same fiber bundle in telecom bands (see Fig. 6.1). We implement an extensible architecture that enables the nodes to operate fully independently at large distance, mitigates the effects of photon loss on the entangling rate and allows for full heralding of entanglement generation. Furthermore, the network architecture features precise polarization and timing control as well as active stabilization of the relative optical phase between photons emitted from the nodes, enabling the use of the loss-resilient single-click protocol for efficient entanglement generation [34, 35]. We benchmark the performance of the architecture by parameter monitoring and by generating entanglement in post-selection. Finally, we use the full network capabilities of heralding and real-time feedback to deliver entangled states shared between the nodes ready for further use. This demonstration establishes a critical capability for future applications and scaling and presents a key milestone towards large-scale quantum networking.

6.2. DEPLOYED QUANTUM NETWORK LINK ARCHITECTURE

In order to meet the challenges of metropolitan-scale entanglement generation, we designed and implemented the control architecture depicted in Fig. 6.2A. Each node contains a CVD grown diamond chip hosting a Nitrogen-Vacancy (NV) center electronic spin qubit that can be faithfully initialized and read out by resonant laser light and controlled using microwave pulses. The NV center optical transition at 637 nm is used for generating qubit-photon entanglement.

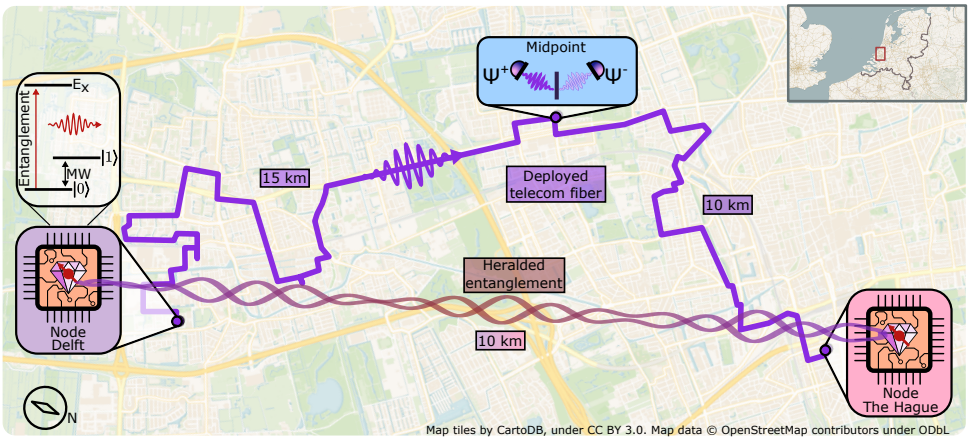

Figure 6.1: **The metropolitan-scale quantum link.** Cartographic layout of the distant quantum link and the route of the deployed fiber bundle, with similar quantum processor nodes in Delft and The Hague. Fiber length between node Delft and midpoint is 15 km, and between node The Hague and midpoint is 10 km, with losses on the quantum channels at 5.6 dB and 5.2 dB, respectively. Inset to the quantum processor are the used qubit energy levels where the qubit is encoded in the electronic ground state addressable with microwave pulses (MW), and the spin-selective optical transition ($\lambda = 637$ nm) is used for entanglement generation and state readout.

Each node is equipped with a stand-alone quantum frequency converter (QFC) unit that converts the 637 nm NV photons down to the telecom L-band at 1588 nm such that photon loss in the deployed fiber is minimized. The QFCs further serve as a tuning mechanism for compensating strain-induced offsets between the native emission frequencies typical for solid-state qubits. Through independent feedback on the frequency of the individual QFC pump lasers, we achieve conversion to a common target wavelength despite the few gigahertz difference in qubit emission frequencies [36]. The QFC in Delft is based on a novel noise-reduced approach (NORA) [37] that produces two orders of magnitude lower background counts than the periodically-poled Lithium Niobate (ppLN) with integrated waveguide based QFC in The Hague [38].

To further mitigate photon loss, we employ the single-click entangling protocol [34, 35, 39] which employs the number basis encoding for the photons. For this protocol the entangling rate favourably scales with the square root of the photon transmission probability across the entire link, as opposed to schemes using photonic polarization or time-bin encoding which exhibit a linear scaling of rate with transmission [8–11, 13–15, 28, 29]. In the single-click protocol, each qubit is first prepared in an unbalanced superposition

state $|\psi\rangle = \sqrt{\alpha}|0\rangle + \sqrt{1-\alpha}|1\rangle$. Application of an optical π-pulse resonant for qubit state $|0\rangle$ and subsequent spontaneous emission then results in qubit-photon entanglement, where the photonic qubit is encoded in the photon number state (0 or 1). Overlap of the photonic states at the beam splitter at the midpoint removes the which-path information, followed by single-photon detection by superconducting nanowire single photon detectors. Upon measurement of one photon after interference, entanglement of the qubit states is heralded to $|\Psi^{\pm}\rangle = \left(|01\rangle \pm e^{i\theta}|10\rangle\right)/\sqrt{2}$ with maximum fidelity $1-\alpha$, where the $\pm$ sign is set by which output arm the photon was detected in. The entangled state phase θ is dependent on the optical phase difference between the photonic modes arriving at the interference beam splitter from Delft and The Hague. Note that choosing the value of α involves a trade-off between higher signal-to-noise (larger α) and higher fidelity (smaller α). We use $\alpha = 0.25$ in the current work.

This entanglement generation critically relies on photon indistinguishability at the heralding station and therefore all degrees of freedom of the photons (frequency, arrival time, phase, polarization) must be actively controlled at the metropolitan scale. A defining feature of our architecture is that stabilization laser light used for phase locking and polarization stabilization is time-multiplexed with the single-click signals used for entanglement generation and sent over the same fiber from the nodes to the midpoint. To this end, we operate the link at a pre-defined heartbeat at 100 kHz, defining a common time division. During each heartbeat period of 10 µs, stabilization light is sent to the midpoint continuously, except for a 2 µs period where the entangling photonic states are sent out. This allows for near-continuous stabilization with high feedback bandwidth while performing entanglement generation. Below we discuss the major sources of drift at metropolitan scale affecting the entangled state generation and our strategy for mitigating them.

First, length drift of the deployed fibers can result in reduced overlap of the photonic modes on the beam splitter. The timing of the optical π-pulse is locally controlled and disciplined by an optically linked distributed clock that doubles as Ethernet connection (White-Rabbit protocol [40]) over a dedicated fiber. Fig. 6.2B shows a histogram of measured offsets in time-of-arrival for the two deployed-fiber segments over 24 hours, with the inset displaying the drift speeds ($\sigma = 5\,\mathrm{ps\,min^{-1}}$). By using this data to compensate for the drift via timing adjustments of the control electronics every ~15 minutes, the offset is kept below 50 ps, much smaller than the photon $1/e$ decay time of 12 ns. The resulting entangled state infidelity due to length drifts is below 0.1%. Second, as the phase difference of the photonic modes interfering at the beam splitter is imprinted on the entangled state, this phase must be known in order for the generated entangled states to be useful. To achieve a known and constant optical phase setpoint, five individual phase locking loops are implemented across the total link, see Fig. 6.2A. At each node, a local phase lock is closed between reflection of the resonant excitation light off the qubit device surface and the stabilization laser light via the controllers θ_1 and θ_2, stabilizing the in-fiber and free-space excitation and collection optics. Phase noise from the long fiber and excitation laser is mitigated by the controllers θ_3 and θ_4 via interference of light from the midpoint reference telecom laser and frequency down-converted stabilization light at nanowatt levels. Importantly, analog phase feedback is performed locally at the midpoint directly on the incoming light yielding a high stabilization bandwidth exceeding

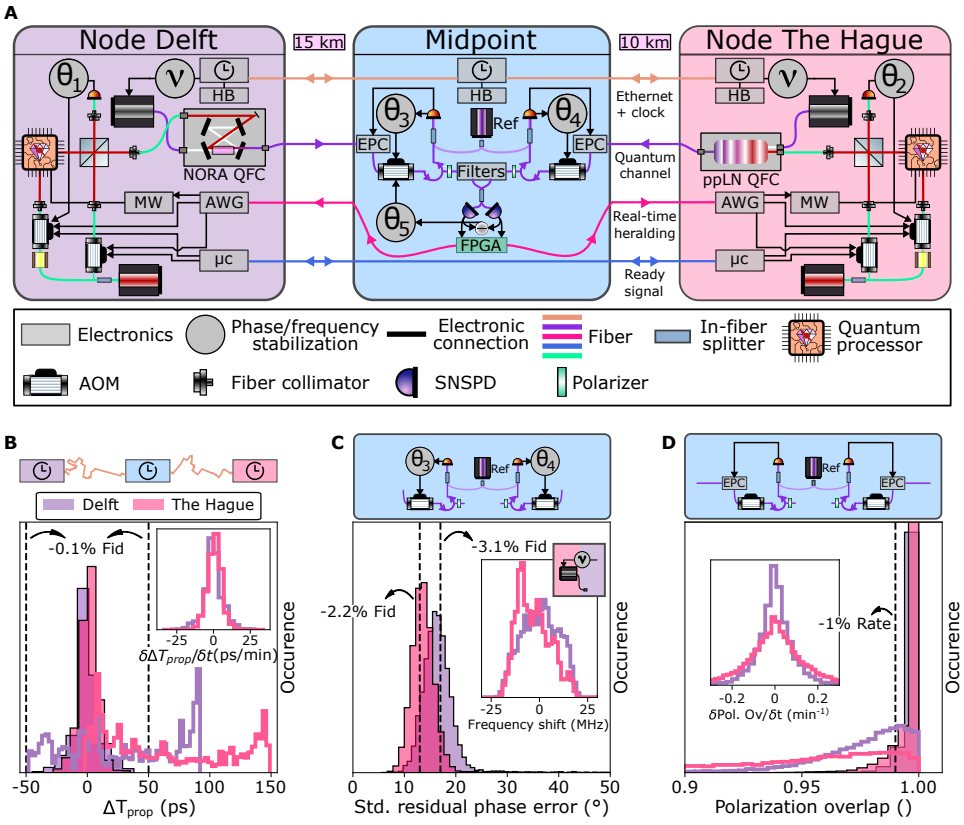

Figure 6.2: **Quantum node components and metropolitan-scale stabilization performance** **(A)** Detailed components of the quantum nodes and fiber link connections. A micro-controller (μc) orchestrates the experiment, which together with an arbitrary waveform generator (AWG) shapes laser- and microwave (MW) pulses. Solid-state qubit entangled photon emission and stabilization light from each node is converted to the telecom L-band by the NORA (ppLN) based QFC in node Delft (node The Hague) and sent to a central midpoint. There, long distance qubit-qubit entanglement is heralded via single photon measurement (superconducting nanowire single photon detector (SNSPD), efficiency$\approx 60\%$, darkcount rate $\approx 5s^{-1}$) with detection outcomes fed back in real-time. The stabilization light is used for phase locking at the nodes (θ_1, θ_2), at the midpoint ($\theta_3, \theta_4, \theta_5$) and for phase lock desaturation to the QFC pump lasers at the nodes (ν). The performance of stabilization over the deployed link over 24hrs is shown for **(B)** Time of arrival, **(C)** Phase and frequency and **(D)** Polarization. Hardware providing active feedback (header) keeps these parameter that are drifting over time (line histogram) stable (shaded histograms) by enabling continuous feedback faster than the experienced drifts (insets). Vertical lines show the modeled impact on fidelity and rate.

200 kHz. Lastly, interference of telecom stabilization light from both nodes at the central beam splitter is measured by the single-photon detectors and input to controller θ_5, closing the global phase lock between the nodes (see Sec. 6.7 for additional details). We note that the modularity of this architecture directly allows for the connection of multiple nodes to the same midpoint in a star topology, as the synchronization of all incoming signals to a central reference and relative phase stabilization between links can be performed using the control system at the midpoint.

Fig. 6.2C displays a histogram of the resulting phase errors during 24 hours of operation. Stable operation is achieved with a few-percent impact on the entangled state fidelity per connection. As this architecture yields full control over the phase difference at the beam splitter, the phase θ of the entangled state can be tuned on demand by adjusting the setpoint of the phase lock (see Sec. 6.7). In order to maintain the phase lock under frequency drifts at the nodes, two individual feedback loops (ν) between the nodes and the midpoint adjust the frequency of the individual QFC pump lasers at an update rate of 500 Hz. Importantly, this desaturation allows for a large dynamic range of the phase feedback, as required to handle the observed frequency drift range of >50 MHz, see Fig. 6.2C inset. Third, polarization drifts, though considerably slower than phase drift, must also be mitigated. To this end, the stabilization light is additionally used for electronic polarization compensation (EPC) at the midpoint. The amplitude of the error signal input at θ_3 and θ_4 is dependent on polarization overlap with an in-fiber polarizer. We use this as input for a gradient ascent algorithm to feedback on the polarization of the incoming light at the midpoint. Data on the deployed link (inset Fig. 6.2D) shows that polarization drift occurs on second-timescales; our feedback at a few Hz bandwidth keeps the polarization aligned to within a few percent (Fig. 6.2D). Any remaining polarization mismatch is removed by the polarizers at the cost of a slightly reduced entanglement generation rate.

6.3. POST-SELECTED ENTANGLEMENT GENERATION OVER A DEPLOYED LINK.

We now turn to the performance of the deployed link in generating entanglement between the solid-state qubits at the remote nodes. The proper functioning of all components of our system is first validated in a set of experiments with all devices of the link in a single lab in Delft, showing successful entanglement generation at state fidelities exceeding 0.6 (see Suppl, Fig. 6.11). After connecting and calibrating the equipment at the remote locations, we first focus on generating entanglement in post-selection. In this protocol the qubits are measured directly after generating spin-photon entanglement, and successful photon detection at the midpoint is used in post-processing to analyze entanglement generation. This scenario is compatible with quantum key distribution, but does not allow for more advanced protocols as the entangled state is not available for further use [3].

Our implementation of the post-selected entanglement generation is depicted in the space-time diagram of Fig. 6.3A, where each horizontal grey line depicts one 10 µs heartbeat period. Both nodes signal their start-of-experiment after passing their own charge-resonance check (CR Check) that ensures that the lasers are on resonance with the relevant optical transitions [17]. After communicating their readiness they resolve the earliest heartbeat to start attempting entanglement generation. In the first 20 heartbeat periods both nodes stabilize their local phase, followed by 540 rounds of entanglement generation, with one attempt per heartbeat period. Every seventh entanglement round also contains optical pulses for maintaining stability of the local phase. The operations performed at the nodes for each round are detailed in the pop-out of Fig. 6.3A. The sequence returns to the CR Check after completing the preset number of rounds.

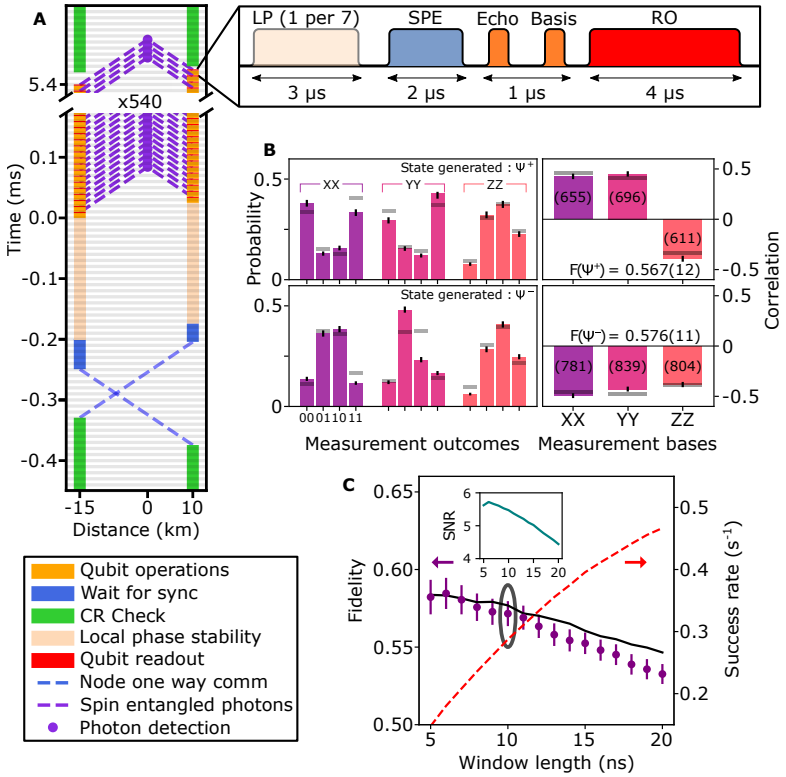

Figure 6.3: **Post-selected entanglement over the deployed link (A)** Space-time diagram depicting the generation of entanglement in post-selection. Horizontal grey lines indicate the periodic heartbeat of 100 kHz. Local qubit control used to generate entanglement and perform state readout (pop-out) all fit within one heartbeat period of 10 µs. A local phase (LP) pulse is followed by spin-photon entanglement (SPE) generation, an echo and basis selection microwave pulse. Finally, the state is read out (RO).**(B)** Outcome of correlation measurements, with different detector signature for the top and bottom panels. We show the qubit-qubit readout outcomes per correlators(left), as well as the resulting values per correlator (right). The calculated state fidelity is given inside each figure. The number in parenthesis indicates the amount of events recorded for that correlator. Horizontal grey bars indicate the theoretical model. **(C)** Average state fidelity (left vertical axis) and entanglement generation rate (right vertical axis) for varying photon acceptance window length. Circling indicates the window used in (B), black solid line is a model with no free parameters (see Sec. 6.7). Inset shows signal-to-noise ratio for the various window lengths. All measurement outcomes are corrected for tomography errors, errorbars are 1 standard deviation.

We characterize the generated non-local states by measuring qubit-qubit correlations in different readout bases. In Fig. 6.3B we plot the outcomes for the three basis settings split out per detector, showing the expected (anti-)correlations. Combining the outcome probabilities we calculate the correlators $\langle ZZ \rangle$, $\langle XX \rangle$ and $\langle YY \rangle$. Note that as the two detectors herald different Bell states (Ψ^+ vs Ψ^-), the corresponding $\langle XX \rangle$ and $\langle YY \rangle$ correlations have opposite sign. We also plot the values predicted by our detailed model without any free parameters (grey lines, see Sec. 6.7), and observe good agreement with the data. The asymmetry in the amount of events is caused by a difference in

quantum efficiency between the two single-photon detectors. We find that the measured fidelities $F(|\Psi^{\pm}\rangle) = \frac{1}{4} * (1 - \langle ZZ\rangle \pm \langle XX\rangle \pm \langle YY\rangle)$ with respect to the ideal Bell states are significantly above 0.5, proving the generation of post-selected two-qubit entanglement (Fig. 6.3B).

In the above analysis, we included photon emission up to 10 ns after the optical π-pulse. By varying the analysis window of the photon detection, we can explore the trade-off between rate and fidelity (Fig. 6.3C). We find that the entangled state fidelity slowly decreases with increasing window length, due to the decreasing the signal-to-noise ratio of the photon detection at the midpoint (see inset to Fig. 6.3C) in addition to the window-size dependent influence of spectral diffusion [36, 39]. Other examples of sources of infidelity are the residual optical phase noise and the probability of double optical excitation, all taken into account by our model (black line, see Sec. 6.7). At the same time, as more photon detection events are accepted with increasing window length, the success rate increases. The achieved entanglement generation rate reaches 0.48 Hz (success probability per attempt of $7.2 \cdot 10^{-6}$) for a 20 ns window.

6.4. FULLY HERALDED ENTANGLEMENT GENERATION OVER A DEPLOYED QUANTUM LINK

In a final demonstration that highlights the capabilities of the deployed platform, we generate fully heralded qubit-qubit entanglement. In contrast to the post-selected entanglement generation described above, "live" entangled states are now delivered to the nodes that can be further used for quantum information tasks. Such live entanglement delivery is a fundamental requirement for many future applications of long-range entangled states [3].

We emphasize that this protocol requires that all relevant heralding signals (including which detector clicked) are processed at the node before the entanglement delivery is completed. To this end, we employ the experimental sequence depicted in Fig. 6.4A. To preserve the qubit states with high fidelity while waiting for the heralding signals to return and be processed, the refocusing echo pulse is applied to the qubits halfway the sequence to dynamically decouple them from spin bath noise in their solid-state environment. Fig. 6.4B shows the resulting qubit preservation as a function of time depicting periodic revivals of coherence due to interactions with nearby nuclear spins [41]. We note that with established advanced pulse sequences these revivals can be set with high timing resolution and the NV qubit coherence time can be extended towards a second [42]. While the qubits are protected at the nodes, the photons travel to the midpoint in about 52 µs and 73 µs from The Hague and Delft, respectively. An FPGA at the midpoint processes the output of the single-photon detectors, establishing whether a photon was detected in a predetermined time window and in which detector. The electronic output of the FPGA is optically communicated to the nodes, taking another 52 µs (73 µs). There, the signal is detected and processed live to choose the next action. The time at which this final processing is completed per node is indicated by the solid pink lines in Fig. 6.4B.

We choose to use the first echo revival (orange dotted vertical line in Fig. 6.4B) after the expected arrival time of the heralding signal to complete the delivery of the entangled state. For these setpoints, a detailed measurement of the echo contrast shows that

the wait times introduce a 1.3 (3.2) percent reduction in coherence for node Delft (The Hague). We note that using more advanced dynamical decoupling sequences the NV qubit coherence time could be extended towards a second [42].

The entanglement generation runs are automatically repeated by the nodes until a successful heralding signal is received from the midpoint. Once such a signal is received, the system jumps to a different control sequence in which a basis selection gate is applied to each qubit followed by single-shot qubit readout. This control sequence incor-

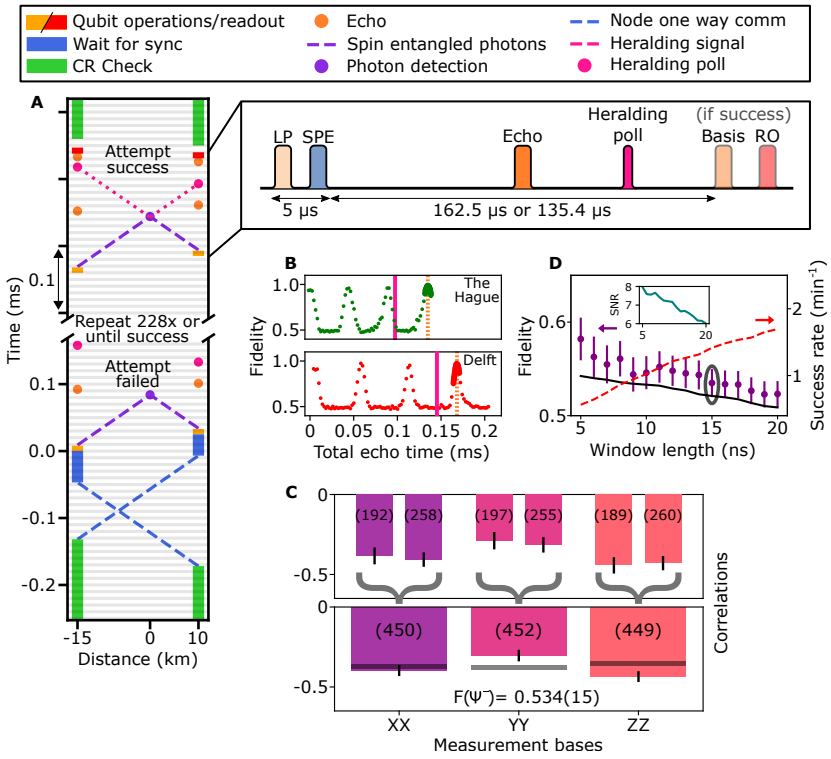

Figure 6.4: **Fully heralded entanglement over the deployed link (A)** Space-time diagram of fully heralded entanglement generation. An attempt is successful upon registering a heralding signal at the polling time, after which a feed-forward is applied on the qubit and readout is performed. Absence of a heralding signal communicates a failed attempt, where we retry for a maximum of 228 attempts or until success. Pop-out depicts the local qubit control, basis selection and readout pulses. The time between spin-photon entanglement (SPE), heralding poll and basis selection is node-dependent. **(B)** Hahn-echo experiment on the communication qubit, showing the revivals of the coherence [41]. Solid vertical line indicates the heralding poll, the dotted line the time of the basis selection. All times are with respect to echo sequence start. **(C)** Correlation measurement for full heralding, showing both detector outcomes delivering the same Ψ^- state. Upper (lower) plot shows events per detector (combined). Bars indicate data, the number in parenthesis indicate the amount of events. Horizontal lines indicate the theoretical model. **(D)** Average state fidelity (left axis) and entanglement generation rate (right axis) for varying photon acceptance window length. Circling indicates the window used in (C), black line is a model with no free parameters (see Sec. 6.7). Inset shows signal-to-noise ratio for respective window lengths. Measurement outcomes are corrected for tomography errors, errorbars are 1 st.dev.

porates the which-detector information communicated from the midpoint in real time. We exploit this full heralding capability to apply a phase flip conditioned on which detector clicked, thereby delivering the same Bell state $\Psi^- = \frac{|01\rangle - |10\rangle}{\sqrt{2}}$ for each of the two possible heralding signals.

The measured correlations per readout basis are shown in Fig. 6.4C, showing the expected anti-correlated outcomes for all three bases. The top bars show the outcomes divided per detector, displaying now the same Ψ^- thus showing the successful operation of the real-time feedback. We find that the delivered entangled states have a fidelity of 0.534(15). This result establishes the first demonstration of heralded qubit-qubit entanglement at metropolitan scale, with all the heralding signals processed in real-time and the entangled states delivered ready for further use.

Fig. 6.4D displays the rate-fidelity trade-off in analogy to Fig. 6.3C, showing a similar trend. The reduction in rate ($0.022\,\mathrm{s}^{-1} = 1.3\,\mathrm{min}^{-1}$ at the pre-defined 15 ns window length) compared to the post-selected case is mainly due to the added communication delay needed for the heralding signal to travel to the nodes, making each attempt a factor of ≈ 20 slower. The observed fidelity vs. window size is well captured by our model without any free parameters, with the reduction in fidelity compared to the post-selected case mainly coming from the additional decoherence and a reduced phase stability (black line, see Sec. 6.7). The improved SNR (Fig. 6.4D inset) compared to Fig. 6.3C is due to an improved trade-off between detection efficiency and dark counts following an optimization of the single-photon detector bias currents.

6.5. CONCLUSION AND DISCUSSION

We have realized a deployed quantum link and demonstrated heralded entanglement delivery between solid-state qubits separated at metropolitan scale. The architecture and methods presented here are directly applicable to other qubit platforms [14, 28, 43–46] that can employ photon-interference to generate remote entanglement and frequency conversion to minimize photon losses. Additionally, the ability to phase-lock remote signals without the need for ultra-stable reference cavities can be of use for ensemble-based quantum memories [30–32, 47].

This work can benefit from future developments in the following ways. Real-time correction of false heralds [18] can be realized by using detection events of phonon sideband photons on the nodes, upon which the fidelity of the delivered entangled state improves (see Fig. 6.12). Near-term developments can substantially improve the signal-to-noise ratio, which is currently limiting the entangled state fidelity (about 30% contribution) through false heralding events and forcing a high value of α (protocol error). For instance, the signal can be substantially boosted by embedding the NV-centre in an open micro-cavity [48, 49] or by using different color centers that exhibit a more efficient spin-photon interface [25, 29, 50, 51]. As a quantitative example, replacing the NV center with a diamond SnV center (which has a 16 times higher probability of coherent photon emission), employing NORA QFCs at all nodes [37] (here used only in the Delft node), and fixing a known imperfection in the local phase stabilization would already increase the heralded state fidelity to above 80%. Furthermore, improving coherence protection using XY8 sequences and systematic reduction of the remaining small error

sources could lift the fidelity beyond 90% (see Table 6.4). The extensible nature of our architecture opens the door to connecting more than two qubit nodes to a midpoint, without additional overhead by locking to the same reference which, in combination with using local memory qubits [15, 26, 52, 53], would enable the exploration of more advanced protocols on a metropolitan-scale network [18, 19, 54], as well testing quantum control stacks [16] on a distributed multi-node quantum network.

6.6. MATERIALS AND METHODS

The experimental set-ups used in this work are built on top of the hardware described in Ch. 3. A detailed schematic of the quantum nodes, midpoint and their connections is shown in Fig. 6.2. Hardware control is enabled through use of software based on the Quantum Measurement Infrastructure, a Python 3 framework for controlling laboratory equipment [55]. We will give a brief overview of the relevant parts of the set-up below.

6.6.1. QUANTUM NODE

Each node houses a diamond-based quantum processor consisting of a Nitrogen-Vacancy (NV) center electronic spin qubit in the negative charge state. The ground-state spin levels are split using a small permanent magnetic field aligned with the NV axis of $\approx 3\,\mathrm{mT}$, allowing for arbitrary qubit rotations with a microwave pulse frequency of $\approx 2.8\,\mathrm{GHz}$. Initialization, read out and qubit-photon entanglement generation is achieved through resonant excitation at 637 nm.

6.6.2. QUANTUM FREQUENCY CONVERTERS

We employ both an in-house built ppLN QFC module and the NORA QFC described in Ch. 2 and this article [56]. The NORA QFC mitigates the amount of noise photons generated by the frequency conversion due to imperfections in the waveguide and poling period of periodically poled Lithium Niobate (ppLN) crystals. We compare the NORA QFC to the ppLN QFC in Table 3.2.

6.6.3. PHASE STABILITY

To allow for phase stability between physically separated setups, we use a prototype TOPTICA DLC DL pro 637 nm employing optical feedback from an additional cavity to reduce the phase noise to $< 40\,\mathrm{mrad}$ integrated from 100 kHz to 100 MHz. We use a combination of five interferometers with heterodyne detection and feedback that together lock the phase to a controlled setpoint. On both nodes we define local interferometers that lock the excitation laser path to the stabilization path of the respective set-ups. On the midpoint we stabilize the incoming light from each node to the same telecom wavelength reference. The relative optical phase between the nodes is stabilized using interference at the central beam splitter in the midpoint and measured with SNSPDs. The optical fields and respective frequencies used are shown in Fig. 6.6, and the combination of the stabilization fields with the NV control fields is shown in Fig. 6.7 and 6.8.

6.6.4. MIDPOINT

The midpoint provides phase feedback, polarization control, spectral filtering and single-photon detection. The phase feedback uses frequency modulation of AOMs for phase-locking of the node excitation lasers to the midpoint telecom reference at ≈ 1588 nm. Two Electronic Polarization Controller allow for full control over the polarization state to compensate for fiber drifts. Two low-loss Variable Optical Attenuators (VOAs) shield the SNSPDs from bright stabilization light coming from the nodes. Per node, all the error signals for the phase- and polarization stabilization, and temperature of the ultra-narrow fiber Bragg-grating (FBG) filters are generated on the same balanced photodiode, and subsequently extracted by a combination of power-splitters, bandpass filters and amplifiers. An FPGA development board processes electrical signals to allow for real-time heralding to the nodes of photon detections at the midpoint.

6.7. SUPPLEMENTARY INFORMATION

6.7.1. EXPERIMENTAL SETUP DETAILS

QUANTUM NODE

We exchanged the diamond quantum device of Node The Hague used in Ch. 3 for a newly fabricated one. All parameters of the substrate (Element Six) and device, such as purity, crystal orientation and carbon isotopes are the same as previously reported. To allow for phase stability between physically separated setups, the TOPTICA DLC DL pro 637 nm was exchanged for an upgraded prototype employing optical feedback from an additional cavity to reduce the phase noise to < 40 mrad integrated from 100 kHz to 100 MHz.

PHASE STABILITY ON THE NODES

On both nodes we added the components to define the local interferometers that lock the excitation laser path to the stabilization path of the respective set-ups. We use a combination of up- and down-shift Acousto-Optical Modulators (AOM, Gooch and Housego Fiber-Q), already used for amplitude modulation, to define a 400 MHz frequency offset. The excitation light reflected off the diamond surface is separated from the zero-phonon-line (ZPL) path by a polarizing beam splitter (PBS), where it spatially overlaps with the stabilization light. We guide the light to a set of birefringent crystals that maximize the complex overlap between the orthogonally polarized reflected beam and the stabilization light. A polarizer then selects a common polarization such that both beams can interfere in intensity, after which we focus the light into a multi-mode fiber (core diameter ≈ $100um$) and measure the interference beat signal using a fast avalanche photodiode (Menlo Systems APD210). After amplification and filtering, we extract the phase of the interference by mixing it with an electronic reference signal generated by a stable RF source (Anapico APSIN6010). The feedback signal generated is passed through a Track-And-Hold amplifier (Texas Instruments OPA1S2384) and input to the Frequency Modulation input of the Excitation light AOM RF-driver (TimeBase DIM3000), which closes the feedback loop. Because the frequency modulation has integral feedback on the phase that can not be switched on/off fast, any bias/offset in the error-signal reduces

the free evolution time during which the local phase remains stable. In a future implementation, this actuator will be replaced by a linear phase shifter, and an improvement of the local phase-stability can be realized.

MIDPOINT

The previous design of the midpoint used for two-photon quantum interference discussed in Ch. 3 suffered from an increased noise floor due to the presence of bright laser pulses incident on the nanowires every 200 µs. To reach an adequate feedback bandwidth for phase-locking of our excitation lasers to the telecom reference, we have to reduce the period of bright pulses to 10 µs, making this even more challenging. We have made the following improvements to allow for polarization and fast phase feedback, to reduce crosstalk between optical channels and lower the background counts in the SNSPDs:

- Split the high-power reference light into three paths, two used to generate an optical beat to lock the stabilization light coming from each node to the reference laser, and one used to generate an error signal to stabilize the ultra-narrow Fibre-Bragg grating filters.
- Added two low-loss Variable Optical Attenuators (VOAs, Boston Applied Technologies Nanona VOA) that shield the detectors from bright pulses coming from the nodes.
- Added two Electronic Polarization Controller (OZOptics EPC-400-11-1300/1550-9/125-S-3A3A-1-1) to allow for full control over the polarization state to compensate for fiber drifts.
- Added two AOMs to have fast and integral control of the phase of the incoming light, used for phase stabilization.
- Removed one circulator from the design and splicing multiple connectors where the single-photons pass through to reduce single-photon loss

All the error signals for the phase- and polarization stabilization, and the ultra-narrow fiber Bragg-grating (FBG) for one node are generated on the same balanced photodiode (Thorlabs PDB480C-AC), and subsequently extracted by a combination of power-splitter, bandpass filters and amplifiers.

HERALDING

To allow for low-latency feedback of photon detections at the midpoint, the midpoint was upgraded with an FPGA development board (Digilent Arty-A7) with custom-built PCBs converting the external pin I/O to SMA connectors with the possibility of 50 Ω matching. Single photon signals were input on a custom pulse-stretcher, cleaning up the electrical pulse from the SNSPD to a block-like pulse shape of around 1 µs and input on the I/O of the FPGA. The complete I/O of the FPGA is shown in Fig. 6.5. The acceptance window of sending out a heralding signal is predetermined at the time within a heartbeat period where we expect spin-photon entangled photons to arrive. The exact timing of the acceptance window is derived from the centralized clock and heartbeat

signal available at the midpoint. To be able to signal which detector clicked on a photon count, we use two digital pulses to herald, one for the success, and one for which detector clicked. Since the delay in time-of-flight between the nodes is different, the digital pulses need to be aligned individually to arrive at the nodes at the same time within one heartbeat. To clarify, this does not mean they arrived at the same global time at the nodes, but that the digital pulses arrive at the same time modulo the heartbeat (10 µs) at the nodes.

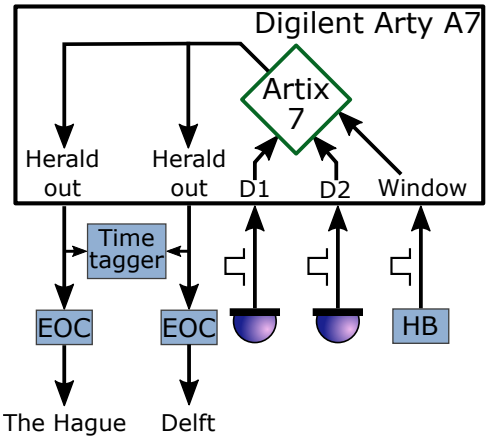

Figure 6.5: Single photon detection signals are processed by custom FPGA-code on the Digilent Arty A7. If photons arrive within the externally derived acceptance window from the heartbeat (HB), a heralding signal is sent to both locations through an Electrical-to-Optical-Converter (EOC). The heralding signal is also recorded on the timetaggers on all the three locations.

Lastly, a local FPGA code loading server was employed that could upload compiled-VHDL that was either manually or automatically generated remotely. A change in timing of sending out pulses could be updated on the underlying VHDL code automatically based on a custom template code. This allowed fast multi-core compilation locally and remote upload to significantly reduce debugging time when determining the required exact timing of the heralding pulses.

6.7.2. PHASE STABILIZATION IN THE MIDPOINT

We stabilize the incoming light from each node to the same telecom reference (fast stabilization). The relative optical phase between the nodes is stabilized using interference at the central beam splitter in the midpoint, and measured with the SNSPDs (global stabilization). The optical fields and respective frequencies are shown in Fig. 6.6, and the distribution of the fields in time shown in Fig. 6.7 and 6.8.

FAST STABILIZATION

Part of the stabilization light used in the local phase lock also propagates via the QFC, through the same deployed fiber, to the midpoint. There it is split off in frequency from the single-photons via the FBG, subsequently interfered with a telecom reference laser

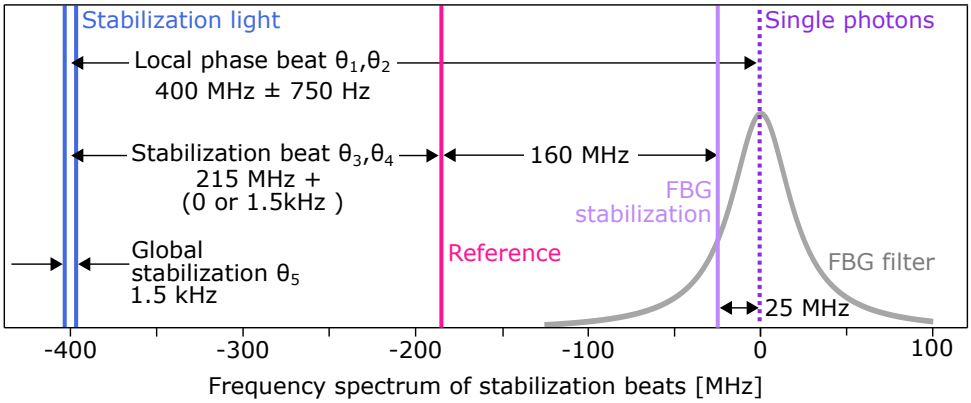

Figure 6.6: Frequency of relevant optical fields for the phase lock in the midpoint. The grey Lorentzian shape is the ultra-narrow fibre-bragg grating filter (FBG). It is stabilized using a 160 MHz beat generated by the reference laser and a frequency-shifted tap-off that is back-propagated through the flank of the FBG (25 MHz from the transmission peak). The stabilization light is located far from the filter resonance, detuned by 400 MHz from the filter peak and excitation laser/single-photons, which is locked by the local phase lock controllers θ_1 and θ_2. This stabilization light is reflected off the FBG and interferes with the reference laser generating a $\approx$ 215 MHz beat, which is stabilized by the fast phase lock controller θ_3 and θ_4. The slight offset between the nodes of 1.5 kHz is measured by the SNSPDs and input to controller θ_5, to close the phase lock between Delft and The Hague.

(NKT Adjustik fiber laser), where a heterodyne interference beat is measured by the balanced photodiode. A phase-frequency detector (Analog Devices HMC3716LP4E) processes this signal by comparing it to a reference signal (Wieserlabs FlexDDS-NG DUAL). Its output serves as the error-signal for a high-speed servo controller (Newport LB1005-S) performing PID control. This controller provides feedback on the AOM to stabilize the incoming light, synchronizing it with the reference at a bandwidth of over 200 kHz. To stay within the low-loss performance of the AOM close to the central frequency, we offload the accumulation of phase error (frequency drifts) to the QFCs at the nodes. This can be done much slower (500 Hz) and makes the feedback only limited by the frequency range of the QFCs ($\gg$1 GHz). The fast feedback removes all high-frequency noise from the incoming light, which contains the excitation laser line-width, as well as phase noise introduced by expansion/contraction and vibrations of the deployed fiber.

GLOBAL STABILIZATION

To further compensate phase drift that occurs in the midpoint and to set the relative phase between the incoming optical modes, we employ a control loop based on the stabilization light from both nodes that interferes at the central beam splitter. This light leaks through the FBG, and is of sufficient low power to not blind the SNSPDs. The voltage pulses from the SNSPDs are amplified, and a difference amplifier (Krohn-Hite Model 7000) generates a heterodyne beat by subtracting the count-rates from each detector. This beat is compared to a reference signal (AimTTi) by mixing it and low-pass filtering (150 Hz), generating an error-signal. This is again input to a servo controller (Newport LB1005-S), of which the output is used to modulate the phase of the reference of one of the fast stabilization controllers.

VERIFYING PHASE STABILITY

We can verify the performance of the full optical phase stabilization by interfering the two excitation lasers from the nodes at the central beam splitter in the midpoint, using the time-resolved counts in the SNSPDs to generate the error signal. By changing the phase of the reference signal, we can measure a full visibility fringe of the interference. By correcting the measured interference for the imbalance in photon flux from each node, we can calculate the interference contrast, see Fig. 6.10B. A more in-depth description and technical analysis of the total phase stabilization is given in the previous Chapter 5.

6.7.3. OVERVIEW COMMUNICATION TIMES AND DECISIONS

In this subsection we discuss the different optical and electrical pulses or feedback signals that are needed to control this distributed experiment. We will first discuss the local nodes, then which signals are necessary to be timed at the midpoint for single photon processing and phase stability. Lastly, we will discuss how we align the arrival time of the photonic states at the midpoint telecom detectors.

PULSES AND TIMING AT NODE

Since the central clock in the midpoint is distributed to the nodes by the White Rabbit enabled switches, it provides a common reference frame to align the time-of-arrival for each of the entanglement generation attempts.

A full timing overview of a single heartbeat length when we perform a full entanglement attempt without heralding is shown in Fig. 6.7A and with heralding in Fig. 6.7B. The entanglement generation attempt with heralding contains exactly the same pulses as in Fig. 6.7A, except for that the time between the spin superposition state generation and basis-selection pulse is at a revival of the spin coherence, as previously shown in the pop-out of Fig. 6.4A of the main text.

PULSES AND TIMING AT MIDPOINT

The laser, electrical and feedback pulses used at the midpoint by design operate agnostically of the experiment that is being run. For about ~8 µs we can perform phase, frequency and FBG stability actions using the interference from the reference light and the incoming stabilization light from the node (see Fig. 6.8). In the remaining ~2 µs the local reference light is shut off, the phase Track-and-Hold amplifier is set to 'hold' and the VOAs opened fully to allow for single photons to pass through to the SNSPDs.

TIME-OF-ARRIVAL ALIGNMENT

One of the requirements for indistinguishability of the photons is the time aligned photonic mode overlap at the beam splitter in the midpoint. The timing of the emission of the photonic state determines, together with the time of flight (ToF), the time at which the photonic state arrives from the node at the midpoint. This is especially crucial in the metropolitan distance case, where fiber distance varies with tens of picoseconds per hour (see Table 6.2). Since we have unbalanced fiber connection lengths between the nodes-midpoint, Node Delft will be allowed to send its photon as soon as possible. Node The Hague has to hold its pulse sequence start for 3 heartbeats. Both nodes require sub-heartbeat timing alignment to align the arrival time of the solid-state entangled photons

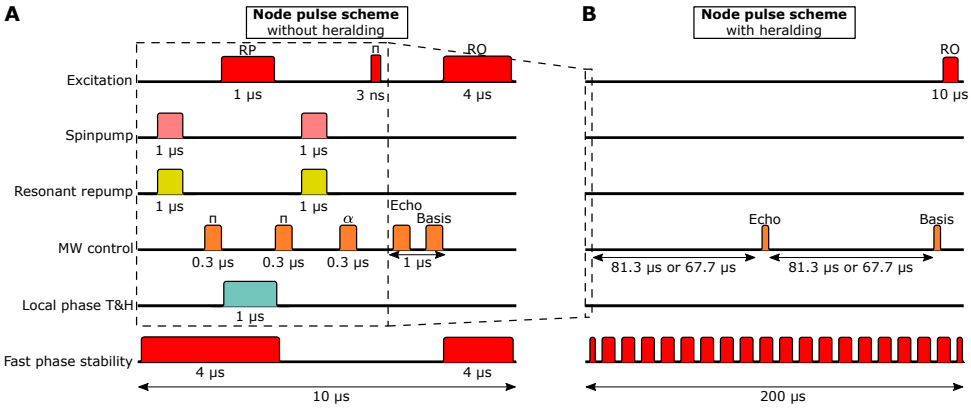

Figure 6.7: **(A)** Local node pulse scheme for the duration of one heartbeat when performing entanglement generation without heralding. Red and yellow pulses are laser, orange are microwave pulses, blue-green is electrical feedback. The NV center is (re-)initialized in the correct spin and charge state via pumping resonant with $|1\rangle$ (637 nm) and the ZPL of NV^0 (575 nm), respectively. We limit resonant optical excitation during local phase stability by preparing the qubit state in the opposite spin state a using microwave π-pulse. After the local phase stability, we initialize the spin into the $|0\rangle$ state, create the unequal superposition with a microwave pulse with rotation angle α, and optically excite using a short optical excitation, completing the spin-photon entangled state generation. A microwave π-pulse echos the spin state, and a $\frac{\pi}{2}$-pulse selects the readout basis for the resonant optical readout that follows. **(B)** Node pulse scheme during entanglement generation. This sequence now takes 20 heartbeat periods (200 µs). All pulses required to perform the local phase stability and spin-photon entanglement are repeated exactly as in (A). However, now the rephasing echo pulse is played at its calibrated value of 82 µs(68 µs) for Node Delft (The Hague), while the stabilization light still is periodically sent to the midpoint such that phase stability feedback can be applied there. The total duration of 200 µs is for one whole entanglement generation attempt where wait time padding is added node specifically (not shown) to allow for a common repetition period when dealing with the different node-midpoint communication delays.

in the last ~2 µs of the midpoint scheme (Fig. 6.8). This last alignment step is achieved with the arbitrary waveform generator (AWG, Zurich Instruments HDAWG) sequencer and the built in skewing parameter of the AWG outputs.

Due to the constantly changing ToF, the alignment in time is performed in two steps. A first time alignment is required to be performed manually where laser pulse timing is recorded at the midpoint timetagger (PicoQuant Multiharp, 80 ps resolution), after which the time difference between arrival times of the pulses from the two nodes can be calculated and adjusted. This value is recorded as calibration parameter. Secondly, the reported ToF from the time synchronization system is used to automatically adjust the skewing parameter every ~15 minutes with the difference in fiber ToF with respect to the initial calibration.

6.7.4. OTHER MIDPOINT STABILIZATION

POLARIZATION STABILIZATION

We continuously stabilize the polarization of the incoming stabilization light using the same beat generated on the balanced photodiode as mentioned in the phase stability section (Section S2) . Because of our in-fiber polarizer, the amplitude of the beat will de-

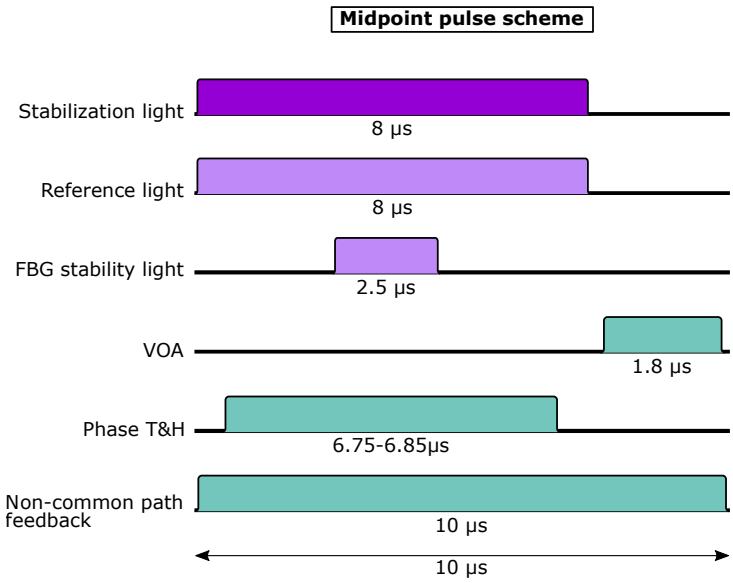

Figure 6.8: Midpoint pulse scheme for the duration of one heartbeat. This sequence is agnostic to the experiment is run. Purple colors are telecom wavelength laser light, blue-green is electrical signal. Stabilization light is converted light coming from the nodes. The reference and FBG stability light are both originated from the telecom laser at the midpoint. The error signal for the fast lock is processed by a Track and Hold (T&H) amplifier before being processed by the controllers. Variable optical attenuators are used to shield the detectors during the times where stabilization/reference light is propagating in the system, and they are only opened for 2 µs where single photons from the nodes can arrive. The global control task is not modulated, as the feedback bandwidth is much slower than the low-pass filtering of the error signal (150 Hz). For all above pulse schemes holds that absolute block sizes are not to scale, the denoted time duration is leading.

pend on the overlap of the incoming light with the polarizer. Maximizing this amplitude will guarantee the same polarization between the nodes, as needed for interference. Using a phase-gain detector (Analog Devices EVAL-AD8302) we can monitor the amplitude of the beat by comparing it to an in-phase RF tone (generated by Wieserlabs FlexDDS-NG DUAL) over multiple orders of magnitude. We sample the output of this phase-gain detector with an Analog Discovery 2 (Digilent), and process the error signal in a python process running a Gradient Ascent algorithm. This in turn sends commands to the EPC that adapts the polarization state and completes the control loop. The whole process can be monitored and adjusted via a Graphical User Interface.

ULTRA-NARROW FBG STABILIZATION

We adapted the control loop for the temperature stabilization of the ultra-narrow FBGs (UNF) to allow for a significant reduction of the optical power reflected back to the SNSPDs. We achieved this by using a heterodyne beat measurement that is sensitive to the transmission through the UNF, instead of a simple power measurement at DC. This allows for multiple orders higher sensitivity, and allows us to stabilize the filters with only ≈ 10 fW of light traveling through the filter in the backwards direction.

6.7.5. DEPLOYED FIBER CHARACTERIZATION AND STABILITY

We use a fiber bundle with four fibers to perform all the communication between the locations. These are provided to us by KPN, a major Dutch telecom provider, and are part of their telecom infrastructure. The reality of using deployed fibers means that it is built up of sections of continuous fiber, which are spliced or connected together at various locations along the path. Therefore the losses per kilometer of deployed fiber are significantly higher than the ideal losses of $\approx$0.2 dB km^{-1} @ 1580 nm, and can differ from fiber to fiber. During the period of measuring over the deployed link in 2023, several parts of the fiber were adapted and re-routed as part of restructuring of the network by KPN, changing both their length ($\pm$ 100 m) and loss ($\pm$ 1 dB) multiple times over the span of a few weeks. Table 6.2 shows typical loss values measured during this period. Thanks to the modular approach of our system, we have complete freedom in changing the arrival time of the photon in the midpoint, allowing for easy re-alignment of the propagation delay, both for the fiber restructuring as well as the daily expansion and contraction.

6.7.6. CALIBRATIONS

ENTANGLEMENT GENERATION

We employ a method where we interleave the generation of entanglement with three calibrations that measure and re-calibrate critical parameters and settings. These calibrations are an adapted version of the entanglement generation sequence that measure specific key elements of the entanglement generation: the signal-to-noise ratio (SNR), optical phase stability (PHASE) and the entangled state phase (XsweepX). Typical results of these three calibrations are shown in Fig. 6.9. When these calibrations have passed their threshold, we proceed to measure the correlators used to calculate the entangled state fidelity, FID for short.

The first calibration is the measurement of the single-photon signal from both nodes and the background (Fig. 6.10A), which includes all the losses that are present in the system. We prepare the communication qubit in the $|0\rangle$ to maximize the single photon signal. The measurement is the same experimental sequence as shown in Fig. S4A, where now the state generation α pulse is removed to measure the signal, and replaced by a π-rotation to measure the noise. Furthermore, the arrival time of the photons is shifted by 100 ns to measure the brightness of both nodes individually.

Second is determining the contrast and phase of the relative optical phase between the nodes. We realize this by interfering a bright pulse (1 µs) of the excitation lasers which we reflect off the diamond surface, and follows the exact path as the NV-center emission from there. By varying the setpoint of the phase in the stabilization scheme, we can measure a full interference fringe at the SNSPDs as seen in Fig. 6.10B and characterize the residual phase noise of the system at the specific time window where single photons interfere. Furthermore, this calibration is used to set the phase of the optical interference at any point along this fringe, which can be used to optimize the entangled state fidelity [39]. We show the capability of changing the optical phase to two different setpoints of 0° and 180°.

The third and last calibration is the measurement of the entangled state phase, which has an offset with respect to the optical phase setpoint. Using the single-click protocol

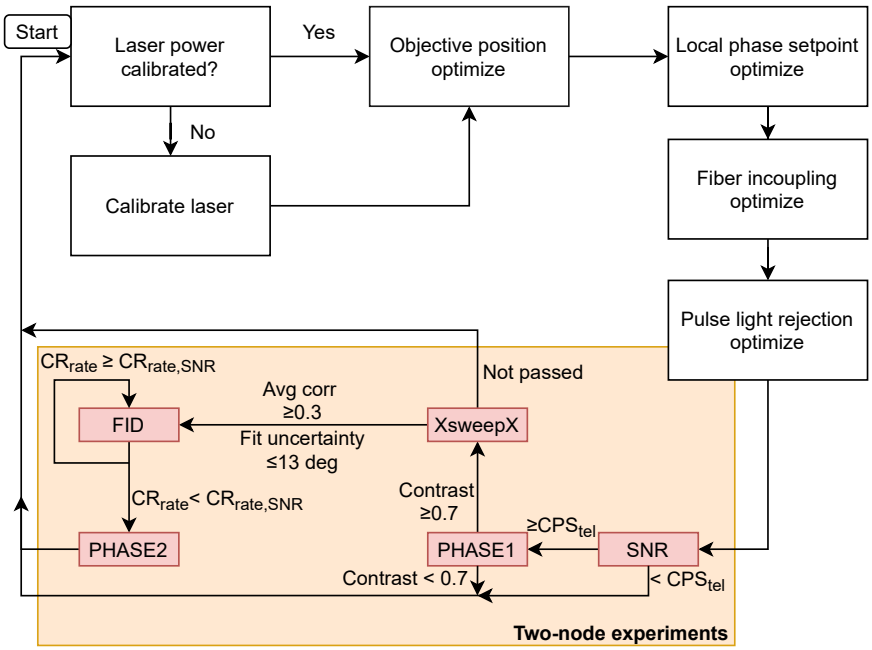

Figure 6.9: Flowchart for calibrations and performing the sequence of two-node experiments for the purpose of measuring the entanglement fidelity of the entangled state that is aimed to be generated. Between the different steps of the measurement sequence thresholds are checked of measured parameters that decide continuation of the sequence. Calibrations are started with a signal-to-noise (SNR) measurement, where the counts-per-shot of telecom signal from the nodes ($\mathrm{CPS_{tel}}$) is checked. We continue with PHASE and XsweepX and check their respective parameters. If all thresholds are satisfied, we continue with the fidelity measurements (FID) until the Charge Resonance passing rate ($\mathrm{CR_{rate}}$) drops below the calibrated value it had during the SNR ($\mathrm{CR_{rate,SNR}}$). Finally, we do another PHASE check before we restart the entire cycle.

we create a correlated spin-spin state that we can use to probe this phase. We do this by measuring correlations in the rotated basis X on Node Delft, while varying the readout basis in the Bloch sphere equator plane for Node The Hague. We can extract this entangled state phase by fitting the resulting oscillation with a single cosine, see Fig. 6.10C. We feed-forward this phase in the entanglement measurements to always generate the $\Psi^{\pm} = \frac{1}{\sqrt{2}}(|01\rangle \pm |10\rangle)$ during the entanglement generation.

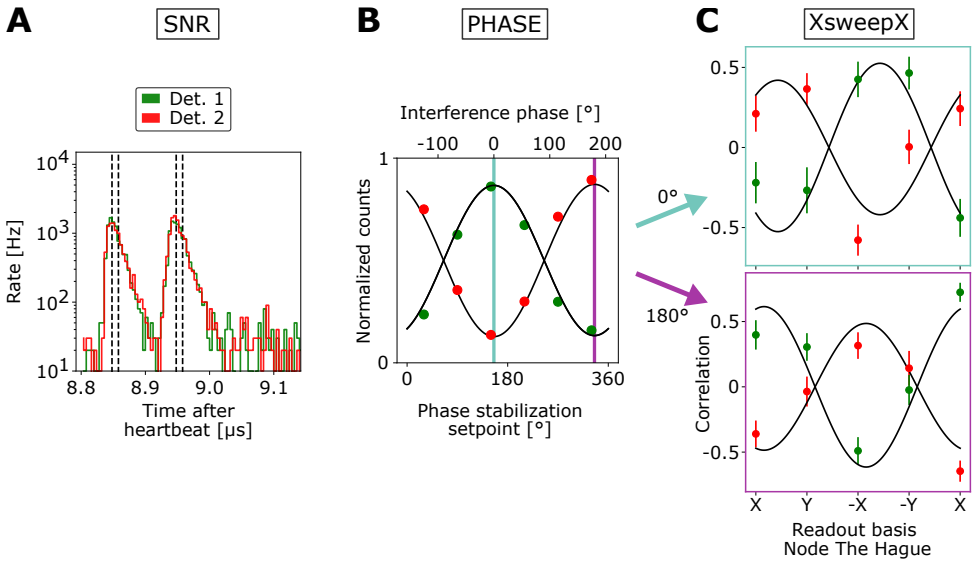

Figure 6.10: Typical calibration outcomes of: **(A)** signal strength (SNR) where the dotted lines show the used 'signal' window for both nodes respectively. The same windows are used to measure the 'noise' when the NV qubit state is rotated to the $|1\rangle$ (=dark) state.**(B)** Optical phase stability (PHASE), with fitted contrast (black lines). The vertical lines project to the top horizontal axis to determine the interference phase for the following measurements.**(C)** The entangled state phase (XsweepX) for an interference phase of 0° and 180°, showing the capabilities of the stabilization system to set a specific phase setpoint. The fitted phases (black solid lines) are 219(6) and 14(6) for the interference phase 0° and 180°, respectively.

EXPERIMENTAL SETUP PERFORMANCE

We maintain similar performance parameters of the experimental setup by performing calibrations of many different settings at different timescales. On a daily timescale, performance parameters of the communication qubit are re-calibrated:

1. Laser power (see Fig. 6.9)
2. Single-Shot Readout
3. Microwave qubit control (π, $\pi/2$, α)
4. Optical excitation (optical π pulse) for entanglement generation attempt
5. QFC efficiency

Roughly every 20 minutes, a set of shorter timescale calibrations are run. Some are dependent on performance parameters that are available live during or right after a measurement set. See Fig. 6.9 for the flowchart showing the calibrations and decisions made. As discussed in the previous section, we require several types of measurements to calibrate the phase of the entangled state. If in any of those measurements we are outside of the bound of acceptance, we restart the sequence. Additionally, the FID measurement sequence is cut into smaller blocks of 10k (30k) successful CR-checks for the heralded

(delayed-choice) metropolitan distance experiments. After each block, the CR-check passing rate is checked against the average CR-check rate during the SNR sequence (per node). If the passing rate is below this value, we exit the FID sequence and continue. We do this because the CR-check passing rate is a value that includes many derived underlying performance parameters of the setup as a whole, e.g. laser wavelengths, laser power, objective position and others. If any of those values changed significantly the CR-check passing rate is negatively impacted, which we use as a signal that an underlying parameter of the experiment is drifting off ideal and subsequently we break out of FID data taking. As can be seen in the flowchart, afterwards all calibrations are restarted, and we start from a calibrated setup with the SNR sequence, which is when we expect the highest CR check passing rate, and as such, use that to define our threshold for the rest of the experiment.

6.7.7. MODELING THE GENERATED ENTANGLED STATE

To assist in setting up the experiment and simulating the outcomes, we employ a Monte-Carlo simulation based on the model described in [39]. This is an extensive description of generating entanglement between remote nodes using the single-click protocol. It considers the spin-spin density matrix, based on the detection events where at most two photons reach the central detectors. By calculating the probability of each detection pattern and its corresponding spin-state, it arrives at the average density matrix given non photon-number resolving detectors. It takes into account many physical parameters that have an impact on the entangled state fidelity, such as photon loss, photon indistinguishably, and the photon wavepacket shape. It also includes several experimental parameters such as the effects of residual phase noise, dephasing noise and darkcount probability.

In the experiments presented in the main text we do not apply a post-processing correction using the Charge-Resonance check after the readout of the spin-state. This correction can be done to identify sequences where one of the nodes is in the NV^0 state, and no longer optically responsive to the excitation laser, but only in a post-processed fashion. To accurately model the effect of including events when the NV-center is ionized on the fidelity with the ideal state, we extend the model by including the probability of one of the nodes being ionized. We assume that, when an NV photon from a particular node in the midpoint is detected, this node can not be in the ionized state, but the other node can be with a probability p_{ion}. If the event in the midpoint is due to a noise photon, either of the nodes can be in the ionized state. This probability is measured by saving the CR-outcomes after the readout sequence. We include this ionized state as a third level of our qubit, that is outside the space addressed by our microwave control. When applying a readout pulse however, it will be read out as the $|1\rangle$ (=dark) state. The single shot readout (SSRO) fidelity of the solid-state NV qubits are given in Table 6.3. State readout correction is performed according to iterative Bayesian unfolding as described in this thesis [59].

An overview of all the simulation parameters used and their measured/used value for the simulation is given in Table 6.3. We have also simulated near-term performance of

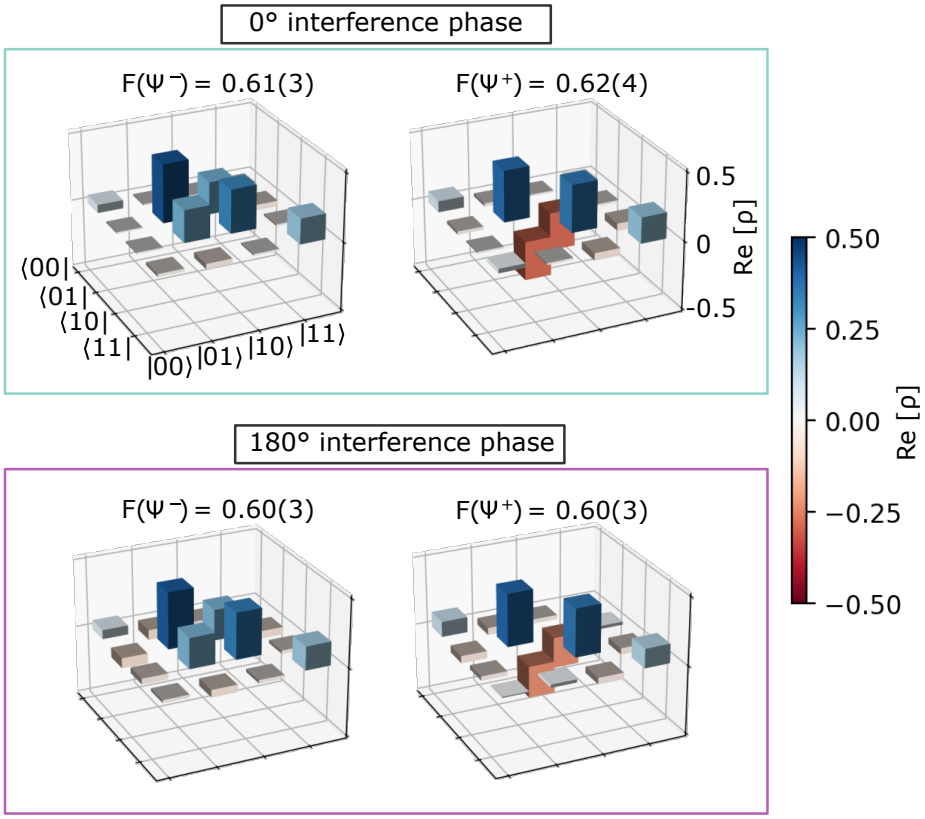

Figure 6.11: Bayesian estimation of density matrix for both phase setpoints, using the post-selected entanglement generation scheme, with both nodes in the same lab in Delft. We measure all two-spin correlators $\langle M_i M_j \rangle$ with $M_{i,j} \in [X, Y, Z]$ and use Bayesian estimation for tomography [57, 58] to find the most likely density matrix. The calibration measurements in Fig. 6.10 allow us to generate the same entangled state, at two different optical phase setpoints. The overlap with the ideal state for the most likely density matrix is given as numerical value, that is above 0.6 for both phase setpoints and detector outcomes.

the same link based on SnV centers (keeping the collection efficiency the same), which have 16 times higher coherent photon emission probability per optical excitation, full use of the improved QFC technology and improved phase stability, shown in Table 6.4.

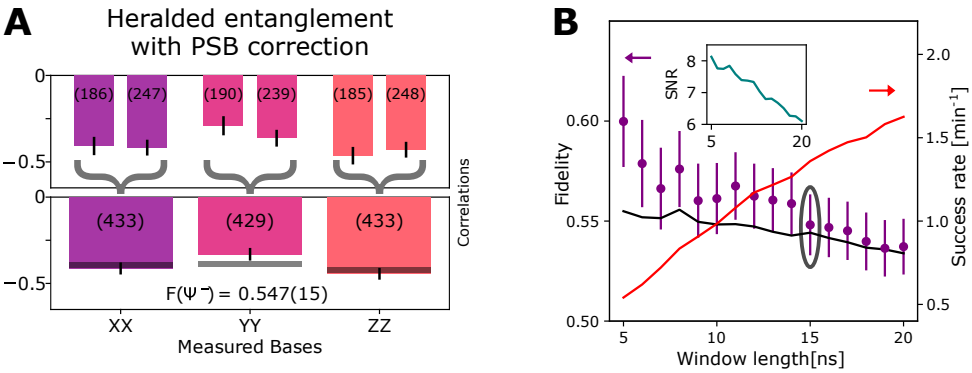

Figure 6.12: **(A)** Correlation measurement for full heralding with correction on discarding events accompanied by a measured PSB photon, independent of detector outcome. Upper plot shows events per detector, lower for both detectors combined. Bars indicate measured data, the number in parenthesis indicate the amount of events. Horizontal lines indicate the theoretical model. **(B)** State fidelity and entanglement generation rate for varying photon acceptance window length. Inset shows signal-to-noise ratio for the same window lengths. All measurement outcomes are corrected for tomography errors, errorbars are 1 standard deviation.

6

QFC	Node	Non-linear medium	Efficiency (front to end)	Noise $[s^{-1}\,GHz^{-1}]$	Eval. at filter bandwidth
QuTech [24, 36]	The Hague	ppLN waveguide	50%	2104	50 MHz
Fraunhofer ILT [37]	Delft	bulk KTA	48%	19	374 GHz

Table 6.1: Comparison of the QFCs used in the experiment.

Table 6.2: **Parameters of fibers used for quantum channel on the Quantum Link.**

Link	Loss local	Loss deployed fiber	Total	Typ. Round-trip time, drift
The Hague to midpoint	3 dB QFC, 4.9 dB filters	5.2 dB, 0.51 dB km^{-1}	13.1 dB	103.16 µs ±40 ps h^{-1}
Delft to midpoint	4 dB QFC, 4.5 dB filters	5.6 dB, 0.39 dB km^{-1}	13.9 dB	145.31 µs ±80 ps h^{-1}

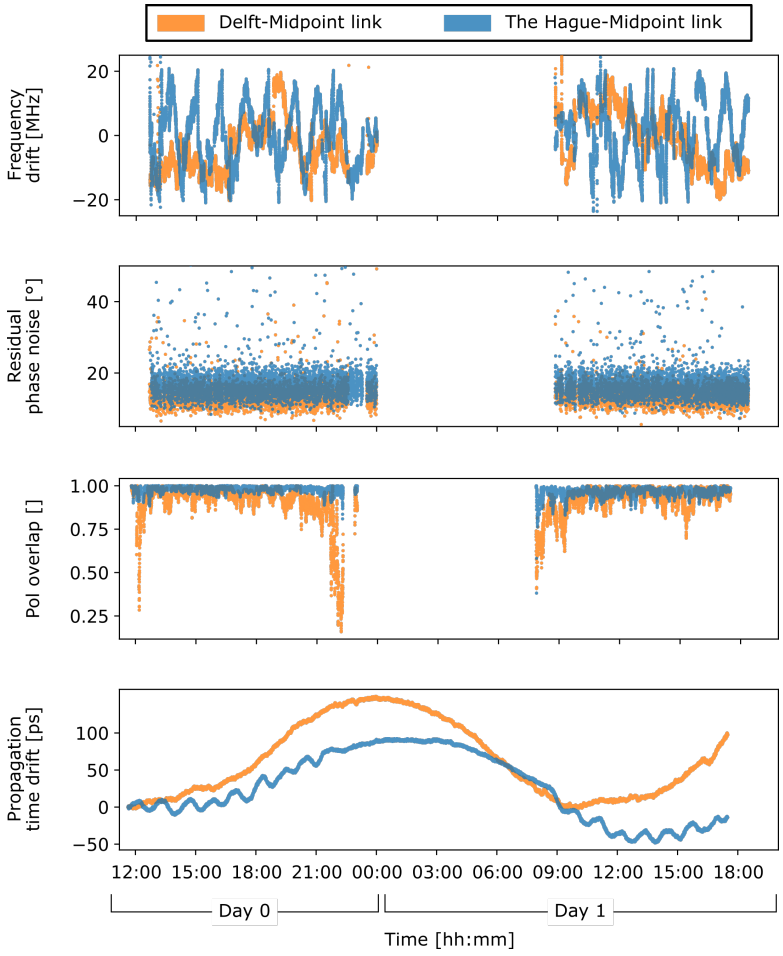

Figure 6.13: Continuous data of important parameters over deployed fiber link. From top to bottom: the frequency drift, phase noise, polarization and time of flight as measured by the individual systems and logged into a central database. For the frequency, phase and polarization we have conditioned the data on the respective feedback system being active. The pause in the system overnight was due to one of the feedback systems being out of lock, which got reset the next morning.

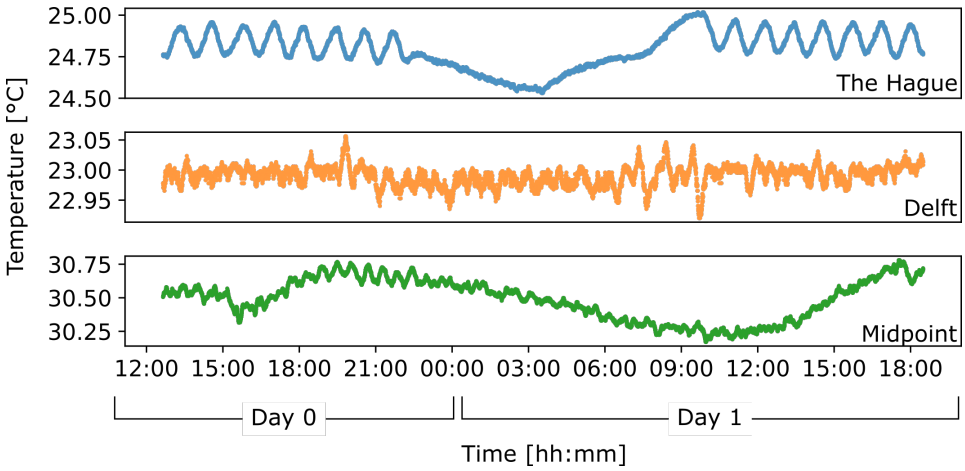

Figure 6.14: Temperature logging of the three locations during the same time as the continuous data logging of Fig. 6.13.

Table 6.3: **Error budget of deployed link post-selected and heralded entangled states.** Parameters noted with * are averages of data measured between the fidelity measurements, other are calibrated in separate experiments. The probability to detect a photon is given for $\alpha = 1$. If only one value is mentioned it is considered equal for both nodes. The infidelity contribution is given as if it was the only error present, to make direct comparison easier. Note that due to the large contribution of noise counts, the infidelity of the final simulated state with all the contributions taken into account does not follow the sum of the individual contributions.

Simulation parameter	Delayed-choice		Fully heralded	
	Value	Error con.	Value	Error con.
Det. prob.* (Delft, DH) []	10.6e-6, 8.4e-6	32.7%	10.0e-6, 7.1e-6	28.5%
α* []	0.25 and 0.25		0.25 and 0.25	
Backgr. counts* (Det1, Det2) [Hz]	40.3, 42.8		23.8, 22.0	
Double excitation probability []	0.04, 0.1	3.7%	0.04, 0.1	3.8%
Res. phase noise std* [°]	35	9.8%	45.3	14.3%
Dephasing probability []	0.01, 0.01	2.3%	0.02, 0.04	4.5%
Spectral diffusion FWHM [MHz]	13	4.5%	13	4.8%
Beam splitter imperfections []	0.95		0.95	
Detection window length [ns]	10	-	15	-
Optical Excitation Rabi angle [°]	150, 150	-	150, 150	-
Ionization probability* []	0.035, 0.045%	5.4%	0.046	6.2%
PSB collection efficiency []	0.1, 0.1	-	0.0, 0.0	-
Simulated error (all params)	-	43.1%, 42.2%	-	45.6%
Simulated Fidelity	0.568, 0.576	-	0.544	-
Measured error	-	43.2%, 42.4%	-	46.6%
Avg. SSRO fidelity	95.14%, 94.49%	-	94.13%, 94.98%	

Table 6.4: **Error budget of near-term and future improvements.** For the near-term performance, we simulated an improved ZPL fraction of the SnV, the implementation of the improved QFC on both nodes, and an improvement of the local phase-stabilization. For future improvements on the system with we have added improvements in qubit coherence via dynamical decoupling, reduction of double excitation via shorter optical excitation, reduced ionization by better control of the charge state of the emitter and improved mode overlap at the central beamsplitter.

Simulation parameter	Near-term		Future	
	Value	Error con.	Value	Error con.
Det. prob. (Delft, DH) []	16x10e-6, 16x10e-6	4.6%	16x10e-6, 16x10e-6	4.6%
α []	0.05 and 0.05		0.05 and 0.05	
Backgr. counts (Det1, Det2) [Hz]	5.0, 5.0		5.0, 5.0	
Double excitation probability []	0.04, 0.04	1.3%	0.01, 0.01	0.3%
Res. phase noise std [°]	15	1.7%	15	1.7%
Dephasing probability []	0.02, 0.04	3.0%	0.01, 0.01	1.0%
Spectral diffusion FWHM [MHz]	13	3.3%	13	1.3%
Beam splitter imperfections []	0.95		0.99	
Detection window length [ns]	15	-	15	-
Optical Excitation Rabi angle [°]	150, 150	-	150, 150	-
Ionization probability []	0.046	4.7%	0.01	1.0%
PSB collection efficiency []	0.1, 0.1	-	0.1, 0.1	-
Simulated error (all params)	-	17.2%	-	10.0%
Simulated Fidelity	0.828	-	0.90	-

REFERENCES

[1] A. J. Stolk *et al.*, *Metropolitan-scale heralded entanglement of solid-state qubits,* Science Advances **10** (2024), 10.1126/sciadv.adp6442.

[2] H. J. Kimble, *The quantum internet,* Nature **453**, 1023 (2008).

[3] S. Wehner, D. Elkouss and R. Hanson, *Quantum internet: A vision for the road ahead,* Science **362**, eaam9288 (2018).

[4] H. Buhrman, R. Cleve, J. Watrous and R. de Wolf, *Quantum fingerprinting,* Phys. Rev. Lett. **87**, 167902 (2001).

[5] M. Ben-Or and A. Hassidim, *Fast quantum byzantine agreement,* in *Proceedings of the Thirty-Seventh Annual ACM Symposium on Theory of Computing*, STOC '05 (Association for Computing Machinery, New York, NY, USA, 2005) p. 481–485.

[6] D. Gottesman, T. Jennewein and S. Croke, *Longer-baseline telescopes using quantum repeaters,* Phys. Rev. Lett. **109**, 070503 (2012).

[7] J. F. Clauser, M. A. Horne, A. Shimony and R. A. Holt, *Proposed experiment to test local hidden-variable theories,* Phys. Rev. Lett. **23**, 880 (1969).

[8] D. L. Moehring *et al.*, *Entanglement of single-atom quantum bits at a distance,* Nature **449**, 68–71 (2007).

[9] S. Ritter *et al.*, *An elementary quantum network of single atoms in optical cavities,* Nature **484**, 195 (2012), number: 7393 Publisher: Nature Publishing Group.

[10] J. Hofmann *et al.*, *Heralded Entanglement Between Widely Separated Atoms,* Science **337**, 72 (2012).

[11] H. Bernien *et al.*, *Heralded entanglement between solid-state qubits separated by three metres,* Nature **497**, 86–90 (2013).

[12] R. Stockill *et al.*, *Phase-Tuned Entangled State Generation between Distant Spin Qubits,* Physical Review Letters **119**, 010503 (2017), publisher: American Physical Society.

[13] L. Stephenson *et al.*, *High-Rate, High-Fidelity Entanglement of Qubits Across an Elementary Quantum Network,* Physical Review Letters **124**, 110501 (2020), publisher: American Physical Society.

[14] V. Krutyanskiy *et al.*, *Entanglement of Trapped-Ion Qubits Separated by 230 Meters,* Physical Review Letters **130**, 050803 (2023).

[15] P. Drmota *et al.*, *Robust Quantum Memory in a Trapped-Ion Quantum Network Node,* Physical Review Letters **130**, 090803 (2023).

[16] M. Pompili *et al.*, *Experimental demonstration of entanglement delivery using a quantum network stack,* npj Quantum Information **8**, 1 (2022).

[17] M. Pompili *et al.*, *Realization of a multinode quantum network of remote solid-state qubits,* Science **372**, 259–264 (2021).

[18] S. L. N. Hermans *et al.*, *Qubit teleportation between non-neighbouring nodes in a quantum network,* Nature **605**, 663 (2022).

[19] P. Drmota *et al.*, *Verifiable blind quantum computing with trapped ions and single photons,* (2024), 10.48550/arXiv.2305.02936, arXiv:2305.02936.

[20] M. Bock *et al.*, *High-fidelity entanglement between a trapped ion and a telecom photon via quantum frequency conversion,* Nature Communications **9**, 1998 (2018).

[21] V. Krutyanskiy *et al.*, *Light-matter entanglement over 50 km of optical fibre,* npj Quantum Information **5**, 1 (2019).

[22] M. Bock *et al.*, *High-fidelity entanglement between a trapped ion and a telecom photon via quantum frequency conversion,* Nature Communications **9**, 1998 (2018).

[23] M. Schäfer, B. Kambs, D. Herrmann, T. Bauer and C. Becher, *Two-stage, low noise quantum frequency conversion of single photons from silicon-vacancy centers in diamond to the telecom c-band,* Advanced Quantum Technologies , 2300228 (2023), https://onlinelibrary.wiley.com/doi/pdf/10.1002/qute.202300228 .

[24] A. Tchebotareva *et al.*, *Entanglement between a Diamond Spin Qubit and a Photonic Time-Bin Qubit at Telecom Wavelength,* Physical Review Letters **123**, 063601 (2019).

[25] E. Bersin *et al.*, *Telecom networking with a diamond quantum memory,* PRX Quantum **5** (2024), 10.1103/prxquantum.5.010303.

[26] C. Bradley *et al.*, *A Ten-Qubit Solid-State Spin Register with Quantum Memory up to One Minute,* Physical Review X **9**, 031045 (2019).

[27] V. Krutyanskiy, M. Canteri, M. Meraner, V. Krcmarsky and B. P. Lanyon, *Multimode ion-photon entanglement over 101 kilometers of optical fiber,* (2023), 10.48550/arXiv.2308.08891, arXiv:2308.08891.

[28] T. van Leent *et al.*, *Entangling single atoms over 33 km telecom fibre,* Nature **607**, 69 (2022).

[29] C. M. Knaut *et al.*, *Entanglement of nanophotonic quantum memory nodes in a telecom network,* Nature **629**, 573–578 (2024).

[30] D. Lago-Rivera, S. Grandi, J. V. Rakonjac, A. Seri and H. de Riedmatten, *Telecom-heralded entanglement between multimode solid-state quantum memories,* Nature **594**, 37–40 (2021).

[31] X.-Y. Luo *et al.*, *Postselected entanglement between two atomic ensembles separated by 12.5 km,* Phys. Rev. Lett. **129**, 050503 (2022).

[32] J.-L. Liu *et al.*, *Creation of memory–memory entanglement in a metropolitan quantum network,* Nature **629**, 579–585 (2024).

[33] D. Lago-Rivera, J. V. Rakonjac, S. Grandi and H. d. Riedmatten, *Long distance multiplexed quantum teleportation from a telecom photon to a solid-state qubit,* Nature Communications **14**, 1889 (2023).

[34] C. Cabrillo, J. I. Cirac, P. García-Fernández and P. Zoller, *Creation of entangled states of distant atoms by interference,* Physical Review A **59**, 1025–1033 (1999).

[35] S. Bose, P. L. Knight, M. B. Plenio and V. Vedral, *Proposal for Teleportation of an Atomic State via Cavity Decay,* Physical Review Letters **83**, 5158 (1999).

[36] A. J. Stolk *et al.*, *Telecom-Band Quantum Interference of Frequency-Converted Photons from Remote Detuned NV Centers,* PRX Quantum **3**, 020359 (2022).

[37] J. Geus *et al.*, *Low-noise short-wavelength pumped frequency down-conversion for quantum frequency converters,* Optica Quantum (2023), 10.1364/opticaopen.23684502.v1, optica Open 107563.

[38] A. Dréau, A. Tchebotareva, A. E. Mahdaoui, C. Bonato and R. Hanson, *Quantum frequency conversion of single photons from a nitrogen-vacancy center in diamond to telecommunication wavelengths,* Phys. Rev. Appl. **9**, 064031 (2018).

[39] S. L. N. Hermans *et al.*, *Entangling remote qubits using the single-photon protocol: an in-depth theoretical and experimental study,* New Journal of Physics **25**, 013011 (2023).

[40] E. F. Dierikx *et al.*, *White rabbit precision time protocol on long-distance fiber links,* IEEE Transactions on Ultrasonics, Ferroelectrics, and Frequency Control **63**, 945 (2016).

[41] C. A. Ryan, J. S. Hodges and D. G. Cory, *Robust Decoupling Techniques to Extend Quantum Coherence in Diamond,* Physical Review Letters **105**, 200402 (2010).

[42] M. H. Abobeih *et al.*, *One-second coherence for a single electron spin coupled to a multi-qubit nuclear-spin environment,* Nature Communications **9**, 2552 (2018).

[43] P. Lodahl, *Quantum-dot based photonic quantum networks,* Quantum Science and Technology **3**, 013001 (2017).

[44] C. Bradac, W. Gao, J. Forneris, M. E. Trusheim and I. Aharonovich, *Quantum nanophotonics with group iv defects in diamond,* Nature Communications **10**, 5625 (2019).

[45] N. T. Son *et al.*, *Developing silicon carbide for quantum spintronics,* Applied Physics Letters **116**, 190501 (2020).

[46] M. Ruf, N. H. Wan, H. Choi, D. Englund and R. Hanson, *Quantum networks based on color centers in diamond,* Journal of Applied Physics **130**, 070901 (2021).

[47] J. V. Rakonjac *et al.*, *Transmission of light–matter entanglement over a metropolitan network,* Optica Quantum **1**, 94–102 (2023).

[48] M. Ruf, M. Weaver, S. van Dam and R. Hanson, *Resonant excitation and purcell enhancement of coherent nitrogen-vacancy centers coupled to a fabry-perot microcavity,* Physical Review Applied **15**, 024049 (2021).

[49] D. Riedel *et al.*, *Deterministic enhancement of coherent photon generation from a nitrogen-vacancy center in ultrapure diamond,* Phys. Rev. X **7**, 031040 (2017).

[50] A. Sipahigil *et al.*, *An integrated diamond nanophotonics platform for quantum-optical networks,* Science **354**, 847–850 (2016).

[51] M. Pasini *et al.*, *Nonlinear quantum photonics with a tin-vacancy center coupled to a one-dimensional diamond waveguide,* Physical Review Letters **133** (2024), 10.1103/physrevlett.133.023603.

[52] P.-J. Stas *et al.*, *Robust multi-qubit quantum network node with integrated error detection,* Science **378**, 557–560 (2022).

[53] V. Krutyanskiy *et al.*, *Telecom-Wavelength Quantum Repeater Node Based on a Trapped-Ion Processor,* Physical Review Letters **130**, 213601 (2023).

[54] N. Kalb *et al.*, *Entanglement distillation between solid-state quantum network nodes,* Science **356**, 928–932 (2017).

[55] I. T. Raa *et al.*, *QMI - Quantum Measurement Infrastructure, a Python 3 framework for controlling laboratory equipment,* (2023).

[56] J. Geus *et al.*, *Low-noise short-wavelength pumped frequency down-conversion for quantum frequency converters,* Optica Open (2023), 10.1364/opticaopen.23684502.v1.

[57] C. Granade, J. Combes and D. G. Cory, *Practical bayesian tomography,* New Journal of Physics **18**, 033024 (2016).

[58] C. Granade *et al.*, *Qinfer: Statistical inference software for quantum applications,* Quantum **1**, 5 (2017).

[59] M. Pompili, *Multi-Node Quantum Networks with Diamond Qubits*, Ph.D. thesis, Delft University of Technology (2021).

7

CONCLUSIONS AND OUTLOOK

All I know is that I know nothing.

Socrates

We have shown our efforts toward bringing entanglement generation out of the lab and into the real word. We have investigated all the requirements for generating solid-state entanglement over a metropolitan link, realizing frequency conversion and stabilization schemes to complement an NV based quantum network node. Using these developments, we performed heralded entanglement generation between two solid-state nodes separated on a metropolitan scale over a deployed telecom fiber network. In this Ch. we summarize all the work shown, and give an outlook on how the road towards a global Quantum Internet might look by discussing the many ways in which the performance for future quantum networks can be improved.

7.1. SUMMARY

This work has focused on bringing quantum networking technologies out of the lab and into the real world, culminating in the generation of heralded entanglement between solid-state, NV-center-based quantum nodes separated on a metropolitan distance, connected with deployed telecom fiber (Ch. 6). To enable this, different technical and scientific challenges had to be overcome, which have been covered in the preceding Ch.s (Chapters 3 and 5). An additional technique, interfacing the NV center with rare-earth-ion compatible photonic qubits is shown in Ch. 4, showing a proof-of-principle to scale the entanglement generation rate by using Tm based multi-mode memories and entangled photon sources operating at both the telecom and visible wavelength. In the following we give a short summary of each of the Ch.s.

- In Ch. 3 we have shown the generation of indistinguishable photons between spectrally distinct NV centers, by converting their emission to the telecom wavelength with Quantum Frequency Converters (QFCs). We built two independent NV-center nodes combined with QFCs, capable of generating single photons and converting them to the Telecom L band. Frequency differences are removed by using a central telecom reference and feedback to the pump laser of the QFCs, resulting in highly indistinguishable photon generation as verified by a Hong-ou Mandel two-photon quantum intereference. We found that the finite visibility mainly arises from background photons generated by the QFC process and detector response to blinding, whilst the photon wave-packets themselves are highly indistinguishable.

- Ch. 4 shows the realization of an interface between a photon compatible with a Tm based quantum memory (λ =795 nm) and an NV-center based quantum network node (λ =637 nm). We have designed and built a noiseless, two-stage conversion processes to facilitate frequency matching, and show near-perfect indistinguishabilty between the NV-center emission and the converted single-photons. We further demonstrate the capabilities of our approach by teleporting a qubit compatible with the Tm memory to the electron spin state of the NV-center, showing the non-classical nature of the teleportation process by beating the bound set by classical strategies. This work highlights the opportunities in matching different quantum networking platforms for large scale quantum networks.

- In Ch. 5 we design, build and test an extendable infrastructure for optical phase stabilization over a deployed fiber link. We describe the need for the stringent requirements on the optical phase in the context of entanglement generation using the single-click protocol. We identify the core challenges which must be overcome to achieve this: phase-noise of the lasers, drifts of free-space optics and long-range fibers, and limited bandwidth due to the large separation of the end nodes. We describe our implemented solution, which divides the problem into separate stabilization of smaller subsets of the system, and describe the design and stabilization performance for each of them. Finally we characterise the complete system over a time from of more than ten hours, showing excellent long-term performance.

- Ch. 6 combines all the advances made in Chapters 2, 3 and 5 into a demonstration of heralded entanglement between two nodes deployed in a metropolitan area in The Netherlands. We built up a quantum link consisting of two nodes separated by 10 km located in Delft and The Hague, and a midpoint in Rijswijk, connected by 25 km of fiber. We build on the QFC approach described in Ch. 3 by implementing a novel conversion approach on one of the nodes, which generates more than two orders less background photons (NORA, Ch. 2). We combine this with the phase-stabilization architecture described in Ch. 5 to implement the single-click protocol, allowing for 0.5 Hz entanglement generation of two distant solid-state NV nodes in post-processing. Furthermore, by combining the excellent coherence properties of the NV center with real-time signal processing and feedback, we generate a fully heralded state between Delft and Den Haag, ready for further use in quantum protocols. We verify the entanglement by measuring the overlap with the ideally generated Bell-state, finding a value significantly above the classical bound.

In this work we have thus tackled the full set of technological challenges involved in bringing heralded entanglement generation between solid-state nodes out of the lab and into the real world. These technological challenges arise from the extreme sensitivity of the entanglement generation to various environmental parameters, and the complexity involved in controlling single quantum systems. To reach the level of control and stabilization needed, various technologies had to be brought together such as accurate timing synchronization [1] and quantum frequency conversion [2–4], and complex feedback systems for optical phase stability had to be developed (Ch. 5). In the following sections we discuss some of the limitations of the work in this thesis, and provide an outlook on recent and future developments which we think will advance this technology from a proof-of-concept demonstration to real-world applications.

7.2. IMPROVING QUANTUM LINKS

The results shown in this work are a powerful demonstration of the possibility of heralded entanglement at the metropolitan scale. Many technological and scientific hurdles have been overcome to make this a reality. It is however by no means close to the implementation needed for a full-scale quantum internet [5], where *anyone* in the network can share an entangled state with *anyone*. Both the rate at which entanglement is generated, and the remaining infidelity with an ideal entangled state are orders of magnitude from being useful for applications. Furthermore, the enormous costs and time involved of designing, building and operating the link makes this current form only accessible for a small amount of people. In order for quantum networks to become a viable platform for applications these challenges need to be overcome.

A basic way of describing the performance of a single quantum link can be done by looking at the rate of entanglement generation:

$$R_{ent} = R_{att} N_{comm} p_{succ}, \tag{7.1}$$

with R_{att} the rate at which we attempt entanglement generation, N_{comm} the number of communication modes involved per attempt and p_{succ} the probability of one of those communication modes successfully being measured to herald an entangled state. We

can recover the values from Ch. 6 by filling in the attempt rate ($\approx 1/150\,\mu s$), amount of qubits used (one) and the success probability ($\approx 7 \times 10^{-6}$) to find the entanglement generation rate of $0.28\,min^{-1}$. We will now provide various ways to improve these different components of the entanglement generation rate.

7.2.1. ATTEMPT RATE

For long-range links, the R_{att} is upper-bounded by the round-trip communication time between the location where the entanglement is heralded, e.g. the midpoint, and the nodes that hold the entangled state. In Ch. 6 this was done over the same optical fiber bundle as the quantum states, resulting in an attempt rate of R_{att} <6.6 kHz. In principle faster communication is possible by using line-of-sight propagation of the classical communication, having the benefit of shorter distances and communication at the speed of light.

7.2.2. MULTIPLEXING

In Ch. 6 the number of communication modes involved in the entanglement generation is one, as we only control one NV center per node and no additional quantum resources. A strategy to improve this factor is called multiplexing, using additional degrees of freedom to extend the resources available for using the communication channel. This is analogous to the methods which have enabled the classical internet to keep up the scaling of the bit-rate [6]. There are a number of ways in which this technique can be applied for quantum networks. For instance by using a memory qubit, such as nuclear spins in the environment, to store the qubit state. This allows for resetting the optical interface and attempting another entanglement generation again before knowing the outcome of the previous attempt, effectively multiplexing with the amount of memory qubits available [7]. Additional ways of multiplexing will be described in a later section.

7.2.3. IMPROVING SUCCESS PROBABILITY

The most immediate reason for the low rate of entanglement generation is the low probability of heralding a photon per attempt to generate entanglement (p_{succ} in Eq. 7.1). This probability can be decomposed as the product of three main probabilities:

- to emit a coherent photon useful for entanglement generation,
- to couple the photon in a well defined mode (e.g. a fiber),
- to measure the photon after transmission.

Compared to our implementation, all three of these probabilities can be significantly improved. Namely, only $\approx 2.5\%$ of the optical emission is coherent and useful for entanglement generation [8]. Second, while this work makes use of microstructures to improve the outcoupling efficiency from the diamond (solid immersion lenses [9, 10]), the collection efficiency into a well-defined single mode after free-space optics is still only $\approx 5\%$. Finally, quantum frequency conversion ($\eta_{\text{qfc}} = 50\%$), subsequent local fiber routing and narrow spectral filtering ($\eta_{\text{filt}} = 20\%$) induce another significant amount of loss. These factors alone brings the chance to detect a photon after excitation to

$p_{succ} < 1.3 \cdot 10^{-4}$, without considering any propagation losses over deployed fiber. We will now discuss some of the ways how all these numbers can be improved.

RESONANT CAVITIES

One can improve both the coherent emission and collection efficiency by placing the NV center in an optical cavity, resonant with the ZPL transition. This can enhance the emission probability into the ZPL through the Purcell effect, and improve the collection efficiency by having a confined optical mode. Together, these two effect would lead to orders of magnitude improvement in the success probability p_{succ}. There have been many advances towards this end over the last decade [11], with the main limitation being the sensitivity of the NV center to local electric fields and charges near surfaces [12]. This sensitivity precludes nanophotonic integration using known fabrication techniques, making enhancement of the emission challenging due to the relatively large mode volumes achievable. Nevertheless, using µm-thickness diamond membranes in fiber-based open micro-cavities Purcell enhancement of near lifetime limited transitions has been achieved [13, 14]. In other systems such as semi-conductor quantum dots, this open microcavity technique has shown to extract on demand single-photons from the emitter exceeding 50% probability [15, 16].

If nanophotonic integration were possible, nanophotonic crystal cavities would enable an alternative approach. In these cavities, structures of below 100 nm in size are patterned in the diamond to manipulate the optical propagation and confine the optical mode, and allow for much smaller mode-volume cavities. The previously mentioned electric field sensitivity prohibits the integration of NV centers in these nano-fabricated structures, which lead to a search for other color centers in diamond. Among these defects, those consiting of the group-IV elements are some of the most promising, due to their similar characteristics such as a high quantum efficiency and a large fraction of emission in the ZPL [11]. All these color centers have a charge state that has an electron spin and are first-order insensitive to electric fields which allows for higher tolerances to the proximity to surfaces and charge-traps. There has been a lot of recent experimental progress towards quantum networking experiments using many of the defects formed with these elements such as SiV[17, 18], GeV [19], SnV [20–23] and PbV [24, 25]. These defects have some challenges, mainly due to an orbital splitting in the ground state. This limits the electron-spin coherence due to phonon induced transitions, most readily overcome with significantly lower operating temperatures than NV centers (< 1K). Furthermore, this orbital splitting complicates direct microwave driving between the spin states [26, 27]. Recent experiments showing entanglement between two SiV centers in different fridges [28] highlight the progress made in the fabrication of these devices and the development of the necessary control to entangle them..

IMPROVED QFCS

The probability to measure the photon after transmission over a long fiber is already significantly improved in this work, by converting the emission at the natural wavelength (8 to 10 $\text{dB}\,\text{km}^{-1}$) to the telecom L band (0.2 to 0.5 $\text{dB}\,\text{km}^{-1}$). However, the conversion method used does introduce a constant overhead of loss in the form of conversion losses and additional filter losses. These additional filter losses strongly depend on the amount

of out-of-band suppression needed, which in turn depends on the spectral profile and magnitude of noise added by spurious processes in the.

The conversion efficiency of a difference-frequency generation processes inside a non-linear medium can in theory reach 100%, and has experimentally reached above 90% [29]. For QFCs that use bulk optics to couple in and out of the non-linear medium, the losses that happen at the interfaces of the crystal in the form of coupling losses and reflections will always be present, and can be minimized with the appropriate anti-reflection coatings and lens design. The added noise photons mainly arise due to the Raman scattering and spurious SPDC are the main reason spectral filtering is needed, which all have transmission/insertion losses. Low-noise QFC [29, 30] can significantly relax these filtering requirements, in turn also improving the overall transmission of the signal via less filtering steps. This make the development of robust, low-noise and highly efficient QFC modules a key enabling technology for near-term quantum networks operating at in the low-loss telecom band.

7.2.4. MINIATURIZATION AND MULTIPLEXING

Now that we have discussed the ways to improve the success probability p_{succ}, we turn to other technological developments from which quantum networks will benefit greatly. As mentioned, the footprint of current solid-state entanglement generation platforms is macroscopic, and can take up large lab spaces. One pathway is to miniaturize the optical components needed to extract, filter and route the photons coming from the solid-state emitter using Photonic Integrated Circuits (PIC).

PHOTONIC INTEGRATED CIRCUITS

Recent developments have shown the realization of programmable photonics on chip using low-loss waveguides, switches and couplers [31–34]. Non-linear optics in on-chip waveguides have been shown to reach high conversion efficiencies using $LiNbO_3$ on Insulator [35, 36] or four-wave mixing in Si_3N_4 [37] for efficient conversion without going off-chip. On-chip detection of single photons has also have been shown in different platforms [38], another important component for local entanglement generation. Part of these developments are related to the push for high-performance integrated optical components needed for photonic quantum computing [39, 40], trying to achieve fault tolerance using single photons and linear optics. The *total* losses allowed for this approach to work are extremely low (≈1%) which has fueled the development to push the transmission of the individual components (waveguides, filters, interpreters, switches and detectors) to near unity [41] for the Silicon On Insulator platform by developing foundry compatible techniques. Similar platforms for quantum networks would benefit greatly from the same kind of development, both in focus and scale.

HETEROGENOUS INTEGRATION

While it is also possible to fabricate optical components directly onto the diamond [42], the fabrication of diamond nano-photonics is complicated by the extreme hardness and chemical stability of the substrate. This results in process flows with many challenging steps, and might be an obstacle to fabricating large amounts of components in a single fabrication flow. Recent developments in the fabrication large (200x200µm), ultra-

thin (down to 10 nm) membranes of diamond [43] have opened the door for the simplified fabrication of high quality factor cavities in diamond [44]. One way to combine the strength of PIC mature manufacturing processes with nano-fabricated diamond structures hosting emitters is the heterogeneous integration of the two platforms. This enables making hybrid chips built from components that are each fabricated independently, decoupling the (already challenging) fabrication flow and enables non-unity fabrication yields to be overcome. Recent demonstrations of this have been done with diamond chiplets containing Group IV color centers, integrated in an AlN PIC [45], as well as the integration of diamond nano-photonic cavities containing SnV centers in an Si_3N_4 PIC [46], demonstrating the feasibility of hybrid integration.

7.2.5. TRANSMISSION LOSSES

To be able to interface to remote nodes, methods of going off chip and into optical fibers will be needed. Not only the loss, but also the ease of alignment, robustness and durability of the coupling are important parameters to consider. Current techniques of coupling into a fiber, e.g. using lensed fibers or tapers on both fibers and waveguides for adiabatic transfer [47, 48] have shown ways to efficiently extract photons from the high refractive index photonic structures. For long-range transmission between quantum nodes, existing optical fiber infrastructure is considered an obvious candidate. For the foreseeable future, making the photons compatible with the low-loss telecom C band is the best strategy to reduce transmission losses. Once transmission loss starts to dominate overall success probability, different transmission can be adopted. A recent proposal using free-space vacuum tubes with concatenated $4f$-systems are an interesting avenue to reduce transmission losses to below $1 \times 10^{-4}\,\mathrm{dB\,km^{-1}}$. Fibers made from an ultra-pure Fluoride glass called ZBLAN could have loss values close to $6 \times 10^{-3}\,\mathrm{dB\,km^{-1}}$ at λ =2.3 µm for future fiber low-loss links [49]. Another approach is to reduce propagation loss between distant parties is to use space-based quantum communication [50, 51], where the feasibility of space-to-ground distribution of entangled photons [52] and quantum key generation [53] have been demonstrated, as well as on-board Bell tests on small-scale satellites [54]. Future constellations of low-earth orbit, small-scale satellites could provide a way to connect distant terrestrial networks.

7.3. SOFTWARE INTEGRATION

The experiments in this work have benefited from the development of a new software infrastructure called QMI [55], which addresses the need to control large distributed experiments over a network. This enabled us to build an extensive library of programs written in Python3 that control various stand-alone tasks in the experiments, sometimes fully automating them. Going forward the amount of information needing to be processed to enable more complex quantum nodes and networks will only increase, and the level of automated controls will have to increase. Various software frameworks for the automatic tune-up of various qubit systems already exist and include commercial offerings such as Orange QS's *Quantum Diagnostics Library* or Q-Ctrl's *Boulder Opal*, and similar system for the characterization of quantum nodes will be needed.

7.4. BEYOND QUANTUM LINKS

A future Quantum Internet will only reach its full potential if we can go beyond point-to-point quantum links to generating entanglement between non-neighbouring nodes in the network [56]. Having every party in the network connected to each other via a direct link is not a scalable approach, and is shown to be limited by channel loss [57, 58]. The no-cloning theorem prevents us from simply copying the (unknown) quantum states and sending them over the network like in the current Internet. That is why a crucial component of large scale quantum networks will be the quantum repeater, which will facilitate overcoming the rate and fidelity limitations of a single link via the processing of quantum information on intermediate quantum nodes.

7.4.1. QUANTUM REPEATERS

A large set of theoretical proposal for quantum repeater protocols, as well as ways of implementing these protocols in a practical quantum platform, of which a large overview is given Ref. [59]. There exist a large spectrum of proposals for quantum repeater architectures, ranging from the use of single-photon, phase-stable schemes [60–62], the incorporation of additional quantum memories to perform entanglement swapping [63–65], or the generation, propagation and measurement of large entangled photon states [66, 67]. These protocols are devised to overcome errors due to photon loss and/or operational errors on the entangled states generated between repeater stations, to deliver a higher fidelity entangled state between the end nodes. Current technology is far from reaching the strict thresholds set by the protocols, but proof of principle experiments have shown progress in repeater-like experiments. Examples of this are the memory assisted quantum communication using an SiV inside a cavity [68], the quantum key distribution over 500 km of deployed fiber [69] and the swapping of entanglement to end nodes via a third, intermediate node [70]. The question whether an experimental quantum repeater actually *repeats* is a difficult question, analogous to whether a quantum error correction code is actually correcting errors and helping to preserve the qubit state.

7.4.2. QUANTUM NETWORK STACK

From a networking perspective, only providing the ability to (probabilistic) generate entanglement between two nodes is not enough to run applications on. Like the internet we have today, a future quantum internet will have layers of software abstraction[71–76] that work together to turn the probabilistic entanglement generation between links into the actual execution of quantum programs over the network. The design of the protocols to run in the different layers to facilitate e.g. the execution of arbitrary operations [77], routing of entanglement [78, 79], or qubit teleportation on the network [80] are all done in different layers, and is an active field of research. All the work discussed in this thesis would be considered the lowest layer, the so-called *physical* layer, on which further layers can be built. A connection of the physical layer with the link layer has been demonstrated using NV centers [81], and work on further integration is an ongoing effort that has many opportunities for new protocols.

7.5. CONCLUSION

In this work we have made a great effort to bring entanglement generation outside of the lab and into the real world. We have done so by bringing all the elements needed for heralded solid-state entanglement together: quantum nodes built up from NV centers and novel quantum frequency converters, combined with a phase-stabilization architecture operating in the telecom L-band. When considering where we are in the time-line of the development of a quantum internet, we are only scratching the surface of what needs to be done. Even more exciting developments are definitely ahead of us!

REFERENCES

[1] E. F. Dierikx *et al.*, *White rabbit precision time protocol on long-distance fiber links,* IEEE Transactions on Ultrasonics, Ferroelectrics, and Frequency Control **63**, 945 (2016).

[2] A. Dréau, A. Tchebotareva, A. E. Mahdaoui, C. Bonato and R. Hanson, *Quantum frequency conversion of single photons from a nitrogen-vacancy center in diamond to telecommunication wavelengths,* Physical Review Applied **9**, 064031 (2018).

[3] A. Tchebotareva *et al.*, *Entanglement between a diamond spin qubit and a photonic time-bin qubit at telecom wavelength,* Phys. Rev. Lett. **123**, 063601 (2019).

[4] J. F. Geus *et al.*, *Frequency down-conversion for efficient, low-noise quantum frequency converters,* in *Quantum Computing, Communication, and Simulation II*, Vol. 12015, edited by P. R. Hemmer and A. L. Migdall, International Society for Optics and Photonics (SPIE, 2022) pp. 24 – 29.

[5] S. Wehner, D. Elkouss and R. Hanson, *Quantum internet: A vision for the road ahead,* Science **362**, eaam9288 (2018).

[6] G. P. Agrawal, *Optical communication: Its history and recent progress,* in *Optics in Our Time* (Springer International Publishing, 2016) p. 177–199.

[7] S. B. v. Dam, P. C. Humphreys, F. Rozpędek, S. Wehner and R. Hanson, *Multiplexed entanglement generation over quantum networks using multi-qubit nodes,* Quantum Science and Technology **2**, 034002 (2017).

[8] D. Riedel *et al.*, *Deterministic enhancement of coherent photon generation from a nitrogen-vacancy center in ultrapure diamond,* Phys. Rev. X **7**, 031040 (2017).

[9] J. P. Hadden *et al.*, *Strongly enhanced photon collection from diamond defect centers under microfabricated integrated solid immersion lenses,* Applied Physics Letters **97** (2010), 10.1063/1.3519847.

[10] L. Robledo *et al.*, *High-fidelity projective read-out of a solid-state spin quantum register,* Nature **477**, 574 (2011).

[11] M. Ruf, N. H. Wan, H. Choi, D. Englund and R. Hanson, *Quantum networks based on color centers in diamond,* Journal of Applied Physics **130**, 070901 (2021).

[12] M. Ruf *et al.*, *Optically coherent nitrogen-vacancy centers in micrometer-thin etched diamond membranes,* Nano Letters **19**, 3987 (2019).

[13] M. Ruf, M. Weaver, S. van Dam and R. Hanson, *Resonant excitation and purcell enhancement of coherent nitrogen-vacancy centers coupled to a fabry-perot microcavity,* Phys. Rev. Applied **15**, 024049 (2021).

[14] V. Yurgens *et al.*, *Cavity-assisted resonance fluorescence from a nitrogen-vacancy center in diamond,* (2024).

[15] N. Tomm *et al.*, *A bright and fast source of coherent single photons,* Nature Nanotechnology **16**, 399–403 (2021).

[16] X. Ding *et al.*, *High-efficiency single-photon source above the loss-tolerant threshold for efficient linear optical quantum computing,* (2023).

[17] M. K. Bhaskar *et al.*, *Experimental demonstration of memory-enhanced quantum communication,* Nature **580**, 60–64 (2020).

[18] P.-J. Stas *et al.*, *Robust multi-qubit quantum network node with integrated error detection,* Science **378**, 557–560 (2022).

[19] R. Høy Jensen *et al.*, *Cavity-enhanced photon emission from a single germanium-vacancy center in a diamond membrane,* Phys. Rev. Appl. **13**, 064016 (2020).

[20] M. E. Trusheim *et al.*, *Transform-limited photons from a coherent tin-vacancy spin in diamond,* Phys. Rev. Lett. **124**, 023602 (2020).

[21] X. Guo *et al.*, *Microwave-based quantum control and coherence protection of tin-vacancy spin qubits in a strain-tuned diamond membrane heterostructure,* (2023).

[22] M. Pasini *et al.*, *Nonlinear quantum photonics with a tin-vacancy center coupled to a one-dimensional diamond waveguide,* (2023).

[23] J. M. Brevoord *et al.*, *Heralded initialization of charge state and optical transition frequency of diamond tin-vacancy centers,* (2023).

[24] P. Wang, T. Taniguchi, Y. Miyamoto, M. Hatano and T. Iwasaki, *Low-temperature spectroscopic investigation of lead-vacancy centers in diamond fabricated by high-pressure and high-temperature treatment,* ACS Photonics **8**, 2947–2954 (2021).

[25] P. Wang *et al.*, *Transform-limited photon emission from a lead-vacancy center in diamond above 10 k,* Phys. Rev. Lett. **132**, 073601 (2024).

[26] L. Orphal-Kobin, C. G. Torun, J. M. Bopp, G. Pieplow and T. Schröder, *Coherent microwave, optical, and mechanical quantum control of spin qubits in diamond,* (2023).

[27] G. Pieplow, M. Belhassen and T. Schröder, *Efficient microwave spin control of negatively charged group-iv color centers in diamond,* Phys. Rev. B **109**, 115409 (2024).

[28] C. M. Knaut *et al.*, *Entanglement of nanophotonic quantum memory nodes in a telecom network,* Nature **629**, 573–578 (2024).

[29] M. Schäfer, B. Kambs, D. Herrmann, T. Bauer and C. Becher, *Two-stage, low noise quantum frequency conversion of single photons from silicon-vacancy centers in diamond to the telecom c-band,* Advanced Quantum Technologies (2023), 10.1002/qute.202300228.

[30] J. Geus *et al.*, *Low-noise short-wavelength pumped frequency down-conversion for quantum frequency converters,* Optica Quantum (2023), 10.1364/opticaopen.23684502.v1, optica Open 107563.

[31] N. C. Harris *et al.*, *Linear programmable nanophotonic processors,* Optica **5**, 1623 (2018).

[32] D. J. Blumenthal, R. Heideman, D. Geuzebroek, A. Leinse and C. Roeloffzen, *Silicon nitride in silicon photonics,* Proceedings of the IEEE **106**, 2209–2231 (2018).

[33] W. Bogaerts *et al.*, *Programmable photonic circuits,* Nature **586**, 207–216 (2020).

[34] D. Zhu *et al.*, *Integrated photonics on thin-film lithium niobate,* Advances in Optics and Photonics **13**, 242 (2021).

[35] C. Wang *et al.*, *Ultrahigh-efficiency wavelength conversion in nanophotonic periodically poled lithium niobate waveguides,* Optica **5**, 1438 (2018).

[36] X. Wang *et al.*, *Quantum frequency conversion and single-photon detection with lithium niobate nanophotonic chips,* npj Quantum Information **9** (2023), 10.1038/s41534-023-00704-w.

[37] I. Agha, S. Ates, M. Davanço and K. Srinivasan, *A chip-scale, telecommunications-band frequency conversion interface for quantum emitters,* Optics Express **21**, 21628 (2013).

[38] S. Ferrari, C. Schuck and W. Pernice, *Waveguide-integrated superconducting nanowire single-photon detectors,* Nanophotonics **7**, 1725–1758 (2018).

[39] E. Knill, R. Laflamme and G. J. Milburn, *A scheme for efficient quantum computation with linear optics,* Nature **409**, 46–52 (2001).

[40] J. L. O'Brien, *Optical quantum computing,* Science **318**, 1567–1570 (2007).

[41] K. Alexander *et al.*, *A manufacturable platform for photonic quantum computing,* (2024).

[42] S. Mi, M. Kiss, T. Graziosi and N. Quack, *Integrated photonic devices in single crystal diamond,* Journal of Physics: Photonics **2**, 042001 (2020).

[43] X. Guo *et al.*, *Direct-bonded diamond membranes for heterogeneous quantum and electronic technologies,* (2023).

[44] S. W. Ding *et al.*, *High-q cavity interface for color centers in thin film diamond,* (2024).

[45] N. H. Wan *et al.*, *Large-scale integration of artificial atoms in hybrid photonic circuits,* Nature **583**, 226–231 (2020).

[46] K. C. Chen *et al.*, *A scalable cavity-based spin–photon interface in a photonic integrated circuit,* Optica Quantum **2**, 124 (2024).

[47] T. G. Tiecke *et al.*, *Efficient fiber-optical interface for nanophotonic devices,* Optica **2**, 70 (2015).

[48] S. Khan *et al.*, *Low-loss, high-bandwidth fiber-to-chip coupling using capped adiabatic tapered fibers,* APL Photonics **5** (2020), 10.1063/1.5145105.

[49] I. Cozmuta, S. Cozic, M. Poulain, S. Poulain and J. R. Martini, *Breaking the silica ceiling: Zblan-based opportunities for photonics applications,* in *Optical Components and Materials XVII*, edited by M. J. Digonnet and S. Jiang (SPIE, 2020).

[50] S. Khatri, A. J. Brady, R. A. Desporte, M. P. Bart and J. P. Dowling, *Spooky action at a global distance: analysis of space-based entanglement distribution for the quantum internet,* npj Quantum Information **7** (2021), 10.1038/s41534-020-00327-5.

[51] L. de Forges de Parny *et al.*, *Satellite-based quantum information networks: use cases, architecture, and roadmap,* Communications Physics **6** (2023), 10.1038/s42005-022-01123-7.

[52] J. Yin *et al.*, *Satellite-based entanglement distribution over 1200 kilometers,* Science **356**, 1140–1144 (2017).

[53] S.-K. Liao *et al.*, *Satellite-to-ground quantum key distribution,* Nature **549**, 43–47 (2017).

[54] A. Villar *et al.*, *Entanglement demonstration on board a nano-satellite,* Optica **7**, 734 (2020).

[55] I. T. Raa *et al.*, *QMI - Quantum Measurement Infrastructure, a Python 3 framework for controlling laboratory equipment,* (2023).

[56] S. Wehner, D. Elkouss and R. Hanson, *Quantum internet: A vision for the road ahead,* Science **362** (2018), 10.1126/science.aam9288, publisher: American Association for the Advancement of Science Section: Review.

[57] M. Takeoka, S. Guha and M. M. Wilde, *Fundamental rate-loss tradeoff for optical quantum key distribution,* Nature Communications **5** (2014), 10.1038/ncomms6235.

[58] S. Pirandola, R. Laurenza, C. Ottaviani and L. Banchi, *Fundamental limits of repeaterless quantum communications,* Nature Communications **8** (2017), 10.1038/ncomms15043.

[59] K. Azuma *et al.*, *Quantum repeaters: From quantum networks to the quantum internet,* Reviews of Modern Physics **95**, 045006 (2023).

[60] C. Cabrillo, J. I. Cirac, P. García-Fernández and P. Zoller, *Creation of entangled states of distant atoms by interference,* Physical Review A **59**, 1025–1033 (1999).

[61] S. Bose, P. L. Knight, M. B. Plenio and V. Vedral, *Proposal for Teleportation of an Atomic State via Cavity Decay,* Physical Review Letters **83**, 5158 (1999).

[62] M. Lucamarini, Z. L. Yuan, J. F. Dynes and A. J. Shields, *Overcoming the rate–distance limit of quantum key distribution without quantum repeaters,* Nature **557**, 400–403 (2018).

[63] H.-J. Briegel, W. Dür, J. I. Cirac and P. Zoller, *Quantum repeaters: The role of imperfect local operations in quantum communication,* Physical Review Letters **81**, 5932–5935 (1998).

[64] L.-M. Duan, M. D. Lukin, J. I. Cirac and P. Zoller, *Long-distance quantum communication with atomic ensembles and linear optics,* Nature **414**, 413–418 (2001).

[65] L. Childress, J. M. Taylor, A. S. Sørensen and M. D. Lukin, *Fault-tolerant quantum communication based on solid-state photon emitters,* Physical Review Letters **96** (2006), 10.1103/physrevlett.96.070504.

[66] K. Azuma, K. Tamaki and H.-K. Lo, *All-photonic quantum repeaters,* Nature Communications **6** (2015), 10.1038/ncomms7787.

[67] F. Schmidt, D. Miller and P. van Loock, *Error-corrected quantum repeaters with gkp qudits,* (2023).

[68] M. Bhaskar *et al.*, *Quantum Nonlinear Optics with a Germanium-Vacancy Color Center in a Nanoscale Diamond Waveguide,* Physical Review Letters **118**, 223603 (2017).

[69] J.-P. Chen *et al.*, *Twin-field quantum key distribution over a 511km optical fibre linking two distant metropolitan areas,* Nature Photonics **15**, 570–575 (2021).

[70] M. Pompili *et al.*, *Realization of a multinode quantum network of remote solid-state qubits,* Science **372**, 259–264 (2021).

[71] R. Van Meter, T. Ladd, W. Munro and K. Nemoto, *System design for a long-line quantum repeater,* IEEE/ACM Transactions on Networking **17**, 1002–1013 (2009).

[72] A. Dahlberg *et al.*, *A link layer protocol for quantum networks,* in *Proceedings of the ACM Special Interest Group on Data Communication*, SIGCOMM '19 (ACM, 2019).

[73] W. Kozlowski and S. Wehner, *Towards large-scale quantum networks,* in *Proceedings of the Sixth Annual ACM International Conference on Nanoscale Computing and Communication*, NANOCOM '19 (ACM, 2019).

[74] A. Pirker and W. Dür, *A quantum network stack and protocols for reliable entanglement-based networks,* New Journal of Physics **21**, 033003 (2019).

[75] W. Kozlowski, A. Dahlberg and S. Wehner, *Designing a quantum network protocol,* in *Proceedings of the 16th International Conference on emerging Networking EXperiments and Technologies*, CoNEXT '20 (ACM, 2020).

[76] J. Illiano, M. Caleffi, A. Manzalini and A. S. Cacciapuoti, *Quantum internet protocol stack: A comprehensive survey,* Computer Networks **213**, 109092 (2022).

[77] A. Dahlberg *et al.*, *Netqasm—a low-level instruction set architecture for hybrid quantum–classical programs in a quantum internet,* Quantum Science and Technology **7**, 035023 (2022).

[78] M. Pant *et al.*, *Routing entanglement in the quantum internet,* npj Quantum Information **5** (2019), 10.1038/s41534-019-0139-x.

[79] K. Chakraborty, F. Rozpedek, A. Dahlberg and S. Wehner, *Distributed routing in a quantum internet,* (2019).

[80] Y. Zhao and C. Qiao, *Quantum transport protocols for distributed quantum computing,* (2021).

[81] M. Pompili *et al.*, *Experimental demonstration of entanglement delivery using a quantum network stack,* npj Quantum Information **8**, 1 (2022).

ACKNOWLEDGEMENTS

This is the part where I attempt to thank all the people that have inspired, supported and helped me on my journey during my PhD and writing this thesis. I have undoubtedly forgot many people that I have came across these past 6+ years. Please do not feel offended if I did not mention you, it is only a reflection of my bad memory and a consequence of the fact that it has been a great joy for me to get to know so many inspiring and amazing people.

Of course I have to start by thanking the person who without, my journey would not even have started in the first place. **Ronald** you have created an environment where everyone who is passionate about science and quantum mechanics can truly thrive. As a Msc student in your group I got fascinated by the incredible experiments that were going on and enjoyed the freedom with which I got to explore the lab in my own way. Your vision of bigger things, and idea of 4 metropolitan nodes in 2020 sounded, so appealing that I knew that my quantum journey should continue in Delft. A decision that I still stand by, even though it wasn't always easy. During my PhD you have been a great support and allowed me to make the most (and more!) of my time in your group. Thank you for putting your faith in me to complete the long journey of the Qlink experiment and beyond, I am looking forward to the things we are going to achieve *truly* outside of the lab.

Tim you are my co-promotor, but I want to thank you additionally for your guidance during my early years at QuTech as a MSc student. Your supervision and critical insights have helped me grow and motivated me to keep going further in research. I am always amazed by the incredible progress you and your group are making in controlling nuclear spins and new colour centers.

I would also like to thank my committee: **Christoph Becher**, **Hugues de Riedmatten**, **Leo Dicarlo**, **Lieven van der Sypen**, **Bas Hensen**, and **Miriam Blaauboer**, thank you for reading my thesis and I am looking forward to your questions.

To go back to my time as a Master student, I can not go without mentioning my daily supervisor **Julia Cramer**, who as been the best introduction to the scientific world I can imagine. I still remember the plots you showed me on your screen of DynamicalDecoupling spectra of individual nuclear spins that you happily explained were qubits. I immediately wanted to know more about them and you were happy to take me on the journey, and the rest is history... Thank you for showing me the ropes, from filling cryostats to how to make an enticing presentation with a story, I would not be the researcher I am without you. Consider this a rectification of the fact that I never wrote an acknowledgement for my MSc thesis! With that I would like to thank the rest of 'early' team Diamond for the solid foundation that they built, not only research but also group culture wise, you know who you are!

Kian, I very happy that next to being a great colleague during the long and hard journey of Qlink, we have also become a great friend outside the madness of Quantum. Thank you for being there both during the long hours of experiments and data-taking,

but also the equally long hours of occasional escapades far outside the lab and the country! We developed good (*Anytime* fitness) and less good (0DTE before it was cool) habits together, which made my PhD time a much deeper and more enjoyable experience! Your open and friendly personality makes you stand out in our usually cold and shy environment, and you will find your way in the exciting future of quantum technologies. I am sure our paths will cross more often and whatever happens, know that I will always say yes to an Oliver Heldens concert, quote me on that. Good luck in preparing for your defense coming up soon!

Marie-Christine I am happy that I did not scare you away after your internship in the group and you returned for a Post-Doc. Those DM optimization plots fascinated us all! You are an amazing person and you have positive impact on everyone around you, for me personally and the whole Qlink team. Thank you for taking up the tasks and providing structure when it was missing, both in the research when writing papers or doing simulations, but also in meetings (retrospectives yay). We totally killed when organizing baking pancakes online with everyone! Good luck with the (non!-) quantum endeavours in Vienna together with Josh.

Maarten you were my first office mate as a PhD student and we immediately hit it off when we arranged our desks as absolute kings in our office (good old days). We also built some great things together in the lab, where I enjoyed solving many of the inevitable bugs/hacks with you. I just want to say I was happy to have moved to a different setup when you were building your magnetic field contraption of DOOM. Thank you for the great memories in and out of the lab! **Conor** you tend to show up on many papers/acknowledgements in our group, which is not only a testament to the breadth of your knowledge, but also your willingness to help out others, including me. Early on in my journey you have been a great companion in and outside the lab, either when trying to paste diamonds to PCBs at 9am or exploring Norway with Maarten. I am excited about the future challenges we are tackling!

Sophie you have been a great person to have met, both in serious meetings as well as to share some classic Dutch memes with! I have also really benefited from your great work in developing the single-click density matrix model. I wish you all the best in your future scientific journey, with Daan and your family. **Matteo P. Sr.** the one thing I have to be eternally grateful for is the wisdom you shared with me of the pizza fritto, I will always be grateful for that. A close second would be your great work in taming the software beast in the group for so many years, followed by your musical input into Q2 and the Uitjes. Even though we often do not agree on things outside Quantum, it was great exchanging ideas with each other! I know you are doing great things in the U.S., together with Grace, and I am sure we will meet each other more often in the future! **Hans** from your days as a MSc student up until today you have been a great person to have in the group. I ~~think~~ know you are the last person who would get tired of debating random topics with me, something that I regret not having exploited to the fullest during our time together in the group. Thank you for showing me (and the group) how awesome the Waddenzee can be. Good luck with writing up your thesis with the awesome tin control and your family together with Sophie! **Christopher** your calm and positive attitude make you a great person to be around. Good luck with entangling those tins, we're counting on you!

Simon it was great to have you met you, especially as one of the only 'green' people

in the group. Labels aside, it meant that you had a positive impact on the people in the group also on a personal level, something that I also experienced first hand. I also remember we figured out together that blocking a laser beam with a white card not reduce the photons into the fiber, crazy how physics does not cheat!

Julia it was great fun to hang out with you, not only in the lab but also outside: exploring the States and various places with you. Also thank you for your great ideas on how improve many processes, from giving feedback to paper readings, you have helped make them better! You can be proud of all the cool things you have achieved with the tin's in and outside of waveguides! Who knows what the future will hold for you and Bart when you decide on your future moves! **Christian** as a PhD student you were the final member of our F007 office and made it complete. Thank you for the suggestions on the youtube series on the Roman Empire, and good luck making some amazing experiments with devices in silicon!

Matteo P. Jr. I can not think of any topic that we agree on (maybe it is the name?) but that does not mean I enjoyed our trips and time spent together any less. Now that I think about it, we might both agree the Encore in Boston is a weird place! Thanks for being such a passionate and fun person to hang out with, I am sure you will do great at your new place in Barca, especially now that a 1 hour bike ride to the beach will no longer be needed! **Tim** and **Dani** you are going to accelerate the SnV efforts in the group! Good luck with all the great experiments you have planned, and most of all do not forget to have fun whilst doing it! **Niv** you have the honourable job of figuring out what is actually going on using simulations, I wish you a lot of fun with all your projects! **Mariagrazia** you bring some unique energy into the group, like making carbonara for 25+ people in the kitchen of a boat type energy. That's amazing and I have enjoyed it a lot during our work but also on the awesome trips abroad! You have had a big task in managing the networks setups, which have had their ups and downs. You are already achieved some great results, also on THE project with myself, so no stress for graduating! Thank you for being my paranymph!

Alejandro you were easily my top three PostDoc, thank you for being not afraid to say what you think, I respect that. I really enjoyed one of the most complex WK poule I have ever played, and keep killing it at HSBC! **Lorenzo** somehow you are on all the interesting papers I am reading, so naturally I am looking forward to the new things you are doing in Grenoble! Thanks for

Yanik I have seen you build up the HilaCav from scratch and I am amazed every time I walk into your lab. You can be proud of bringing the open micro-cavity project to its conclusion, which has been a long standing challenge. Thank you for the fun times in the States, showing me the true culture of the Red Roof highway motel, and good luck with writing up! **Julius** you have driven the Cavity project forward together with Yanik, but have equally driven many activities in the group/QuTech. Thanks for being such a great person, always willing to explain when I enter the lab on a random afternoon. Good luck with the final stretch of amazing experiments!

Nina you have always been doing the things I know nothing about: magic in the cleanroom. Your hard work will definitely pay off, and you should be proud of it, even if it sometimes feels like nothing is going right. Thank you for your great sense of humor and partying with me. Good luck in finding your (future) next steps! **Leo** you are in the

running to become the person with most years spent in Team-Diamond (after Ronald ofc.)! Records are meant to be broken, just make sure you keep making awesome devices while you are doing it! **Max** can't mention diamond Fab without mentioning you, even though you are very knowledgeable on so many other things! Thanks for the occasional catch-up and advice, and all the best in New-Zealand! **Matthew** we had some good fun together trying to measure single-photon detection efficiencies. Thanks for being a great person and keep it up at Qphox! **Mohamed** you always know where to get some proper food, thanks for all the chats over dinner on campus and your hospitality when showing us around in Boston!

Marianne you were my first master student that started early on. That meant we had to figure things out together, and I think it worked out pretty well. Thank you for doing some useful simulations on metropolitan scale entanglement using the single click protocol, something that we would only achieve many years later! **Stein** you were a very organized and reliable student. Thank you for your work on the CR-checking feedback algorithm! **Annick** even though you were Kian's master student I still enjoyed having you on our project, where we had some interesting sessions on how to count coincidences properly. Thanks for writing those down and your cool result of self interference! **Otmar** you always have a happy, and it is great that you brought that to our group. Thank you for diving into the theory of the NV center and Stark tuning, something that came in very handy when you returned to help out with QNE. All the best with your endeavours at TNO! To all the many, *many* Master students that joined our group over all those years, thank you for all the great work you all put in, but also the fun that you bring to the group and labs!

Ofcourse I have also met many amazing in the rest of QuTech. To start off I would like to thank members of the other half of Team-Diamond^{TM} **Hans** I always found your spin-pairs fascinating, good luck at TNO and thank you for your template and handy instructions for the thesis, also kindly compiled by **Sjoerd**. Sjoerd we unfortunately always had excuses to dodge each other, already from the start of my PhD when you were looking for a MSc Thesis. The interactions that we did end up having were a lot of fun, most notably the Diamond cup! I look forward to working a bit together! **Guido** you managed to graduate a week before me, congrats and have a great time at Stanford! **Laurens** thanks a lot for you help behind the camera and helping out with 3D printing, I knew I could rely on your artistic input! Looking forward to what you and **Gerben** cook up next! **Benjamin** and **Nico**, thank you for answering my questions on Carbon Control and when inevitably the HDAWG is being a POS, good luck with combining them with long-range entanglement! I am rooting for you! **Jiwon** very impressive results on the GateSet tomography, good luck in defining your next steps! **Margriet**, **Christina** and **Kai**: keep pushing the limits of what the NV and surroundings can do! To the other people at QuTech, thank you for being such amazing colleagues to have worked and interacted with: **Stephanie** thank you for the effort of kicking of Qlink and being a huge force championing for the Quantum Internet! The work done in your group is instrumental to bring it into reality! **Josh**, **Gert-Jan**, **Arno**, **Ling-Ling** and **Vanessa**, we put together the best Uitje QuTech ever, thanks for exploring Arnhem together! Josh, you have been paving the way in many ways, helping us by helping KPN get their fibers and workspaces in order, thanks for that! Also personally you have been a great support and an awesome friend to have met! Also

launching Q*Bird with Ingrid and Remon has put you on an impressive journey, good luck in the future together with Marie-Christine! **Ingrid** also thank you for your help in the early days of the Qlink project and keep doing great things with Q*Bird! **Anta** like clockwork you would be at QuTech on a random Saturday, great effort in finishing up that PhD! Have fun at ICFO together with Matteo!

Additionally I would like to thank all the technical staff that have solved many of the issues that I encountered over the years: **Raymond**, **Raymond**, **Roy** and **Berend**, thank you for the amazing Electronics course and help with making amazing devices for our experiments. They are the secret sauce of everly lab in QuTech. **Jason**, **Olaf** and **Remco** thank you for always being there when one of the cryostat would have issues! Your expertise has saved me many times over! Also a major thanks to all the other technicians and engineers: **Jelle**, **Roy**, **Nico** but especially **Siebe** and **Vinod** in helping out with the move to Den-Haag. **Hitham** thank you for taking safety seriously, but also helping everyone to make safety practical in the labs! Also **Regis** thank you for taking over the care for one of the Nodes, it is in good hands :)! It is impressive how you have made it into something that is useful for others already! Next to all the hardware, I can not be more thankful for all the amazing software engineers that have helped me. **Sidney** and **Joris** and the crew from **Jigsaw**, you have been instrumental in both the Qlink project, as well as my own personal knowledge of how software works! Thank you for all the fun sessions in the lab testing and debugging and the great solutions you came up with. Also **Ludo**, **Pieter**, **Henri** and **Ravi** thank you for all the great work over the years! Special shoutout to Pieter to continue the entanglement journey even longer! Also thank you **Ingmar** and **Wojchiech** to their contribution the Qlink project, and with your work on the higher software architecture with the rest of the Stack team. Even though the hardware could not keep up we should see that change in the near future!

Also a big thank you to the QuTech communications team! **Aldo** and also **Erik** thank you for being proactive and organizing great events for the QuTech speakers. Your encouragement and resources have made me a better communicator! Aldo thanks for all the brainstorming and help with the story around the metropolitan link, it really made the project much more visible. Good luck with your next endeavours! **Leonie** thank you for always being happy to have a chat and giving me opportunities to get outside my comfort zone! Good luck in your new role at the Dreamhall! Thanks to **Chantal**, **Esther** and **Sara** I never had to worry about the details when it came to shipping or scheduling meetings. Thank you for all the quick answers to my questions and meeting requests! Also all the other support staff **Jenny**, **Shannon**, **Marja** for organizing all the events and day to day tasks that make QuTech such a great place to be. **David Sayago** my first conference as a PhD student was in Brussels, where we put up a nice show! Thank you for your positive attitude and great ideas. At the end of my PhD we came together again with **Grazia** thinking about education. I still think it is a great opportunity, I hope it gains more traction somewhere in the future!

Then I have a lot of people to thank from the other half of QuTech, TNO, which has been instrumental in many stages of the Qlink project. **Jaco** you have been at the birth of the Qlink project, were crucial in setting it up and left your mark on it. I admire the structure and clarity that you brought in, thank you for all your input and hard work! **Erwin** thank you for all the questions and suggestions you bring to every meeting. I

learned a lot from your engineering perspective! Also thanks to all the optics-, control- and mechanical-engineers for: **Ronald Hagen** beign a lifesaver for QFC alignment and fiber splicing, **Martin** as optics wizard, **Ad** building the QFC, **Wouter** being especially productive on saturday when it is crunch time and right around Christmas, **Benjamin Biemond** teaching me a lot when we were taking data in the lab, **Arjan** coming in clutch in setting things straight in the midpoint and for the move, **Boudewijn** helping us out in the lab, **Andrey** getting stuff going with the frequency lock, **Rodolf** for investigating the linewidth reduced laser performance and **Shobhit** for the VOA characterization work. All your help was greatly appreciated, in the end we managed to get an awesome result and publications out of it. Thank you **Sander**, **Klaas-Jan** and **Theo** for the project management and giving me advice and opportunities for outside the project! A special thanks to the QNE team which I was happy to join in the later stages: **Jared**, **Alex**, **Christine**, **Rick**, **Mark**, **David** and **Margherita**, you have been great to work with and achieve great milestones, although bittersweet we could not reach entanglement together!

I can not forget our great colleagues and friends from Fraunhofer ILT, without whom Qlink would still be looking for signal in the noise... A million thank-yous to **Fabian**, for delivering your promise and always being on stand-by for additional efforts with the QFC! Also thanks to **Florian** and **Bernd** for having a great impact on the NORA project, as well as championing quantum networks more broadly! It was great working with you!

There are many more people that I would like to thank. Cheers **Ramiro** for being a fun roommate for so long, thanks for the chats about basically anything, and congrats on finally defending your PhD!

Bedankt heren uit Vinkeveen en omstreken: **Matthias**, **Johan**, **Wouter**, **Jos**, **Derk**, **Ruben**, **Reinier**, **Arwin**, bedankt voor alle keren dat er gewoon weer stom geouweho-erd kon worden, en alle herinneringed dat er ook nog andere dingen zijn naast werk. Ik waardeer het erg dat het altijd ouderwets gezellig is, en dat de uitnodigingen er altijd zijn zelfs als ik niets van me laat horen.

Pappa en **Mamma**, bedankt voor alle ondersteuning die ik over alle jaren van jullie heb mogen ontvangen. Bedankt ook voor jullie geduld wanneer dingen langer duurde of zelfs niet door konden gaan zoals we hoopte, niet alleen voor deze thesis maar ook daarbuiten. Bedankt ook dat jullie me de vrijheid en tools hebben gegeven om mijzelf te ontwikkelen op mijn eigen manier. Ik hoop nog veel mooie momenten met jullie te kunnen delen. **Leontine** en **Arie** door de jaren van het onderzoeken/schrijven van deze thesis zijn er veel dingen veranderd in jullie gezin. Bedankt dat jullie mij en Vincy er bij willen betrekken. Het is altijd een gezellige tijd bij jullie en de kids! **Antoinette** and **Yasser** it has been a difficult period for you, and I struggle a bit to write something witty or funny here. Thank you for making the journey to Delft with the kids, I truly cherish those memories and I hope to see you soon again. Stay safe and I keep you in my thoughts. **Mathilde** thank you for all your support over the years. You were always around the corner in Leiden, something that I maybe could have exploited more often. Thank you for always listening to my rants and being interested in what was bothering me, and for involving me in your studies as well. Your help in wedding planning was also greatly appreciated! I am also happy that you and **Daan** have a place together, and I hope to have many more dinners with you! **Vincy** thank you for all of the sacrifices that you had to make over the last years and for being with me through the ups and downs. I am

thankful for all the support you give me, and that you keep pushing me to achieve great things. You make me happy every day and I can not imagine my life without you, lets keep building and enjoy our future journey together! Love you a lottle!

LIST OF PUBLICATIONS

9. ⊗**A.J. Stolk***, K.L. van der Enden*, M.-C. Slater, I. te Raa-Derckx P. Botma, J. van Rantwijk, J.J.B. Biemond, R.A.J. Hagen, R.W. Herfst, W.D. Koek, A.J.H. Meskers, R. Vollmer, E.J. van Zwet, M. Markham,3 A.M. Edmonds, J.F. Geus, F. Elsen, B. Jungbluth, C. Haefner, C. Tresp, J. Stuhler, S. Ritter, R. Hanson *Metropolitan-scale heralded entanglement of solid-state qubits*, 2024, Science Advances **10** eadp6442

8. ⊗**A. J. Stolk**, J. J. B. Biemond, L. van Dooren, K. L. van der Enden, E. J. van Zwet, and R. Hanson *Extendable optical phase synchronization of remote and independent quantum network nodes over deployed fibers*.arxiv:2408.12464

7. ⊗ M. Iuliano*, M.-C. Slater*, **A. J. Stolk**, M. J. Weaver, T. Chakraborty, E. Loukiantchenko, G. C. do Amaral, N. Alfasi, M. O. Sholkina, W. Tittel, R. Hanson *Qubit teleportation between a memory-compatible photonic time-bin qubit and a solid-state quantum network node* arXiv:2403.18581

6. ⊗J. Geus, F. Elsen, S. Nyga, **A. Stolk**, K. van der Enden, E. van Zwet, C. Haefner, R. Hanson, B. Jungbluth. *Low-noise short-wavelength pumped frequency down-conversion for Quantum Frequency Converters.* 2023, Optica Open 107563.

5. ⊗**A.J. Stolk***, K. van der Enden*, M.-C. Roehsner, A. Teepe, S. Faes, C. Bradley, S. Cadot, J. van Rantwijk, I. te Raa, R. Hagen, A. Verlaan, J. Biemond, A. Khorev, R. Vollmer, M. Markham, A. Edmonds, J. Morits, T. Taminiau, E. van Zwet, R. Hanson. *Telecom-Band Quantum Interference of Frequency-Converted Photons from Remote Detuned NV Centers.* 2022, PRX Quantum 3, 020359.

4. M. Pompili*, C. Delle Donne*, I. te Raa, B. van der Vecht, M. Skrzypczyk, G. Ferreira, L. de Kluijver, **A.J. Stolk**, S. L. N. Hermans, P. Pawełczak, W. Kozlowski, R. Hanson, S. Wehner. *Experimental demonstration of entanglement delivery using a quantum network stack.* 2022, npj Quantum Information 8, 1–10.

3. A. Dahlberg*, M. Skrzypczyk*, T. Coopmans, L. Wubben, F. Rozpędek, M. Pompili, **A.J. Stolk**, P. Pawełczak, R. Knegjens, J. de Oliveira Filho, R. Hanson, S. Wehner. *A link layer protocol for quantum networks.* Proceedings of the ACM Special Interest Group on Data Communication, ACM, of SIGCOMM '19.

2. A. Villar, **A.J. Stolk**, A. Lohrmann, A. Ling. *Enhancing SPDC brightness using elliptical pump shapes.* 2019, Optics Express 27, 32235.

1. A. Lohrmann, A. Villar, **A.J. Stolk**, A. Ling. *High fidelity field stop collection for polarization-entangled photon pair sources.* 2018, Applied Physics Letters, 113.

⊗ (Partially) Included in this thesis.
*Equally contributing authors.

CURRICULUM VITÆ

Adriaan Johannes STOLK
August 31st, 1992, De Ronde Venen, The Netherlands

2011-2014 **Bachelor of Science**, Applied Physics
Delft University of Technology, Delft, The Netherlands
Thesis: *"Effects of noise on the fidelity of multiple qubits during twirling."*
Supervisor: Dr. Miriam Blaauboer

2014-2016 **Master of Science**, Applied Physics
Delft University of Technology, Delft, The Netherlands
Exchange student with the National University of Singapore
Thesis: *"Better control of weakly coupled ^{13}C spins surrounding an NV-centre"*
Supervisors: Dr. Julia Cramer and Dr. ir. Tim Taminiau

2015-2017 **Research Assistant**, Quantum Optics
Centre for Quantum Technologies, National University Singapore, Singapore
Performed theoretical modeling and improved experimental designs for the SpooQy-1 CubeSat entangled photon payload
Supervisor: Prof. Alexander Ling

2018-2024 **Ph.D**, Applied Physics
QuTech, Delft University of Technology, Delft, The Netherlands
Conducted pioneering research in the field of Quantum Networks, generating solid-state heralded entanglement between two Dutch cities.
Thesis: *"Going the distance: Metropolitan scale entanglement of NV-centers over deployed telecom fiber."*
Promotors: Prof. dr. ir. Ronald Hanson and Dr. ir. Tim Taminiau

2023-now **Founder of Qiraffe**
Founded a technology consulting company aimed at providing high-tech solutions and advice for institutes and start-ups in the field of Quantum Communication and Quantum Networks.

This page has been intentionally left not-blank.